MEASURING AND MODELING SEDIMENT DISPERSION IN SMALL STREAMS

by

Marianni de Aragão Nogare

B.Eng., Federal University of Rio Grande do Sul, 2015

A THESIS SUBMITTED IN PARTIAL FULFILLMENT OF

THE REQUIREMENTS FOR THE DEGREE OF

MASTER OF SCIENCE

in

THE COLLEGE OF GRADUATE STUDIES

(Earth and Environmental Sciences)

THE UNIVERSITY OF BRITISH COLUMBIA

(Okanagan)

March 2020

The following individuals certify that they have read, and recommend to the College of Graduate Studies for acceptance, a thesis/dissertation entitled:

Measuring and modeling sediment dispersion in small streams

submitted by Marianni de Aragão Nogare in partial fulfillment of the requirements of

the degree of Master of Science.

Dr. Bernard Bauer, Irving K. Barber School of Arts and Sciences

Supervisor

Dr. Jeff Curtis, Irving K. Barber School of Arts and Sciences

Supervisory Committee Member

Dr. Deborah Roberts, School of Engineering

Supervisory Committee Member

Dr. Joshua Brinkerhoff, School of Engineering

University Examiner

ABSTRACT

Turbidity-based events in multiple-use watersheds can potentially lead to negative impacts on water quality. This is of particular concern in small streams that serve as drinking water sources in the Province of British Columbia. The one-dimensional advection-dispersion equation (1D ADE) is the most common approach to modeling the transport of substances in flowing water. However, relatively little is known about its applicability to suspended sediment, especially regarding the sink term that accounts for sediment settling. The aim of this study was to assess the degree to which the 1D ADE accurately predicts suspended sediment dispersion in small channels. In addition, an evaluation of the applicability of predictive formulas for the longitudinal dispersion coefficient to small channels was undertaken.

Tracer experiments were conducted in three different channels: (1) a concrete channel; (2) a semi-natural channel; and (3) a natural channel. Sodium chloride and suspended sediment were injected simultaneously in the channels. The sediment particle sizes ranged from <0.075 mm to 1 mm. Sodium chloride was treated as a conservative tracer (i.e., no losses or gains during transport), and the sodium chloride plumes were modeled first to obtain best-fit estimates for the longitudinal dispersion coefficients. Suspended sediment plumes were modeled subsequently using the best-fit longitudinal dispersion coefficients from the sodium chloride plumes with an additional settling rate parameter to account for the sediment loss.

The 1D ADE was capable of reproducing the observed curves with ±50% relative error. The settling rate term was found to be essential to properly simulate the suspended sediment plumes. The commonly used formula for settling rate (settling velocity/depth) overestimated the loss of particles and it was not applicable to the observed data. Twenty-six predictive formulas for the longitudinal dispersion coefficient were evaluated on their ability to reproduce the observed plumes. None of the predictive formulas were able to predict the dispersion process in the small channels with less than ±50% error. The formulas from Sattar and Gharabaghi (2015) had the best performance overall. Findings from this thesis can serve as a guideline for engineers and scientists working with tracer data and water quality models in small streams.

LAY SUMMARY

Elevated sediment content in small streams located on Crown Land is of particular concern in the Province of British Columbia. Such streams serve as drinking water sources for urban centers downstream. The purpose of this study was to determine to what degree a common model utilized in water quality studies can be applied to the transport of sediment plumes in small streams as well as to assess the accuracy of predictive formulas that determine the rate of dilution of such plumes in the downstream direction. The results indicate that the model can be applied with errors within ±50% if the values for the coefficients in the model are quantified accurately. Most of the formulas available for predicting the key coefficient describing downstream mixing are not applicable to small streams because they have errors that are greater than ±50%.

PREFACE

This research was conducted by Marianni de Aragão Nogare under the supervision of Dr. Bernard Bauer. Marianni de Aragão Nogare was the primary researcher and was responsible (with assistance from Dr. Bauer) for the main study design, data collection, analysis, interpretation and writing of the content. Additional conceptual and analytical support was provided by Supervisory Committee members, Dr. Deborah Roberts and Dr. Jeff Curtis. All guidance provided by the Supervisory Committee and all literature referenced is correctly cited.

Funding for this project was provided by the BC Ministry of Forests, Lands, Natural Resource Operations and Rural Development (FLNRORD) through contracts to Dr. Bauer and Dr. Roberts to investigate multiple stressors on water quality in Crown Lands.

TABLE OF CONTENTS

LIST OF TABLES

LIST OF FIGURES

LIST OF SYMBOLS

Symbols used frequently throughout the thesis are defined here. All symbols are defined where they appear.

A = cross-sectional area

c = concentration (three-dimensional)

c_z = concentration (depth-averaged)

$\overline{C}$ = concentration (cross-sectional averaged)

D = molecular diffusion coefficient

e_i = turbulent diffusion coefficient in the i-th direction

E_y = lateral dispersion coefficient (depth-averaged)

Fr = Froude number

g = gravitational acceleration

H = flow depth

q_i = flux in the i_{th} direction per unit time per unit area

K_x = longitudinal dispersion coefficient (cross-sectional averaged)

M = mass

M_d = mass density

Pe = Peclet number

Q = discharge

S = slope

u_i = average velocity in the i-th direction

$\overline{U}$ = average cross-sectional velocity

u_* = cross-sectional average shear velocity

R_h = hydraulic radius

S_i = sinuosity factor

x = Cartesian coordinate in the streamwise direction

y = Cartesian coordinate in the lateral direction

W = flow width

z = Cartesian coordinate in the vertical direction

t = time

AKNOWLEDGMENTS

As I come to the end of this Master's journey, I would like to express my gratitude for those who were essential to me during the development of this research.

I would like to thank my supervisor, Dr. Bauer, for the opportunity of working and learning with him. Thank you for the countless hours, constant support, and essential feedback. I am also thankful for the support of the rest of my supervisory committee, Dr. Deborah Roberts and Dr. Jeff Curtis, for their valuable insights during our meetings and help during fieldwork.

I am very grateful for the field assistance provided by Alexander MacDuff, Taylor McRae, Lisa Hettrich, Polina Orlov, and Sierra Collins. Thanks for helping set up the equipment, surveying, and holding those cameras for so many hours. In the same context, many thanks to Christian St. Pierre from the BC Ministry of Forests, Lands, Natural Resource Operations and Rural Development (FLNRORD), who participated in the field experiments and conducted the discharge measurements. Thanks to Al Dolman, who graciously granted us access to his property for the natural channel experiments. Finally, thanks to Greg Courtice for lending some of the sensors utilized for the measurements.

I would like to thank the amazing faculty and staff from the Department of Earth, Environmental and Geographic Sciences, Dr. Nichol, Dr. Hornibrook, Dr. Scott, Stuart, Janet, and Christina, who I worked with and helped me during these years. Azam and Grace, thanks for the great lunches and conversations that made those long days at the office more enjoyable.

I am thankful to the BC Ministry of Forests, Lands, Natural Resource Operations and Rural Development (FLNRORD), in particular, Rob Dinwoodie and Dave Maloney, for providing financial support that allowed me to complete this research. I am also grateful to The University of British Columbia for providing additional financial support.

Lastly, I would like to thank my loving family, who has supported me in every decision and, even far away, has always been there for me. To my awesome friends, thanks for all the laughs and the support during the great and the difficult times. I ultimately would like to thank my partner, Martin, for being with me throughout this journey helping me see the good side of everything.

Chapter 1: Introduction

1.1.Motivation

Surface water is the main source of drinking water in the Province of British Columbia (BC), serving as a supply for approximately 80% of the population (Okanagan Basin Water Board 2019). However, the watersheds of BC are also used for recreational activities, forestry operations, mining, agriculture, livestock grazing, and wildlife presence. The detrimental effects of these activities in the watershed can be transferred downstream, thereby affecting water supplies far away from potential contaminant sources. The rising number of forest service roads and the traffic related to forestry operations and recreational vehicles, as well as the presence of grazing cattle and wildlife, can lead to increased delivery of sediment and other particulate matter and pathogens into the water systems. The Province of British Columbia is particularly concerned with the effect of heightened turbidity events in small streams located on Crown Land that serve as drinking water sources for urban centers downstream.

Suspended sediments and turbidity can cause several problems related to water quality, including mobilization, transportation and deposition of heavy metals, pesticides, nutrients, pathogenic bacteria, and viruses, as well as oxygen depletion. Typically, these contaminants are generated in one location within the watershed and transferred downstream within the drainage network, creating challenges for water treatment facilities located at lower elevations. Therefore, it is necessary to understand the dynamics of sediment plume transport and dispersion in order to evaluate the risks associated with multiple use watersheds.

The one-dimensional advection-dispersion equation (ADE) is the most common approach to modeling the transport and fate of substances in flowing water, focusing on longitudinal (streamwise) dispersion only (Camacho Suarez et al. 2019; Launay et al. 2015). It is a one-dimensional model because complete lateral and vertical mixing is assumed (i.e., differences in concentration in the vertical and lateral direction caused by velocity gradients are considered negligible). Thus, the one-dimensional ADE is only applicable after a certain distance downstream of the injection point, where complete vertical and lateral mixing have been achieved. Furthermore, the model does not account for transient storage effects (e.g., presence of dead zones, secondary currents, and hyporheic exchange). Despite these well-known limitations, several studies have demonstrated that the one-dimensional ADE is capable of reproducing observed

concentration curves with an acceptable degree of accuracy (Ani et al. 2009; Karwan and Saiers 2009; Launay et al. 2015). While some contaminants, such as dissolved salt, are often assumed to be conservative (i.e., no losses or gains during transport), suspended sediments will naturally settle to the bottom. Application of the one-dimensional ADE to suspended sediment modeling must, therefore, include a first-order sink term (i.e., the substance loss depends linearly on the substance concentration), which is based on the settling velocity of the particles and the average depth of the flow. The accuracy of this term has not been studied extensively, particularly for large grain size particles.

The most challenging aspect of utilizing the one-dimensional ADE to model plume dynamics is determining reasonable values for the longitudinal dispersion coefficient that align well for the situation being modeled. Ideally, tracer experiments would be conducted in the stream of interest to parameterize the rate of spread of the contaminant plume. Such field measurements, however, are costly and time-consuming. Therefore, a lot of effort has been devoted to associating the basic geometry and flow characteristics of streams with observed values of the longitudinal dispersion coefficient, yielding a large number of predictive (theoretical and empirical) formulas. Given large heterogeneity within natural channels, there remains a large degree of uncertainty associated with the prediction of longitudinal dispersion coefficients, and hence with simulating suspended sediment concentration plumes. Moreover, the majority of tracer studies were conducted in medium-sized to large rivers, resulting in a lack of information regarding the applicability of the predictive formulas to small streams.

An analysis of the applicability and limitations of the one-dimensional ADE to small streams would be of considerable practical use to engineers and scientists that do not have access to tracer data. This provides the motivation for this study.

1.2. Research questions and hypotheses

The overarching objective of this research is to better understand the dynamics of sediment plume dispersion in small streams with a view towards mitigating the potential negative impacts of turbidity-based events on water quality. More specifically, this research will address the following two questions:

1. To what extent does the one-dimensional ADE accurately predict suspended sediment dispersion in small channels if accommodation is made for particle settling via a sink term?

H1o: The one-dimensional ADE with a sink term is not capable of reproducing the observed suspended sediment plumes to an acceptable degree of accuracy.

H1a: The one-dimensional ADE with a sink term is capable of reproducing observed suspended sediment plumes to an acceptable degree of accuracy.

If the null-hypothesis H1o is rejected, leading to consideration of H1a, the following sub-questions can be investigated:

1.1 How important is the sink term in simulating suspended sediment plume dispersion?
1.2 Does the one-dimensional ADE apply everywhere within the study reach, and if not, where does it apply?
1.3 How important are lateral gradients in velocity and suspended sediment concentration when using a one-dimensional ADE approach?
1.4 How important are transient storage effects?

2. How applicable are the range of formulas for predicting the longitudinal dispersion coefficients to small channels?

H2o: None of the available formulas are applicable to small streams.

H2a: At least one of the available formulas is applicable to small streams.

1.3. Thesis outline

Chapter 2 provides a review of advection-dispersion theory as well as of current knowledge regarding its application to natural flows and suspended sediment. Chapter 3 outlines the methodologies utilized for fieldwork and data analysis. The results are reported in Chapter 4, and discussion and interpretation of the results in Chapter 5. Chapter 6 provides a summary of the main outcomes as well as recommendations for future studies. Supplementary materials are presented in the Appendices.

Chapter 2: Literature review

2.1. Governing transport processes: diffusion, advection, and dispersion

A slug of a soluble substance, such as dye or sodium chloride, when introduced in a river, will travel downstream at the mean flow velocity while spreading out and changing shape (Elhadi et al. 1984). The physical processes associated with this phenomenon are advection and diffusion, respectively. When turbulent diffusion processes are averaged over one or more dimensions, new mixing processes referred to as dispersive transport arise. These processes constitute the basis of the advection-dispersion equation, which is commonly used to model the transport of substances in surface waters (Drummond et al. 2012; Rutherford 1994; Wallis and Manson 2004).

2.1.1. Molecular diffusion

Molecular diffusion refers to the spreading out of a substance due to the random motion of molecules in a fluid in the presence of a concentration gradient, which yields a transfer of the substance from areas of large concentration to areas of small concentration (Fick 1995). Molecular diffusion dominates the spread of a substance in still fluids and in laminar flows.

The diffusion process is often described as particles taking a series of steps in a random walk process. Consider a one-dimensional environment where each step has a length of Δx and takes a certain time Δt. Let $p[n\Delta x, m\Delta t]$ represent the probability that a particle is at a location $n\Delta x$ at a time $m\Delta t$. Assume also that all particles are inserted at $\Delta x = 0$ at $t = 0$, thus $p[0,0] = 1$ and $p[n\Delta x, 0] = 0$ and that the particles behave independently. Each particle has a probability p of moving to the right (positive), a probability p of moving to the left (negative), and a probability $1 - 2p$ of remaining in the same position. Formally, $p[n\Delta x, m\Delta t]$ can be written as:

$$p[n\Delta x, m\Delta t] = p[(n-1)\Delta x, (m-1)\Delta t] + p[(n+1)\Delta x, (m-1)\Delta t] + (1-2p)[n\Delta x, (m-1)\Delta t] \quad (1)$$

where $p[(n-1)\Delta x, (m-1)\Delta t]$ = probability that a particle occupying a location to the left of $n\Delta x$ moved to the right; $p[(n+1)\Delta x, (m-1)\Delta t]$ = probability that a particle occupying a location to the right of $n\Delta x$ moved to the left, and $(1-2p)[n\Delta x, (m-1)\Delta t]$ = probability that a particle already at $n\Delta x$ did not move.

The time evolution of the probabilities associated with this random walk process are given in Table 1 for (left, stay, right) probabilities of (0.5, 0, 0.5), (0.33, 0.33, 0.33), and (0.25, 0.5, 0.25). The values in Table 1 show how an initial stack of particles at n = 0 is likely to spread laterally as time increases. As m increases, the probabilities associated with the discrete random walk process become very similar to a continuous distribution and they can be approximated by a Gaussian distribution:

$$p(x,t) = \frac{1}{\sigma_x\sqrt{2\pi}} \exp\left(\frac{-x^2}{2{\sigma_x}^2}\right) dx \qquad (2)$$

where p(x, t) = the probability that a particle is at a location between x and x + dx at time t, x = location, and σ_x = standard deviation.

At every step, the probability (p) that a particle is going to be at a certain position away from the origin decreases. The probability of finding the particle near the origin is large because the particle can always move back once it has moved away. However, as distance from the origin increases, the probability of particles occupying those central locations decreases.

Table 1. Time evolution of the probabilities associated with the random walk process for (left, stay, right) probabilities of (0.5, 0, 0.5), (0.33, 0.33, 0.33), and (0.25, 0.5, 0.25).

(0.5, 0,0.5)	**n =**	**-5**	**-4**	**-3**	**-2**	**-1**	**0**	**1**	**2**	**3**	**4**	**5**
m												
0							1.000					
1						0.500	0	0.500				
2					0.250	0	0.500	0	0.250			
3				0.125	0	0.375	0	0.375	0	0.125		
4			0.063	0	0.250	0	0.375	0	0.250	0	0.063	
5		0.031	0	0.156	0	0.313	0	0.313	0	0.156	0	0.031

(0.33, 0.33, 0.33)	**n =**	**-5**	**-4**	**-3**	**-2**	**-1**	**0**	**1**	**2**	**3**	**4**	**5**
m												
0							1.000					
1						0.333	0.333	0.333				
2					0.111	0.222	0.333	0.222	0.111			
3				0.037	0.111	0.222	0.259	0.222	0.111	0.037		
4			0.012	0.049	0.123	0.198	0.235	0.198	0.123	0.049	0.012	
5		0.004	0.021	0.062	0.123	0.185	0.210	0.185	0.123	0.062	0.021	0.004

(0.25, 0.50, 0.25)	**n =**	**-5**	**-4**	**-3**	**-2**	**-1**	**0**	**1**	**2**	**3**	**4**	**5**
m												
0							1.000					
1						0.250	0.500	0.250				
2					0.063	0.250	0.375	0.250	0.063			
3				0.016	0.094	0.234	0.313	0.234	0.094	0.016		
4			0.004	0.031	0.109	0.219	0.273	0.219	0.109	0.031	0.004	
5		0.001	0.010	0.044	0.117	0.205	0.246	0.205	0.117	0.044	0.010	0.001

.

Considering an ensemble of N particles (a plume) released at location x_0 and at time t_0, the number of particles located between x and x + dx at a later time t is given by:

$$N(x,t) = N(x_0,t_0)\ p(x,t) \tag{3}$$

Assuming that each particle has a density ρ_p and occupies a volume V_p, the total mass of the ensemble located between x and x + dx at a time t is given by $m_p = \rho_p V_p\ N(x_0,t_0)p(x,t)$. The concentration of particles (in mass per volume) can be determined by dividing the total mass of the particles by the volume defined by the cross-sectional area times dx, which is an incremental distance in the flow-parallel direction. These considerations yield:

$$c(x,t) = \frac{\rho_p V_p\ N(x_0,t_0)\ p(x,t)}{A\ dx} = \frac{M_d\ p(x,t)}{dx} \tag{4}$$

where c(x, t) = concentration of particles at location x at a time t (ML^{-3}), A = cross-sectional area of the one-dimensional environment perpendicular to the transport direction (L^2), and M_d = mass density (ML^{-2}).

The concentration at a certain location x at a certain time t is proportional to the probability of finding the particles at that certain location. Substituting p(x, t) by the right-hand side of (2), Equation 4 can be rewritten as:

$$c(x,t) = \frac{M_d}{\sigma_x\sqrt{2\pi}} \exp\left(\frac{-x^2}{2{\sigma_x}^2}\right) \tag{5}$$

Figure 1 shows the time evolution of concentration as given by Equation 5.

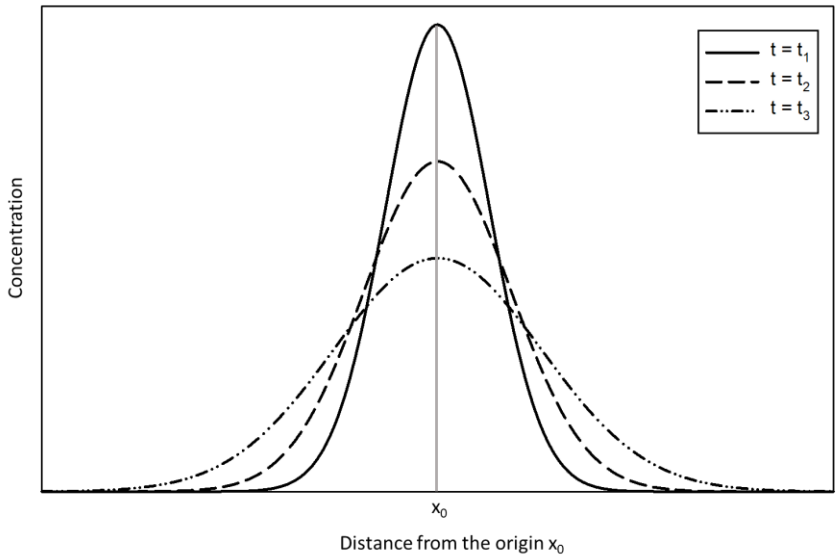

Figure 1. Time evolution of concentration as a consequence of the molecular diffusion process.

Basic properties of Equation 5 can be obtained by analyzing its spatial moments. The total mass density of the plume can be obtained by the zero-th spatial moment (i.e., the integral of c(x,t) over dx):

$$M_d = \int_{-\infty}^{\infty} c(x,t)\, dx \tag{6}$$

The mean position of the plume (μ) away from the origin at a certain time t can be obtained by the first spatial moment normalized by the total mass density:

$$\mu = \frac{\int_{-\infty}^{\infty} x\, c(x,t)\, dx}{\int_{-\infty}^{\infty} c(x,t)\, dx} \tag{7}$$

For a Gaussian distribution, since the particles have the same probability of moving in the positive and negative directions, the mean is zero, $\mu = 0$. This result, albeit somewhat trivial, demonstrates that the mean position of a particle ensemble does not change even though individual particles may shift their position away from the starting location.

The spatial variance (σ_x^2) of the plume can be obtained by the second spatial moment of Equation 5 centered on the mean and normalized by the total mass. Noting that the mean is zero, the spatial variance is given by:

$$\sigma_x{}^2 = \frac{\int_{-\infty}^{\infty}(x-\mu)^2\, c(x,t)\, dx}{\int_{-\infty}^{\infty} c(x,t)dx} = \frac{\int_{-\infty}^{\infty} x^2\, c(x,t)\, dx}{M_d} \quad (8)$$

The spatial variance is a measure of the width of the plume from the origin after a certain time. Given that the movement of the particles is random, the precise location of any single particle cannot be predicted deterministically. However, it is possible to make predictions regarding ensemble behavior. Substituting (4) in (8) yields:

$$\sigma_x{}^2 = \frac{\int_{-\infty}^{\infty} x^2\, M_d\, p(x,t)\, dx}{M_d} = \int_{-\infty}^{\infty} x^2\, p(x,t)\, dx = < x^2 > \quad (9)$$

where x^2 = squared displacement of the particles from the origin at x = 0, and the angle brackets < > symbolize the ensemble average for that position.

Equation 9 demonstrates that the spatial variance of a plume is equivalent to the ensemble mean square displacement of the particles away from the origin. This is an essential relation, that will be utilized later to define the spread of plumes in turbulent flows. In a Gaussian distribution, approximately 95% of the plume lies between $-1.96\sigma_x$ and $+1.96\sigma_x$ (i.e., the region that captures most of the solute mass). Therefore, $4\sigma_x$ is a common way to estimate the plume width.

The net flux of particles in the direction of transport can be obtained by analyzing the number of particles, $N(n\Delta x, m\Delta t)$, that are transported over a distance Δx at every time step Δt. For an ensemble of particles starting at the origin 0 at time-step m, $N(0, m\Delta t)$, some fraction of the particles will move to the right or the left over a distance Δx after a certain time Δt according to their probabilities of moving right or left. The net number of particles moving to the left (negative direction) is, on average, equal to the number of particles moving to the right (positive direction), which is given by:

$$\frac{1}{2}[N(0, m\Delta t) - N[(0 + \Delta x, m\Delta t)] \quad (10)$$

Since the distribution is symmetrical, we need only consider the positive direction. The net flux of particles (# per unit area per unit time) in the direction of transport is obtained by dividing the number of particles by the cross-section area perpendicular to the movement of the particles, A, and the duration of the step Δt:

$$q_{d,x} = \frac{1}{2A\Delta t}[N(0, m\Delta t) - N(\Delta x, m\Delta t)] \quad (11)$$

Multiplying both sides of Equation 11 by Δx^2 and rearranging to bring the negative sign outside the square brackets, one can obtain the particle number flux in terms of the difference in concentration between positions Δx and 0:

$$q_{d,x} = -\frac{\Delta x^2}{2\Delta t}\frac{1}{\Delta x}\left[\frac{N(\Delta x, m\Delta t)}{A\Delta x} - \frac{N(0, m\Delta t)}{A\Delta x}\right] \quad (12)$$

The term $\Delta x^2/2\Delta t$ is taken as being a constant of proportionality because, in the random walk process imagined above, the horizontal steps (Δx) are fixed and integrally linked to the time steps given by Δt. The constant of proportionality is referred to as the molecular diffusion coefficient (D), and its substitution in Equation 12 yields:

$$q_{d,x} = -D\frac{1}{\Delta x}[c(\Delta x) - c(0)] \quad (13)$$

Note that the terms in square brackets in Equation 13 are now expressed as concentrations. In the development of Equation 12, however, these terms were numbers of particles per unit volume, where the volume domain was defined explicitly by the cross-sectional area perpendicular to the transport direction, A, and the spatial step, Δx, associated with the time step, Δt, used to define D. Thus, there is an integral co-dependency between how D is defined and how concentration should be quantified with respect to time and space steps. This issue will be re-visited later in the thesis, but for now, a generalized version of Equation 13 is sought. In the limit, as $\Delta x \to 0$, Equation 13 can be written as a partial derivative:

$$q_{d,x} = -D\frac{\partial c}{\partial x} \quad (14)$$

$q_{d,x}$ = particle mass flux by molecular diffusion in the x direction (of flow) per unit area per unit time ($ML^{-2}T^{-1}$), D = molecular diffusion coefficient (L^2T^{-1}), and $\partial c/\partial x$ = mass concentration gradient in the x direction ($ML^{-3}L^{-1}$).

Equation 14 is known as Fick's First Law of Diffusion (Fick 1995), which shows that the mass flux by molecular diffusion is proportional to the concentration gradient. Similar fluxes can be written for the y and z directions in a three-dimensional environment. The molecular diffusion

coefficient, D, is a property of the fluid, just as density or viscosity, because in the example above there was no flow invoked. For a given combination of solvent, solute, and temperature, D is usually considered a constant (Rutherford 1994). Because mass is transported from areas of large concentration to areas of smaller concentration, the negative sign on the diffusive fluxes converts a negative concentration gradient (over positive distance) into a positive flux (Schnoor 1996).

The term $\Delta x^2/2\Delta t$ was used to define the molecular diffusion coefficient in Equation 13, which leads to:

$$\sigma_x{}^2 = < x^2 > = 2Dt \tag{15}$$

This means that the spatial variance of the particles (i.e., the width of the plume) increases linearly with time for a normal distribution. This is a key property of the molecular diffusion process, which will help define the turbulent diffusion process. Substituting (15), Equation 5 becomes:

$$c(x,t) = \frac{M_d}{2\sqrt{\pi Dt}} \exp\left(\frac{-x^2}{4Dt}\right) \tag{16}$$

The use of this equation is strictly based on the assumption that the molecular diffusion coefficient, D, is a constant, as stated by (15).

Considering that the diffusion process occurs within a finite volume, the rate of change in concentration over time $\partial c/\partial t$ at a point locally within the finite volume can be defined by applying the principle of mass conservation to an infinitesimal control volume with dimensions dx, dy, and dz embedded within the larger finite volume (Figure 2):

$$\left(\frac{\partial c}{\partial t}\right) dxdydz = m_{in} - m_{out} + \dot{m} \tag{17}$$

where m_{in} = rate of mass entering the control volume (MT^{-1}), m_{out} = rate of mass leaving the control volume (MT^{-1}), and $\dot{m}$ = internal sources/sinks (MT^{-1}).

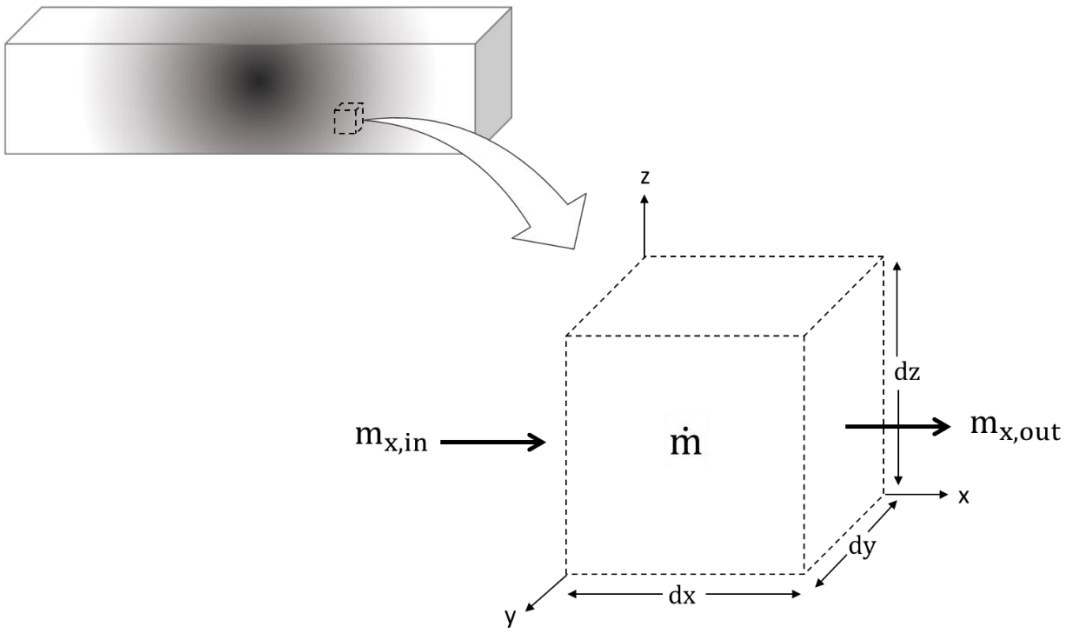

Figure 2. Infinitesimal control volume defined by dxdydz located inside a larger volume where there are concentration gradients.

The mass transport rate through the control volume in any cardinal direction is represented by the product of a flux times the cross-sectional area perpendicular to flux direction:

$$m_i = q_i \times A \tag{18}$$

where m_i = rate of mass transport in the i-th direction (MT^{-1}), q_i = mass flux in the i-th direction per unit area per unit time (ML^2T^{-1}), and A = surface area perpendicular to the mass flux (L^2), as originally used in Equation 12. Note that in Equation 18, q_i is a general flux that may be due to advective or diffusive processes or a combination of both.

The mass fluxes across opposite faces of the control volume are evaluated by utilizing the Taylor series expansion (to first order), yielding:

$$q_{x+dx} = q_x + \left(\frac{\partial q_x}{\partial x}\right) dx \tag{19}$$

$$q_{y+dy} = q_y + \left(\frac{\partial q_y}{\partial y}\right) dy \tag{20}$$

$$q_{z+dz} = q_z + \left(\frac{\partial q_z}{\partial z}\right) dz \tag{21}$$

Substituting Fick's Law for Diffusion (Equation 14) for each of the fluxes in (19)-(21), and assuming no internal source/sink terms in Equation 17 ($\dot{m} = 0$), yields the following equation for the rate of change of concentration inside the control volume caused by molecular diffusion alone:

$$\frac{\partial c}{\partial t} = \frac{\partial}{\partial x}\left(D\frac{\partial c}{\partial x}\right) + \frac{\partial}{\partial y}\left(D\frac{\partial c}{\partial y}\right) + \frac{\partial}{\partial z}\left(D\frac{\partial c}{\partial z}\right) \tag{22}$$

Assuming that D is constant in the fluid domain regardless of direction, Equation 22 becomes (Fick 1995; Fischer et al. 1979; Rutherford 1994):

$$\frac{\partial c}{\partial t} = D\left(\frac{\partial^2 c}{\partial x^2} + \frac{\partial^2 c}{\partial y^2} + \frac{\partial^2 c}{\partial z^2}\right) \tag{23}$$

Equation 23 is Fick's Second Law of Diffusion (Fick 1995), which states that the rate of change in concentration caused by diffusion is proportional to the variation of the concentration gradient in each direction.

2.1.2. Advection-diffusion

The diffusion equation derived in 2.1.1 considers particle diffusion in a still fluid. In rivers and streams, the particles are also being transported downstream by advection as diffusion occurs. Advection is the movement of a substance (dissolved or suspended) in a flow at the mean flow velocity without spread or distortion (Benettin et al. 2013; Van Genuchten et al. 2013; Schnoor 1996). The advective flux of a substance is a function of flow velocity and concentration of the substance:

$$q_{a,i} = u_i c \tag{24}$$

where $q_{a,i}$ = advective flux in the i-th direction per unit time per unit area ($ML^{-2}T^{-1}$), u_i = velocity in the i-th direction (perpendicular to the unit area) (LT^{-1}), and c = substance mass concentration (ML^{-3}).

Substituting the advective flux for each of the fluxes in (19)-(21), and solving Equation 17 from a Eulerian frame of reference where fluid passes through an infinitesimal control volume and

with the assumption that there are no sources/sinks inside the control volume ($\dot{m} = 0$), the rate of change of concentration inside the control volume caused by advection is given by:

$$\frac{\partial c}{\partial t} = -\frac{\partial (u_x c)}{\partial x} - \frac{\partial (u_y c)}{\partial y} - \frac{\partial (u_z c)}{\partial z} \tag{25}$$

Assuming that advection and diffusion are independent and additive processes, Equations 23 and 25 can be combined to yield a general three-dimensional advection-diffusion equation in Cartesian coordinates:

$$\frac{\partial c}{\partial t} + \frac{\partial (u_x c)}{\partial x} + \frac{\partial (u_y c)}{\partial y} + \frac{\partial (u_z c)}{\partial z} = D\left(\frac{\partial^2 c}{\partial x^2} + \frac{\partial^2 c}{\partial y^2} + \frac{\partial^2 c}{\partial z^2}\right) \tag{26}$$

There is no general solution to this partial differential equation. However, knowing the flow velocities, the molecular diffusion coefficient, as well as initial and boundary concentrations, it is possible to predict the concentration changes over time and space using Equation 26 (Rutherford 1994).

2.1.3. Advection-diffusion in turbulent flows

In laminar flow, the viscous forces are stronger than the inertial forces, therefore, the fluid elements follow smooth paths that do not cross each other (Rutherford 1994). In turbulent flows, the inertial forces dominate and there are random velocity fluctuations in the form of eddies that cause fluid mixing. This mixing by eddies facilitates diffusion of solutes and particles suspended in the flow. Thus, turbulent diffusion is more rapid than molecular diffusion (Rutherford 1994).

In turbulent flows the velocities vary randomly with time, therefore, it is difficult to make deterministic predictions of the position of fluid molecules (Rutherford 1994). A similar behavior is observed for non-fluid particles (or substances) embedded within the flow because the velocity fluctuations induce the turbulent mixing process. As with molecular diffusion, averaging is utilized to describe the statistical (probabilistic) behavior of the velocities and concentrations over time and space. Ideally, the ensemble average of tracer concentration at a certain time and location downstream of the injection point would be obtained by conducting several similar injection experiments. But this can be costly and impractical, so time averaging and coordinate averaging are often invoked depending on the specifics of the situation under interest.

In order to use Equation 26 for practical applications, the velocity and concentration terms must be estimated by quantities that are relevant for turbulent flows. Reynolds suggested that the instantaneous velocities and concentrations in turbulent flows can be separated into two components: an ensemble-averaged steady component ($< u_i >$, $< c >$) and a fluctuating random component (u_i', c') (Julien 2010; Rutherford 1994):

$$u_i =< u_i > +u_i' \tag{27}$$

$$c =< c > +c' \tag{28}$$

where u_i = velocity in the i-th direction.

The steady (averaged) component is responsible for advection, while the fluctuating component arises due to small-scale turbulent eddies that are responsible for mixing (i.e., turbulent diffusion). Substituting (27) and (28) into (26) yields:

$$\begin{aligned}\frac{\partial}{\partial t}(< c > +c') + \frac{\partial(< u_x > +u_x')(< c > +c')}{\partial x} + \frac{\partial\big(< u_y > +u_y'\big)(< c > +c')}{\partial y} \\ + \frac{\partial(< u_z > +u_z')(< c > +c')}{\partial z} \\ = D\left(\frac{\partial^2}{\partial x^2}(< c > +c') + \frac{\partial^2}{\partial y^2}(< c > +c') + \frac{\partial^2}{\partial z^2}(< c > +c')\right)\end{aligned} \tag{29}$$

Equation 29 can be expanded using the product rule, yielding:

$$\begin{aligned}\frac{\partial < c >}{\partial t} + \frac{\partial c'}{\partial t} + \frac{\partial < u_x >< c >}{\partial x} + \frac{\partial < u_x > c'}{\partial x} + \frac{\partial u_x' < c >}{\partial x} + \frac{\partial u_x' c'}{\partial x} + \\ \frac{\partial < u_y >< c >}{\partial y} + \frac{\partial < u_y > c'}{\partial y} + \frac{\partial u_y' < c >}{\partial y} + \frac{\partial u_y' c'}{\partial y} + \frac{\partial < u_z >< c >}{\partial z} + \\ \frac{\partial < u_z > c'}{\partial z} + \frac{\partial u_z' < c >}{\partial z} + \frac{\partial u_z' c'}{\partial z} = \\ D\left(\frac{\partial^2 < c >}{\partial x^2} + \frac{\partial^2 c'}{\partial x^2} + \frac{\partial^2 < c >}{\partial y^2} + \frac{\partial^2 c'}{\partial y^2} + \frac{\partial^2 < c >}{\partial z^2} + \frac{\partial^2 c'}{\partial z^2}\right)\end{aligned} \tag{30}$$

Given that the fluctuations around the mean are random, in order to assess Equation 30, it is necessary to take its ensemble average. The following Reynolds averaging rules apply when taking the ensemble average:

i. The ensemble average of an ensemble average $\ll c \gg$, is simply the ensemble average; therefore, products such as $<< c >< u_i >>$ are equal to $< c >< u_i >$;

ii. The ensemble average of the velocity and concentration fluctuations are zero ($< u_i' > = 0, < c' > = 0$), given that they are random fluctuations around a steady value. Therefore, products such as $<< c >< u_i' >>$ and $<< c' >< u_i >>$ are zero;

iii. Products of two random fluctuations, however, are not zero and must be evaluated ($<< c' >< u_i' >> \neq 0$);

iv. The ensemble average of a partial differential such as $< \partial u_i/\partial i >$ is the partial differential of the ensemble average $\partial < u_i >/\partial i$.

Therefore, terms such as:

$$\frac{\partial < c' >}{\partial t}, \frac{\partial < u_i >< c' >}{\partial i}, \frac{\partial < u_i' >< c >}{\partial i}, \frac{\partial^2 < c' >}{\partial i^2}$$

are zero and Equation 30 becomes:

$$\begin{aligned} \frac{\partial < c >}{\partial t} + \frac{\partial < u_x >< c >}{\partial x} + \frac{\partial < u_x' c' >}{\partial x} + \frac{\partial < u_y >< c >}{\partial y} \\ + \frac{\partial < u_y' c' >}{\partial y} + \frac{\partial < u_z >< c >}{\partial z} + \frac{\partial < u_z' c' >}{\partial z} \\ = D\left(\frac{\partial^2 < c >}{\partial x^2} + \frac{\partial^2 < c >}{\partial y^2} + \frac{\partial^2 < c >}{\partial z^2}\right) \end{aligned} \tag{31}$$

If the statistical properties of the velocity and concentration are assumed to be independent of time over some interval T, the ensemble averages can be approximated by their time average (Rutherford 1994):

$$< u_i > \approx \frac{1}{T}\int_0^T u_i = \bar{u}_i \tag{32}$$

$$< c > \approx \frac{1}{T}\int_0^T c = \bar{c} \tag{33}$$

where the overbar represents a time average, yielding:

$$\frac{\partial \bar{c}}{\partial t} + \frac{\partial \overline{u_x c}}{\partial x} + \frac{\partial \overline{u_y c}}{\partial y} + \frac{\partial \overline{u_z c}}{\partial z} + \frac{\partial \overline{u_x' c'}}{\partial x} + \frac{\partial \overline{u_y' c'}}{\partial y} + \frac{\partial \overline{u_z' c'}}{\partial z} = D\left(\frac{\partial^2 \bar{c}}{\partial x^2} + \frac{\partial^2 \bar{c}}{\partial y^2} + \frac{\partial^2 \bar{c}}{\partial z^2}\right) \quad (34)$$

The additional terms containing the products of velocity and concentration fluctuations (similar to those associated with turbulence closure) represent the additional mixing processes caused by the turbulence in the flow, and these are responsible for turbulent diffusion. Because turbulent mixing is driven by the velocity fluctuations, this diffusive process is dependent on the flow conditions, unlike molecular diffusion which depends on the properties of the fluid. In order to address this challenge, the turbulent diffusion terms are generally related to some property of the average concentration, borrowing from Fick's development of molecular diffusion (Elhadi et al. 1984; Rutherford 1994):

$$-\overline{u_x' c'} = e_x \frac{\partial \bar{c}}{\partial x} \quad (35)$$

$$-\overline{u_y' c'} = e_y \frac{\partial \bar{c}}{\partial y} \quad (36)$$

$$-\overline{u_z' c'} = e_z \frac{\partial \bar{c}}{\partial z} \quad (37)$$

where e_i = turbulent diffusion coefficient in the i-th direction.

Substituting the turbulent fluxes (35)-(37) in Equation 34 yields:

$$\frac{\partial \bar{c}}{\partial t} + \frac{\partial \bar{u}_x \bar{c}}{\partial x} + \frac{\partial \bar{u}_y \bar{c}}{\partial y} + \frac{\partial \bar{u}_z \bar{c}}{\partial z} = \frac{\partial}{\partial x}\left((D + e_x)\frac{\partial \bar{c}}{\partial x}\right) + \frac{\partial}{\partial y}\left((D + e_y)\frac{\partial \bar{c}}{\partial y}\right) + \frac{\partial}{\partial z}\left((D + e_z)\frac{\partial \bar{c}}{\partial z}\right) \quad (38)$$

Unlike the molecular diffusion coefficient, the turbulent diffusion coefficient is a property of the flow, therefore, it will vary according to the flow directionality and turbulence intensity. Since $e_i \gg D$, D is often omitted from the equations with the understanding that molecular diffusion is subsumed within turbulent diffusion. Equation 38 then reduces to:

$$\frac{\partial \overline{c}}{\partial t} + \frac{\partial \overline{u}_x \overline{c}}{\partial x} + \frac{\partial \overline{u}_y \overline{c}}{\partial y} + \frac{\partial \overline{u}_z \overline{c}}{\partial z} = \frac{\partial}{\partial x}\left(e_x \frac{\partial \overline{c}}{\partial x}\right) + \frac{\partial}{\partial y}\left(e_y \frac{\partial \overline{c}}{\partial y}\right) + \frac{\partial}{\partial z}\left(e_z \frac{\partial \overline{c}}{\partial z}\right) \quad (39)$$

Equation 39 represents the basis for most transport mixing problems. It can be simplified if it is assumed that the diffusion coefficients are invariant in space, in which case they appear outside the differential, as is quite common. Similarly, averaging in one or more directions (e.g., depth or width) leads to a simpler expression. However, the equation can become more complex with the addition of source/sink terms in cases where the substance being modeled undergoes physical, biological, or chemical reactions.

The theoretical justification for modeling turbulent diffusion using Fick's Law for molecular diffusion was provided by Taylor (1922). Taylor (1922) studied diffusion in turbulent flows with stationary, homogeneous turbulence, assuming a straight channel with constant depth and great width. Stationary turbulence occurs when flow properties such as velocity, velocity variance, and correlations are constant over time. Homogeneous turbulence occurs when the velocity fluctuations and correlations for a given direction are constant in space (Rutherford 1994). Despite the random nature of turbulent fluctuations, the particle velocities are correlated over short times and distances (Rutherford 1994). The correlation is inversely proportional to the distance separating the points, such that at some large distance separating points 1 and 2, the velocity fluctuations at point 1 are no longer correlated to those at point 2. The largest distance at which velocities remain correlated is determined by the size of the largest eddies (Rutherford 1994). In rivers, the maximum size of the eddies in the vertical and lateral directions is determined by the depth and the width of the channel, respectively (Rutherford 1994). Taylor (1922) utilized a Lagrangian reference frame, where a fluid element is tracked as it moves through time and space. He demonstrated that for an ensemble of particles injected in turbulent flow, the ensemble average of the squared displacement in the x-direction is given by:

$$< x^2 > = 2 < u_x{}'^2 > \int_{s=0}^{t} (t - s) R(s)\, ds \quad (40)$$

where $< x^2 >$ = ensemble average of the squared displacement in the x-direction, $< u_x{}'^2 >$ = ensemble average of the squared velocity fluctuations in the x-direction, t = time since injection, s = time difference between the velocity fluctuation observations, $R(s)$ = Lagrangian autocorrelation function.

The ensemble average square displacements in the y- and z-directions have equivalent expressions. The Lagrangian autocorrelation function determines the correlation between the velocity of a certain particle at a time t_1 and the velocity of the same particle at a later time t_2, where the time passed between t_2 and t_1 is equal to s. Although the autocorrelation function cannot be predicted theoretically, by definition it is assumed that at very short times ($s \to 0$) the velocities are completely correlated, therefore:

$$R(0) = 1 \tag{41}$$

On the other hand, at large times ($s \to \infty$), the velocities are assumed to be completely uncorrelated, therefore:

$$R(\infty) = 0 \tag{42}$$

The amount of time it takes for the velocities to become completely uncorrelated is known as the Lagrangian time scale T_L, defined as:

$$T_L = \int_0^\infty R(s)ds \tag{43}$$

Taking Equations 43 and 44 as alternative limits to a diffusive process, it is possible to identify two distinct scenarios (one where particle trajectories are correlated in time and another where they are independent). Using these limits in Equation 40 yields two expressions for the mean squared displacement.

When $t << T_L$, the integral of $t - s$ over ds ($ts - s^2/2 + constant$) is evaluated at the limits 0 and t yielding:

$$< x^2 > \approx < u_x{}'^2 > t^2 \qquad \text{when } t \ll T_L \tag{44}$$

When $t >> T_L$, (42) can be integrated by parts, yielding:

$$< x^2 > \approx 2 < u_x{}'^2 > T_L t + constant \qquad \text{when } t \gg T_L \tag{45}$$

where $< x^2 >$ = ensemble average of the squared displacement, $< u_x{}'^2 >$ = ensemble average of the autocorrelation between velocity fluctuations, t = time from injection, and T_L = Lagrangian time-scale.

Utilizing Reynolds analogy and assuming that turbulent eddies transfer momentum and mass at almost the same rate (Rutherford 1994), the ensemble average of the squared displacement of the particles defined in (44) and (45) also define the ensemble average squared displacement of tracer particles. Furthermore, as it was demonstrated in 2.1.1, the ensemble average of the squared displacement is equivalent to the spatial variance of the plumes (Equation 9). Therefore, close to the injection time, the velocity fluctuations of the particles are strongly correlated with their initial values and the spatial variance of the plume increases with t^2 (Equation 44). This period when $t \ll T_L$ is known as the advective period. When $t \gg T_L$, the spatial variance of the plume increases linearly with time (Equation 45). This period is known as the equilibrium period, and since the particle trajectories are not correlated (i.e., independent, random) this is the domain to which the diffusion processes embodied in Equation 39 applies. The fact that the spatial variance grows linearly with time in turbulent flows, downstream of the advective zone, suggests that turbulent diffusion can be modelled in a manner similar to molecular diffusion as long as enough time has elapsed since the tracer release (i.e., $t \gg T_L$) (Roberts and Webster 2002; Rutherford 1994).

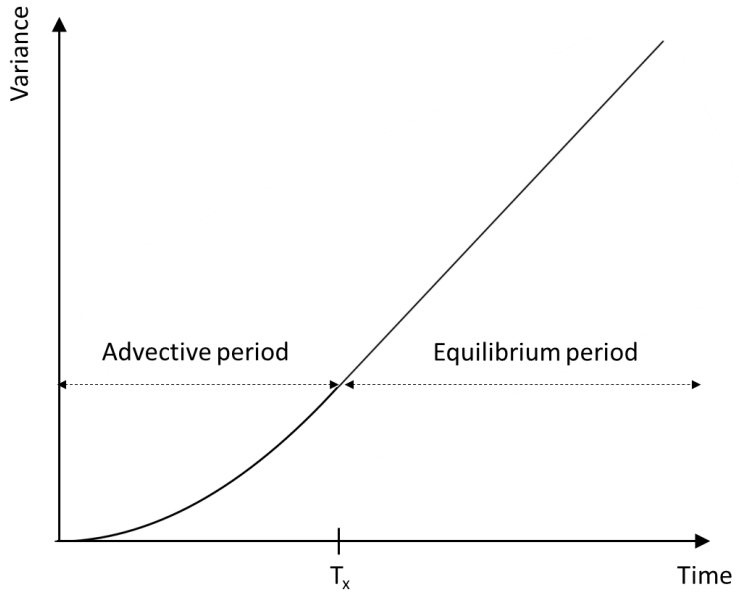

Figure 3. Behavior of variance over time in the advective and equilibrium periods.

On dimensional grounds, it is possible to define a Lagrangian length scale, L_L, given by:

$$L_L = \sqrt{< u_x'^2 >}\, T_L \tag{46}$$

Therefore, the advective and equilibrium periods have analogues in space, commonly referred to as advective and equilibrium zones.

An important consequence of Taylor's analysis involves the temporal behavior of the turbulent diffusion coefficients under homogeneous, stationary turbulence. In laminar flows, the rate of spread of the plume is determined by the molecular diffusion coefficient. Differentiating Equation 15 with time yields:

$$\frac{1}{2}\frac{d < x^2 >}{dt} = D \tag{47}$$

When turbulent diffusion is present, since $e_i >> D$, the spread of a plume is mainly governed by the turbulent diffusion coefficients. Differentiating Equations 44 and 45 with time yields the rates of spread for each case:

$$\frac{1}{2}\frac{d<x^2>}{dt} = < u_x'^2 > \; t = e_x \qquad \text{for } t \ll T_L \tag{48}$$

$$\frac{1}{2}\frac{d<x^2>}{dt} = < u_x'^2 > T_L = e_x \qquad \text{for } t \gg T_L \tag{49}$$

Equations 48 and 49 suggest it is possible to determine the turbulent diffusion coefficients if the velocity field is known (i.e., turbulent diffusion depends on the turbulent velocity fluctuations). Equation 48 shows that in the advective period ($t \ll T_L$), the turbulent diffusion increases with time (i.e., it is not a constant). Equation 49 shows that in the equilibrium period, the turbulent diffusion coefficient becomes a constant (Roberts and Webster 2002; Rutherford 1994) and Equation 39 can be utilized to estimate concentrations over time and space. However, without extensive knowledge about the velocity field, it is difficult to determine the boundary between the advective and equilibrium zones, hence, where (39) can be applied with confidence. This problem will be reviewed in 2.1.5.1 with a focus on the one-dimensional ADE.

2.1.4. Dispersion

In real channels with side-walls and beds that impart flow resistance, neutrally buoyant particles are advected downstream at different speeds depending on their distance from the wetted perimeter. This process is known as differential advection (Wallis and Manson 2004). Equation 41 provides the basis for analyzing mixing processes in open-channel flows. However, it requires a large amount of information regarding velocity distributions and diffusion coefficients, which are not practical to obtain during field studies in natural channels (Rutherford 1994). Therefore, Equation 41 is often simplified by averaging terms over one or more dimensions. This process of averaging velocity fields over one or more dimensions yields additional mixing processes referred to as dispersive transport, shear-induced dispersion, or simply, dispersion (Rutherford 1994; Wallis and Manson 2005). The basic processes involved in dispersive transport are advection and diffusion. If one has complete knowledge of the velocity fields and turbulent diffusion in all directions, there is no need to account for dispersion explicitly (Elhadi et al. 1984), but this is rarely the case.

Consider a vertical line source of tracer introduced into the middle of a channel, far away from the banks. The tracer particles close to the bed move slower than the particles close to the surface, creating concentration gradients in the vertical direction (Figure 4A). There can be lateral and horizontal mixing (forward and backward) associated with molecular and turbulent diffusion, as described previously. But as the velocity profile distorts the plume, concentration gradients in the vertical are created. These concentration gradients induce vertical exchange by molecular and turbulent diffusion that is more effective than the lateral and horizontal mixing. A depth-averaged concentration graph of the plume in a region close to the injection point will have a spatial distribution that is strongly skewed with most of the particles of the plume being concentrated in the upper flow domain where the flow is fastest. The tail of the distribution accounts for the slow-moving tracer near the bed. As the shearing action continues, the upper sections of the plume are advanced well ahead of the middle and lower sections, all the while experiencing vertical mixing via turbulent diffusion. After a certain distance downstream (or time since injection), the plume will be evenly distributed in the vertical direction, and the depth-averaged concentration can be utilized to describe its behavior downstream.

A similar analysis can be conducted for a horizontal line source. Assuming that the tracer is completely mixed vertically after a very short time after injection, the lateral velocity profile will carry particles that are closer to the center of the channel faster than the particles that are located near banks. This lateral shearing action will distort the plume, as shown in Figure 4B. Once the plume assumes a parabolic shape, it creates concentration gradients over the cross-section, that promote lateral turbulent diffusion, mixing the plume over the cross-section of the channel.

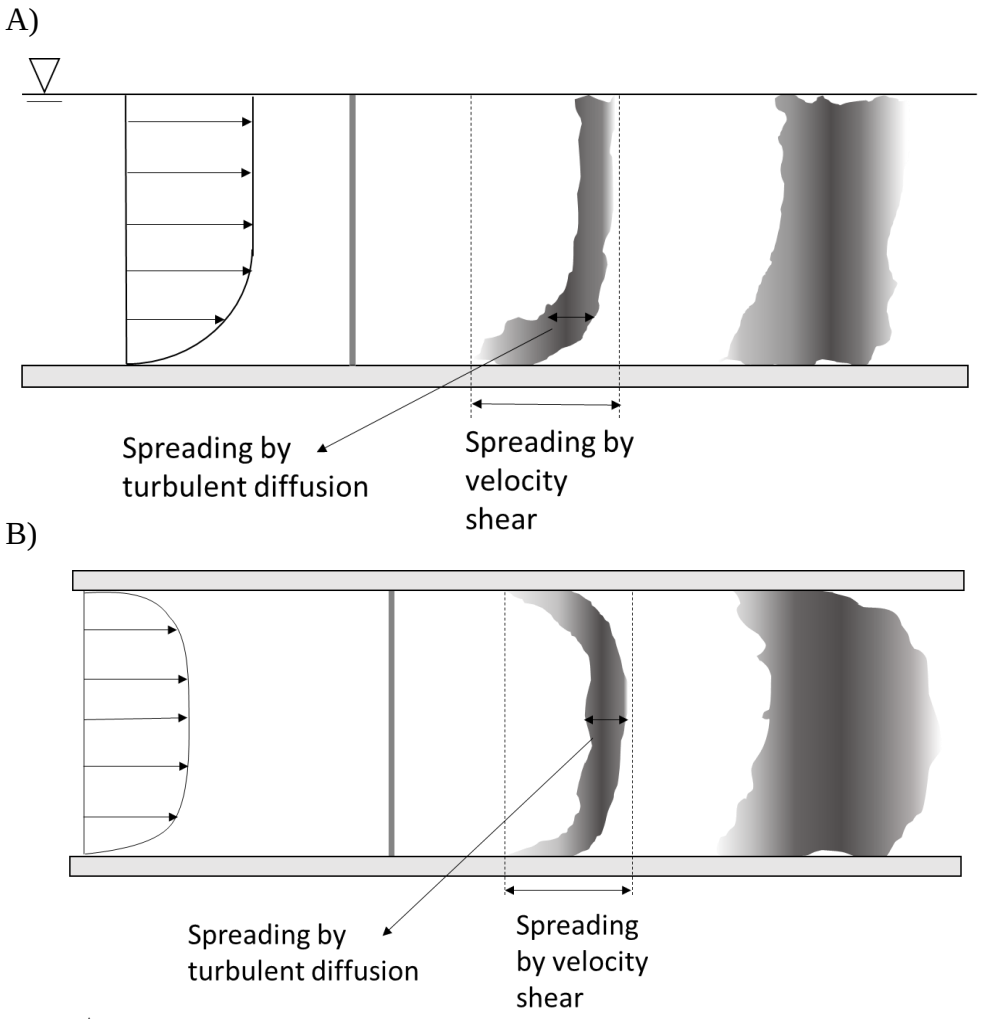

Figure 4. Effects of velocity shear and turbulent diffusion over a: A) vertical line source released at t = 0; B) transverse line source released at t = 0. Modified with permission of John Wiley & Sons – Books from River mixing, Rutherford, J. C., 1994; permission conveyed through Copyright Clearance Center, Inc.

The most common injection type utilized in the literature is a point (slug) injection. Assuming a slug injection into the middle of a channel, the concentration will vary in all directions immediately downstream of the injection point (near field), therefore, a three-dimensional analysis is necessary (Figure 5). Given the characteristics of most channels, where the depth is much smaller than the width, vertical mixing is usually the first to be completed (Elhadi et al. 1984; Rutherford 1994; Sharma and Ahmad 2014). In the intermediate-field, vertical mixing is concluded and it is possible to integrate over depth, removing the terms related to the vertical direction (z). This simplifies the analysis to two dimensions, including only the lateral and longitudinal concentration gradients. Finally, at sufficient distance downstream (far-field), the vertical and lateral mixing processes are completed, and the concentration of a substance becomes evenly distributed over the cross-section. Therefore, the analysis can be further simplified to a one-dimensional problem. The location of the near, intermediate, and far-fields will vary according to the characteristics of the channel, flow, and source. Furthermore, no explicit correlation between the location of the near, intermediate, and far-fields and the advective and equilibrium zones exist. However, in the case of a one-dimensional analysis, the equilibrium zone will be located somewhere farther downstream of the far-field boundary.

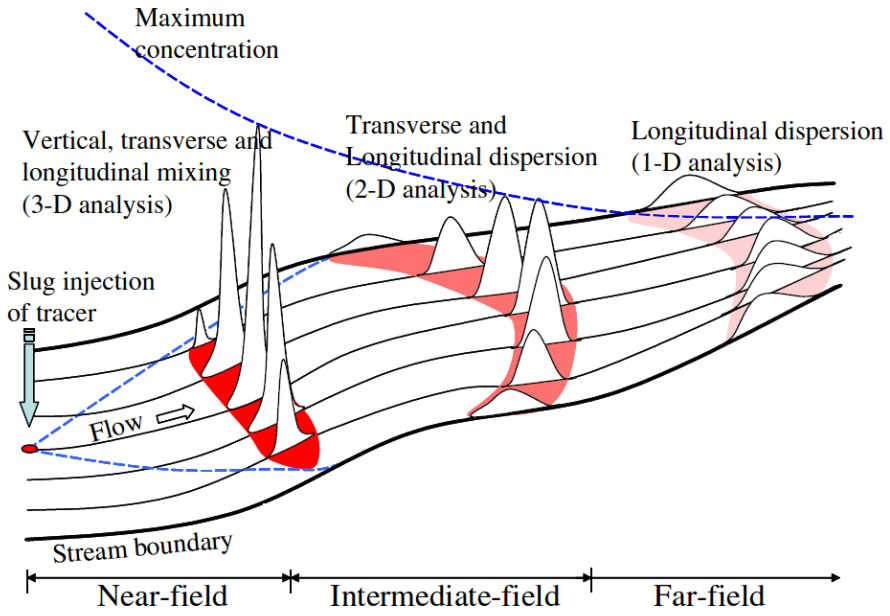

Figure 5. The mixing process of a slug injection. Reprinted from Advances in Water Resources, 33(12), Baek, K. O., and Seo, I. W., Routing procedures for observed dispersion coefficients in two-dimensional river mixing, 1551–1559, Copyright (2010), with permission from Elsevier.

*2.1.4.1. **Depth averaging***

Assuming H as the flow depth at a certain location (x, y, z), one can integrate Equation 39 from -H to 0 using Leibniz's rule (Holley et al. 1972; Rutherford 1994). Knowing that the fluxes normal to the boundaries (bed and surface) are zero (for a conservative tracer), yields:

$$\int_{-H}^{0} \frac{\partial \bar{c}}{\partial t} dz + \int_{-H}^{0} \frac{\partial \bar{u}_x \bar{c}}{\partial x} dz + \int_{-H}^{0} \frac{\partial \bar{u}_y \bar{c}}{\partial y} dz = \int_{-H}^{0} \frac{\partial}{\partial x}\left(e_x \frac{\partial \bar{c}}{\partial x}\right) dz + \int_{-H}^{0} \frac{\partial}{\partial y}\left(e_y \frac{\partial \bar{c}}{\partial y}\right) dz \quad (50)$$

The local velocities (in the x and y directions) and concentrations can be expressed as two components: one mean vertical component (u_{iz}, c_z) and a vertical deviation from the mean component (u_{iz}', c_z'), as another application of the Reynolds decomposition (Figure 6):

$$\bar{u}_x = u_{xz} + u'_{xz} \quad (51)$$

$$\bar{u}_y = u_{yz} + u'_{yx} \quad (52)$$

$$c = c_z + c'_z \quad (53)$$

where the subscript z denotes a depth-average.

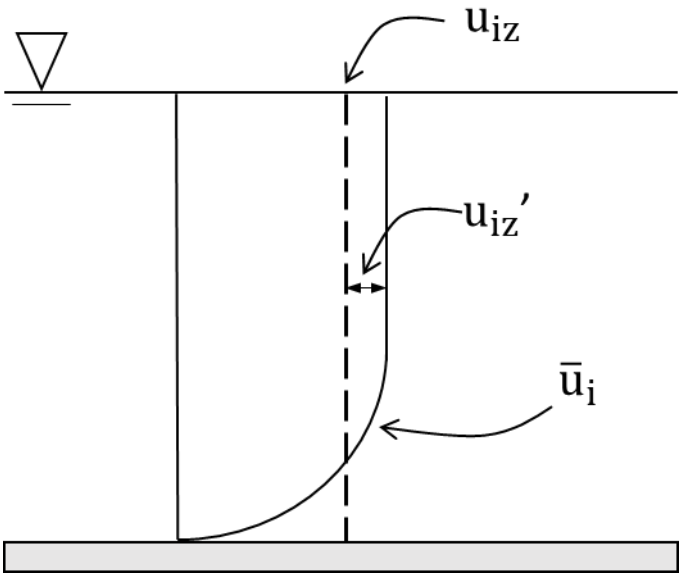

Figure 6. Decomposition of local velocities ($\bar{u}_i$) into a depth-averaged component (u_{iz}) and a vertical deviation from the average component (u_{iz}').

Substituting (51)-(53), Equation 50 becomes:

$$\int_{-H}^{0} \frac{\partial(c_z + c_z')}{\partial t} dz + \int_{-H}^{0} \frac{\partial(u_{xz} + u_{xz}')(c_z + c_z')}{\partial x} dz + \int_{-H}^{0} \frac{\partial(u_{yz} + u_{yz}')(c_z + c_z')}{\partial y} dz = \int_{-H}^{0} \frac{\partial}{\partial x}\left(e_x \frac{\partial(c_z + c_z')}{\partial x}\right) dz + \int_{-H}^{0} \frac{\partial}{\partial y}\left(e_y \frac{\partial(c_z + c_z')}{\partial y}\right) dz \quad (54)$$

The integrals over depth are defined by:

$$V_z \equiv \frac{1}{H}\int_{-H}^{0} V \, dz \quad (55)$$

where 0 = water surface level, H = channel depth, V = variable to be integrated, and the subscript z denotes a depth-averaged quantity.

The depth averages of the deviations u_{xz}', u_{yz}', and c_z' are zero by definition, given that they are deviations from the depth-averaged mean. Therefore, Equation 54 becomes:

$$\frac{\partial(Hc_z)}{\partial t} + \frac{\partial(Hu_{xz}c_z)}{\partial x} + \frac{\partial(Hu_{yz}c_z)}{\partial y} = \frac{\partial}{\partial x}\left(-Hu_{xz}'c_z' + He_{xz}\frac{\partial c_z}{\partial x}\right) + \frac{\partial}{\partial y}\left(-Hu_{yz}'c_z' + He_{yz}\frac{\partial c_z}{\partial y}\right) \quad (56)$$

where e_{iz} = depth-averaged turbulent diffusion coefficient in the i-th direction.

The process of averaging has yielded new terms involving correlations between velocity and concentration fluctuations as was the case for Equation 34 when turbulent diffusion was parameterized. Mathematically, a similar approach is used, which yields a dispersion coefficient that is analogous to the coefficients for molecular and turbulent diffusion. In other words, the dispersion process is assumed to behave according to Fick's Law (Elhadi et al. 1984; Rutherford 1994; Sharma and Ahmad 2014):

$$-u_{xz}'c_z' = E_x \frac{\partial c_z}{\partial x} \quad (57)$$

$$-u'_{yz}c'_z = E_y \frac{\partial c_z}{\partial y} \tag{58}$$

where E_i = depth-averaged dispersion coefficient in the i-th direction.

Substituting (57) and (58), Equation 56 becomes:

$$\frac{\partial(Hc_z)}{\partial t} + \frac{\partial(Hu_{xz}c_z)}{\partial x} + \frac{\partial(Hu_{yz}c_z)}{\partial y} = \frac{\partial}{\partial x}\left(H(E_x + e_{xz})\frac{\partial c_z}{\partial x}\right) + \frac{\partial}{\partial y}\left(H(E_y + e_{yz})\frac{\partial c_z}{\partial y}\right) \tag{59}$$

The e_{iz} coefficients are often omitted from the equations with the understanding that molecular diffusion and turbulent diffusion are subsumed within dispersion. Equation 59 then reduces to:

$$\frac{\partial(Hc_z)}{\partial t} + \frac{\partial(Hu_{xz}c_z)}{\partial x} + \frac{\partial(Hu_{yz}c_z)}{\partial y} = \frac{\partial}{\partial x}\left(HE_x\frac{\partial c_z}{\partial x}\right) + \frac{\partial}{\partial y}\left(HE_y\frac{\partial c_z}{\partial y}\right) \tag{60}$$

In this equation, E_x and E_y are depth-averaged coefficients as are all the variables.

*2.1.4.2. **Cross-sectional averaging***

After the mixing process is completed over the cross-section, i.e., the tracer is completely spread out over the vertical and lateral directions, the main process responsible for spreading out the tracer plume is called longitudinal dispersion. In such cases, the average cross-section concentration is able to provide a good approximation of the results, and Equation 60 can be further reduced to a one-dimensional form. Following the same steps as in the depth-averaging process, every term is integrated across the width of the channel to account for cross-sectional shear dispersion. The other mixing coefficients are often omitted from the equations with the understanding that the longitudinal dispersion coefficient K_x represents all the mixing processes (molecular diffusion, turbulent diffusion, and dispersion), yielding:

$$\frac{\partial(A\bar{C})}{\partial t} + \frac{\partial(A\bar{U}\bar{C})}{\partial x} = \frac{\partial}{\partial x}\left(AK_x\frac{\partial \bar{C}}{\partial x}\right) \tag{61}$$

where $\bar{C}$ = cross-sectional averaged concentration (ML^{-3}), A = cross-sectional are (L^2), $\bar{U}$ = cross-sectional averaged velocity (LT^{-1}), and K_x = longitudinal dispersion coefficient (L^2T^{-1}).

Assuming steady flow over a uniform channel (i.e., the cross-sectional area does not change in the downstream direction), and that the longitudinal dispersion coefficient does not change in the downstream direction for a certain combination of flow/channel geometry characteristics. Equation 61 is further simplified to:

$$\frac{\partial \bar{C}}{\partial t} + \bar{U}\frac{\partial \bar{C}}{\partial x} = K_x \frac{\partial^2 \bar{C}}{\partial x^2} \tag{62}$$

Equation 62 is commonly referred to as the advection-dispersion equation or the Fickian model of longitudinal dispersion. Given the larger scales of the eddies in the lateral direction, the cross-sectional averaged mixing process, represented by K_x, is much more effective than in the vertical direction or by the mixing caused by turbulent and molecular diffusion.

2.1.5. Analytical solutions of the one-dimensional ADE

An analytical solution to a differential equation can be described as the integration of the governing equation that provides an exact and continuous solution in time and space (Rutherford 1994). There are many analytical solutions for several different forms of the ADE available in the literature, however, the solutions have been developed in different disciplines with different boundary conditions depending on the specifics of the problem (Rutherford 1994; Wallis and Manson 2004). Analytical solutions to (62) are easily obtained given initial and boundary conditions. Table 2 shows the most common solutions of the one-dimensional ADE for an instantaneous injection assuming steady flow in a uniform channel.

Table 2. Analytical solutions of the one-dimensional ADE for an instantaneous injection.

Solution	Equation		Initial conditions	Boundary conditions
Taylor	$\bar{C}(x,t) = \frac{M}{2A\sqrt{\pi K_x t}} \exp\left(-\frac{(x-\bar{U}t)^2}{4K_x t}\right)$	(63)	$\bar{C}(x,0) = \frac{M}{A}\delta(x)$ $\delta(x) = 0$ everywhere, except at x = 0, where: $\int_{-\infty}^{\infty} \delta(x)dx = 1$	$\bar{C}(+\infty,t) = 0$ $\bar{C}(-\infty,t) = 0$

Solution	Equation	Initial conditions	Boundary conditions
Hayami	$\bar{C}(x,t) = \frac{Mx}{2A\bar{U}t\sqrt{\pi K_x t}} \exp\left(-\frac{(x-\bar{U}t)^2}{4K_x t}\right)$ (64)	$\bar{C}(+\infty,0) = 0$ $\bar{C}(-\infty,0) = 0$	$\bar{C}(0,t) = \frac{M}{A\bar{U}}\delta(t)$ $\delta(t) = 0$ for all values of t, except at t = 0, where: $\int_{-\infty}^{\infty}\delta(t)dt = 1$

$\bar{C}(x,t)$ = cross-sectional average concentration (ML^{-3}), M = tracer mass injected (M), A = cross-sectional area (L^2), $\bar{U}$ = cross-sectional average velocity (LT^{-1}), x = location downstream of injection (L), t = time after injection (T), and K_x = longitudinal dispersion coefficient (L^2T^{-1}).

The Taylor solution is the most utilized in the literature, while the Hayami solution is not cited as often. In the Taylor solution, the mass is considered to be entering the channel instantaneously at t=0 (i.e., as an initial condition). Most pollutant and tracer discharges to channels, however, occur at a fixed-point x as a function of time (i.e., as a boundary condition) and concentration data are measured likewise. When measuring temporal concentration profiles, the parts of a tracer plume that pass by the sampling location first are "younger" than the ones that pass at later times (Chatwin 1971). This means that the tail has been exposed to dispersion longer than the leading edge of the plume. This is not the case if the concentration is measured spatially at a fixed time t. Therefore, in order to apply the Taylor solution to observed data, it has to be assumed that the plume does not go through dispersion during the time it takes to pass through the sampling point. This assumption is commonly known as the "frozen cloud approximation" (Fischer 1968; Rutherford 1994). The frozen cloud approximation, however, is not completely accurate in most natural streams, given that dispersion does have an important effect on the concentration curves even in short amounts of time.

A comparison between the Taylor and the Hayami solutions (Figure 7) demonstrates that the results converge as time increases (Rutherford 1994). Given that both solutions are only valid at large t values (i.e., outside the advective zone), the differences between them are negligible far downstream of the injection point (Barnett 1983). Barnett (1983) suggests, however, that the Hayami solution is the only analytically acceptable basis for routing temporal distributions, given

that it was derived considering the mass injection as a boundary condition, not an initial condition. Even so, the Taylor solution is widely utilized for this procedure in the literature (e.g., Iwasa and Aya 1991; Kim 2012; McQuivey and Keefer 1974; Oliveira et al. 2017; Seo and Cheong 1998).

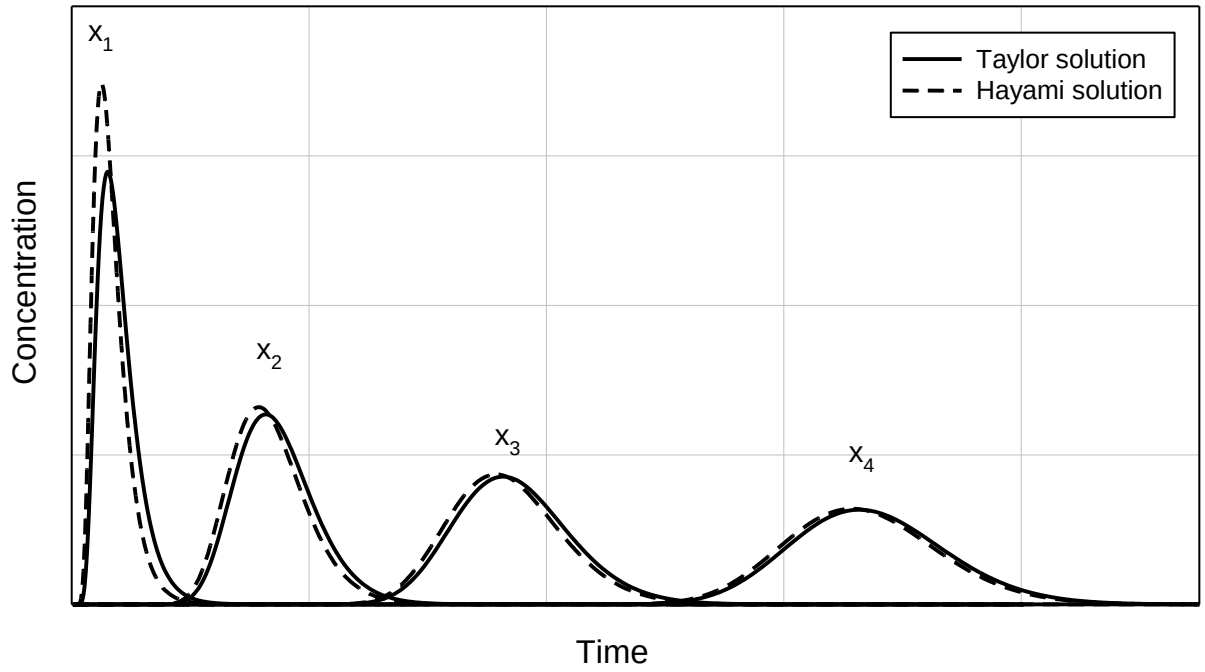

Figure 7. Comparison between the concentration versus time profiles calculated using Taylor and Hayami solutions at four different locations downstream, x_1, x_2, x_3, and x_4.

2.1.5.1. Advective zone length for the one-dimensional ADE

The one-dimensional ADE can only be applied with confidence in the equilibrium zone where the longitudinal dispersion coefficient is constant. As mentioned in 2.1.4, in a one-dimensional analysis, the equilibrium zone will be located somewhere farther downstream of the start of the far-field. Physically, the equilibrium zone is explained as being the region where shear action and turbulent diffusion reach equilibrium, i.e., the tracer particles have experienced the whole extension of the vertical and lateral velocity fields and are now uniformly distributed over the cross-sectional area of the channel (Rutherford 1994).

Given the difficulty in measuring turbulent velocity and concentration fluctuations, it is difficult to determine the precise ending point of the advective zone. In practice, most studies rely on empirical estimates of the advective zone length and measure concentration curves downstream of a certain point, assuming it is the equilibrium zone. The length of the advective zone can be

assessed on dimensional grounds based on characteristics of the channel. Fischer (1967) derived an expression for the length of the one-dimensional advective zone on the basis of flow characteristics:

$$L_L = \alpha \frac{\bar{U} L_t^2}{E_y} \tag{65}$$

where L_L = advective zone length (L), α = constant, $\bar{U}$ = cross-sectional average velocity (LT^{-1}), L_t = transverse length scale (L), and E_y = depth-averaged lateral dispersion coefficient (L^2T^{-1}).

The transverse length scale is assumed to be the distance between the thread of maximum velocity and the farthest bank, and it is taken as $L_t = 0.5W$ in symmetrical channels and $L_t = 0.7W$ in natural channels (Fischer et al. 1979). The parameter α depends on the type of source (point or line) and location (mid-channel or near the banks) of the source, the roughness of the channel, presence of dead-zones, and sinuosity, among others (Rutherford 1994; Sharma and Ahmad 2014). Therefore, it is case-specific and difficult to evaluate. Several authors have conducted tracer and numerical experiments in order to estimate the value of α. The values vary between 0.2 obtained via numerical experiments (Fischer 1973) and >10 in an irrigation channel with dead zones (Valentine and Wood 1979). Without the presence of dead zones, numerical and laboratory experiments suggest that $0.3 < \alpha < 0.6$ (Fischer 1967, 1968). This coefficient then tends to increase proportionally to the volume of dead zones in the channel, as observed by Valentine and Wood (1979).

The lateral dispersion coefficient can be estimated by (Elder 1959; Rutherford 1994):

$$E_y = \beta H u_* \tag{66}$$

where E_y = depth-averaged lateral dispersion coefficient (L^2T^{-1}), β = a constant (dimensionless), H = flow depth (L), and u_* = cross-sectional averaged shear velocity (LT^{-1}), $\sqrt{\tau_0/\rho}$, τ_0 = boundary shear stress ($ML^{-1}T^{-2}$), ρ = density (ML^{-3}).

The value of β is also obtained empirically through experiments and numerical models. It depends on the shape of the channel cross-section and the shape of the velocity distribution across the stream. Sharma and Ahmad (2014) compiled several β values observed in the literature; the values varied between 0.13 in a rectangular channel with steel mesh bottom (Chau 2000) and 4.65

in wide shallow rivers (Demetracopoulos and Stefan 1983). Given the large ranges obtained for α and β, there is still considerable difficulty in estimating the length of the advective zone without detailed tracer experiments in the stream of interest.

When data are available, the concentration curves can be analyzed to define whether the sampling locations are located in the advective or equilibrium zone. Theoretically, the start of the equilibrium zone can be identified analyzing the point where the spatial variance of concentration curves starts to increase linearly with time as predicted by (45). However, concentration time series observed in real channels often have long tails that affect the rate of increase of the variance (Nordin and Sabol 1974), therefore, this method is not very useful in practice. Alternatively, the relative importance of advection and dispersion can be estimated utilizing the Peclet number. The Peclet number is a dimensionless number that defines the relative importance of advective and dispersive fluxes being defined as (Pannone 2017):

$$\mathrm{Pe} = \frac{\bar{\mathrm{U}}\mathrm{L}}{\mathrm{K_x}} \tag{67}$$

where $\bar{U}$ = average flow velocity (LT^{-1}), L = characteristic length (L), and K_x = longitudinal dispersion coefficient (L^2T^{-1}).

In the one-dimensional case (longitudinal dispersion), the characteristic length is the width of the channel because depth-averaged variables are used. A flow is considered to be advection dominated if $\mathrm{Pe} \gtrsim 5$ and dispersion dominated if $\mathrm{Pe} \lesssim 1$ (Koussis et al. 1983). When Pe ~ 1, it means that advection and dispersion are in equilibrium, i.e., the plume is in the equilibrium zone. Nevertheless, it is not always clear what the value of K_x should be, and as noted above, K_x subsumes a number of mixing processes including molecular diffusion, turbulent diffusion, and shear-induced dispersion vertically and laterally.

2.2. Advection-dispersion in natural flows

As noted by Fischer (1979), natural channels differ from the wide, uniform channel utilized in Taylor's analysis in three main respects: depth is not uniform, there are bends and curves, and the banks are irregular. These factors lead to secondary flows and areas of flow acceleration and stagnation. Natural channels also contain obstacles such as logs and vegetation. As a consequence,

an equilibrium zone where the effects of velocity shear and turbulent diffusion are in equilibrium is rarely achieved (Bottacin-Busolin 2017; Cushman and O'Malley 2015; Fischer et al. 1979; Liu and Cheng 1980). Thus, the Fickian behavior predicted by theory is not commonly observed.

2.2.1. Transient storage

Observed concentration time series in natural channels are more skewed than what is predicted by the Fickian model. The plumes have steep fronts and elongated tails (Rutherford 1994). This means that the front part of the plume is travelling with a velocity that is faster than the tail. Taylor (1954) observed that the concentration time series in turbulent pipe flow had longer tails when the Reynolds Number (the ratio of inertial forces to viscous forces in a fluid) decreased. The explanation is that the laminar region of the boundary layer can be quite thick in low Reynolds Number flows, thereby increasing the amount of solute that is moved slowly close to the wall. In natural channels, processes such as trapping of solutes in recirculation zones and laminar boundary layers, and exchange with porous media on the bed and banks (Launay et al., 2015) have been identified as the main cause of long tails in concentration curves. These processes are collectively named transient storage. Transient storage can also be caused by the presence of bedforms, pools, large obstacles in the flow, such as trees and rocks, riparian vegetation, among others (Chanson 2004; Rutherford 1994). As a consequence, some parts of the plume are temporally trapped and travel at velocities slower than the mean flow velocity. As they are released in the flow at different speeds, they increase the duration of the plume and create long tails (Figure 8).

The main consequences of transient storage to the dispersion process are (i) it increases the length of the advective zone given the increased amount of time required for the tracer particles to experience the velocity fields across the channel as particles are diffused in and out of the main flow; and (ii) it increases the rate of dispersion, given that parts of the plume are transported at slower velocities and later become part of the tail, instead of the main body of the plume.

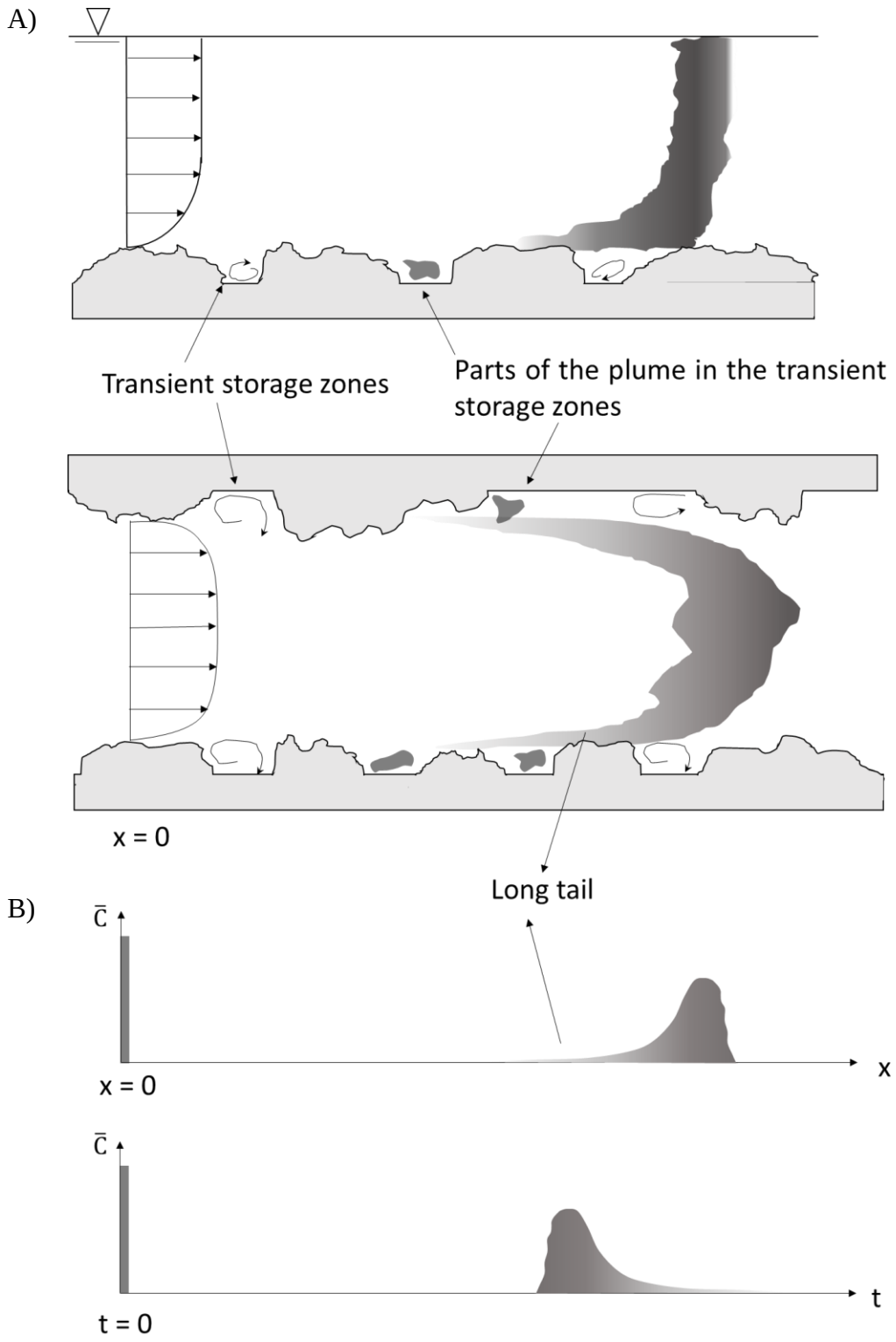

Figure 8. A) Transient storage zones. B) Concentration versus distance and concentration versus time graphs showing the long tails on the plumes caused by transient storage. Modified from Environmental hydraulics of open channel flows, Chanson, H., Turbulent dispersion in natural systems, 488 p., Copyright (2004), with permission from Elsevier.

Several authors have worked on developing non-Fickian models for dispersion (Van Mazijk and Veling 2005; Schmid 2002). The effects of transient storage have been studied by Bottacin-Busolin (2017), Cheong and Seo (2003), and Schmid (2002) for example. The results indicate that the transient-storage model is capable of explaining some of the skewness observed in concentration curves during tracer experiments. However, the additional variables (solute concentration and cross-section area of storage zones) and coefficients (stream storage exchange) needed to parameterize the model are difficult to quantify and apply in practice (Launay et al., 2015). Thus, the one-dimensional ADE without transient storage is still utilized as an approximation to processes in natural channels.

2.2.2. Lateral concentration gradients in the presence of velocity shear

The development of the one-dimensional ADE (Equation 62) assumed that shear-induced concentration gradients were balanced by turbulent and molecular diffusion in the equilibrium zone. This has led to the misconception that there are no lateral concentration gradients in the far-field (Rutherford 1994). Although this is true for a continuous injection source, it is not the case for an instantaneous line injection, for example. In natural channels, non-uniformities in the channel and flow caused by channel shape, size, alignment, slope, and bed material (Wallis and Manson 2004), imply that the depth-averaged velocity in the x-direction is not constant across the channel (Fischer et al. 1979). Despite the tendency for a substance to mix across the channel as a result of lateral turbulent diffusion, lateral velocity shear will always result in the substances being carried faster in the thalweg than near the banks. As a consequence, lateral gradients never completely vanish (Rutherford 1994) (Figure 9).

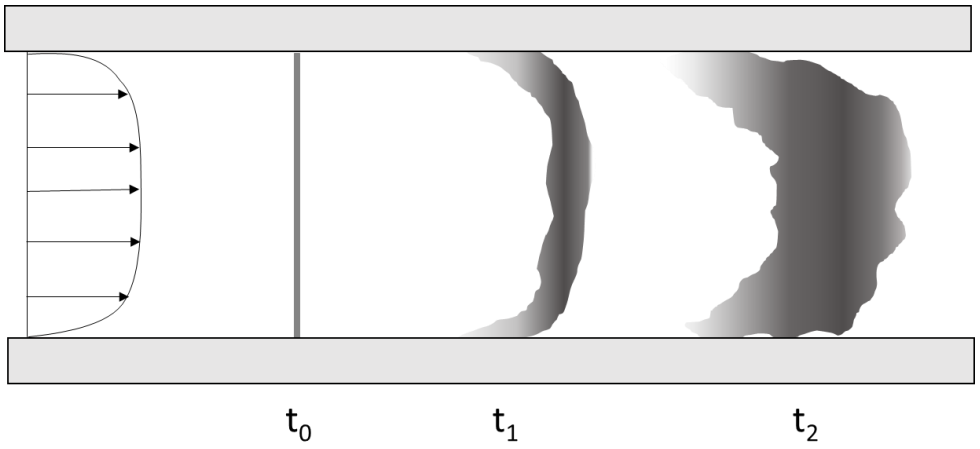

Figure 9. Effects of lateral velocity shear on an instantaneous transverse line source in a natural flow.

In practice, this means that observed data from an instantaneous injection will always have some deviation from the cross-sectional averaged concentration depending on the sampling location over the cross-section. The degree of deviation will depend on the lateral velocity profile, as well as the presence of lateral transient storage zones, which slow down the lateral edges of the plumes. Furthermore, the presence of velocity shear introduces more skewness to the concentration time series than predicted by solutions such as (63) and (64).

2.2.3. Variable longitudinal dispersion coefficient

Taylor's (1922) analysis of turbulent diffusion is based on homogeneous, stationary turbulence. Given the heterogeneities of natural flows, there might not be enough time for the equilibrium between shear dispersion and turbulent diffusion to be reached before the tracer is carried farther downstream to different turbulence environments (Rutherford 1994), such as in a riffle-pool reach transitioning to a meandering reach. As a consequence, the longitudinal dispersion coefficient is not constant in natural channels, even beyond the advective zone. Therefore, attempts to explain the dispersion process with a fixed coefficient have not had much success (Atkinson and Davis 2000).

When applying the one-dimensional ADE to natural channels, the non-uniformities can be accounted for by dividing the channel into small reaches, where the geometry and flow conditions

are approximately constant (Atkinson and Davis 2000). Each reach can be modeled with a different longitudinal dispersion coefficient. The division of experimental rivers and streams into reaches is usually defined practically by the location of the monitoring stations (Ani et al. 2009; Duarte and Boaventura 2008; Velísková et al. 2014).

Despite its well-known limitations and the existence of alternative models, the one-dimensional ADE is the simplest approach to mixing problems. Therefore, it is still the most widely utilized model in water quality studies. The use of a more complex model and the amount of data that needs to be collected to populate it can only be justified in situations where greater precision is required (Rutherford 1994). Several studies (e.g., Ani et al. 2009; Launay et al. 2015) have demonstrated that the one-dimensional ADE is able to reproduce field observations with sufficient accuracy for most water quality studies (Camacho Suarez et al. 2019) if the dispersion coefficients can be quantified correctly.

2.3. Quantifying the longitudinal dispersion coefficient

Several factors can affect the longitudinal dispersion coefficient, including fluid density, fluid viscosity, channel width, flow depth, flow velocity, shear velocity, bed slope, bed material, bedforms, and sinuosity (Van Genuchten et al. 2013). The confidence in any prediction obtained with the ADE is directly related to the reliability of the longitudinal dispersion coefficient (Camacho Suarez et al. 2019; Wallis and Manson 2004). Therefore, a lot of effort has been devoted to developing and improving methods to estimate the longitudinal dispersion coefficients (Wallis and Manson 2004).

Despite a large amount of research, there are still no preferred methods to estimate the longitudinal dispersion coefficient. In practice, observed tracer data are usually not available and/or can be difficult and costly to obtain. Therefore, most dispersion studies rely on estimates from predictive formulas that quantify the dispersion coefficient based on flow characteristics. When tracer data are available, the most common methods utilized to estimate the longitudinal dispersion coefficient include the method of moments and curve-fitting procedures based on adjusting the longitudinal dispersion coefficient to match the observed data.

2.3.1. Predictive formulas

There have been a large number of studies attempting to provide predictive formulas for the longitudinal dispersion coefficient. Most studies begin with a theoretical framework to define the important variables (e.g., dimensional analysis) followed by statistical curve fitting or soft computing techniques to optimize the fit of the equations to empirical data. The data sets utilized differ from study to study, therefore, there are a large number of equations and great uncertainty as to which is more applicable. Table 3 shows a select number of these formulas. The formulas were compiled from the literature based on all published studies that included tag words such as longitudinal dispersion, longitudinal dispersion coefficient, one-dimensional ADE, and one-dimensional mixing.

Table 3. Empirical equations used to predict the longitudinal dispersion coefficient.

Reference	Equation		Notes
Taylor (1954)	$K_x = 10.1 r u_*$	(68)	Theoretical approach for turbulent flow in a pipe.
Elder (1959)	$K_x = 5.93 H u_*$	(69)	Expanded Taylor's (1954) equation to open channels assuming uniform flow in an infinitely wide channel; velocity is a function of depth only and assumed to have a logarithmic profile.
Parker (1961)	$K_x = 14.28 R_h^{1.5} \sqrt{2gS}$	(70)	Adapted Taylor's (1954) equation to open channels by substituting the hydraulic radius for the halfpipe radius.
Fischer (1966)	$K_x = -\frac{1}{A}\int_0^W H\bar{U}' \int_0^y \frac{1}{E_y H} \int_0^y H\bar{U}' \, dydy$	(71)	Theoretical approach considering the lateral velocity profile.
McQuivey and Keefer (1974)	$K_x = 0.058 \frac{Q}{SW} = 0.058 \frac{H\bar{U}}{S}$	(72)	Empirical equation obtained through an analogy between the 1D dispersion equation and the 1D flow equation. The parameter 0.058 was obtained through linear regression based on 40 data points conducted on 18 natural channels. For Fr < 0.5.
Fischer (1975)	$K_x = 0.011 \frac{\bar{U}^2 W^2}{H u_*}$	(73)	Developed based on the triple integral approach (65) but utilizing some approximations for average velocity, distance between the point of maximum velocity and the banks, and lateral turbulent diffusion coefficient.
Liu (1977)	$K_x = \beta \frac{\bar{U}^2 W^2}{H u_*}$ where $\beta = 0.18 \left(\frac{u_*}{\bar{U}}\right)^{1.5}$	(74)	Expanded Fischer's (1975) work by adding a parameter related to the lateral velocity distribution and the shape of the cross-section. The linear regression was based on 14 data points obtained in 7 channels.

Reference	Equation		Notes
Iwasa and Aya (1991)	$K_x = 2Hu_* \left(\frac{W}{H}\right)^{1.5}$	(75)	Reviewed data points from 62 laboratory experiments in small scale flumes and field data sets from 79 rivers/canals. Excluded data points from flumes with small W/H ratios, and some data in actual rivers/canals. Formula obtained by regression.
Koussis and Rodríguez-Mirsasol (1998)	$K_x = \Phi \frac{u_* W^2}{H}$ $\Phi \approx 0.6$	(76)	Based on Fischer's (1975) theoretical equation. The value of 0.6 was the mean observed from 24 data points from 15 rivers with W/H > 6.
Seo and Cheong (1998)	$K_x = 5.915Hu_* \left(\frac{W}{H}\right)^{0.620} \left(\frac{\overline{U}}{u_*}\right)^{1.428}$	(77)	Parameters selected based on dimensional analysis. Coefficients based on 35 data points from 27 channels in the US (rivers, streams, and canals). Formula obtained by a nonlinear multi regression method.
Deng et al. (2001)	$K_x = \frac{0.15Hu_*}{8E_{y0}} \left(\frac{W}{H}\right)^{5/3} \left(\frac{\overline{U}}{u_*}\right)^2$ $E_{y0} = 0.145 + \left(\frac{1}{3520}\right)\left(\frac{\overline{U}}{u_*}\right)\left(\frac{W}{H}\right)^{1.38}$ $E_{yz} = E_{y0} Hu_*$	(78)	Formula derived by a theoretical method based on Fischer's (1966) triple integral. The constant 0.15 was obtained based on 73 data points from 29 rivers in the US (including 58 out of the 59 data points utilized by Seo and Cheong 1998). For W/H > 10. The significant contribution of this equation relies on the fact that it considers the lateral dispersion coefficient, something that had not been attempted by other studies.
Kashefipour and Falconer (2002)	Formula 1: $K_x = 10.612H\overline{U} \left(\frac{\overline{U}}{u_*}\right)$	(79)	Parameters selected based on dimensional analysis. Coefficients based on 81 data points from 30 channels (rivers, streams, and canals). The first formula was obtained

Reference	Equation		Notes
	Formula 2: $K_x = H\overline{U}\left[7.248 + 1.775\left(\frac{W}{H}\right)^{0.620}\left(\frac{u_*}{\overline{U}}\right)^{0.572}\right]\left(\frac{\overline{U}}{u_*}\right)$		by multiple regression analysis; the second formula was obtained by a linear combination of formula 1 and the formula from Seo and Cheong (1998).
Devens (2006)	$K_x = 0.000355\frac{\overline{U}^{-0.793}W^{0.793}}{H^{1.610}S^{0.026}}$	(80)	Parameters selected based on dimensional analysis. Coefficients based on 13 data points from 2 rivers in Brazil. Formula obtained by multiple regression analysis. Includes the effect of the Reynolds number (assumes T = 20°C for the calculation of kinematic viscosity).
Sahay and Dutta (2009)	$K_x = 2Hu_*\left(\frac{W}{H}\right)^{0.96}\left(\frac{\overline{U}}{u_*}\right)^{1.25}$	(81)	Parameters based on an analysis of previous equations. Formula derived using genetic algorithms. Coefficients based on 65 data points from 29 rivers in the US. Besides that, Equation 81 seems to be particularly useful for wide rivers, where the calculated coefficients are very close to measured data (Sahay and Dutta 2009).
Ribeiro et al. (2010)	$K_x = 7.326{u_*}^{0.303}H^{1.316}W^{0.445}\overline{U}^{1.458}$	(82)	Parameters selected based on dimensional analysis. Coefficients based on 8 data points from 2 rivers in Brazil (W > 21 m). Formula obtained by multiple regression analysis.
Etemad-Shahidi and Taghipour (2012)	$K_x = 15.49Hu_*\left(\frac{W}{H}\right)^{0.78}\left(\frac{\overline{U}}{u_*}\right)^{0.11}, \ \frac{W}{H} \leq 30.6$ $K_x = 14.12Hu_*\left(\frac{W}{H}\right)^{0.61}\left(\frac{\overline{U}}{u_*}\right)^{0.85}, \ \frac{W}{H} > 30.6$	(83)	Formula obtained by model tree analysis. Coefficients based on 119 data points.

Reference	Equation		Notes
Li et al. (2013)	$K_x = 2.2820 Hu_* \left(\frac{W}{H}\right)^{0.7613} \left(\frac{\overline{U}}{u_*}\right)^{1.4713}$	(84)	Coefficients obtained by differential evolution (an iterative algorithm that defines the values of the coefficients in the formula by minimizing the sum-square error between the actual and predicted dispersion coefficients (65 data points from 29 rivers in the US; data set from Deng et al. (2001)).
Sahay (2013)	$K_x = 2 Hu_* \left(\frac{W}{H}\right)^{0.72} \left(\frac{\overline{U}}{u_*}\right)^{1.37} S_i^{1.52}$	(85)	New formula structure including sinuosity. Coefficients determined by 45 data points from 22 rivers in the US. Formula obtained by genetic algorithm.
Zeng and Huai (2014)	$K_x = 5.4 H\overline{U} \left(\frac{W}{H}\right)^{0.7} \left(\frac{\overline{U}}{u_*}\right)^{0.13}$	(86)	Parameters defined by the dimensional analysis of Kashefipour and Falconer (2002). Coefficients obtained based on 116 data points from rivers in the US and UK.
Disley et al. (2015)	$K_x = 3.563 Hu_* Fr^{-0.4117} \left(\frac{W}{H}\right)^{0.6776} \left(\frac{\overline{U}}{u_*}\right)^{1.0132}$	(87)	Parameters selected based on previous formulas on the literature but included Froude number. 56 data points from 24 rivers in the US and Canada. Formula obtained by multiple regression analysis.
Sattar and Gharabaghi (2015)	$K_x = Hu_* \alpha \left(\frac{\overline{U}}{u_*}\right)^{b} \left(\frac{W}{H}\right)^{c} Fr^{d}$ $\alpha = (2.9 \times 4.6^{\sqrt{Fr}})$, $b = 1 + \sqrt{Fr}$, $c = 0.5 - Fr$, and $d = 0.5$, for formula 1, and $\alpha = 8.45$, $b = 1.65$, $c = 0.5 - 0.514 Fr^{0.516} + \frac{\overline{U}}{u_*} 0.42^{\overline{U}/u_*}$, and $d = 0$ for formula 2	(88)	Parameters based on Disley et al. (2015). Formulas obtained by a novel gene expression programming model. Based on 100 published data points from natural streams in the United States, Canada, Europe, and New Zealand.

Reference	Equation		Notes
Wang and Huai (2016)	$K_x = 17.648 H u_* \left(\frac{W}{H}\right)^{0.3619} \left(\frac{\overline{U}}{u_*}\right)^{1.16}$	(89)	Theoretical formula based on the triple integral. Coefficients initially obtained for flume experiments by regression analysis. Final coefficients obtained based on 93 data points from natural channels through regression analysis.
Alizadeh et al. (2017)	$K_x = 5.319 H u_* \left(\frac{W}{H}\right)^{1.206} \left(\frac{\overline{U}}{u_*}\right)^{0.075}$, $\frac{W}{H} \leq 28$ $K_x = 9.931 H u_* \left(\frac{W}{H}\right)^{0.187} \left(\frac{\overline{U}}{u_*}\right)^{1.802}$, $\frac{W}{H} > 28$	(90)	Formula obtained by multi-objective particle swarm optimization (PSO) technique. 124 data points from Disley et al. (2015) and Etemad-Shahidi and Taghipour (2012).
Oliveira et al. (2017)	$K_x = 0.744 \frac{H^{0.036} \overline{U}^{1.59}}{{u_*}^{2.22} W^{0.66}}$	(91)	Parameters selected based on dimensional analysis. Coefficients based on 15 data points from 2 rivers in Brazil. Formula obtained by multiple linear regression.
Wang et al. (2017)	$K_x = \left(0.718 + 47.9 \frac{H}{W}\right) \overline{U} W$	(92)	Parameters and formula obtained by genetic programming. Coefficients were determined based on 47 data points from the Zeng and Huai (2014) data set.

r = pipe radius (substituted by the hydraulic radius in open-channel flows); H = flow depth; u_* = cross-sectional average shear velocity; R_h = hydraulic radius; g = gravitational acceleration; S = channel slope; $\overline{U}'$= deviation from the cross-sectional average velocity; E_y = depth-averaged lateral dispersion coefficient; Q = flow discharge; W = channel width; $\overline{U}$ = cross-sectional average flow velocity; Si = sinuosity factor; Fr = Froude number.

There is a large degree of inconsistency among the predictive equations with regard to the parameters, constants, and exponents. Most formulas utilize two dimensionless terms: the aspect ratio (W/H) and the surface roughness ratio ($\bar{U}/u_*$). The longitudinal dispersion coefficient is directly proportional to the aspect ratio given that in wide, shallow channels the lateral variation of the velocity is large, increasing the effect of differential advection (Rutherford 1994). The surface roughness ratio represents the importance of resistance to flow on the longitudinal dispersion process. Increased resistance will increase velocity shear, therefore, increasing longitudinal dispersion. The $\bar{U}/u_*$ ratio is directly related to friction factors that determine resistance to flow, such as the Darcy-Weisbach friction factor (f), the Chezy coefficient (C), and the Manning roughness coefficient (n) (Julien 2010):

$$\frac{\bar{U}}{u_*} = \sqrt{\frac{8}{f}} = \frac{C}{\sqrt{g}} = \frac{{R_h}^{1/6}}{n\sqrt{g}} \tag{93}$$

McQuivey and Keefer (1974) and Parker (1961) included the channel slope in their formulas, which can also be seen in Devens' (2006) formula. Disley et al. (2015) were the first to include the Froude number. Their work was further expanded by Sattar and Gharabaghi (2015), who developed two models where the exponents are not constants, but a function of the Froude number. According to Sattar and Gharabaghi (2015), this is the key reason why their formulas have a better performance than previous ones. Sahay and Dutta (2009) performed a sensitivity analysis based on the dimensionless form of the longitudinal dispersion coefficient (K_x/Hu_*) in order to identify the importance of the different terms in the formula. The $\bar{U}/u_*$ ratio caused the greatest variation in the output, which was almost 10 times larger than the variation caused by W/H. On the other hand, the formulas from Sattar and Gharabaghi (2015) are mostly affected by the W/H ratio, followed by the Froude number, and lastly by the $\bar{U}/u_*$. Etemad-Shahidi and Taghipour (2012) suggested that different flow regimes might exist for different W/H ratios and that $\bar{U}/u_*$ is mostly important under large values of W/H. This factor is reflected in the formulas developed by Alizadeh et al. (2017) and Etemad-Shahidi and Taghipour (2012), where the exponents of the $\bar{U}/u_*$ ratio are larger for large W/H ratios than for small W/H ratios.

The formulas shown in Table 3 are assumed to be applicable to all kinds of channels unless otherwise stated. However, for formulas with empirically derived coefficients, it seems reasonable

to expect that they should only apply to channels that are similar to those represented in the data set to calibrate the formula. Therefore, a formula might be accurate when tested against a certain data set but fail to perform well against another data set (Wang et al. 2017). Camacho Suarez et al. (2019), for example, assessed the accuracy of six recent equations (Deng et al. 2001; Disley et al. 2015; Etemad-Shahidi and Taghipour 2012; Wang et al. 2017; Wang and Huai 2016; Zeng and Huai 2014). Camacho Suarez et al. (2019) compared the observed values of the dispersion coefficient utilized to calibrate each formula against the values predicted by the formulas and found that relative errors between observed and modeled values varied from approximately -50% to 32%.

For the studies that reported complete calibration data sets, a cursory analysis of the parameters (width, depth, velocity, shear velocity, etc.) indicates that most of the data (93%) were obtained for channels with widths between 5-25 m (Figure 10). There are only 25 reported data points (17%) collected in channels with width smaller than 5 m and six of the formulas analyzed here (Alizadeh et al. 2017; Devens 2006; Disley et al. 2015; Etemad-Shahidi and Taghipour 2012; Oliveira et al. 2017; Sattar and Gharabaghi 2015) include at least one of these points. A similar situation occurs with respect to the average flow area. Overall, there are 17 (7%) longitudinal dispersion coefficients from flows with $A < 1\ m^2$. Three of the formulas reported here included at least one of these points (Devens 2006; Disley et al. 2015; Oliveira et al. 2017). Although most of the formulas include at least one longitudinal dispersion coefficient obtained in channels with small discharge rates ($Q \sim 1\ m^3s^{-1}$), overall there are 28 data points (12%) collected in such channels. This points to the general lack of data on small channels in comparison to medium-sized and large channels.

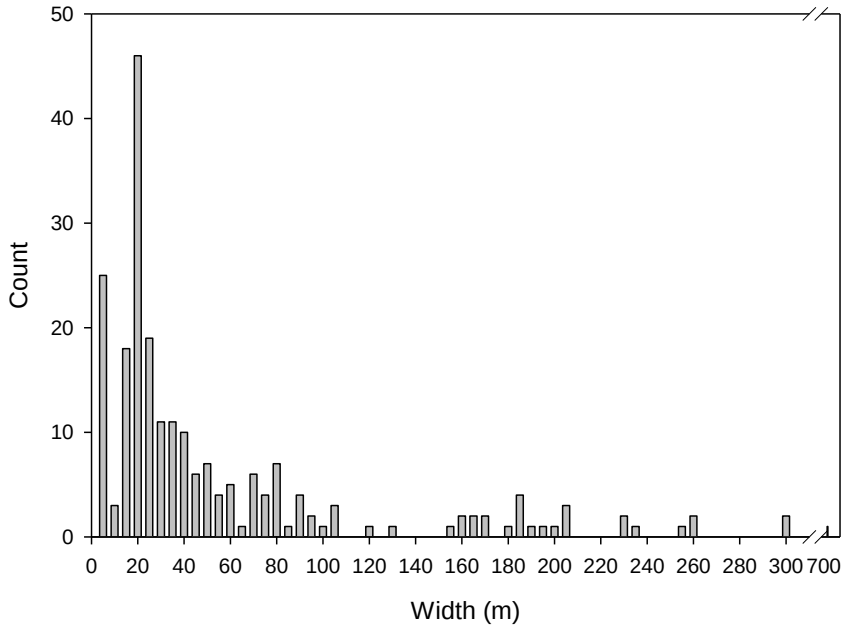

Figure 10. Frequency distribution of channel width in the data utilized to derive the predictive formulas of the longitudinal dispersion coefficient in Table 3.

Despite the large number of formulas available in the literature, only a few studies have actually used these estimated values for the longitudinal dispersion coefficient in the one-dimensional ADE to predict concentration profiles. El Kadi Abderrezzak et al. (2015) evaluated 10 predictive formulas by comparing modeled data with observed data from a 20 cm wide rectangular flume and a 400 m wide natural channel. The formulas of Elder (1959) and Fischer (1975) were capable of reproducing the concentration curves observed in the flume with the smallest relative errors, however, they were not capable of reproducing the concentrations observed in the natural channel. The formulas of Koussis and Rodríguez-Mirsasol (1998), Liu (1977), and Magazine et al. (1988) were not appropriate for large W/H ratios (>50) but still performed well in the flume case. The formulas of Deng et al. (2001); Kashefipour and Falconer (2002), and Seo and Cheong (1998), on the other hand, performed better when predicting the concentrations on the natural channel than the flume. Most of the equations were therefore useful for the flume or the natural channel, but not both. The formula from Iwasa and Aya (1991) was the best overall performer, being able to predict the concentrations in the flume and the natural channel with relatively small errors.

Kashefipour and Falconer (2002) utilized a numerical finite volume method to compare their own two formulas for K_x against four others (Fischer 1975; Koussis and Rodríguez-Mirasol 1998; McQuivey and Keefer 1974; Seo and Cheong 1998) while predicting suspended-sediment concentration in an estuary. Their two formulas provided the best agreement with the suspended sediment concentration, yielding a percent error of approximately 35%. The formula from Fischer (1975) yielded the largest value of the longitudinal dispersion coefficient and had the maximum percent error of 56%. The formulas from Koussis and Rodríguez-Mirsasol (1998), McQuivey and Keefer (1974), and Seo and Cheong (1998) had errors between 37 and 45%.

Recently, Camacho Suarez et al. (2019) tested the accuracy of six formulas (Deng et al. 2001; Disley et al. 2015; Etemad-Shahidi and Taghipour 2012; Wang et al. 2017; Wang and Huai 2016; Zeng and Huai 2014) when predicting observed concentration curves from a river in Chile (W = 16.4 m, H = 0.7 m, A = 10.6 m^2, $\overline{U}$ = 0.45 ms^{-1}) utilizing Monte Carlo analysis. Five out of the six equations underestimated the peak concentration by an average of 29%. The formula by Etemad-Shahidi and Taghipour (2012) produced the largest error, underestimating the peak by 64%. Most of the modeled curves failed to reproduce the start time of the plumes, being faster than the observed curve. The formula by Deng et al. (2001) yielded the closest agreement with the observed data. Therefore, there is still a clear need to apply and evaluate the accuracy of these predictive formulas, particularly in small channels.

2.3.2. Method of moments

The traditional method utilized to estimate K_x from observed data is the method of moments (Wallis et al. 2014), which consists of the evaluation of the spatial moments of concentration profiles observed at two (or more) locations downstream of injection (Fischer et al. 1979; Rutherford 1994; Wallis and Manson 2004). This method is based on the analysis of Taylor (1922) and the characteristics of Fickian diffusion, which shows that the spatial variance of a tracer cloud increases linearly with distance downstream of the advective zone (Rutherford 1994; Wallis and Manson 2004):

$$K_x = \frac{1}{2}\frac{d\sigma_x^2(t)}{dt} = \frac{1}{2}\frac{\sigma_x^2(t_2) - \sigma_x^2(t_1)}{t_2 - t_1} \quad (94)$$

The difficulty in applying this equation is that it requires data acquired at several locations at a fixed time to estimate the spatial variance. Most data are acquired over time at a fixed location. Therefore, in practice, Equation 94 is transformed based on the "frozen cloud approximation". Considering that the temporal variance is measured at a location x and the spatial variance is measured at the time of passage of the centroid ($t_{centroid}$), at large times when both variances become large, the difference

$$\overline{U}^2\sigma_t^2(x) = \sigma_x^2(t_{centroid}) \quad (95)$$

becomes small and this approximation can be used on Equation 94, yielding:

$$K_x = \frac{1}{2}\frac{d[\overline{U}^2\sigma_t^2(x)]}{dt} = \frac{1}{2}\overline{U}^2\frac{\sigma_t^2(x_2) - \sigma_{t_1}^2(x_1)}{t_{centroid,2} - t_{centroid,1}} \quad (96)$$

Assuming that the plume centroid velocity is the same as the average flow velocity, then $t_{centroid,1} = x_1/\overline{U}$ and $t_{centroid,2} = x_2/\overline{U}$. Substituting these terms in Equation 96, yields:

$$K_x = \frac{1}{2}\frac{d[\overline{U}^2\sigma_t^2(x)]}{dt} = \frac{1}{2}\overline{U}^3\frac{\sigma_t^2(x_2) - \sigma_{t_1}^2(x_1)}{x_2 - x_1} \quad (97)$$

The average velocity can be obtained through direct field measurements or estimated based on the observed concentration curves if a conservative tracer is used. Wallis and Manson (2004) suggest the use of the centroid velocity. Nevertheless, it is well known that the temporal variance of the concentration curves is greatly affected by the presence of long tails and/or missing data (Fischer 1975), and the variance does not grow linearly with time as predicted by Taylor's analysis. Therefore, this method can lead to unreliable results (Seo and Cheong 1998). The long tails observed on concentration curves from natural channels have a large effect on the variance values, resulting in large values of K_x.

2.3.3. Curve fitting

Modeled concentration curves are obtained by applying the predicted longitudinal dispersion coefficient to solutions of the one-dimensional ADE. Exact solutions are provided by analytical solutions of the one-dimensional ADE, such as the Taylor (63) and Hayami (64) solutions.

When observed data are available, analytical solutions of the one-dimensional ADE can be utilized to estimate the longitudinal dispersion coefficient based on a trial-and-error procedure. The values of $\bar{U}$ and K_x are simultaneously adjusted in order to optimize the fit between the observed and modelled temporal concentration curves (Deng et al. 2001). Similar to the method of moments, in order for this method to apply, the observed concentration curves must be located downstream of the advective zone, where the longitudinal dispersion coefficient is assumed to be constant. When utilizing the average values of the cross-sectional area and velocity, this method will result in a reach–averaged value for K_x. The main disadvantage of both the method of moments and the curve-fitting approach is that they assume equilibrium conditions all along the channel (i.e., the dispersion coefficient is constant from the injection point to the observation point). The skewness introduced by velocity shear in the advective zone is not accommodated.

To overcome this shortcoming, the most common method currently utilized to obtain the longitudinal dispersion coefficient is the routing procedure (Kim 2012; Seo and Cheong 1998). This method was introduced by Fischer (1968) and it involves routing an observed upstream concentration profile to determine the concentration profile at another point downstream (Fischer 1968; Rutherford 1994; Wallis and Manson 2004). Similar to the curve-fitting approach, the values of $\bar{U}$ and K_x are simultaneously adjusted in order to find the best fit between the observed and modelled temporal concentration curves, often using a least-squares analysis (McQuivey and Keefer 1974). According to Wallis and Manson (2004), the routing procedure is theoretically superior to other approaches because it does not require modeling the tracer since the injection point through the advective zone. This is only true if the upstream measured concentration profile is downstream of the advective zone. Routing provides a better fit to observed data than the purely analytical solution based on injection because the input to the model is an observed concentration curve that inherently captures the skewness caused by the non-uniformities of natural channels as they are propagated downstream. On the other and, since the routing method depends on an

observed concentration profile upstream of the point of interest, the method cannot be utilized when no observations are available.

The routing equation for temporal concentration profiles is based on the Hayami analytical solution of the one-dimensional ADE (Equation 64). The upstream concentration curve is discretized in several equal step times, and the concentration is assumed to be constant over each step time. Each concentration point is multiplied by the discharge yielding a mass fraction. Each mass fraction is then treated as a new mass injection at time τ after injection and routed downstream using the Hayami solution yielding a concentration curve. The concentration points of this concentration curve are summed up yielding a concentration point at location x_2, $C(x_2, \tau)$ (Carr 2007):

$$C(x_2, \tau) = \sum_{i=1}^{n} \frac{C(x_1, \tau) Q \Delta x}{2A\bar{U}(n-i)\Delta t\sqrt{\pi K_x (n-i)\Delta t}} \exp\left(-\frac{[\Delta x - \bar{U}(n-i)\Delta t]^2}{4K_x(n-i)\Delta t}\right) \quad (98)$$

where, $C(x_1, \tau)$ = observed concentration at location 1, $C(x_2, \tau)$ = predicted concentration at location 2, τ = time from injection, Δx = distance between sites 1 and 2, Δt = time step duration (assumed constant), $\bar{U}$ = mean flow velocity, and i = time step.

Modeling dispersion in channels where the average characteristics change between reaches is another important application of the routing procedure. The output from an upstream reach is utilized as the upstream boundary when predicting the concentration output of a downstream reach.

The routing procedure yields results that are very similar to the analytical solution, but it is not error-free. The discretization of the time variable assumes that the concentration is constant for the span of Δt, which creates small differences when the routed concentrations are added up. This effect is known as numerical dispersion. Numerical dispersion is essentially the same as curve smoothing and it has the same effect as physical dispersion on the concentration profile by decreasing the concentration (Shahrabadi et al. 2016). Therefore, the concentration curves exhibit more dispersion than can be accounted for by the longitudinal dispersion coefficient. The effect of numerical dispersion can be reduced by adopting smaller time steps with a cost to computational efficiency. Numerical dispersion is also observed when numerical methods are utilized to model concentration curves. Such methods, however, require the discretization of both, the time and spatial variables. Depending on the numerical method, for concentration curves modeled at very

small time intervals (e.g., 1 s), the spatial intervals must be equally small (e.g., 1 m) in order to maintain the stability of the numerical solutions. This increases the requirement for more geometry data and can lead to very large computational times (Benedini 2011).

2.4. Suspended sediment dispersion

The conventional form of the one-dimensional ADE (62) is based on the assumption of a conservative tracer with no losses or gains. For substances that undergo chemical reactions or settling in the flow, extra terms related to sources or sinks must be added to the ADE (Elhadi et al. 1984). The type of source/sink term ($\dot{m}$) will depend on the characteristics of the processes involved. The most common process is a first-order decay, which is also applicable to particle settling (Elhadi et al. 1984; Fischer et al. 1979):

$$\frac{\partial \bar{C}}{\partial t} + \bar{U}\frac{\partial \bar{C}}{\partial x} = K_x \frac{\partial^2 \bar{C}}{\partial x^2} - k\bar{C} \tag{99}$$

where k = settling rate (T^{-1}).

The Hayami analytical solution with a settling rate is given by:

$$\bar{C}(x,t) = \frac{Mx}{2A\bar{U}t\sqrt{\pi K_x t}} \exp\left(-\frac{(x-\bar{U}t)^2}{4K_x t} - kt\right) \tag{100}$$

Figure 11 shows the time series curves for a conservative and non-conservative substance.

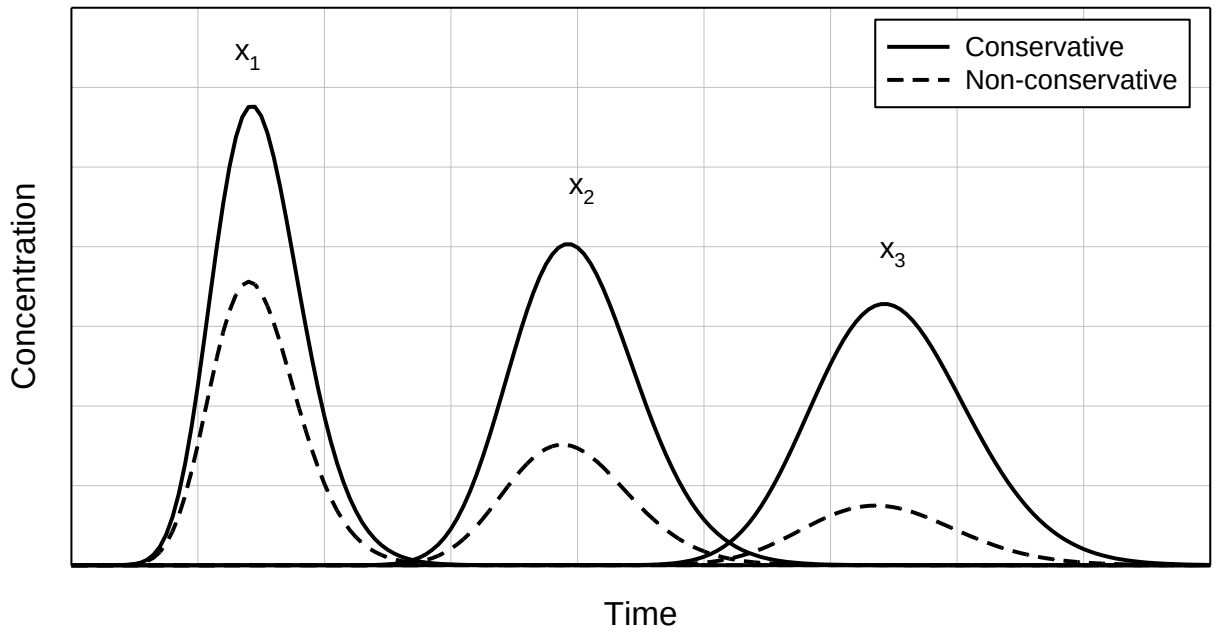

Figure 11. Comparison between the concentration versus time curves of a conservative and non-conservative substance at three different locations downstream x_1, x_2, and x_3.

In turbulent flow, particles are subjected to upward diffusion by turbulent eddies as well as downward settling by gravity. The relationship between these two opposing fluxes determines the transport mode of the particles. In most cases, only very fine particles (e.g., clays) can be constantly carried in suspension (no settling) and are referred to as wash load (Julien 2010). As the diameter increases, particles are more difficult to entrain and suspend. Therefore it becomes necessary to add a settling parameter to the ADE to account for the particles that settle out of the flow (Palu and Julien 2019). Commonly the suspended sediment settling rate for one-dimensional models is given by (Göransson et al. 2012; Ji 2008; Julien 2010; Palu and Julien 2019):

$$k = \frac{\omega}{H} \tag{101}$$

where ω = settling velocity (LT^{-1}) and H = flow depth (L).

This approach assumes that sediment concentration and depth are uniform over the cross-section. The potential re-mobilization of sediment from the bed is not included in this formulation. Therefore, it is assumed that all particles that settle to the bed are permanently removed from the water column.

The transport mode can be defined by the relation between the settling velocity of the particles and the shear velocity of the flow, also known as the Rouse Number (Rouse 1937):

$$\mathrm{Ro} = \frac{\omega}{\kappa u_*} \tag{102}$$

where Ro = Rouse Number, ω = settling velocity (LT^{-1}), κ = von Karman constant (0.41), and u_* = shear velocity (LT^{-1}).

It is estimated that suspension is the main transport mode when Ro < 1.25, which means that the ratio between shear velocity and settling velocity and is larger than 2 (Table 4) (Julien 2010).

Table 4. Classification of sediment transport mode according to the shear and settling velocities (Julien 2010).

Ro	**u_*/ω**	**Mode of sediment transport**
>12.5	<0.2	No motion
~12.5	~0.2	Incipient motion
12.5-5	0.2-0.5	Bedload
5-1.25	0.5-2	Mixed load
<1.25	>2	Suspension

The ADE can be applied to model suspended sediment concentration as long as the actual volume occupied by the particles is negligible (Sayre 1975) and that the coefficients such as the average flow velocity and dispersion coefficient do not vary significantly with the given sediment concentration (Sayre 1969). These conditions are satisfied if the sediment concentrations are not large enough to change the turbulence and velocity distribution characteristics of the flow (Sayre 1969). Singh (1987, as cited in Ahmad 1997) observed no changes in the flow characteristics for sediment concentrations < 5 gL^{-1} of particles between 0.0058 and 0.058 mm. Ahmad (1997) expanded Singh's research using concentrations from 0.5 gL^{-1} to 11 gL^{-1} of fine sands (0.064 mm and 0.164 mm) and found that dispersion increased with increased suspended sediment concentration. For example, flows with concentrations 0, 4.725, and 6.028 gL^{-1} yielded longitudinal dispersion coefficients of 0.04, 0.06, and 0.10 m^2s^{-1}, respectively. There was no effect of sediment size on the longitudinal dispersion coefficient.

Despite their importance for water quality management (Ballantine et al. 2008; Chaudhry and Malik 2017; Rickson 2014), sediment particles have not been widely used as tracers in dispersion

studies. Sayre and Chang (1968) conducted several experiments utilizing fine particles as tracers and compared the dispersion with a conservative fluorescent dye in a rectangular recirculating flume. The particles utilized were natural silt between 15-30 μm, natural silt between 53-62 μm, glass beads <44 μm, and glass beads between 53-62 μm. The particles and dye injections were conducted separately under similar flow conditions, and the observed data were compared with Taylor's one-dimensional analytical solution of the ADE (63). The observed sediment concentration curves agreed well with the analytical solution of the ADE for most runs, even more so than some of the dye curves. Coarser particles yielded lower concentration peaks, confirming that larger particles tend to settle faster. The coarse particle plumes also had more pronounced tails, which was attributed to larger concentrations of particles moving slower near the bed (larger concentration gradient) thereby retarding their dispersion. Karwan and Saiers (2009) analyzed the dispersion of fine particles in a mountain stream. They compared the dispersion process between a conservative solute, sodium bromide (NaBr), and titanium dioxide (TiO_2) particles (0.45 μm) under three different flow conditions (drought, base, and high flow). The rates of advection and longitudinal dispersion of the conservative solute matched those of the fine particles under all flow conditions. While transient storage affected mostly the solute transport, increasing the tails of the concentration curves, the storage of the particles was irreversible during the duration of the experiments and was attributed to settling.

Other studies have been able to successfully model observed natural suspended sediment concentrations using the one-dimensional ADE. Göransson et al. (2012) also obtained good agreement while analyzing suspended sediment plumes created by a landslide event. The sizes of the particles were not measured, but they were estimated to be in the clay, silt, and sand fractions. More recently, Palu and Julien (2019) modeled the sediment load of a dam break. The D_{50} of the suspended sediment particles modeled varied from 6 to 18.1 μm, being in the clay and fine silt range.

There is a clear need for more studies analyzing the dispersion of suspended sediment plumes in natural channels, in particular when settling becomes an important factor in the transport process. This will provide more insight into the behavior of external sources of sediment particles

and possible pollutants attached to them as well as to the applicability of the ADE to model sediment plume transport.

Chapter 3: Methodology

Several experiments were conducted to analyze the dispersion process in environments with different levels of complexity: a concrete channel, a semi-natural (drainage) channel, and a natural channel. The data collected included geometry and discharge for each channel, and tracer experiments utilizing sodium chloride (NaCl) and sediment (<0.075 mm up to 1 mm). The tracer experiments were complemented with hydraulic modeling of all three channels in order to obtain estimates of parameters required for the analysis of dispersion that could not be measured in the field.

3.1. Instrumentation

Sodium chloride was monitored utilizing conductivity sensors, while suspended sediment was monitored utilizing optical back-scatterance (OBS) sensors.

3.1.1. Conductivity sensors

Five conductivity sensors, numbered 1 through 5, were utilized during the experiments (1 Thermo Orion 130A, 1 Hach HQd Portable Meter, and 3 WTW Multi-parameter portable meters Multi – models 3410, 3510 IDS, and 3620 IDS). Prior to each experiment, the sensors were calibrated in the laboratory against a solution of 0.01 M of Potassium Chloride (KCl) to ensure accurate and consistent response among instruments. In the field, the conductivity sensors were used to develop calibration curves in order to obtain a specific relation between conductivity and sodium chloride concentration that accounts for the natural background conductivity levels in the stream water. The resultant calibration curves are shown in Figure 12. The calibration curves obtained were highly linear and consistent between sensors (Table 5).

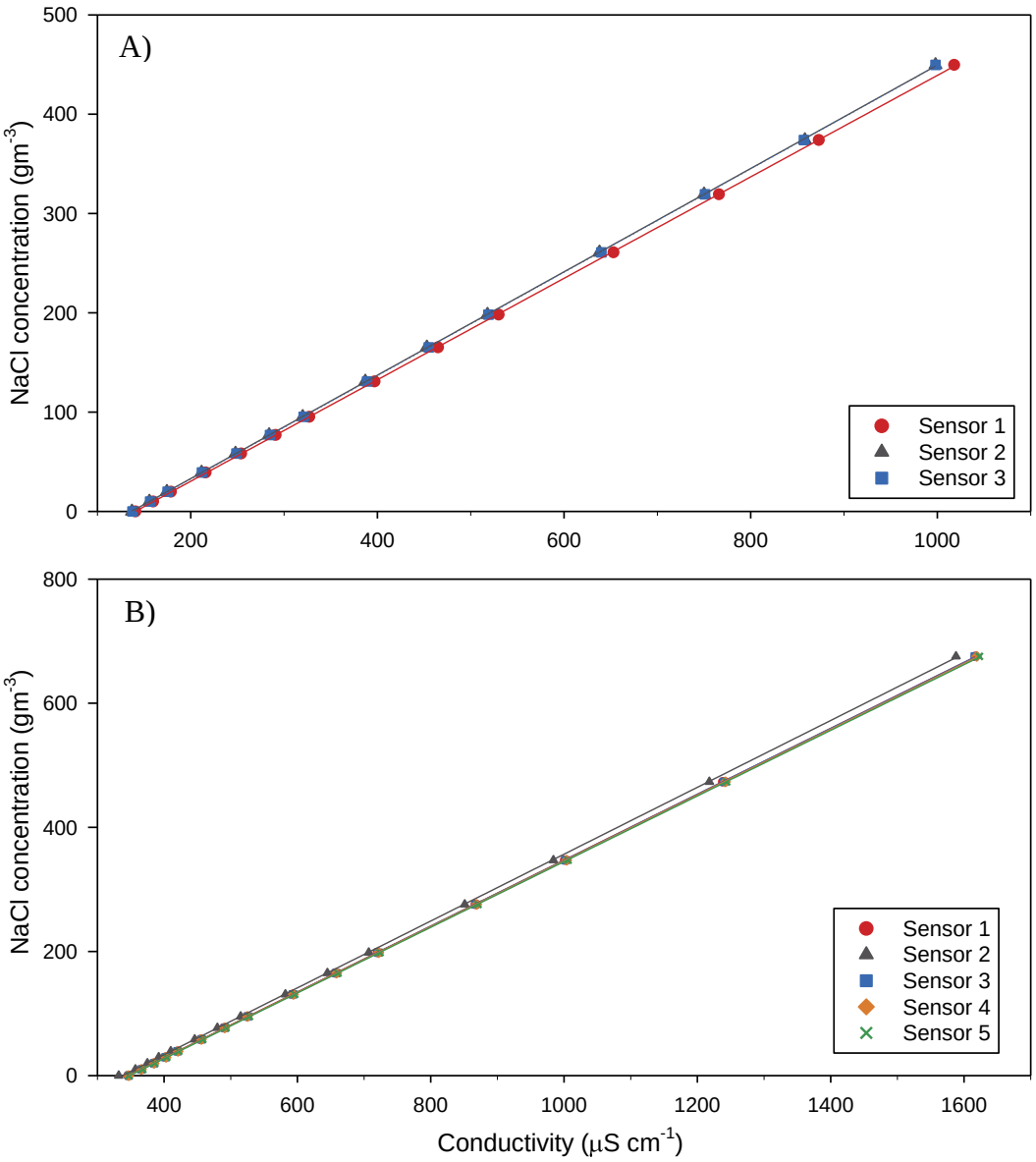

Figure 12. Calibration curves for the conductivity sensors. A) Concrete channel; B) Semi-natural and natural channels. Note that the dependent and independent variables were reversed for purposes of creating calibration equations used for predicting concentration on the basis of measured conductivity. Note also the change in scale on both axes.

Table 5. Calibration curves for the conductivity probes.

Sensor	Equation	R^2
	Concrete channel	
1	$\text{NaCl}\ (\text{gL}^{-1}) = -0.07183588 + 0.00051092 * \text{Conductivity}\ (\mu\text{S cm}^{-1})$	0.999
2	$\text{NaCl}\ (\text{gL}^{-1}) = -0.07102960 + 0.00052045 * \text{Conductivity}\ (\mu\text{S cm}^{-1})$	0.999
3	$\text{NaCl}\ (\text{gL}^{-1}) = -0.07169615 + 0.00052090 * \text{Conductivity}\ (\mu\text{S cm}^{-1})$	0.999
	Semi-natural and natural channels	
1	$\text{NaCl}\ (\text{gL}^{-1}) = -0.18393538 + 0.00053109 * \text{Conductivity}\ (\mu\text{S cm}^{-1})$	0.999
2	$\text{NaCl}\ (\text{gL}^{-1}) = -0.18188136 + 0.00053866 * \text{Conductivity}\ (\mu\text{S cm}^{-1})$	0.999
3	$\text{NaCl}\ (\text{gL}^{-1}) = -0.18430477 + 0.00053122 * \text{Conductivity}\ (\mu\text{S cm}^{-1})$	0.999
4	$\text{NaCl}\ (\text{gL}^{-1}) = -0.18396008 + 0.00052997 * \text{Conductivity}\ (\mu\text{S cm}^{-1})$	0.999
5	$\text{NaCl}\ (\text{gL}^{-1}) = -0.18434563 + 0.00052907 * \text{Conductivity}\ (\mu\text{S cm}^{-1})$	0.999

3.1.2. OBS sensors

The OBS sensors measure the level of turbidity in the water by sending out a pulsed infrared beam into the water column and measuring the intensity of light that is scattered back to the sensor in the same wavelength band (Downing 2008a). The proportion of returned light depends on the type and nature of scattering elements in the water column (e.g., sand, silt, clay), and they were designed to reduce sensitivity to organic matter and bubbles as well as to reject ambient light (Downing 2008b).

In total, eight OBS sensors, referred to by serial number, were used during the experiments. Six of the OBS sensors (model OBS-3 developed by D&A Instrument Company) operate on a 0 - 5 Volt range: 735, 1433, 1434, 1435, 1436, and 1437. The remaining two (OBS-3+ by Campbell Scientific), operate on a 0 - 2.5 Volt range: 10181 and 10193. Prior to deployment, the gain and offset potentiometers of the 0 – 5 Volt range OBS sensors were adjusted so as to provide similar voltage output for all sensors given the anticipated turbidity levels. To accomplish this, the potentiometers were set to provide a nominal 0 V return signal in clear water and a 5 V return signal when immersed in a clay-silt suspension at a concentration that anticipated the maximum turbidity in the field. The 0 – 2.5 Volt OBS sensors do not allow gain and offset adjustments because they provide two output ranges automatically: a high gain channel that is sensitive to small concentrations and a low gain channel that covers a broad range of concentrations.

All OBS sensors were calibrated in the laboratory across their full range of measurements using fine sediments (<0.075 mm) from the natural channel and a step-wise process of increasing concentration. The sensors were calibrated by measuring the response in clear water (for a period of minutes using a 1 Hz sampling rate) and then adding small portions of the fine-grained sediment incrementally to the water basin. At each stage, the sediment was mixed and maintained in suspension by a recirculating pump while data were being collected by the data logger. Once a steady-state voltage output was achieved, which was determined visually by real-time observation of the data, another mass of sediment was added. This process was repeated until the sensors reached their maximum capacity. A regression analysis of the suspended sediment (SS) concentration and the voltage output was used to develop calibration curves for each sensor (Table 6, Figure 13).

The intensity of the light scattered by a volume of suspended particles is proportional do the area normal to a light beam. A suspension containing large particles will scatter less light than a suspension with the same mass concentration comprised of small particles, yielding smaller mV outputs. It is important to note that the calibration curves were obtained based on the nominal concentration for particles <0.075 mm.

Sensors 735 to 1437 have similar calibration curves, all with a slightly negative offset and slightly different gains. Sensors 735 and 1437 deviate slightly from the other sensors, requiring slightly larger concentration values to produce the same voltage output. Such differences might have been caused by differences in how the potentiometers were set or by slightly different mixing conditions in the water basin during the calibration process. It is worth noting that each sensor had to be calibrated separately because of potential electrical and optical feedback between sensors when two or more sensors were immersed in the same basin. Thus, there is some experimental uncertainty associated with the calibration procedure although the results shown in

Figure 13 suggest that this is minimal. Sensors 10181 and 10193 have virtually identical calibration curves within their operating range, but different coefficients than the other OBS sensors. It should be noted that in the range from 0 to 400 gm^{-3} there is only a very small difference in the calibration curves for all OBS sensors, and this covers the entire range of all the field data

collected. Thus, the difference between sensors is well within the experimental uncertainty encountered in the field.

Table 6. Calibration equations for the OBS sensors.

OBS sensor	Equation	R^2
735	$\mathrm{SSC} = -2.006731 * 10^{-2} + 4.397423 * 10^{-4} * \mathrm{mV} + 2.217476 * 10^{-8} * \mathrm{mV}^2$	0.998
1433	$\mathrm{SSC} = -6.211415 * 10^{-3} + 2.934201 * 10^{-4} * \mathrm{mV} + 5.438174 * 10^{-9} * \mathrm{mV}^2$	0.999
1434	$\mathrm{SSC} = -1.616445 * 10^{-2} + 2.935640 * 10^{-4} * \mathrm{mV} + 1.076402 * 10^{-9} * \mathrm{mV}^2$	0.999
1435	$\mathrm{SSC} = -2.224501 * 10^{-2} + 2.801982 * 10^{-4} * \mathrm{mV} + 7.197105 * 10^{-9} * \mathrm{mV}^2$	0.999
1436	$\mathrm{SSC} = -1.179549 * 10^{-2} + 2.832191 * 10^{-4} * \mathrm{mV} + 6.282588 * 10^{-9} * \mathrm{mV}^2$	0.999
1437	$\mathrm{SSC} = -2.987108 * 10^{-2} + 3.448190 * 10^{-4} * \mathrm{mV} + 2.461714 * 10^{-9} * \mathrm{mV}^2$	0.999
10181	$\mathrm{SSC} = -1.364576 * 10^{-2} + 5.012364 * 10^{-4} * \mathrm{mV} + 2.777686 * 10^{-8} * \mathrm{mV}^2$	0.999
10193	$\mathrm{SSC} = 6.413685 * 10^{-3} + 4.912946 * 10^{-4} * \mathrm{mV} + 3.298723 * 10^{-8} * \mathrm{mV}^2$	0.999

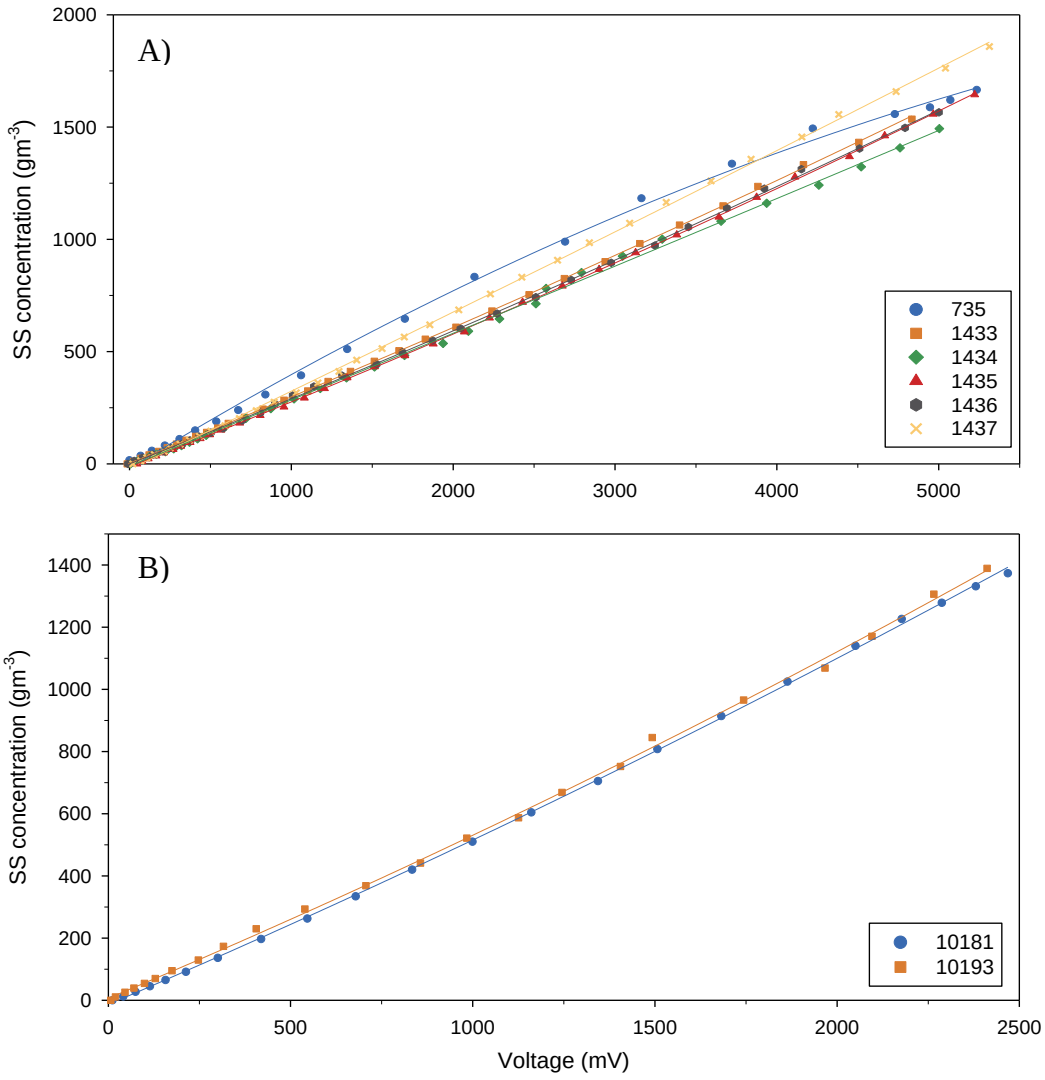

Figure 13. Calibration curves for the OBS sensors. A) OBSs that operate in the 0-5 Volt range; B) OBSs that operate in the 0-2.5 Volt range. Note that the suspended sediment concentration on y-axis represents the concentration obtained for particles <0.075 mm. Note also the change in scale on both axes.

The calibration of the sensors was conducted 6 months and 4 months before the field experiments, for sensors in the 5 V range and 2.5 V range, respectively. Two other calibration procedures were conducted 3 and 6 months after the experiments and demonstrated that the output for the range from 0 to 400 gm^{-3} remained the same.

3.2.Field experiments

The tracer experiments were designed to analyze the applicability of the one-dimensional ADE to model suspended sediment in small channels. Conductivity and turbidity were measured in the lateral and longitudinal directions in order to analyze the main aspects of sediment dispersion: lateral concentration gradients, transient storage, and sediment settling. In total 21 experimental runs were monitored. The sediment was collected from the natural channel (Creighton Creek), dried at 105°C for at least 24 hours, and sieved in small batches to separate the size fractions (<0.075 mm, 0.075-0.125 mm, 0.125-0.25 mm, 0.25-0.5 mm, and 0.5-1 mm). Since the sediment was not exposed to temperatures higher than 105°C, a minor component of organic matter might have been present in it, however, it was not visible by eye.

Prior to injection, the sediment and sodium chloride were combined and pre-mixed with water in order to obtain a uniform slurry. A known mass of slurry was introduced into the channel with the use of a trough that yielded a lateral line injection spanning the full width (Figure 14). The line injection was used to ensure complete lateral mixing and thereby reduce the length of the advective zone. Vertical mixing was very rapid because the flow was shallow and because the placement of the trough in the flow during the emptying process induced considerable local turbulence. The trough was only slightly shorter than the width of the channels, conveniently avoiding any influence from the side walls during the injections.

Figure 14. The trough utilized for the injection of sodium chloride and sediment in the semi-natural channel at the injection site.

3.2.1. Concrete channel (CC)

Injections of sodium chloride and sediment were conducted in a concrete-lined section of Upper Vernon Creek, located in Winfield, Lake Country, BC. The concrete channel is 375 m long and relatively straight and uniform in geometry. The bottom of the channel is approximately 2 m wide, the walls have a 38° angle, and the top of the channel is 7.7 m wide (Figure 15).

Figure 15. Longitudinal view of the concrete channel (looking upstream).

The bed of the channel is also concrete, with some spots being more eroded and deeper than the average channel depth (~0.05 m). It is possible to identify a preferential flow line along the center of the channel, which roughly mimics a slightly meandering thalweg. The experiments at this channel were designed to investigate longitudinal and lateral dispersion at long distances downstream in a channel with uniform geometry and no local sources of sediment. In total, nine injections of sodium chloride and sediment of different grain sizes were conducted (Table 7). The sediment grain sizes varied from <0.075 mm to 1 mm.

Table 7. Summary of the sodium chloride and sediment injections in the concrete channel.

Run	Sodium chloride (g)	Sediment (g)	Sediment size (mm)
CC-1	250.08	365.54	<0.075
CC-2	500.25	500.02	<0.075
CC-3	500.45	500.00	<0.075
CC-4	500.08	1000.59	0.075-0.125
CC-5	500.30	1000.06	0.075-0.125
CC-6	500.61	1000.12	0.125-0.25
CC-7	500.40	999.97	0.125-0.25
CC-8	500.08	1000.05	0.25-0.5
CC-9	500.98	988.75	0.5-1

Conductivity was monitored at three locations while turbidity was monitored at eight locations downstream of the injection line. The conductivity and turbidity sensors were installed in the channel using lengths of rebar attached to wooden supports that spanned the channel (Figure 16).

Figure 16. Conductivity and turbidity sensors in the concrete channel.

Because of slightly meandering thalweg, all three conductivity sensors, as well as at least one of the turbidity sensors on each cross-section, were installed in the main flow domain (away from sidewall effects to the extent possible), in order to capture most of the tracer in case lateral mixing was not even. The conductivity sensors were placed on the channel bed, while the turbidity sensors were installed a few centimeters from the bottom in order to avoid reflection from the bed. Table 8 and Figure 17 show the location of the sensors in the channel.

Table 8. Location of the turbidity and conductivity sensors during the concrete channel experiments.

Location (m)	Monitoring	OBS sensor	Conductivity sensor	Sampling interval (seconds)
42.5 LB	Turbidity	1436	-	1
42.5 RB	Turbidity	735	-	

Location (m)	Monitoring	OBS sensor	Conductivity sensor	Sampling interval (seconds)
80.75 C	Turbidity and conductivity	1433	3	
139.95 LB	Turbidity and conductivity	1435	-	
139.95 RB	Turbidity	1434	1	
190.9 LB	Turbidity	1437	-	
370.15 C	Turbidity	10193	-	
370.15 RB	Turbidity and conductivity	10181	2	

LB = left bank, C = center of the channel, RB = right bank.

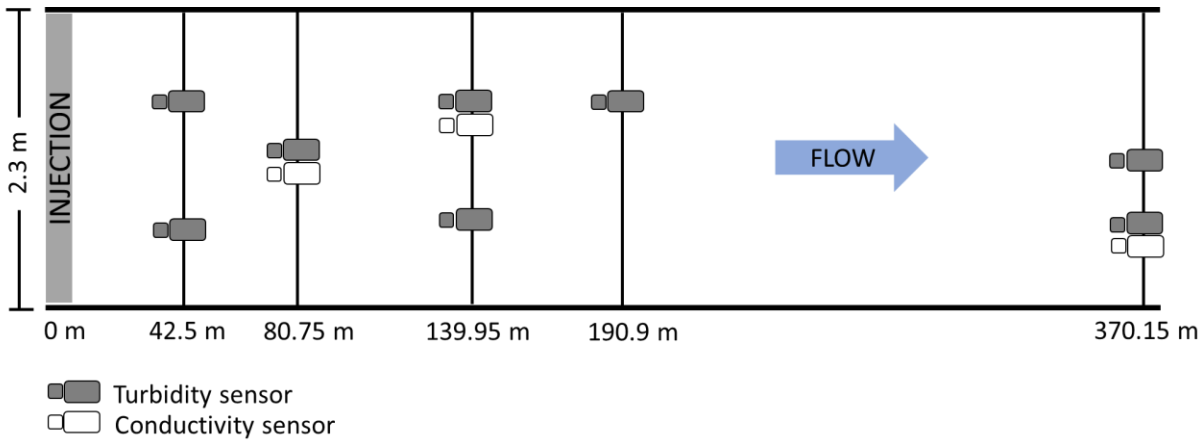

Figure 17. Location of the conductivity and turbidity sensors in the concrete channel.

3.2.2. Semi-natural channel (SNC)

The semi-natural channel was a drainage ditch located along Creighton Creek, in Lumby, BC. The section of the channel selected for the experiments was 90 m long and it had a relatively uniform cross-section, varying from 1.86 to 2.64 m in width (Figure 18). The bed of the channel was mainly gravel with cobbles and sand.

Figure 18. Longitudinal view of the semi-natural channel (looking downstream).

Given the shallow depth of water on the day of the experiments, the OBS sensors were not deployed at this channel. The OBS sensors have a conical sampling area that extends from the sensor face (i.e., smaller in turbid water and larger in clear water). If the boundaries of the cone are influenced by the creek bottom or the water surface, which occurs in depths less than 0.1-0.15 m, false reflections will induce back-scattering and a voltage return signal that are not related to water-column turbidity. A turbulent water surface is particularly problematic because the return signal is time-varying with large spikes and potentially difficult to differentiate from real turbidity fluctuations due to pockets of suspended sediment moving past the probe. Therefore, only sodium chloride injections were conducted (Table 9).

Table 9. Summary of the sodium chloride injections – semi-natural channel.

Run	Sodium chloride (g)
SNC-1	250.83
SNC-2	251.24
SNC-3	250.24

SNC-1 was designed to analyze longitudinal dispersion only, while runs SNC-2 and SNC-3 also included lateral dispersion measurements (Table 10, Figure 19).

Table 10. Location of the conductivity sensors during the semi-natural channel experiments.

Run	Type	Location (m)	Conductivity sensor number	Sampling interval (seconds)
SNC-1	Longitudinal	20 C	1	1
		40 C	2	10
		60 C	3	1
		80 C	4	
		90 C	5	
SNC-2 SNC-3	Longitudinal and lateral	20 LB	1	1
		20 C	2	10
		20 RB	5	1
		60 LB	3	
		60 RB	4	

LB = left bank, C = center of the channel, RB = right bank.

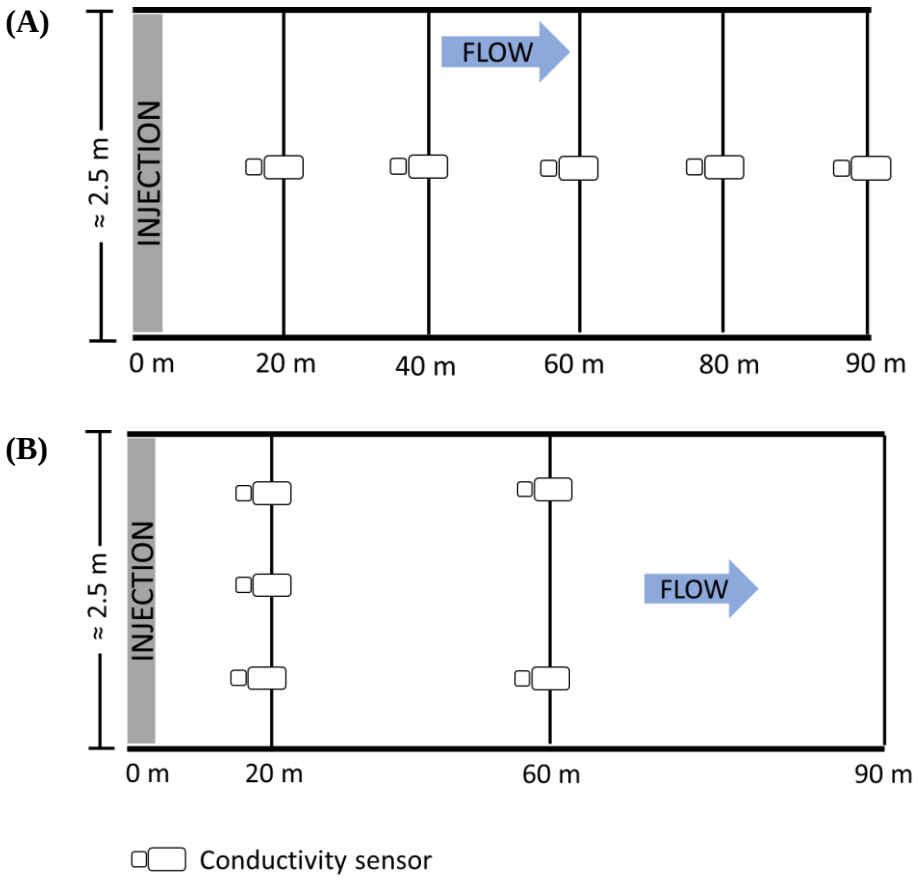

Figure 19. Location of the conductivity sensors in the semi-natural channel. A) Run SNC-1; B) Runs SNC-2 and SNC-3.

3.2.3. Natural channel (NC)

Two sets of experiments were conducted in a natural channel, Creighton Creek, in Lumby, BC. The section of the channel selected for the study was 222 m long, with width varying between approximately 3 m and 7 m. In total, nine injections of sodium chloride and sediment were conducted under two flow conditions (Table 11). The sediment grain sizes varied from <0.075 to 0.5 mm.

Table 11. Summary of the sodium chloride and sediment injections – natural channel.

Run	Discharge (m^3s^{-1})	Sodium chloride (g)	Sediment (g)	Sediment size (mm)
NC-1.1	0.093	500.04	1000.43	<0.075
NC-1.2		500.98	1006.89	0.075-0.125

Run	Discharge (m^3s^{-1})	Sodium chloride (g)	Sediment (g)	Sediment size (mm)
NC-1.3	0.042	500.29	1001.32	0.125-0.25
NC-2.1		501.54	1003.25	0.075-0.125
NC-2.2		508.57	1000.43	0.125-0.25
NC-2.3		502.32	1002.15	0.25-0.5
NC-2.4		500.27	838.41	<0.075
NC-2.5		516.02	1010.46	0.075-0.125
NC-2.6		500.70	1002.52	0.125-0.25

The experiments at this channel were designed to investigate longitudinal and lateral dispersion in a channel with non-uniform geometry. Table 12 and Figure 20 show a summary of the location of each sensor during the natural channel experiments.

Table 12. Summary of sodium chloride and sediment injections conducted at the natural channel.

Run	Type	Distance downstream (m)	Turbidity sensor number	Conductivity sensor number	Sampling interval (seconds)
NC-1.1 NC-1.2 NC-1.3	Longitudinal and lateral	12.5 LB	735	-	-
		12.5 C	1433	-	-
		12.5 RB	1434	-	-
		36 LB	1435	1	1
		36 C	1436	2	10
		36 RB	1437	4	
		49.6 LB	10181	5	
		49.6 RB	10193	3	
NC-2.1 NC-2.2	Longitudinal and lateral	36 LB	735	1	
		36 C	1433	3	
		36 RB	1434	2	
		49.6 LB	1437	-	
		49.6 C	1436	-	
		49.6 RB	1435	-	
		65 LB	10193	-	
		65 RB	10181	-	
NC-2.3		36 LB	735	-	
		36 C	1433	-	1
		36 RB	1434	-	
		49.5 LB	1437	1	
		49.6 C	1436	3	
		49.6 RB	1435	2	
		65 LB	10193	-	
		65 RB	10181	-	
NC-2.4	Longitudinal	12.5	735	-	
		36	1433	2	
		49.6	1434	-	
		73.3	1437	-	
		92	1436	3	
		107	1435	-	

Run	Type	Distance downstream (m)	Turbidity sensor number	Conductivity sensor number	Sampling interval (seconds)
		207	10181	-	
		222	10193	1	
		12	735	-	
		36	1433	3	
		49.6	1434	-	
NC-2.5		73.3	1437	-	
NC-2.6		92	1436	3	
		107	1435	-	
		115.9	10181	-	
		127.9	10193	1	

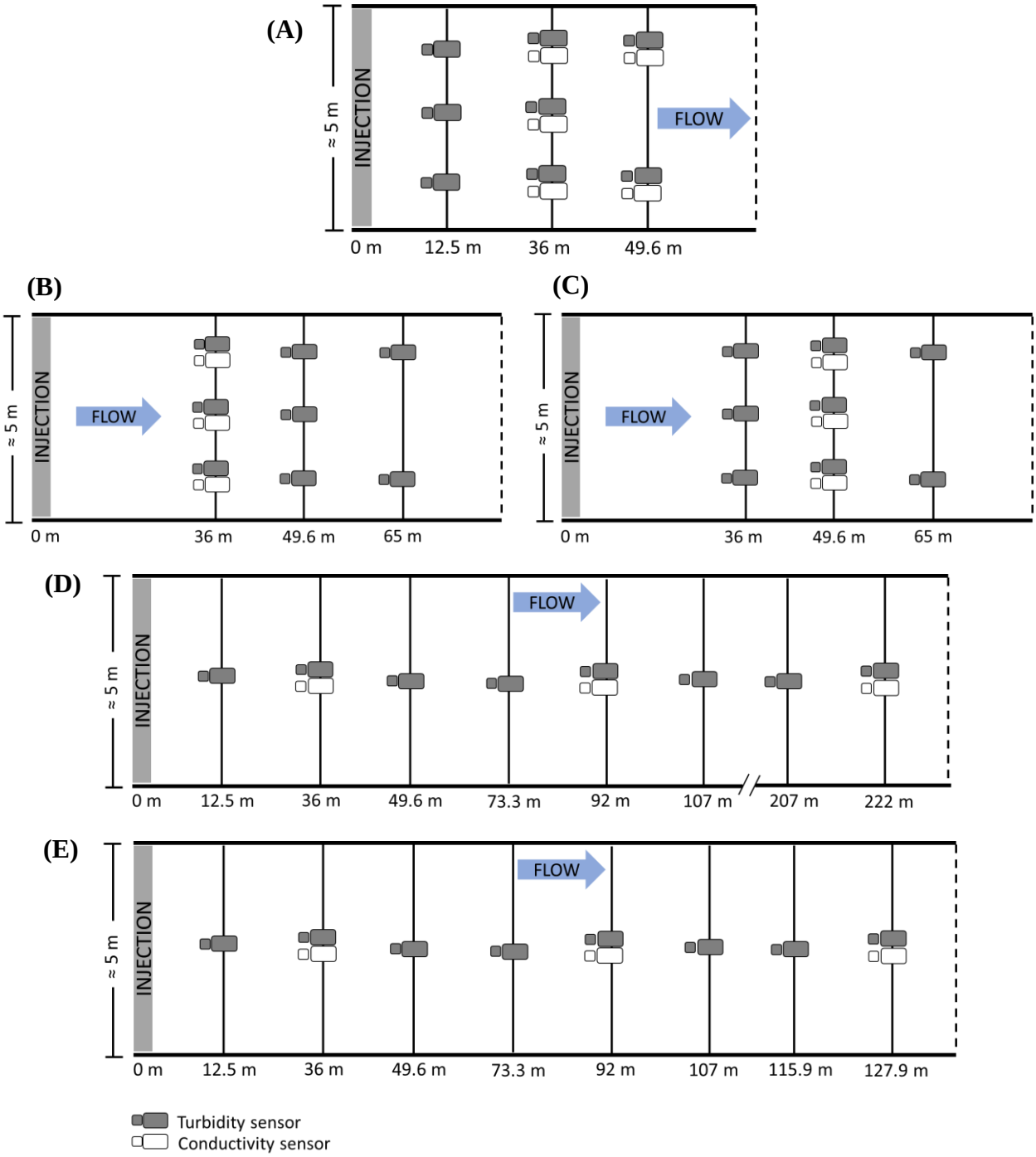

Figure 20. Location of the conductivity and turbidity sensors in the natural channel. A) Runs NC-1.1,1.2, and 1.3; B) Runs NC-2.1, and 2.2; C) Run NC-2.3, D) Run NC-2.4; E) Runs NC-2.5 and 2.6.

3.3.Hydraulic modeling

Given the shallow flow depth on the study channels, it was not possible to measure the lateral velocity profiles in the sampling locations during the field experiments. Furthermore, information from the cross-sections survey provided only a cross-section value for parameters such as flow width, and flow depth. Therefore, in order to obtain estimates of the reach average characteristics (velocity, shear velocity, slope, width, flow, area, and Froude number) the hydraulic conditions of the channels were modeled utilizing the United States Army Corps of Engineers Hydraulic Engineering Center River Analysis System (HEC-RAS 5.07). HEC-RAS was used for this purpose because it is a widely used hydraulic model that has been tested extensively.

The hydraulic models were calibrated utilizing the one-dimensional steady-flow module of HEC-RAS. The geometry data input was based on field surveys of cross-section and waterline elevations. The measured or estimated discharges were entered as steady-state condition inputs and the boundary conditions were defined by surveyed waterlines or normal depth based on the channel slope. The Manning's roughness coefficients (n) were then adjusted iteratively at each cross-section in order to match the observed water levels.

The HEC-RAS model provides cross-section averaged values of each variable (velocity, depth, area, etc.) for every cross-section. The model results were processed to produce a weighted average value of each variable accounting for the distance between the cross-sections (Figure 21). Initially, the results were averaged between every two cross-sections to obtain a sub-reach average for each parameter. Then, the sub-reach values were weighted according to the distance between the cross-sections:

$$\overline{\overline{V}}_{\Delta x_{n+1}} = \frac{(\overline{V}_n \times \Delta x_n) + (\overline{V}_{n+1} \times \Delta x_{n+1})}{\Delta x_n + \Delta x_{n+1}} \quad (103)$$

where $\overline{\overline{V}}_{\Delta x_{n+1}}$ = weighted average of a certain parameter v, $\overline{V}_n$ = average of a certain parameter v for sub-reach n, $\overline{V}_{n+1}$ = average of a certain parameter v for sub-reach n+1, Δx_n = longitudinal distance between cross-sections n and n+1, and Δx_{n+1} = longitudinal distance between cross-section n+1 and n+2.

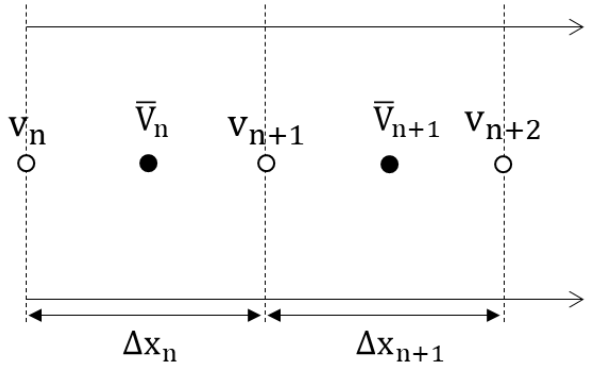

Figure 21. Weighted averaging of HEC-RAS results based on the distance between the cross-sections.

3.4.Data analysis

The conductivity and turbidity outputs were converted to sodium chloride and suspended sediment concentration, respectively, utilizing the calibration curves reported in 3.1. After conversion, the time series of concentration showing the plume structure in the temporal domain were plotted and analyzed. The background concentration was subtracted from the time series that defined each curve, producing a new time series beginning at zero concentration values. The background concentration was defined as the concentration measured prior to the initial rise in concentration following an injection. The sodium chloride background concentration was relatively constant so the value of the background level was easy to determine. The suspended sediment background concentration, however, fluctuated naturally due to various sources of turbidity in the water column not associated with sediment injection. The background level for each run was taken as the average of the 30 seconds prior to the initial rise.

3.4.1. Analysis of concentrations curves

3.4.1.1. Discharge estimates from salt dilution

Concentration curves of conservative tracers such as sodium chloride are often utilized as a proxy for discharge measurements (Leibundgut et al. 2009; Moore 2005). Based on the conservation of mass and the difference between the concentration measured at every sampling

interval and the background concentration, a discharge estimate can be calculated for every sodium chloride plume using (Moore 2005):

$$Q = \frac{M}{\Delta t \sum_0^T (C - C_b)} \tag{104}$$

where Q = discharge (L^3T^{-1}), M = mass injected (M), Δt = sampling interval (T), C = concentration (ML^{-3}) on each sampling interval, and C_b = background concentration (ML^{-3}).

This method is only applicable once complete lateral mixing is achieved and the concentration is similar everywhere in the sampling cross-section (Leibundgut et al. 2009; Moore 2005). In effect, this implies taking measurements in the far-field where complete lateral mixing has been achieved but not so far as to lose the signal via dispersion.

3.4.1.2. Total mass recovery and peak mass recovery

The analysis of concentration curves is usually based on the concept of temporal moments. The n^{th} temporal moment of a concentration curve is defined as (Luo et al. 2006; Rutherford 1994):

$$m_n(x) = \int_0^\infty t^n \, c(x,t) \, dt \tag{105}$$

where m_n = n^{th} temporal moment, t = time, and c = concentration.

The total concentration of the curves was calculated by the zero-th temporal moment:

$$C_{total} = \int_0^T c(x,t) \, dt \tag{106}$$

where, C_{total} = total concentration or sum of all concentrations beneath the curve (ML^{-3}), T = duration of the curve (T), c = concentration per second ($ML^{-3}T^{-1}$).

The total mass of tracer is given by the total concentration multiplied by the discharge at the time of the experiment:

$$M = C_{total} \times Q \tag{107}$$

where, M = total mass of the curve (M), C_{total} = total concentration of the curve (ML^{-3}), Q = stream discharge (L^3T^{-1}).

The total recovered mass of each curve was divided by the injected amount of tracer yielding a recovery percentage (R):

$$R = \frac{M}{\text{Mass injected}} \times 100 \quad (108)$$

where R = recovered portion of the injected mass (%).

The percent recovery provides a sense of how much tracer is transported past each sensor location and allows a comparison of one event magnitude to another in terms of overall impact. For sodium chloride, which is assumed to be a conservative tracer, the recovery should always be 100%, after cross-sectional mixing is achieved. In practice, however, almost all tracer experiments observe some sort of tracer loss partly due to experimental uncertainty (e.g., in discharge estimates or concentration measurements, but also due to instrument position within the channel). Fitting the conservative one-dimensional ADE to a tracer when the losses are significant would lead to an overestimation of the longitudinal dispersion coefficient. Therefore, to account for the losses, the sodium chloride concentration curves were adjusted by:

$$c_{adj}(x,t) = \frac{c\,(x,t)}{R} \quad (109)$$

where c_{adj} (x,t) = concentration adjusted for tracer loss.

The limitation of this procedure is that it assumes that the percent loss is the same for every time increment of the plume, which might not be true. For example, most of the tracer loss might have occurred due to transient storage, affecting the tails more than the peak of the curve. But the adjustment was deemed necessary so that baseline values of the longitudinal dispersion coefficients could be applied to the sediment concentration curves when evaluating settling losses.

The peak concentration for each curve was determined by the maximum value in the curve. The peak concentration was multiplied by the discharge and normalized by the mass injected to yield a percent recovery associated with the peak:

$$R_{peak} = \frac{C_{peak} \times Q}{\text{Mass injected}} \times 100 \quad (110)$$

where C_{peak} = maximum concentration observed (ML^{-3}), R_{peak} = injected mass recovered during the peak of the plume (%).

Similar to the total recovery, the normalized peak recovery allows the comparison of curves generated from different mass injections with the understanding that the peak percentage recovery depends on the time interval of sampling. Thus, the peak recovery will always be a small percentage of the overall mass recovery. In the cases where different instantaneous sampling intervals (1 second and 10 seconds) were utilized (runs SNC-1-3, and NC-1.1-1.3), it is important to note that the peaks might not be directly comparable, given that the maximum concentration value might have occurred during the 10 seconds sampling interval but not recorded by the probe.

*3.4.1.3. **Peak and centroid advection velocities***

The peak advection velocity was estimated by dividing the longitudinal distance between the injection and the sampling locations by the passage time of the peak:

$$\bar{U}_{peak} = \frac{x}{t_{peak}} \quad (111)$$

where $\bar{U}_{peak}$ = peak velocity (LT^{-1}), and t_{peak} = peak travel time.

Moments larger than 0 are commonly normalized by the total concentration in order to allow comparison between curves generated by different amounts of tracer:

$$m_n^* = \frac{m_n}{m_0} = \frac{\int_0^\infty t^n c(x,t)\, dt}{\int_0^\infty c(x,t)\, dt} \quad (112)$$

where m_n^* = normalized moment for $n > 0$.

The centroid travel time of the concentration curves was calculated by the first normalized temporal moment:

$$m_1^* = \frac{m_1}{m_0} = \frac{\int_0^\infty t\, c(x,t)\, dt}{\int_0^\infty c(x,t)\, dt} \quad (113)$$

where m_1^* = centroid travel time.

The centroid velocity was then obtained by dividing the longitudinal distance between the injection and the sampling locations by the passage time of the centroid:

$$\bar{U}_{centroid} = \frac{x}{m_1^*} \quad (114)$$

where $\bar{U}_{centroid}$ = centroid velocity (LT^{-1}), x = longitudinal distance downstream of injection (L), and m_1^* = passage time of the centroid (T).

3.4.2. Longitudinal dispersion coefficients

Longitudinal dispersion coefficients for each run were computed by using the Hayami solution to the one-dimensional ADE (Equation 64) and fitting it to the sodium chloride concentration curve (adjusted for tracer loss). The hydraulic parameters were obtained from the HEC-RAS simulations, and by a process of trial-and-error, an optimized value for the longitudinal dispersion coefficient was arrived at, yielding the best-fit curve to the concentration data.

The reliability of these estimates of the longitudinal dispersion coefficient depends on whether the concentration curves were measured in the advective zone or the equilibrium zone. Only those measurements taken in the equilibrium zone are directly comparable. The estimated length of the advective zone for each channel was calculated based on Equation 65 with the minimum and maximum empirical coefficients (β and α) reported in the literature. The only empirical coefficients available for lateral line sources were obtained in a rectangular smooth channel, where α has been reported to vary between 0.2 (Fischer 1973) and 1 (Rutherford 1994). The coefficient β was varied from 0.13 and 4.65 as mentioned in 2.1.5.1. In addition, the Peclet Number was used as a guide to assess the transition from the advective zone to the equilibrium zone. Concentration curves were defined as being located in the equilibrium zone if the Peclet number was $0.4 < Pe < 2.5$. Since longitudinal dispersion coefficients in the advective zone are not constant, they are

referred to as apparent longitudinal dispersion coefficients. Longitudinal dispersion coefficients obtained in the equilibrium zone are referred to as equilibrium longitudinal dispersion coefficients.

3.4.3. Lateral mixing

For runs where lateral concentration curves were sampled, the degree of lateral mixing was evaluated by comparing the main characteristics of the concentration curves from adjacent instruments: i.e., peak concentration, peak time, start time, and duration, where the duration parameter was determined by the difference between the end time and the start time of the curves. The agreement between curves was evaluated by the relative percent difference between each parameter:

$$\text{Relative \% difference} = \frac{\text{Observed value LB or C} - \text{ observed value RB}}{\text{Observed value RB}} \times 100 \quad (115)$$

The observed right bank curves were taken as the standard for no particular reason other than consistency.

3.5. Assessing the accuracy of the one-dimensional ADE to model suspended sediment dispersion in small-streams

The sediment transport mode (suspension, bedload) was estimated based on the Rouse number for each run. The settling velocity of the sediment was determined from Dietrich's (1982) formula, which is the most comprehensive to date in terms of the data utilized to derive the coefficients (Jiménez and Madsen 2003):

$$W_* = R_3 + 10^{R_1 + R_2} \quad (116)$$

where W_* = dimensionless settling velocity, R_1, R_2, and R_3 are defined by:

$$R_1 = -3.7671 + 1.92944(\log D_*) - 0.09815(\log D_*)^2 - 0.00575(\log D_*)^3 + 0.00056(\log D_*)^4 \quad (117)$$

$$R_2 = \left[\log\left(1 - \frac{1 - CSF}{0.85}\right)\right] - (1 - CSF)^{2.3} \tanh(\log D_* - 4.6) + 0.3(0.5 - CSF)(1 - CSF)^2(\log D_* - 4.6) \quad (118)$$

$$R_3 = \left\{0.65 - \left[\frac{CSF}{2.83}\tanh(\log D_* - 4.6)\right]\right\}^{1+\frac{3.5-P}{2.5}} \quad (119)$$

where D_* = dimensionless particle diameter, P = Power's roundness, and CSF = Corey shape factor.

For typical quartz sediments, P and CSF are assumed to be 3.5 and 0.7, respectively (Dietrich 1982). The dimensionless particle diameter, D_*, is given by:

$$D_* = d\left[\left(\frac{\rho_s}{\rho - 1}\right)\frac{g}{\nu^2}\right]^{1/3} \quad (120)$$

where d = particle diameter, ρ_s = particle density, ρ = fluid density, g = gravitational acceleration, and ν = kinematic viscosity.

For distributions, d is commonly assumed to be the D_{50}. Given that the D_{50} of the sediment fractions utilized were not measured, the D_{50} was estimated using the geometric mean between the smallest and largest particle sizes of each fraction. For the fraction containing sediment <0.075 mm, the sediment particle size was arbitrarily chosen as being 0.063 mm.

The settling velocity was then calculated by:

$$\omega = \left(\frac{W_* (\rho_s - \rho) g \nu}{\rho}\right)^{1/3} \quad (121)$$

The shear velocity was calculated by:

$$u_* = \sqrt{\frac{\tau_o}{\rho}} \quad (122)$$

where τ_o = shear stress (Nm^{-2}), and ρ = density of the water (kgm^{-3}).

For Ro < 1.25, it was assumed that the main transport mode was suspension, therefore, it was possible to test the accuracy of the one-dimensional ADE to model suspended sediment transport.

The accuracy of the one-dimensional ADE to model suspended in small streams was assessed according to the following steps:

i. The sodium chloride and suspended sediment curves were normalized by their peak concentration values in order to remove the effect of tracer loss from the analysis;
ii. The normalized curves were visually compared to determine if the dispersion processes were similar. Assessing parameters included the start time and peak time;
iii. If the normalized curves had a similar behavior, it was concluded that the suspended sediment dispersion process was similar to the sodium chloride dispersion process and that the one-dimensional ADE should be able to reproduce the observed data. Therefore, the longitudinal dispersion coefficient for the equilibrium zone obtained from the sodium chloride curves was applied to model the suspended sediment injections;
iv. Maintaining the average flow velocity and the longitudinal dispersion coefficient fixed, the settling term was calibrated for each suspended sediment curve located in the equilibrium zone. The settling term was calibrated in order to provide the same suspended sediment recovery as the observed data;
v. Maintaining the average flow velocity and the longitudinal dispersion coefficient fixed, the suspended sediment injections were modeled again utilizing the estimated settling rates based on Equation 101;
vi. The final suspended sediment modeled curves were compared against the observed data in order to assess the accuracy of the one-dimensional ADE model. Four parameters were selected to determine the accuracy of the model in relation to the observed curves: start time, peak time, peak concentration, duration;
vii. The accuracy of each modeled parameter was assessed based on the relative percent error:

$$\text{Relative \%error} = \frac{\text{Modeled value} - \text{observed value}}{\text{Observed value}} \times 100 \qquad (123)$$

The relative percent error was chosen given its simplicity and the fact that it clearly states if the modeled values are overestimating or underestimating the observed values, which is a crucial concern when dealing with drinking water safety. It is important to highlight that given the nature of the data, there were no negative modeled values (i.e., zero concentration is the baseline), therefore, the lower limit of the relative percent error is -100%, while the upper limit is infinity;

viii. Finally, the level of agreement between the modeled and observed curves was classified according to the following scale (Figure 22):

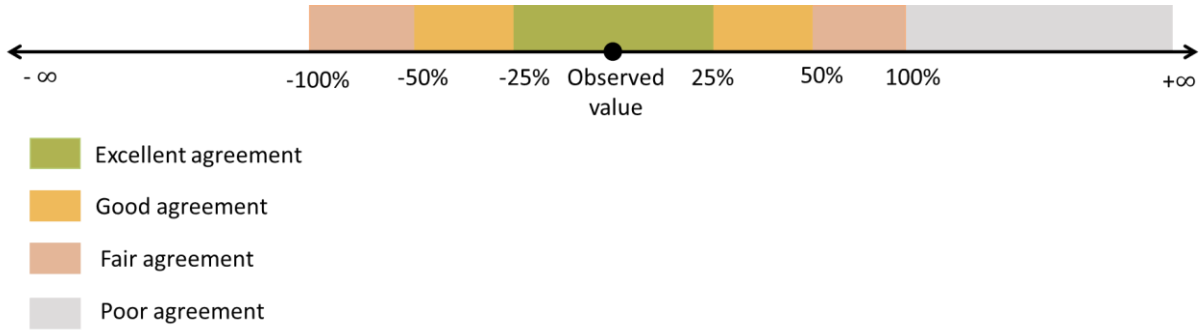

Figure 22. Level of agreement between modeled and observed parameters based on the relative percent error.

ix. In order to reject the null hypothesis, it was established that the model should be able to predict the selected parameters with at least ±50% accuracy (good agreement).

3.6. Evaluating the accuracy of the predictive formulas for the longitudinal dispersion coefficient

The accuracy of the predictive formulas for the longitudinal dispersion coefficient was assessed according to the following steps:

i. The reach-averaged results from the hydraulic models were utilized to calculate the longitudinal dispersion coefficient for each of the 26 formulas in Table 3;
ii. The predicted values of the longitudinal dispersion coefficient were applied to the one-dimensional ADE to model each sodium chloride curve located in the equilibrium zone;
iii. The modeled curves were compared to the observed data. Four parameters were selected to assess the accuracy of each predictive formula: start time, peak time, peak concentration, and duration of the plume;
iv. The accuracy of each modeled parameter (start time, peak time, peak concentration, and duration of the plume) was assessed according to the relative percent error (Equation 123);

v. The level of agreement for each modeled parameter was classified according to the scale shown in Figure 22;

vi. The overall level of agreement for each formula was defined according to the parameter that had the worst level of agreement;

vii. In order to reject the null hypothesis, it was established that at least one formula should be able to predict the characteristics of the concentration curves within ±50% relative error (good agreement).

Chapter 4: Results

4.1. Truncation criterion

The observed concentration time series had long tails indicating prolonged periods of sodium chloride or turbidity slightly above background levels. The majority of the conductivity curves eventually returned to background values after the passage of the plume, therefore, the termination time was easily defined. The suspended sediment concentration curves, however, often had very noisy trailing tails making it difficult to define the exact end of the plumes. Figures 23 and 24 show an example of a sodium chloride plume and a suspended sediment plume measured simultaneously at a certain location. Based on the sodium chloride curve it is possible to determine the end of the plume is at about 7 minutes after the injection, however, based on the suspended sediment plume this is not clear.

In most runs, sodium chloride and suspended sediment were injected as a slurry at the same time, and the termination time from the conductivity time series could be used to indicate the end of the suspended sediment concentration curve. Small spikes in the latter were considered to be due to instrumental error and natural fluctuations in turbidity not directly due to the injected mass. However, in cases when neither the conductivity nor the concentration returned to the background value, the definition of the plumes was hindered. Therefore, it was necessary to define a truncation criterion that could be applied to all curves so as to avoid bias associated with shorter versus longer plume tails, especially since longer tails have poorer signal-to-noise ratios. The literature recommends truncating the plume when the tail reaches a certain percentage (5, 3, and 1%) of the peak concentration (Fischer 1966; Sayre 1973). However, given the fluctuations in the peaks and tails of the measured suspended sediment concentration curves, it would be difficult to utilize this method with confidence.

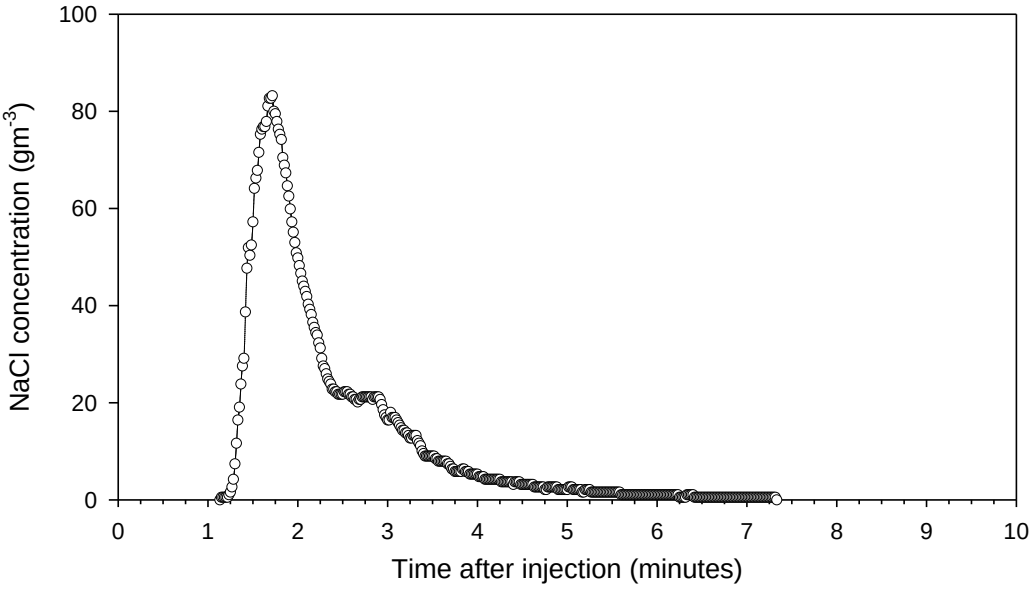

Figure 23. Example of a sodium chloride concentration curve where the values return to background after the passage of the plume.

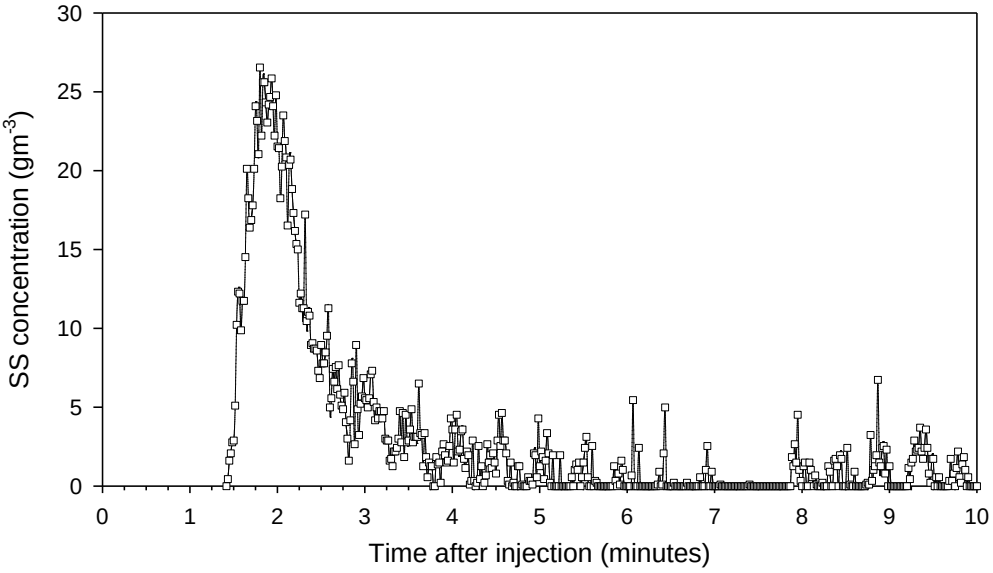

Figure 24. Example of a suspended sediment concentration curve showing a long tail with spikes, exemplifying the difficulty deciding the termination time of the injected plume.

A novel truncation criterion was developed for this study that involved applying a log-transformation to the time axis. When the time series are plotted on a logarithmic time scale, the

skewness decreases and the concentration curves more closely resemble a normal distribution (Figure 25).

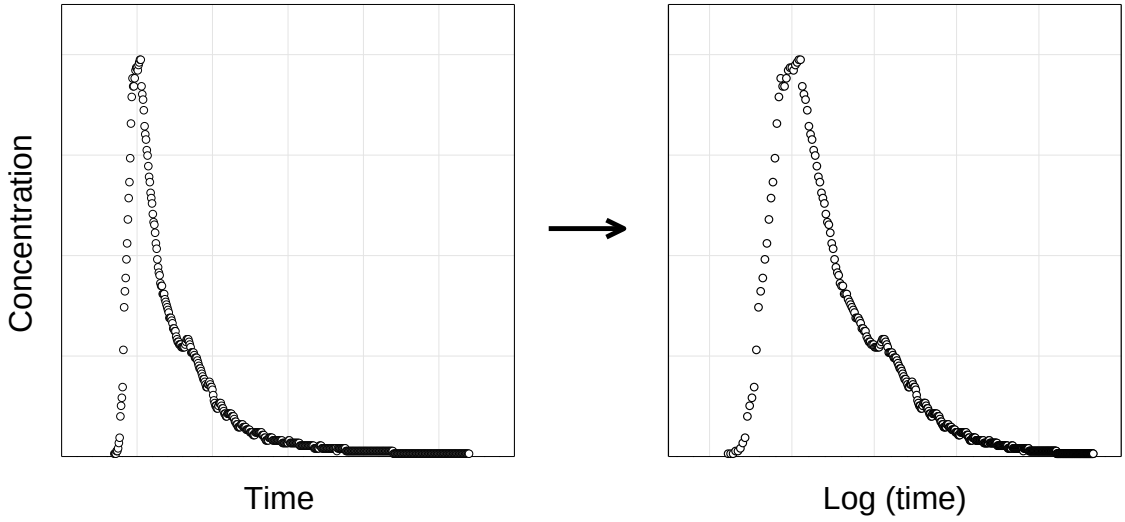

Figure 25. Log-normal transformation of concentration curves.

After the log transformation, all the sodium chloride concentration curves that returned to background concentration values were analyzed in order to identify if there was a relation between the peak time (t_{peak}) and the total duration of the plume (T). Two reference times were considered: (i) the injection time (t = 0); and (ii) the start of the plume ramp-up time (i.e., when the concentration starts to rise from background values). Two ratios were compared to determine which was better suited for deciding curve truncation. The first considered the end time of the plume from injection ($T_{injection}$) to the peak time from the injection ($t_{injection\text{-}peak}$). The second considered the end time of the plume from the start of the plume (T_{start}) to peak time from the start of the plume ($t_{start\text{-}peak}$) (Figure 26).

The results (Table 13) demonstrated that there was a relation between the time to peak and the total duration of the plumes (in log scale) for both reference times (injection and plume start). However, considering the number of log cycles from injection provided more consistent results for all the runs, more so than considering the number of log cycles from the start of the plume. The standard deviation (SD) of the ratios from injection time was consistently smaller than the standard

deviation of the ratios from the plume ramp-up time. Thus, the truncation criterion shown in Figure 26B was adopted for the analysis of suspended sediment concentration plumes.

Table 13. Log (T)/log (t_{peak}) analysis for two alternative truncation criteria.

	Concrete channel	**Semi-natural channel**	**Natural channel**
Log (T_{start})/log ($t_{start-peak}$)	**1.84**	**1.46**	**1.7**
Maximum	2.15	1.77	2.06
Minimum	1.36	1.20	1.36
SD	0.27	0.22	0.18
Log ($T_{injection}$)/log($t_{Injection-peak}$)	**1.14**	**1.20**	**1.30**
Maximum	1.22	1.30	1.48
Minimum	1.06	1.09	1.12
SD	0.04	0.08	0.09

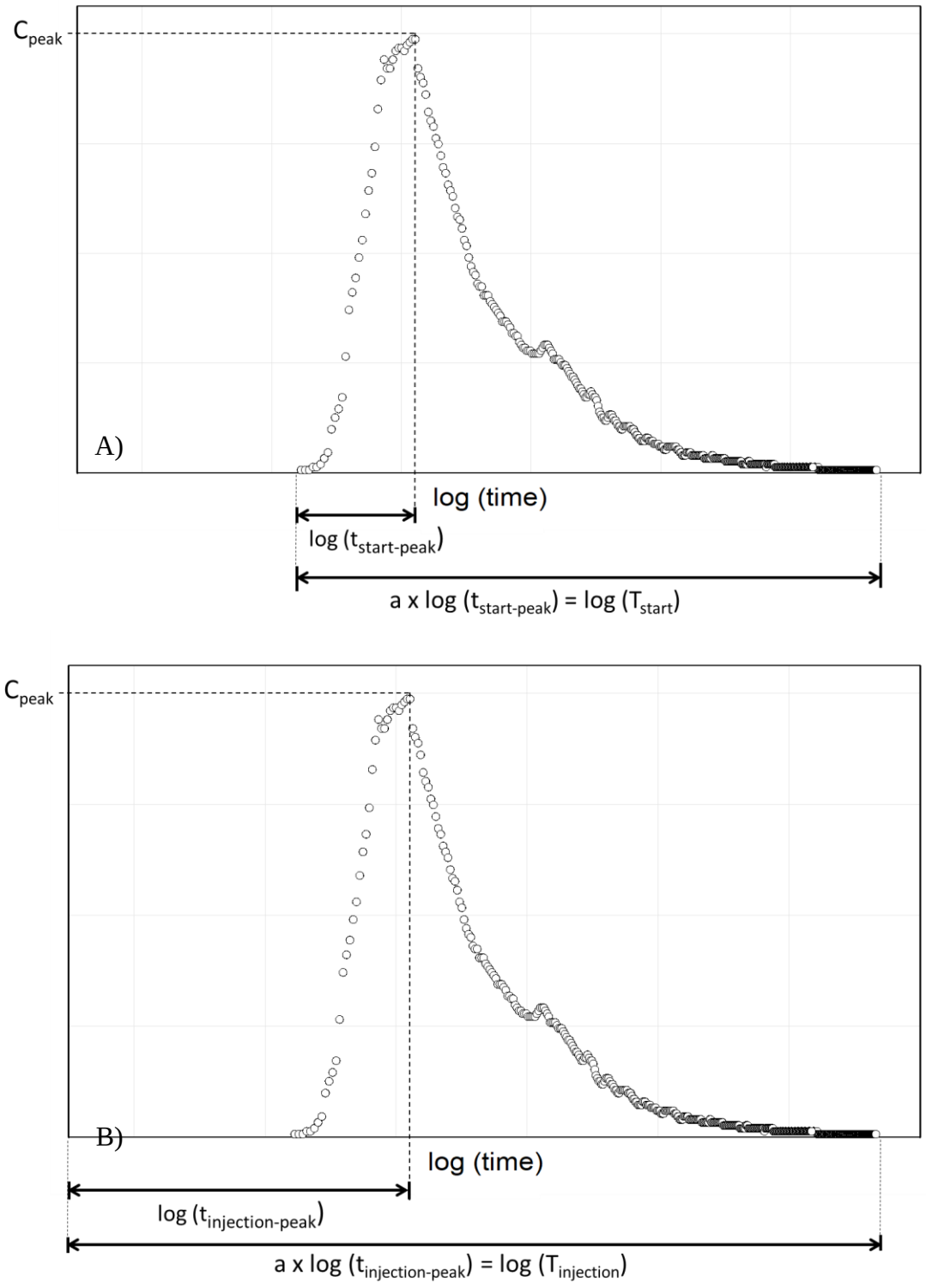

Figure 26. Log (T)/log (t_{peak}) ratios. A) Start of the plume as reference time; B) Injection time as reference time.

On average, it took 1.2 x log ($t_{injection\text{-}peak}$) for the plumes to return to background levels. The curves obtained in the concrete channel exhibited the shortest tails, while the ones in the natural channel had the longest tails. The results suggest that the tails of the plumes (i.e., skewness) increased with the complexity of the channel.

An analysis of the log (T)/log (t_{peak}) ratios also suggests that there is a dependency on the downstream sampling distance that is similar for all three channels (Figure 27). The log (T_{start})/log ($t_{start\text{-}peak}$) ratios decrease in the downstream direction. The log ($T_{injection}$)/log ($t_{injection\text{-}peak}$) ratios, on the other hand, seem to be less affected by the sampling location, particularly in the concrete channel. This outcome provides greater rationale for adopting the second criterion based on time from injection.

Fundamentally, the skewness of the curves is the primary factor to consider in this analysis of time series truncation, and it is influenced by both channel complexity and sampling location (which influence whether measurements have been taken in the advective zone or the equilibrium zone). In the concrete channel, the curves measured at 80.75 m and 139.95 m downstream of the injection line remained strongly positively skewed even after the log transformation. The peak arose quickly after the ramp-up of the plume whereas the tail was long, yielding a large log (T_{start})/log ($t_{start\text{-}peak}$) ratio. At 370.15 m downstream of the injection line, the log-transformed curves are less skewed, the peak times are more symmetrically located between the start and end times, yielding smaller log (T_{start})/log ($t_{start\text{-}peak}$) ratios. On the other hand, the peak time from the injection is determined by the overall travel time of the peak, therefore, it is not as affected by the skewness of the curves. In the semi-natural and natural channels, both ratios decreased with downstream distance. Nevertheless, the standard deviation was larger for the log (T_{start})/log ($t_{start\text{-}peak}$) ratio than the log ($T_{injection}$)/log ($t_{injection\text{-}peak}$) ratio. Therefore, the ($T_{injection}$)/log ($t_{injection\text{-}peak}$) ratio proved to be a better truncation criterion.

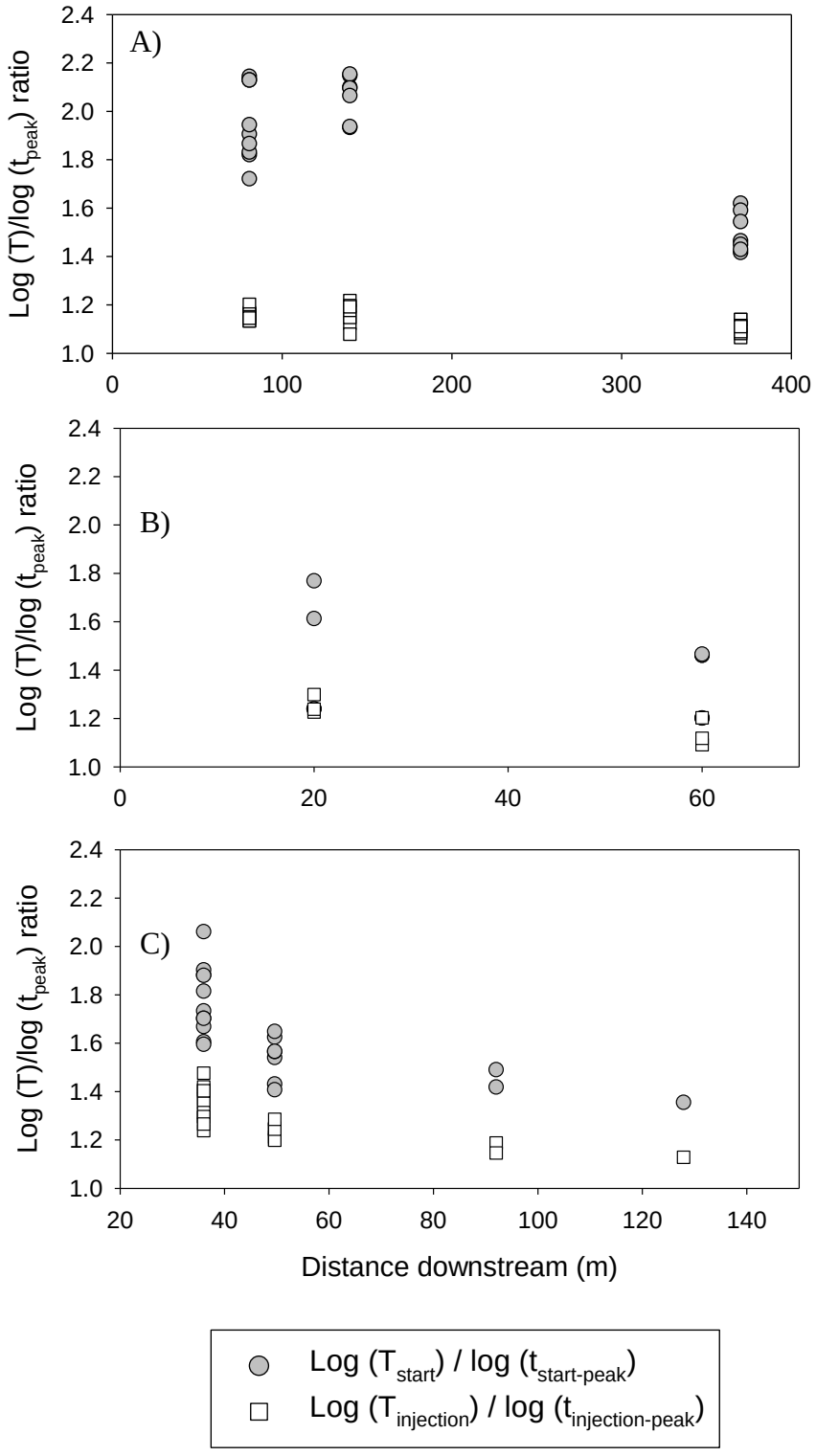

Figure 27. Log (T)/log (t_{peak}) ratios versus distance. A) Concrete channel; B) Semi-natural channel; C) Natural channel. Note change in scale on both axes.

4.1.1. Truncation procedure

The sodium chloride and suspended sediment concentration curves were truncated utilizing the specific log ($T_{injection}$)/log ($t_{injection-peak}$) coefficient calculated for each channel (Figure 28). While this criterion did force truncation of a small number of curves before the concentration values returned to background levels, it was deemed preferable to use the same objective methodology for the analysis of all curves, instead of depending on the subjective judgment of the person analyzing the data for every individual curve.

For the sodium chloride curves (where the end of the plume is known and defined by the return to background level), if the actual end time occurred before the truncation time based on the criterion, no truncation was applied and the actual end time based on background level was used. Otherwise, the truncation criterion was applied to define the end of the plume. In those circumstances when the time series was shorter than what the truncation criterion required (because the data acquisition system was turned off, which occurred on a small number of occasions), the end of the plume was defined by the end of the measurements for both sodium chloride and suspended sediment. Such cases are referred to as experimental truncation (ET).

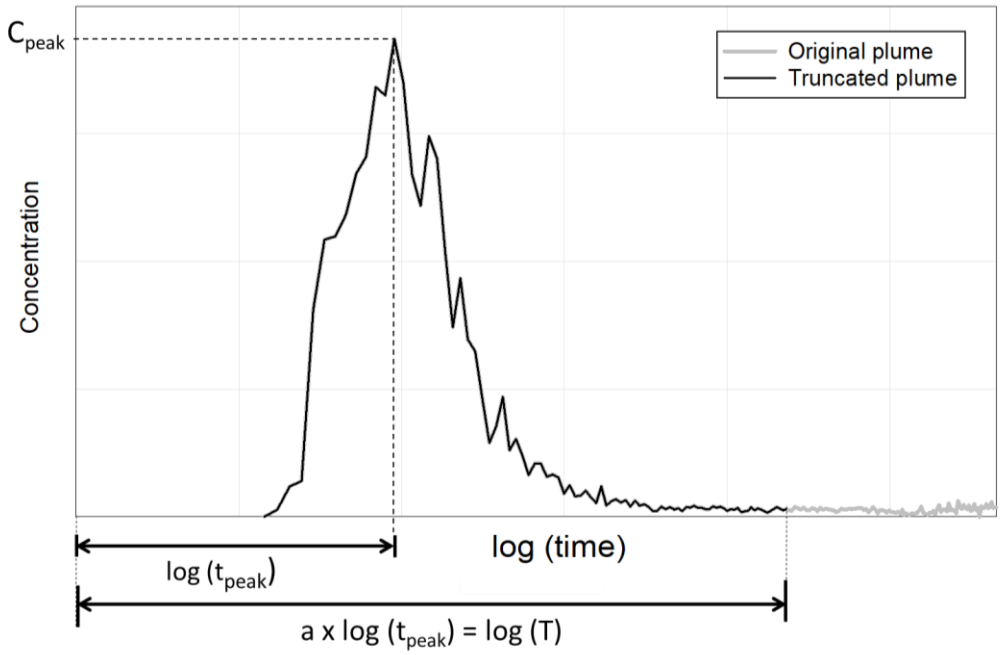

Figure 28. Example of a suspended sediment concentration curve defined utilizing the truncation criterion.

Plume (or event) duration was determined by subtracting the ramp-up (start) time of the plume from the end time. In the case of sodium chloride, with the exception of the experimentally truncated curves, the end of the curves was determined either by return to the background or the truncation criterion. Therefore, it is possible to determine the duration of the curves. In the case of suspended sediment, however, while some curves have small concentration values during the whole duration determined by the truncation criterion, other curves have several values below background (i.e., zero concentration) among small concentration fluctuations included duration determined the truncation criterion. While these concentration values on the tails do not affect the percent recovery rates, they largely affect the duration of the curves. Because it is not reliable to utilize the end from the truncation criteria to define the duration of the suspended sediment curves, this parameter was not considered when analyzing suspended sediment curves.

4.2. Concrete channel

The experiments in the concrete channel were designed to analyze dispersion in a low complexity level environment. The studied concrete channel is a straight, trapezoidal channel, with uniform geometry, and no vegetation. Therefore, the flow characteristics were fairly uniform over the studied reach and the likelihood of transient storage effects was small. The bed and banks are strictly concrete, therefore, there were no local sources of sediment. Hence, it can be expected that the dispersion process in the concrete channel should be the closest to the theoretical model when compared to the semi-natural and natural channels.

4.2.1. Discharge

Given the shallow depth of flow on the day of the experiments, it was not possible to conduct discharge measurements utilizing a flow meter. The discharge was estimated using the salt dilution method applied to every concentration curve before truncation because most curves returned to background level. This approach is consistent with the assumption that sodium chloride is a conservative tracer. The results are shown in Table 14. An average discharge for each sampling location was estimated based only on the curves that returned to the background conductivity value

after the passage of the plume (i.e., excluding the runs with experimental truncation). The average discharge estimates decreased between 80.75 m and 190.95 m downstream of the injection line, and reached its maximum value at 370.15 m, yielding 0.143 m^3s^{-1} on average.

The average discharge chosen as the best estimate of the true discharge was based on the conductivity measurements obtained at 370.15 m, the farthest downstream location, in order for complete lateral and vertical mixing to have occurred. The accuracy of this estimated discharge was assessed by analyzing data from a rating curve for Upper Vernon Creek located upstream of the location of the experiments. The data were obtained through personal communications with the BC Ministry of Forest, Lands, Natural Resources Operations and Rural Development (FLNRORD). According to the provisional rating curve, based on only a limited number of calibration points, the average discharge during the experiments was approximately 0.167 m^3s^{-1}. Both estimates of discharge (salt dilution versus rating curve) are believed to include significant experimental uncertainty, and without additional information available, it was decided that 0.143 m^3s^{-1} provided the best value to use.

Table 14. Summary of discharge values (m^3s^{-1}) estimated through the salt dilution method assuming 100% recovery.

Location	**Run**									**Average**
(m)	**CC-1**	**CC-2**	**CC-3**	**CC-4**	**CC-5**	**CC-6**	**CC-7**	**CC-8**	**CC-9**	
80.75	0.122	0.125	0.127	0.126	0.134	0.131	0.135	0.116	0.130	0.127
139.95	0.126^{ET}	0.105	0.110	0.129	0.115	0.102	0.113	-	0.097	0.112
370.15	0.149	-	0.159	0.146	0.140	0.147^{ET}	0.132	0.137	0.136	0.143

ET = experimental truncation

4.2.2. HEC-RAS hydraulic model

Four cross-sections (at 15.7 m, 45.5 m, 75.7 m, and 139.95 m downstream from the injection line) were surveyed in the field and used as the basis for the channel geometry on HEC-RAS (Appendix A). Several thalweg elevation points were also surveyed between 0 and 330 m downstream of the injection line, yielding a channel slope of 0.0209 (Figure 29). The waterline slope between the injection line (x = 0 m) and approximately 100 m downstream of the injection line was surveyed during a different discharge (0.698 m^3s^{-1}), yielding a similar slope, S = 0.0205.

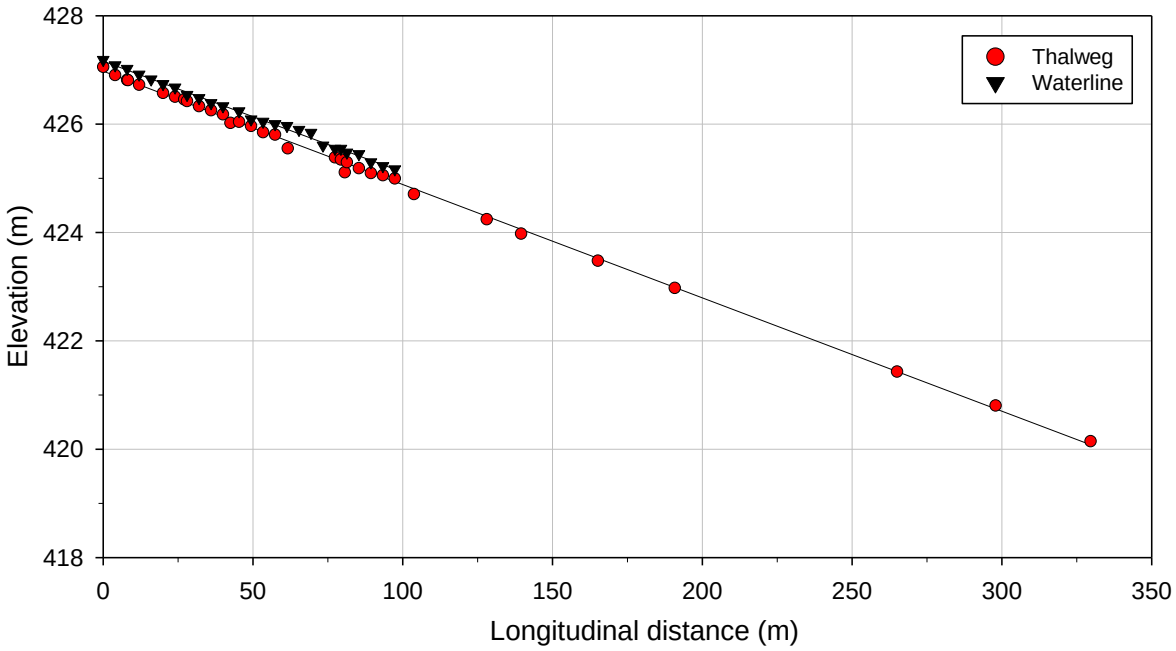

Figure 29. Thalweg and waterline elevations surveyed in the concrete channel.

The surveyed cross-sections and thalweg slope were used to interpolate cross-sectional geometries for all the locations where tracer data were collected (Table 15, Figure 30). The interpolated cross-sections at the upstream and downstream ends of the channel were based on the cross-sections surveyed at 139.95 and 42.5 m, respectively. This was done in order to spread the observed differences in cross-sectional geometry at the measured locations along the length of the channel rather than simply duplicate one cross-section repeatedly. The elevation of the surveyed cross-sections was adjusted using the thalweg slope and the longitudinal distance between locations. The geometry for cross-section 5 was obtained by interpolating between the adjacent surveyed cross-sections using the linear interpolation feature of HEC-RAS. Table 15 and Figure 30 shown the initial geometry input for the concrete channel model on HEC-RAS.

Table 15. Initial geometry input for the concrete channel model on HEC-RAS.

Location (m)	Cross-section number	Geometry
0.00	1	XS 9 adjusted for slope
15.70	2	Surveyed
42.50	3	Surveyed

Location (m)	Cross-section number	Geometry
75.70	4	Surveyed
80.75	5	Interpolated in HEC-RAS
139.95	6	Surveyed
370.15	7	XS 4 adjusted for slope

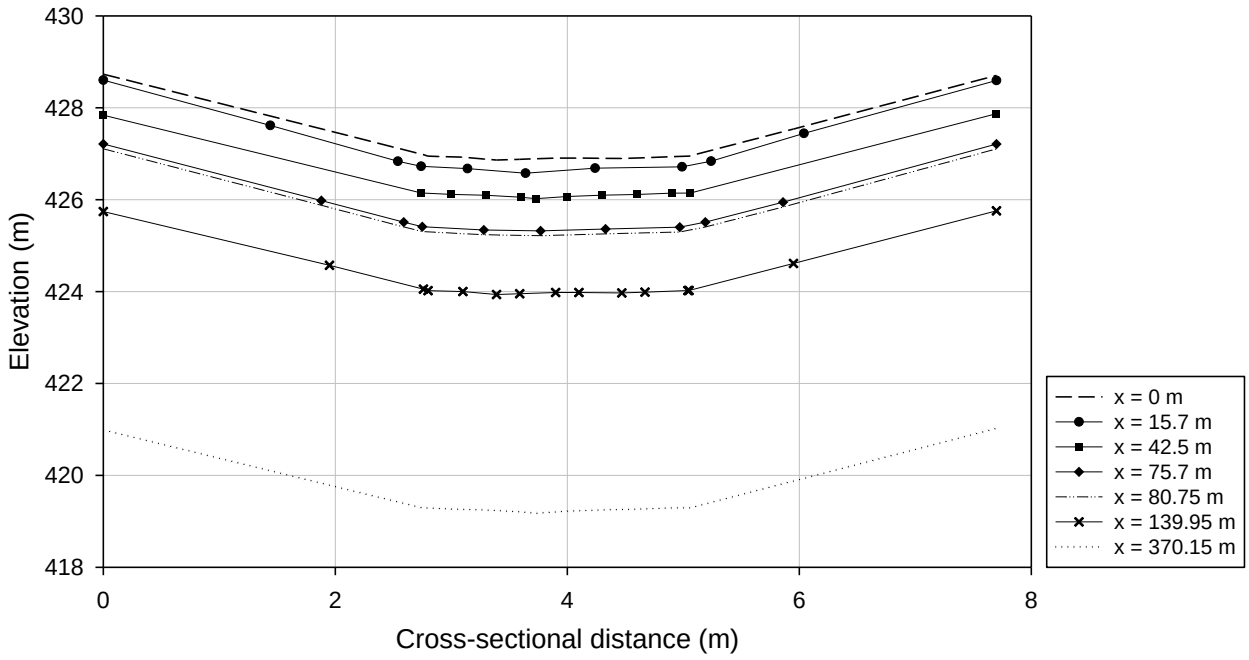

Figure 30. Cross-sectional geometry (surveyed and interpolated) of the concrete channel.

A discharge of 0.143 m^3s^{-1} was utilized for a steady flow simulation in HEC-RAS. The upstream and downstream boundary conditions were determined by the 'normal depth' criterion, based on the waterline slope (S = 0.0205). The model was calibrated by adjusting the Manning's roughness coefficients (n) at each cross-section in order to match the observed water levels (Figure 31).

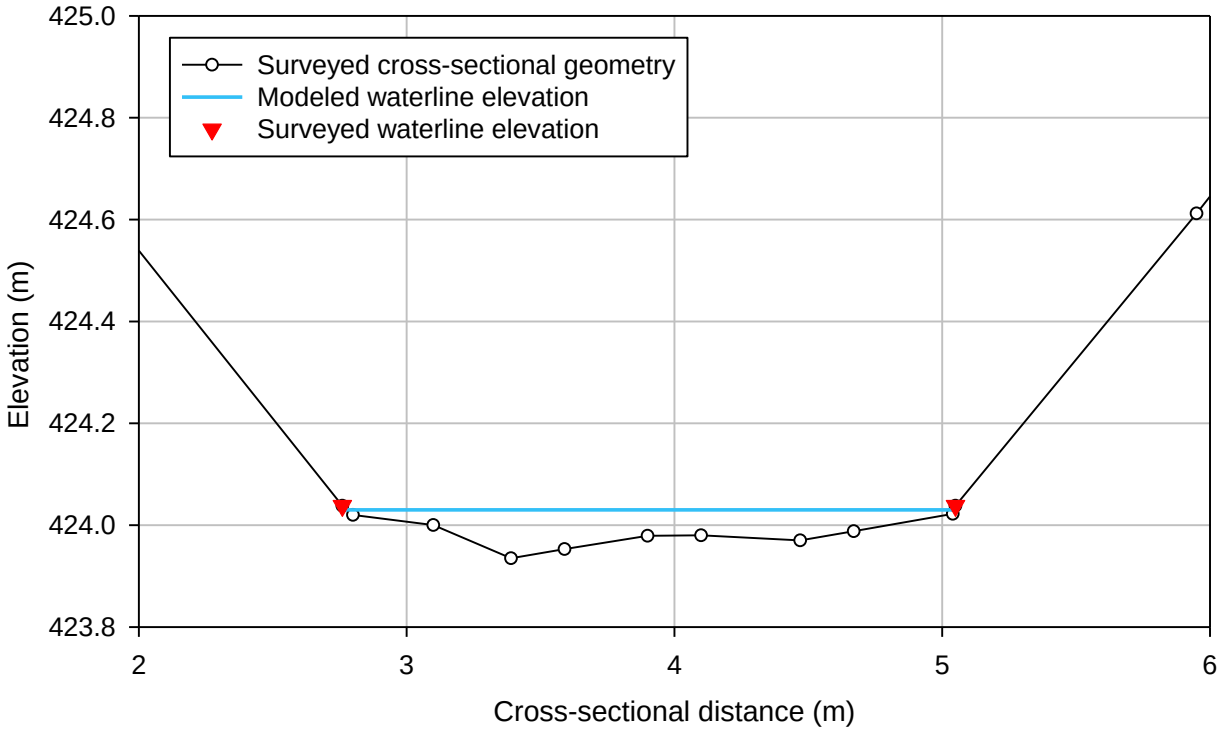

Figure 31. Example of a concrete channel cross-section calibrated on HEC-RAS (x = 139.95 m).

The largest difference between surveyed and modeled waterline elevations was 0.9 cm at cross-section 6, which was deemed acceptable because of the uncertainties associated with the rod-and-level surveys (Table 16). Cross-sections 2 and 4 were surveyed during a different discharge therefore, they were not utilized to calibrate the waterline elevation. Given the uniform nature of the concrete channel, five cross-sections with water levels properly surveyed was considered sufficient for purposes of model calibration.

Table 16. Observed and modeled waterline elevations in the concrete channel.

Location (m)	**Cross-section number**	**Observed/interpolated waterline elevation (m)**	**Modeled waterline elevation (m)**	**|ΔE| (cm)**
0.00	1	426.963[a]	426.955	0.8
15.70	2	-	426.714	-
42.50	3	426.144	426.143	0.1
75.70	4	-	425.409	-
80.75	5	425.301[a]	425.304	0.3

Location (m)	Cross-section number	Observed/interpolated waterline elevation (m)	Modeled waterline elevation (m)	|ΔE| (cm)
139.95	6	424.038	424.029	0.9
370.15	7	419.297[a]	419.296	0.1

a = elevation based on interpolated geometry

The calibrated Manning coefficients varied between 0.012 and 0.022, which are in the typical range for concrete channels (Chow 1959). Table 17 shows a summary of the results obtained for the concrete channel model.

Table 17. Summary of hydraulic conditions for the concrete channel model.

Location (m)	n	Velocity (ms^{-1})	Flow Depth (m)	Top width (m)	Flow area (m^2)	Shear velocity (ms^{-1})	Friction slope	Froude number
0.00	0.015	1.29	0.05	2.27	0.11	0.10	0.0199	1.86
15.70	0.012	1.29	0.05	2.13	0.11	0.08	0.0122	1.80
42.50	0.022	1.31	0.05	2.28	0.11	0.15	0.0459	1.91
75.70	0.012	1.29	0.05	2.22	0.11	0.08	0.0126	1.84
80.75	0.022	1.29	0.05	2.22	0.11	0.14	0.0416	1.83
139.95	0.012	1.30	0.05	2.27	0.11	0.08	0.0125	1.89
370.15	0.020	1.29	0.05	2.30	0.11	0.13	0.0354	1.87
Average	-	1.29	0.05	2.24	0.11	0.11	0.0257	1.86

The velocity varied between 1.29 and 1.31 ms^{-1}, producing an average of 1.29 ms^{-1}. These results agree reasonably well with the estimates that were obtained by releasing an apple into the flow at the injection line and measuring the travel times to three sampling stations. The average apple velocity was 1.11 ms^{-1} (Table 18). This velocity is likely an underestimate of the true flow velocity because the apple had contact with the bed rather than flowing freely given the shallow depth of flow.

Table 18. Velocity estimates obtained using the travel time method.

Location (m)	Velocity (ms^{-1})
42.5	1.02
80.75	0.86

Location (m)	Velocity (ms^{-1})
370.15	1.45
Average	1.11

The flow depth, width, and area were very consistent over the reach, with averages of 0.05 m, 2.24 m, and 0.11 m^2, respectively. The Froude number shows that the flow was supercritical (Fr>1), consistent with field observations. The results from the model were processed according to the methodology described in 3.3 in order to obtain a spatially weighted average for the sub-reach within which a cross-section is located (Table 19). These results will be utilized in further calculations to investigate dispersion characteristics and sediment transport mode.

Table 19. Spatially weighted average of the hydraulic model results for each location in the concrete channel.

Location (m)	Velocity (ms^{-1})	Flow Depth (m)	Top width (m)	Flow area (m^2)	Shear velocity (ms^{-1})	Friction slope	Froude number
15.70	1.29	0.05	2.20	0.11	0.09	0.0160	1.83
42.50	1.30	0.05	2.20	0.11	0.10	0.0242	1.85
75.70	1.30	0.05	2.22	0.11	0.11	0.0264	1.86
80.75	1.30	0.05	2.22	0.11	0.11	0.0265	1.86
139.90	1.30	0.05	2.23	0.11	0.11	0.0267	1.86
370.15	1.30	0.05	2.27	0.11	0.11	0.0250	1.87

4.2.3. Concentration curves

Conductivity was recorded at three measuring locations on seven of nine runs (Appendix B). During runs CC-2 and CC-9, the conductivity sensors located at 370.15 and 139.95 m did not record reliable data. Turbidity measurements were hampered by shallow flow depth and the effects of sunlight. Only two sensors (OBSs 10181 and 10193) located at 370.15 m yielded useful data because the flow was slightly deeper than upstream and the new sensors had upgraded optical properties that were more efficient at filtering solar wavelengths. The older sensors located upstream exhibited large and erratic fluctuations, not allowing the discernment of the sediment concentration curves.

Table 20 summarizes the results for the sodium chloride and sediment injections conducted on the concrete channel. The majority of the sodium chloride curves obtained at 80.75 and 139.95

m were defined based on the 1.14 x log (t_{peak}) truncation criterion. In contrast, all the curves obtained at 370.15 m returned to the background value before the end time determined by the truncation criterion. The sodium chloride curves recorded at 139.95 m on run CC-1 and at 370.15 m on run CC-6 were experimentally truncated. All of the suspended sediment concentration curves had to be truncated using the truncation criterion because of lingering spikiness in the tails of the plumes. Figure 32 shows the sodium chloride and suspended sediment concentration curves from run CC-4.

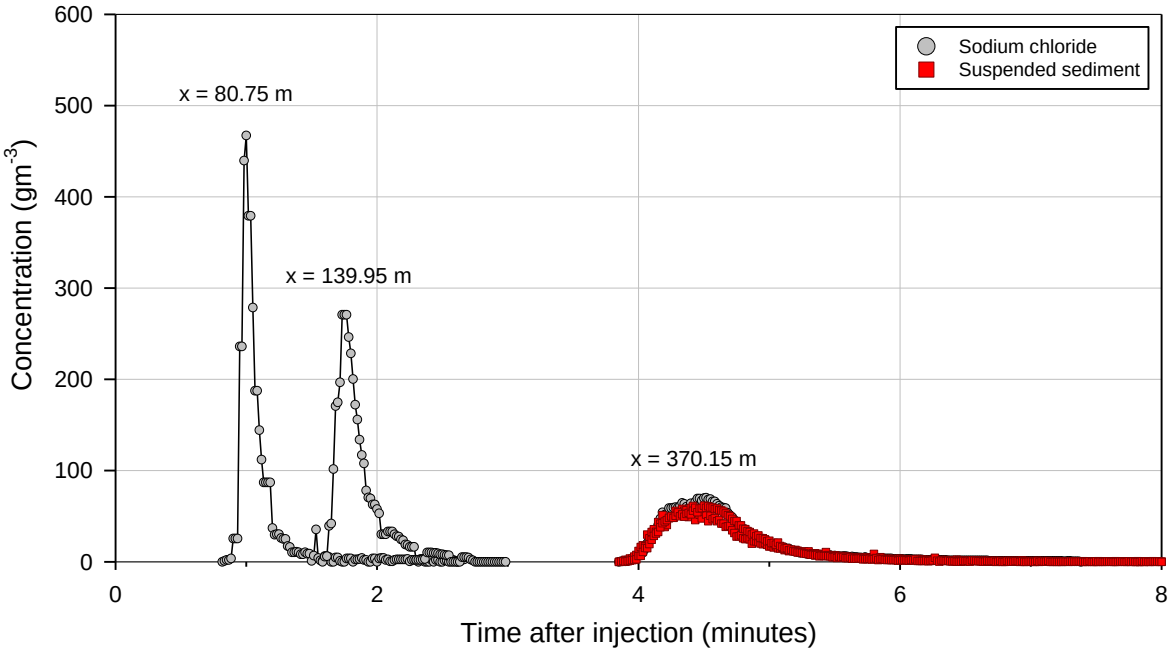

Figure 32. Sodium chloride and suspended sediment curves during run CC-4.

Table 20. Summary of the sodium chloride and suspended concentration curves results obtained in the concrete channel. T = truncation criterion; ET = experimental truncation; BC = return to background; "–" indicates no data because there was no probe at that location for the run or data were not recorded.

Run	Location (m)	Sodium chloride			Sediment		
		RR (%)	R_{peak} (%)	End defined by	Particle size (mm)	RR (%)	R_{peak} (%)
CC-1	80.75 C	118	14	T	<0.075	-	-
	139.95 LB	113	8	ET		-	-
	370.15 C	-	-	-		-	-
	370.15 RB	96	2	BC		-	-
CC-2	80.75 C	114	14	BC	<0.075	-	-
	139.95 LB	135	8	T		-	-
	370.15 C	-	-	-		94	1.8
	370.15 RB	-	-	-		83	1.8
CC-3	80.75 C	113	12	BC	<0.075	-	-
	139.95 LB	131	8	BC		-	-
	370.15 C	-	-	-		80	1.4
	370.15 RB	90	2	BC		81	1.5
CC-4	80.75 C	110	13	T	0.075-0.125	-	-
	139.95 LB	110	8	BC		-	-
	370.15 C	-	-	-		42	1
	370.15 RB	98	2	BC		44	1
CC-5	80.75 C	107	12	T	0.075-0.125	-	-
	139.95 LB	124	7	T		-	-
	370.15 C	-	-	-		48	1
	370.15 RB	102	2	BC		54	1
CC-6	80.75 C	108	13	T	0.125-0.25	-	-
	139.95 LB	138	8	T		-	-
	370.15 C	-	-	-		25	0.5
	370.15 RB	97	2	ET		24	0.5
CC-7	80.75 C	105	11	T	0.125-0.25	-	-
	139.95 LB	125	7	T		-	-
	370.15 C	-	-	-		17	0.6
	370.15 RB	108	2	BC		18	0.7
CC-8	80.75 C	121	13	T	0.25-0.5	-	-
	139.95 LB	-	-			-	-
	370.15 C	-	-	-		11	0.2
	370.15 RB	104	2	BC		11	0.2
CC-9	80.75 C	110	12	T	0.5-1	-	-
	139.95 LB	146	8	T		-	-

Run	Location (m)	Sodium chloride			Sediment		
		RR (%)	R_{peak} (%)	End defined by	Particle size (mm)	RR (%)	R_{peak} (%)
	370.15 C	-	-			10	0.2
	370.15 RB	105	2	BC		8	0.1

4.2.3.1. Recovery rates

Sodium chloride recovery varied between 90 and 146%, yielding an average of 113% for all locations across all runs (Table 20). Recovery at the first sampling station (at 80.75 m) varied between 105 and 121% with an average of 112%. Similar results were observed at the second sampling station (at 139.95 m) where the recovery was 128% on average. At 370.15 m downstream, the average recovery was 100%, varying between 90 and 108%. Recovery rates larger than 100% at the first two sampling stations are likely due to the fact that the measurements were taken at a single point within the dispersing plume and may not reflect the cross-sectional averaged concentration if the sodium chloride was not uniformly mixed laterally. Despite the lateral injection method, there were instances when the slurry was not introduced to the flow completely uniformly. The results suggest that sodium chloride was not completely mixed laterally by dispersive processes until at least 139.95 m downstream of the injection.

The suspended sediment recovery rates were clearly dependent on particle size (Figure 33). The finest fraction (<0.075 mm), corresponding to very fine sand and silt-clay particles, yielded 80-94% recovery rates. On the other hand, the medium and coarse sand fraction yielded recovery rates of approximately 10% or less. Likewise, the peak recoveries also decreased with increased particle size, varying for approximately 2% for the finest fraction (<0.075 mm) to 0.1% for the coarsest fraction (0.5-1 mm). The recovery rates of suspended sediment on center and right bank of the channel at 370.15 m were similar during all runs, suggesting complete lateral mixing at this location (Figure 34).

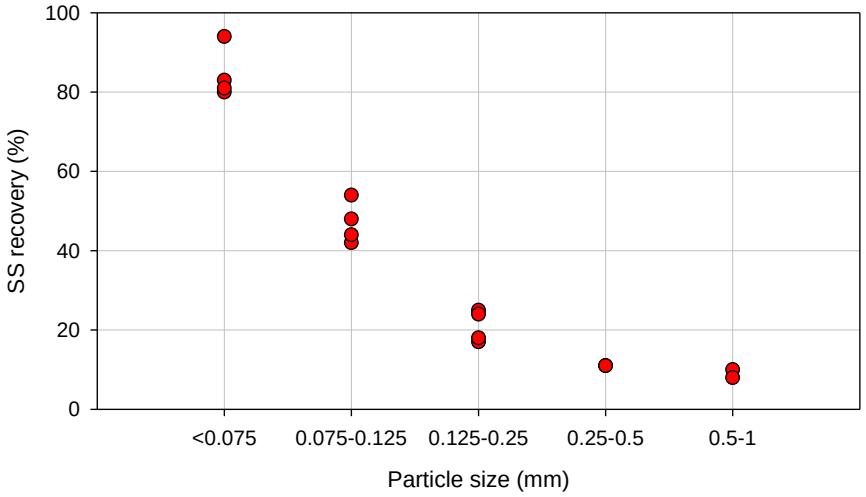

Figure 33. Suspended sediment mass recovered according to particle size in the concrete channel at 370.15 m downstream of the injection line.

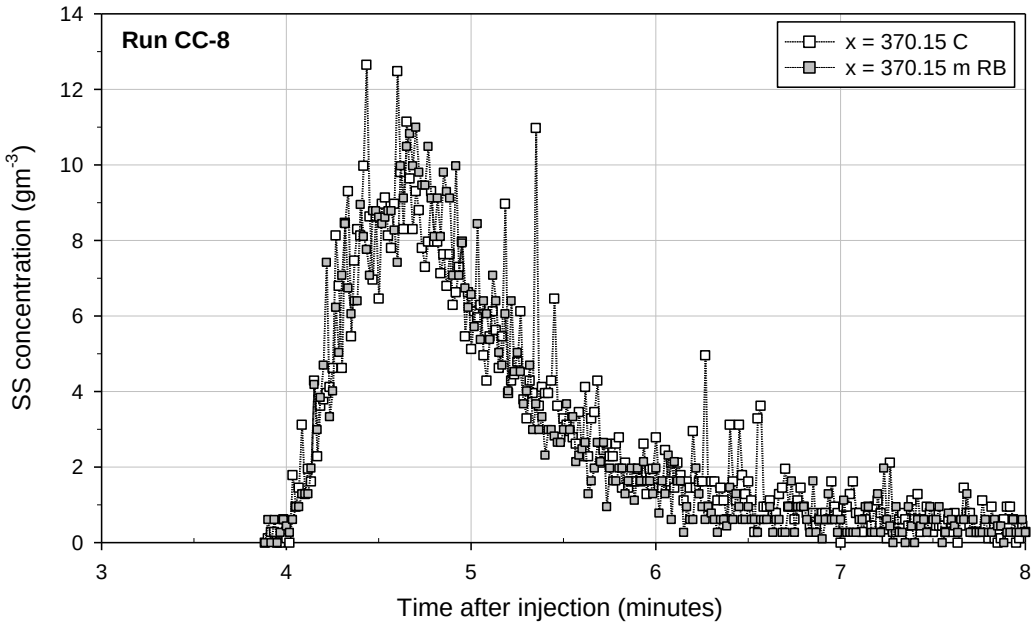

Figure 34. Suspended sediment concentration curves at 370.15 m during run CC-8.

4.2.3.2. Advection velocity

The graphs of travel time versus distance (Figure 35) show a linear relation between time and distance, i.e., a constant advection velocity for both, centroid and peak, over the study reach. The

peak velocities of the sodium chloride curves were slightly larger than the centroid velocities during all runs (Table 21). This shows that the front part of the plume, which contains the peak, was traveling faster than the center of mass. This is confirmed by the positive skewness of the concentration curves. This is to be expected when advection dominates over dispersion. However, in the equilibrium zone (farther downstream) it is expected that advection and dispersion are balanced. Interestingly, the smallest differences between centroid and peak velocities were observed at 370.15 m downstream of the injection, suggesting that the peak and centroid travel times were getting closer together (i.e., the skewness of the curves was decreasing). The centroid velocities were slightly smaller (2-12%) than the average flow velocity estimated by the hydraulic model (1.30 ms^{-1}) at 80.75 m and 139.95 m, becoming very close to the average flow velocity at 370.15 m.

Overall the velocities were very consistent during all the runs, indicating steady flow conditions during the experiments. The variations between centroid velocities at the same sampling locations are slightly larger than for the peak velocities and are directly related to the method utilized to calculate each velocity. While the peak velocity was calculated based on the travel time of the maximum concentration point, the centroid velocity was calculated using the moments method, which is sensitive to small variations in concentration between curves.

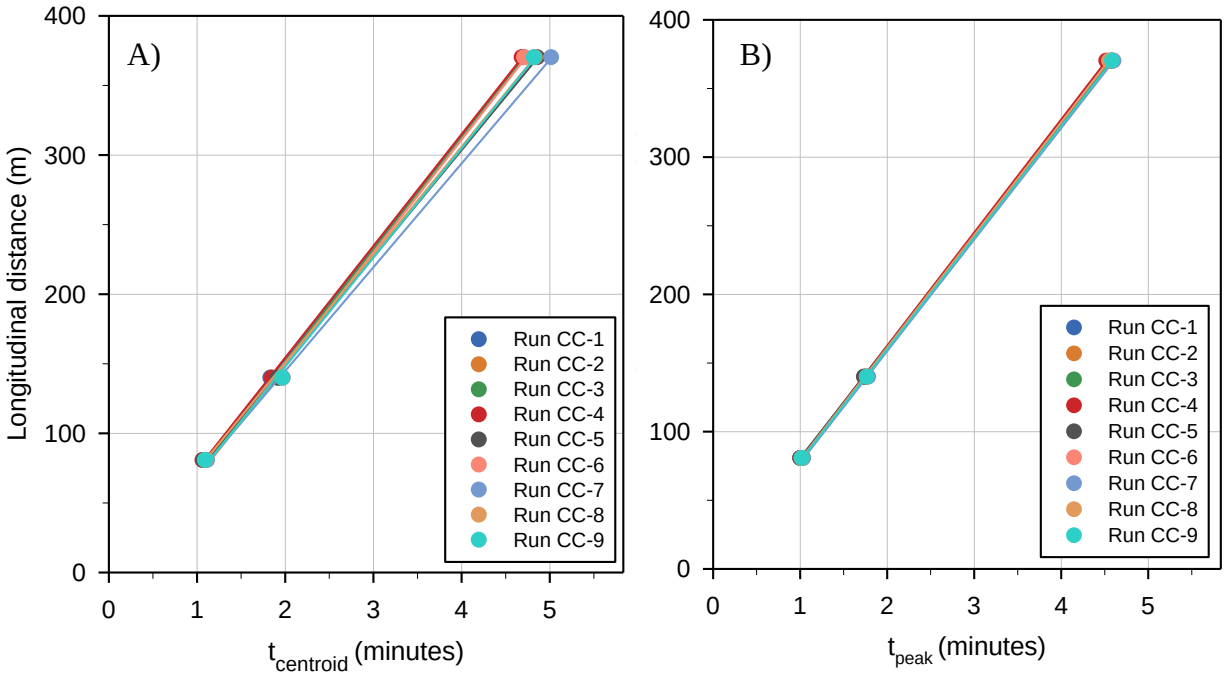

Figure 35. Travel time of sodium chloride concentration curves in the concrete channel. A) Centroid travel times; B) Peak travel times.

Table 21. Centroid and peak velocities of the sodium chloride concentration curves in the concrete channel.

Run	Location (m)								
	80.75 C			139.95 LB			370.15 RB		
	$\bar{U}_{centroid}$	$\bar{U}_{peak}$	$\bar{U}_{peak}$ - $\bar{U}_{centroid}$	$\bar{U}_{centroid}$	$\bar{U}_{peak}$	$\bar{U}_{peak}$ - $\bar{U}_{centroid}$	$\bar{U}_{centroid}$	$\bar{U}_{peak}$	$\bar{U}_{peak}$ - $\bar{U}_{centroid}$
	(ms^{-1})								
CC-1	1.24	1.32	0.08	1.27	1.32	0.05	1.31	1.35	0.04
CC-2	1.24	1.30	0.06	1.21	1.33	0.12	-	-	-
CC-3	1.24	1.30	0.06	1.22	1.33	0.11	1.31	1.35	0.04
CC-4	1.27	1.35	0.08	1.26	1.35	0.09	1.32	1.37	0.05
CC-5	1.25	1.35	0.10	1.22	1.35	0.13	1.27	1.35	0.08
CC-6	1.23	1.32	0.09	1.18	1.32	0.14	1.31	1.34	0.03
CC-7	1.21	1.30	0.09	1.18	1.31	0.13	1.23	1.34	0.11
CC-8	1.23	1.32	0.09	-	-	-	1.28	1.36	0.08
CC-9	1.23	1.32	0.09	1.19	1.32	0.13	1.28	1.35	0.07
Average	1.24	1.32	0.08	1.22	1.33	0.11	1.29	1.35	0.06
CV	1%	1%	17%	3%	1%	26%	2%	1%	43%

CV = coefficient of variation (standard deviation/average).

The trends in the suspended sediment curves were similar to those for the sodium chloride curves, with peak velocities larger (2-17%) than the centroid velocities (Table 22). Both the sodium chloride and sediment curves were positively skewed. The suspended sediment curve centroid velocities were closer to the average flow velocity (1.30 ms^{-1}) than the peak velocities. Overall the velocities observed on the right bank of the channel were slightly faster than those in the center of the channel, confirming that there was a preferential flow line toward the right bank rather than the middle of the channel.

Table 22. Centroid and peak velocities of the suspended sediment concentration curves in the concrete channel.

Run	Location (m)					
	370.15 C			370.15 RB		
	$\bar{U}_{centroid}$	$\bar{U}_{peak}$	$\bar{U}_{peak}$ - $\bar{U}_{centroid}$	$\bar{U}_{centroid}$	$\bar{U}_{peak}$	$\bar{U}_{peak}$ - $\bar{U}_{centroid}$
CC-1	-	-	-	-	-	-
CC-2	1.21	1.33	0.12	1.30	1.33	0.03
CC-3	1.22	1.35	0.13	1.32	1.35	0.03
CC-4	1.31	1.40	0.09	1.32	1.37	0.05
CC-5	1.30	1.41	0.11	1.29	1.35	0.06
CC-6	1.26	1.36	0.10	1.29	1.34	0.05
CC-7	1.20	1.34	0.14	1.20	1.32	0.12
CC-8	1.15	1.39	0.24	1.15	1.31	0.16
CC-9	1.16	1.37	0.21	1.19	1.31	0.12
Average	1.21	1.35	0.14	1.23	1.32	0.08
CV	5%	2%	38%	5%	2%	63%

CV = coefficient of variation (standard deviation/average).

4.2.4. Dispersion

The sodium chloride concentration curves were normalized by their respective peak concentrations (Figure 36). The graphs show that there was a high degree of consistency among all nine runs, particularly at 139.95 m and 370.15 m. This indicates that the dispersion processes were similar during the nine experimental runs.

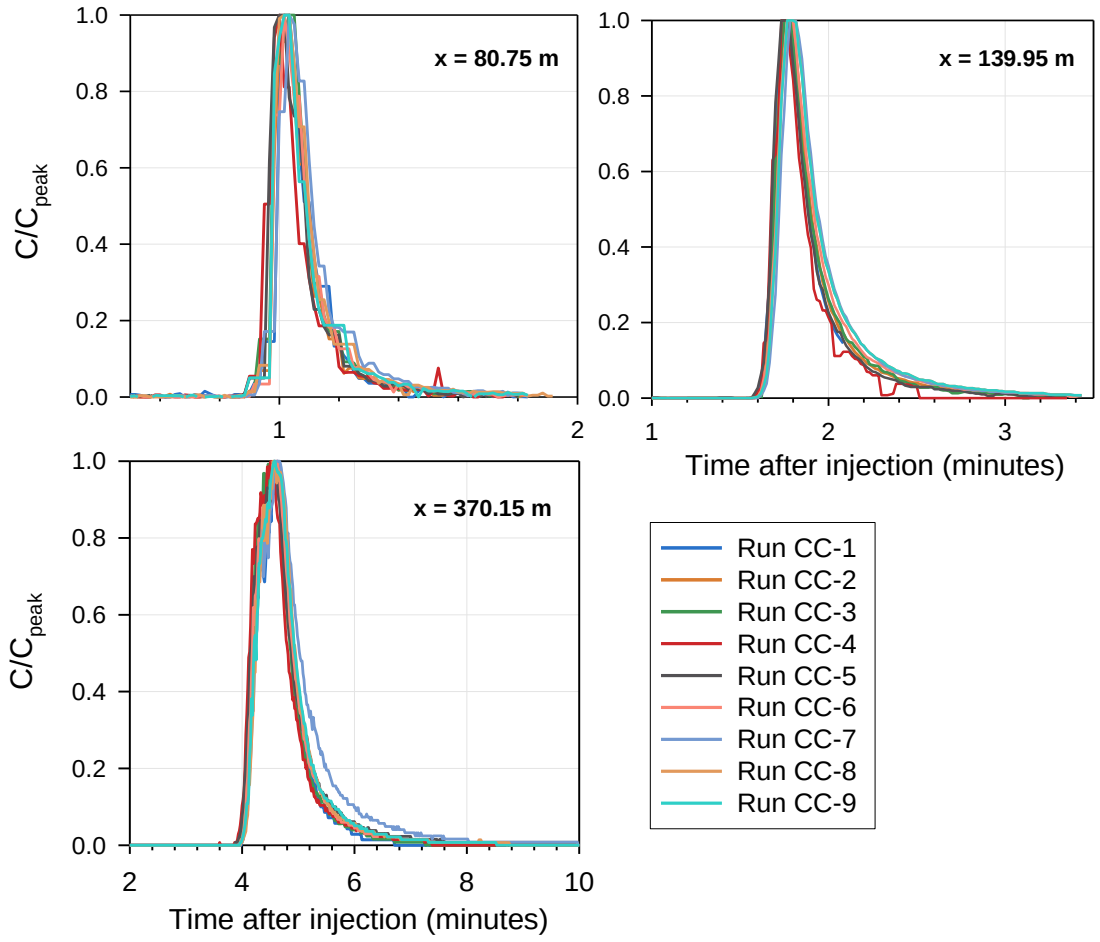

Figure 36. Normalized sodium chloride curves for each run per sampling location (note the scale change on the x-axis).

4.2.4.1. Advective zone length and longitudinal dispersion coefficient

The geometry and flow characteristics of the concrete channel were fairly uniform, and therefore, the longitudinal dispersion coefficient was expected to be constant downstream of the advective zone. Unfortunately, the advective zone length estimates based on Equation 65 varied between 13 and 2310 m (Table 23), so it is difficult to judge whether measurements were taken within the advective zone or not.

Table 23. Advective zone length estimates in the concrete channel based on the minimum and maximum empirical coefficients reported in the literature (Rutherford 1994; Sharma and Ahmad 2014).

β	E_y (m^2s^{-1})	α	L_x (m)
0.13	0.0007	0.2	462

β	E_y (m^2s^{-1})	α	L_x (m)
		1	2310
4.65	0.0248	0.2	13
		1	65

In practice, without observed data to rely upon, the safest approach would be to adopt the largest value and assume the concentration data to be reliable only after the end of the advective zone. However, tracer data can provide additional insights regarding the extent of the advective zone. The Hayami solution of the one-dimensional ADE (64) was utilized to estimate the longitudinal dispersion coefficient for each sodium chloride injection following the methodology introduced in 3.4.2. The results indicate that a single longitudinal dispersion coefficient is not capable of reproducing the concentrations observed at all three sampling locations. The longitudinal dispersion coefficient increases in the downstream direction (Figure 37). Table 24 shows the values of the longitudinal dispersion coefficient obtained by fitting the Hayami solution to each concentration curve.

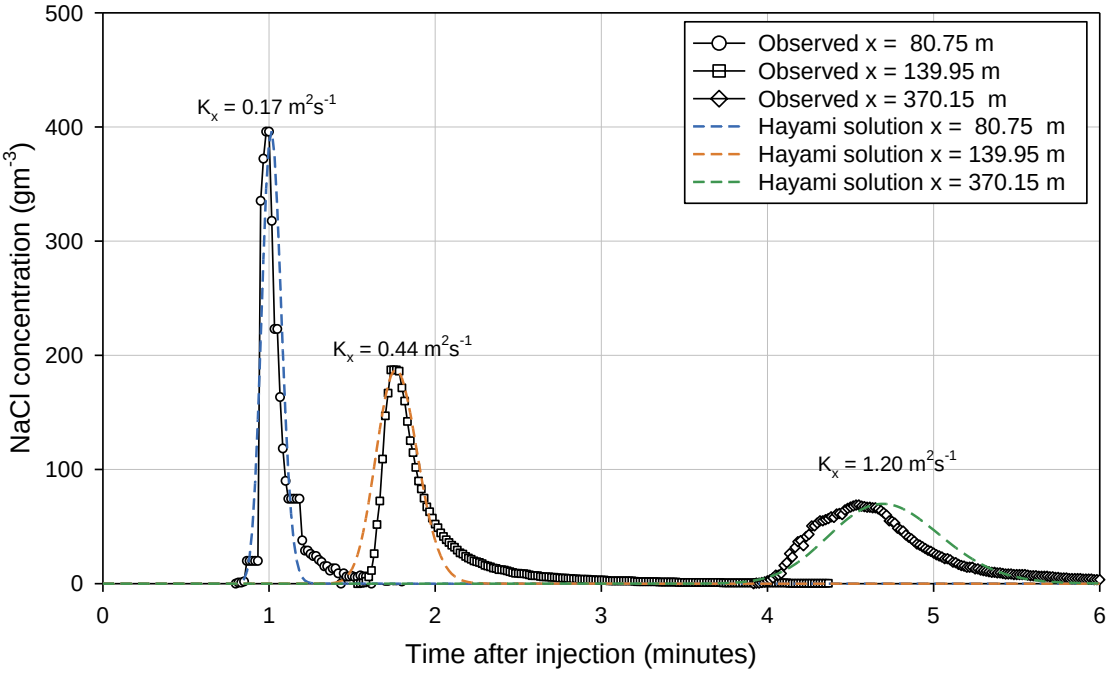

Figure 37. Longitudinal dispersion coefficients obtained for the sodium chloride curves utilizing the Hayami analytical solution of the one-dimensional ADE (run CC-9).

Table 24. Longitudinal dispersion coefficients estimated using the Hayami analytical solution fit on the sodium chloride concentration curves observed in the concrete channel.

Location (m)	K_x (m^2s^{-1})										
	CC-1	**CC-2**	**CC-3**	**CC-4**	**CC-5**	**CC-6**	**CC-7**	**CC-8**	**CC-9**	**Average**	**CV (%)**
80.75 C	0.14	0.14	0.15	0.15	0.17	0.16	0.20	0.19	0.17	0.16	13
139.95 LB	0.25	0.36	0.35	0.25	0.35	0.40	0.42	-	0.44	0.35	20
370.15 RB	1.00	-	1.12	1.10	1.30	1.15	1.65	1.20	1.23	1.23	16

CV = coefficient of variation (standard deviation/average).

The average longitudinal dispersion coefficient at 370.15 m downstream of the injection line was 1.22 m^2s^{-1}. The smallest coefficient of variation (CV), 13%, occurred at the first sampling station (80.75 m), indicating that the longitudinal dispersion coefficients from different runs were the most similar at this location. Since the longitudinal dispersion coefficients were obtained based on a best-fit to peak concentration, this also indicates that the peak concentrations were the most similar at this location. On the other hand, the largest CV, 20%, was observed at the second sampling station (139.95 m).

The Peclet number was calculated for each sampling location and run because it is the ratio of advective to dispersive processes with $0.4 < Pe < 2.5$ indicating an equilibrium between these two processes. The results show that the Peclet number decreases in the downstream direction, as the longitudinal dispersion coefficient increases (Table 25). At 370.15 m the Peclet number decreases to 2.4 on average, suggesting that advection and dispersion may have reached equilibrium.

Table 25. Peclet number calculated based on the apparent K_x values obtained for the concrete channel.

Location (m)	Pe										
	CC-1	**CC-2**	**CC-3**	**CC-4**	**CC-5**	**CC-6**	**CC-7**	**CC-8**	**CC-9**	**Average**	**CV (%)**
80.75 C	21	21	19	19	17	18	15	15	17	18	12
139.95 LB	12	8.1	8.3	12	8.3	7.3	6.9	-	6.6	8.6	23
370.15 RB	2.9	-	2.6	2.6	2.2	2.5	1.8	2.4	2.4	2.4	14

CV = coefficient of variation (standard deviation/average).

Since Pe <2.5 at 370.15 m, it will be assumed that the first two observed locations (80.75 m and 139.95 m), where Pe>>2.5, are located within the advective zone and that the last location

(370.15 m) is located in the equilibrium zone. However, since there are no stations farther downstream of 370.15 m, it is not possible to confirm this assumption utilizing this method. As a consequence, the longitudinal dispersion coefficients obtained at 80.75 m and 139.95 m will be considered "apparent" longitudinal dispersion coefficients. The longitudinal dispersion coefficients obtained at 370.15 m will be assumed as "equilibrium" coefficients. Therefore, only the observed data at the downstream location will be compared with modeled concentration curves.

4.2.4.2. Suspended sediment dispersion

In order to determine if the sediment particles injected with the sodium chloride were carried in suspension, the sediment transport mode was estimated based on the Rouse Number. The analysis was conducted utilizing the average results for shear velocity and flow depth from the HEC-RAS model. The results demonstrate that the Rouse Number was less than 1.25 and therefore the flow was capable of carrying all the studied particle sizes in suspension. The ADE approach should be applicable to model the concentration curves (Table 26).

Table 26. Sediment transport mode classification in the concrete channel.

Run	Sediment size (mm)	Estimated D_{50} (mm)	Water temperature (°C)	ω (ms^{-1})	Rouse Number	$u_*\omega^{-1}$	Mode of sediment transport
CC-1	<0.075	0.063	7.3	0.163	0.04	67.35	Suspension
CC-2							
CC-3							
CC-4	0.075-0.125	0.097		0.214	0.05	51.35	
CC-5							
CC-6	0.125-0.25	0.177		0.307	0.07	35.52	
CC-7							
CC-8	0.25-0.5	0.354		0.425	0.10	23.55	
CC-9	0.5-1	0.707		0.629	0.15	15.87	

A comparison between the concentration curves of sodium chloride and sediment normalized by their respective peak concentrations at 370.15 m (RB) shows that the curves have essentially the same start time, peak time, and shape (Figure 38). The analysis of the normalized curves confirms that the sediment particles were dispersed in a similar way as the sodium chloride.

Therefore, the equilibrium longitudinal dispersion coefficient estimated based on the sodium chloride concentration curves can be applied to model the suspended sediment injections.

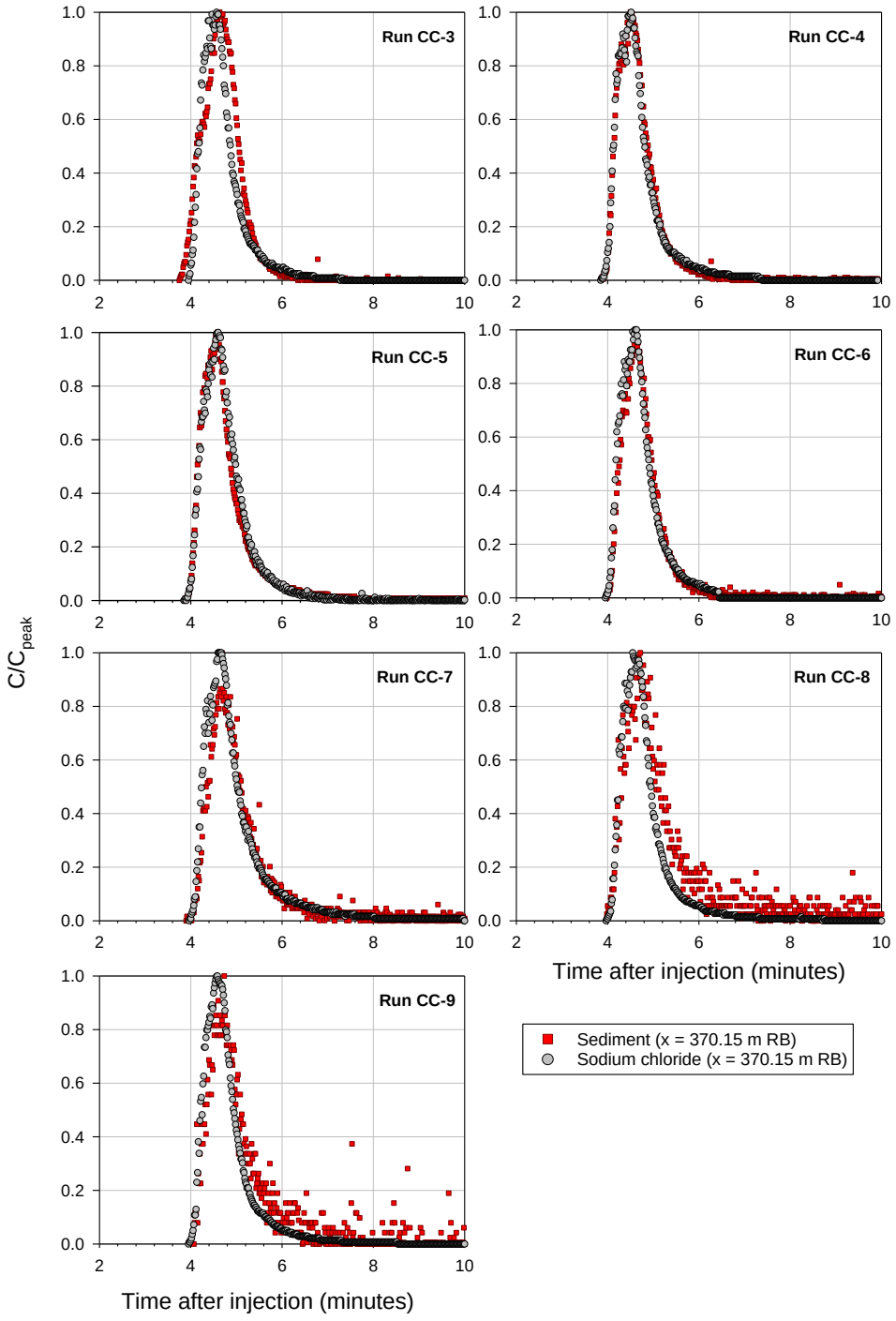

Figure 38. Normalized concentration curves of sodium chloride and sediment measured at 370.15 m downstream of injection.

The observed longitudinal dispersion coefficients obtained for the sodium chloride curves at 370.15 m (Table 24) were utilized to predict the suspended sediment curves. The longitudinal dispersion coefficient for each run was utilized for this process instead of the average value across all runs in order to minimize the uncertainties related to this parameter when evaluating the sediment settling rates. The estimated settling rates were calculated using Equation 101. These values were compared to the observed settling rates, which were obtained utilizing the Hayami solution of the one-dimensional ADE with a settling rate (100) following the methodology described in 3.5. For all runs, the observed settling rates were smaller than the estimated values, which implies that the sediment was staying in suspension longer than expected on the basis of simple particle settling in still water (Table 27, Figure 39).

Table 27. Settling rates (observed and estimated) according to sediment size in the concrete channel.

Run	Sediment size (mm)	D_{50} (mm)	Settling velocity (ms^{-1})	Estimated settling rate (s^{-1})	Observed settling rate (s^{-1})	Estimated - observed (s^{-1})
CC-1	<0.075	0.063	0.0025	0.033	-	-
CC-2					0.0007	0.032
CC-3					0.0007	0.032
CC-4	0.075-0.125	0.097	0.0054	0.043	0.0029	0.040
CC-5	0.075-0.125				0.0022	0.041
CC-6	0.125-0.25	0.177	0.0146	0.072	0.0048	0.057
CC-7	0.125-0.25				0.0048	0.056
CC-8	0.25-0.5	0.354	0.0401	0.093	0.0079	0.085
CC-9	0.5-1	0.707	0.0948	0.139	0.0089	0.130

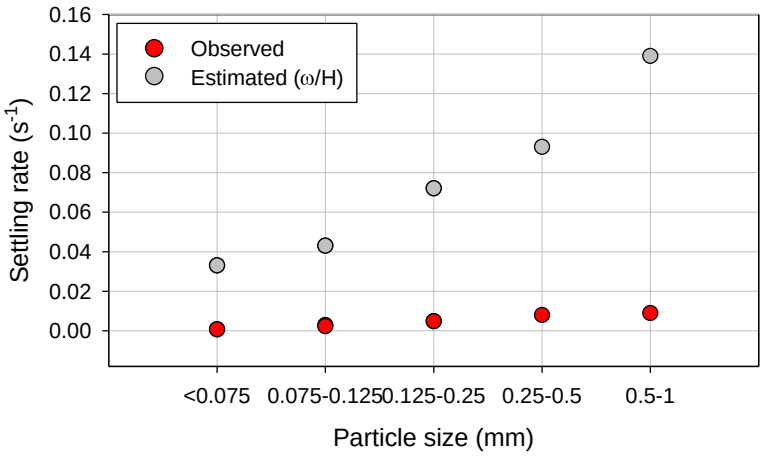

Figure 39. Observed and estimated settling rates according to particle size in the concrete channel.

The observed and estimated settling rates were applied to model the suspended sediment injections (Figure 40). Based on the estimated settling rates, the modeled curves would have zero concentration at 370.15 m. This was clearly not the case, suggesting that the use of estimated settling rates for problems of plume dispersion is an unreliable approach.

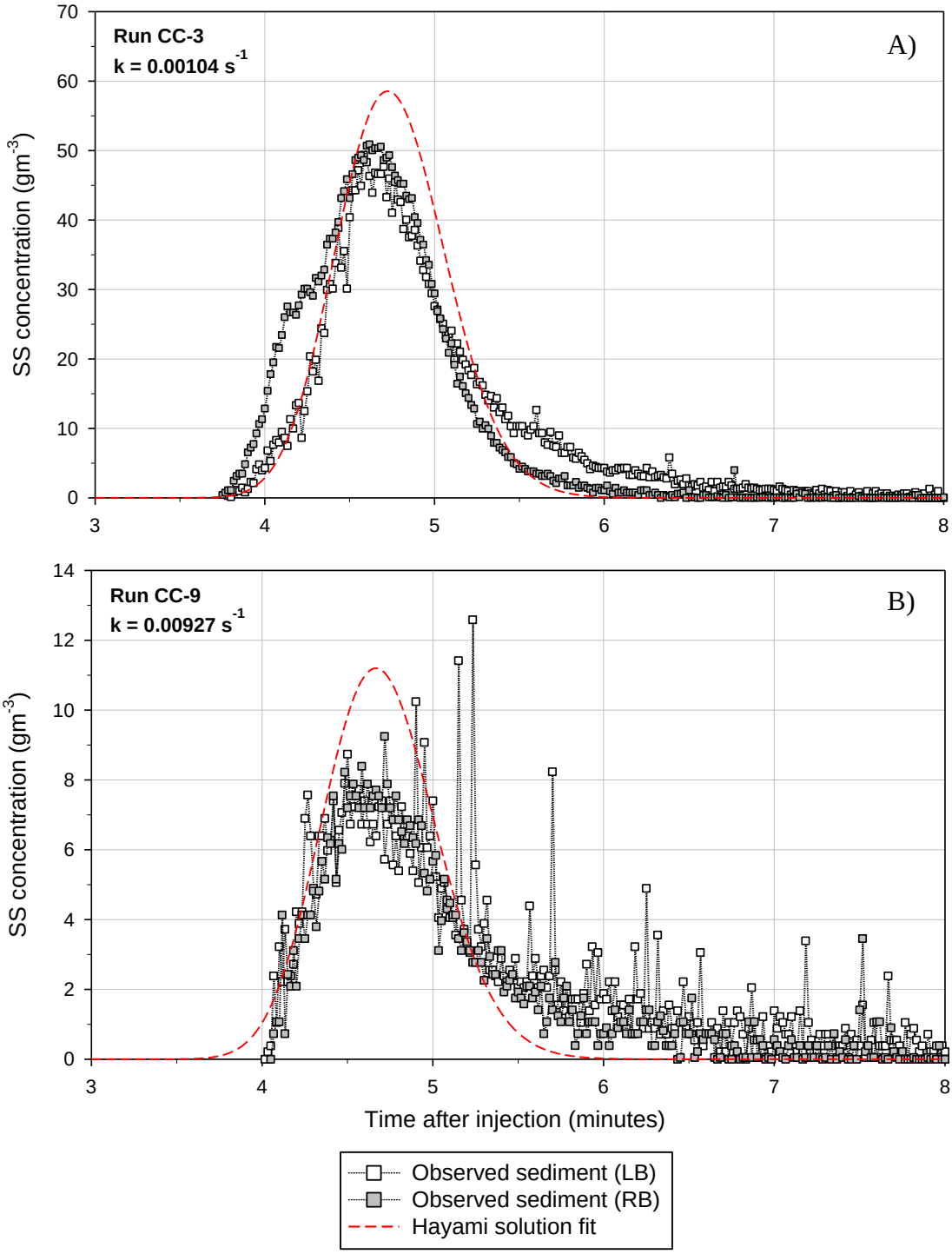

Figure 40. Suspended sediment concentration curves: observed data versus modeled curves utilizing the equilibrium zone longitudinal dispersion coefficients determined by the Hayami solution fit and observed settling rates (note the scale change on the y-axis). A) Run CC-3; B) Run CC-9.

4.2.4.3. Quantifying the accuracy of predictive formulas for K_x

All of the 26 predictive formulas in Table 3 were utilized to estimate the longitudinal dispersion coefficient based on the average characteristics of the flow derived from the HEC-RAS model results (Table 28). The sinuosity factor for the formula of Sahay (2013) was Si =1, which is the value for straight channels. The maximum value of the longitudinal dispersion coefficient was estimated by the formula from Oliveira et al. (2017), $K_x = 79.3\ m^2s^{-1}$. On the other hand, the smallest value was predicted by the formula of Elder (1959), where $K_x = 0.03\ m^2s^{-1}$.

Table 28. Longitudinal dispersion coefficients for the concrete channel estimated from predictive formulas.

Reference	**K_x (m^2s^{-1})**
Elder (1959)	0.03
Taylor (1954)	0.06
Devens (2006)	0.08
Parker (1961)	0.11
Ribeiro et al. (2010)	0.15
McQuivey and Keefer (1974)	0.15
Sattar & Gharabaghi (2015) (Formula 1)	1.13
Sattar & Gharabaghi (2015) (Formula 2)	1.23
Iwasa & Aya (1991)	3.36
Disley et al. (2015)	3.56
Sahay (2013)[1]	5.06
Wang et al (2017)	5.23
Deng et al. (2001)	6.50
Etemad-Shahidi and Taghipour (2012)	6.62
Koussis & Mirassol (1998)	6.77
Wang and Huai (2016)	6.80
Liu (1977)	6.99
Zeng & Huai (2014)	7.01
Kashefipour & Falconer (2002) (Formula 1)	8.15
Li et al. (2013)	8.67
Seo & Cheong (1998)	9.05
Sahay & Dutta (2009)	9.39
Alizadeh et al. (2017)	9.55
Kashefipour & Falconer (2002) (Formula 2)	11.9
Fischer (1975)	17.4
Oliveira et al. (2017)	79.3

The estimated longitudinal dispersion coefficients were applied to the Hayami analytical solution in order to predict the sodium chloride curves at 370.15 m downstream of the injection location (Figure 41). The results show that seven out of the 26 formulas tested overestimated the concentration, while 19 underestimated the observed concentrations.

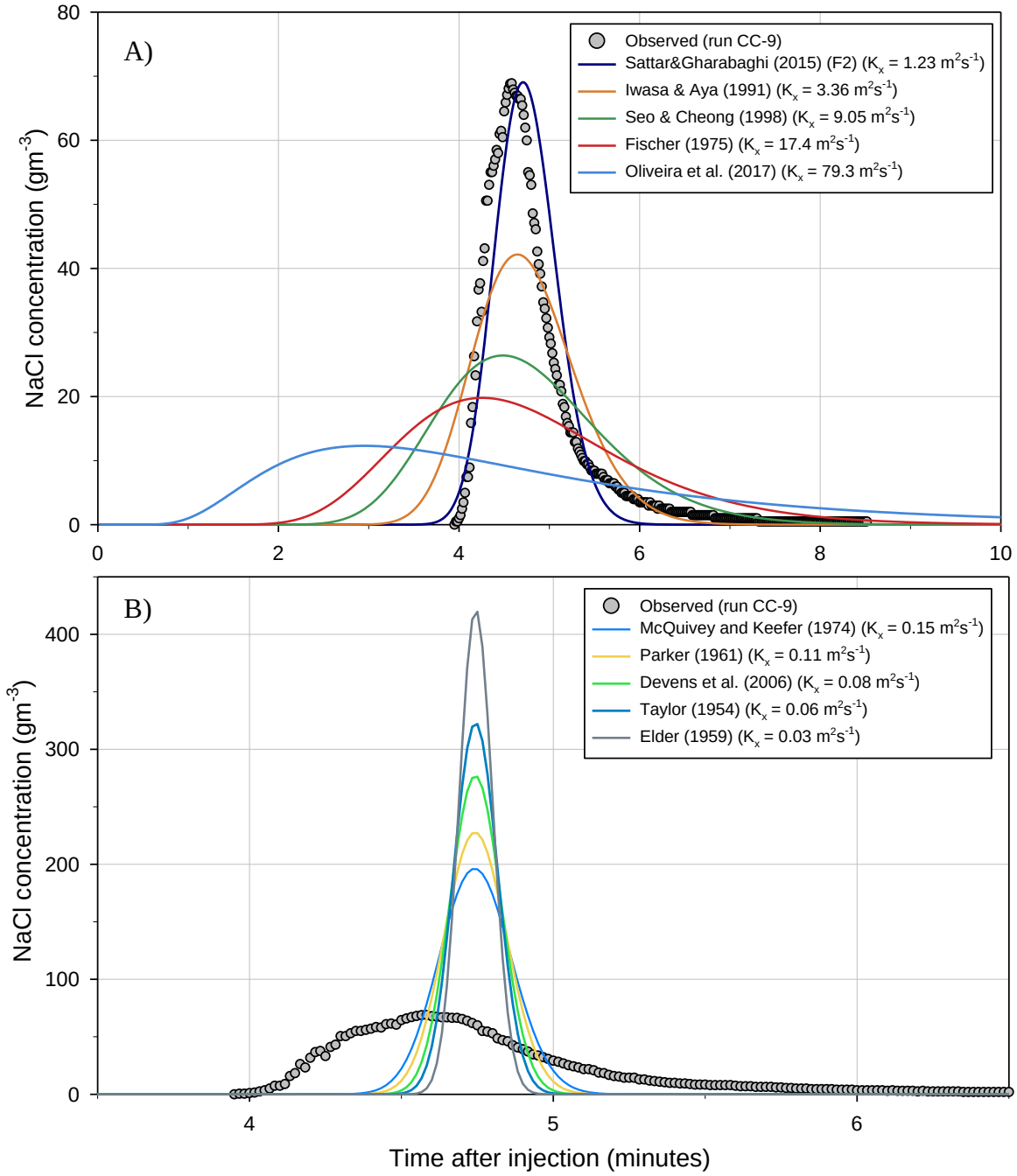

Figure 41. Modeled concentration curves utilizing the longitudinal dispersion coefficients obtained from predictive formulas (note the scale change on both axes). Curve with round symbols corresponding to the observed plume is a common reference for both graphs. A) Coefficients that underestimated the peak concentration; B) Coefficients that overestimated the peak concentration.

4.3. Semi-natural channel

4.3.1. Discharge

Two discharge measurements were conducted (by FLNRORD personnel) using an acoustic Doppler flow meter on the day of the experiments. The measured discharges were 0.015 m^3s^{-1} and 0.017 m^3s^{-1}, yielding an average of 0.016 m^3s^{-1}. The discharge was also estimated for each concentration curve (before truncation) utilizing the salt dilution method (Table 29). At all sampling locations for run SNC-1 and at 60 m downstream of the injection for run SNC-3, the measurements were stopped before the conductivity returned to the background value because of the long duration of the runs (i.e., experimental truncation). These runs were excluded from the analysis for discharge. The average discharge based on the concentration curves that returned to the background level was approximately 0.015 m^3s^{-1}, which is in good agreement with the flow meter estimates.

Table 29. Summary of discharge values estimated through the salt dilution method on the semi-natural channel.

Run	Location (m)	Estimated discharge (m^3s^{-1})
SNC-1	20	-
	40	-
	60	0.010 [ET]
	80	0.010 [ET]
	90	0.010 [ET]
SNC-2	20 LB	-
	20 C	-
	20 RB	0.017
	60 LB	0.017
	60 RB	0.016
SNC-3	20 LB	-
	20 C	0.015
	20 RB	0.019 [ET]
	60 LB	0.014 [ET]
	60 RB	0.011
Average		0.014
CV		25%

CV = coefficient of variation (standard deviation/average).

4.3.2. HEC-RAS hydraulic model

Six cross-sections were surveyed in the field and were utilized as the basis for the channel geometry in the HEC-RAS model (Appendix C). Figure 42 shows the cross-sections located at 0 m and 90 m downstream of the injection line.

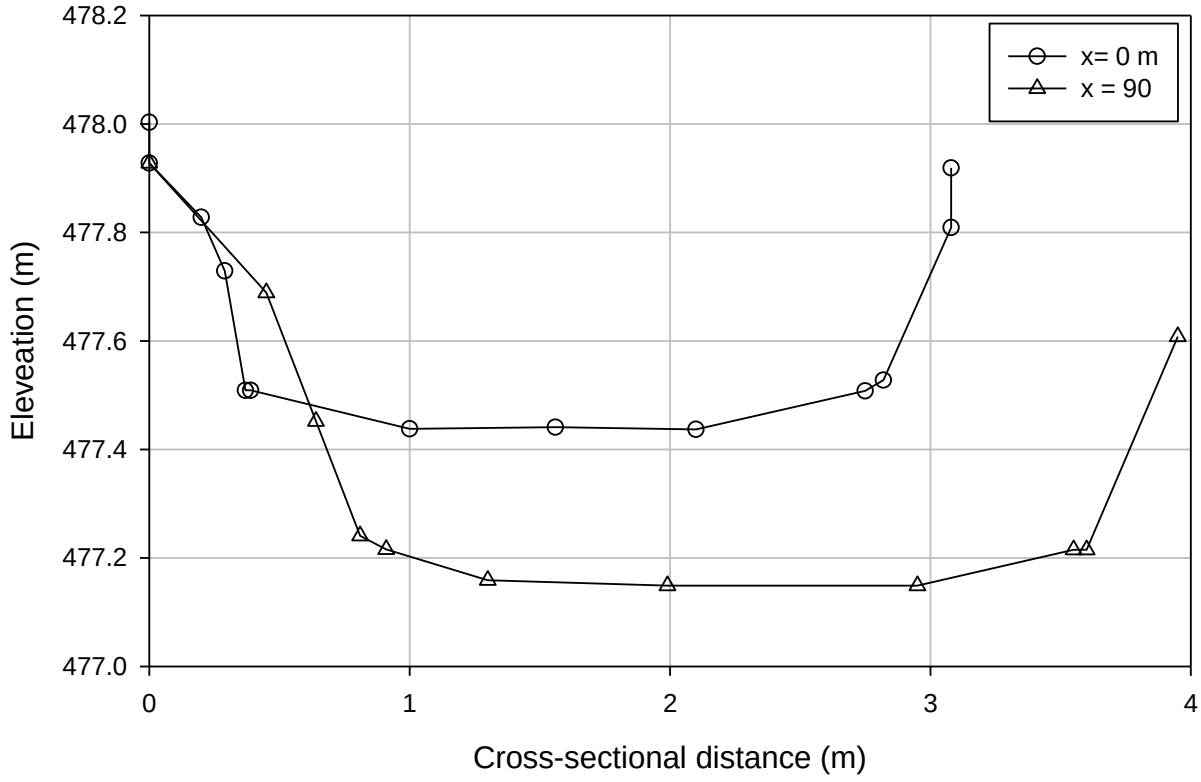

Figure 42. Semi-natural channel geometry. Cross-sections at the upstream (x = 0 m) and downstream boundaries of the study reach (x = 90 m). Cross-sectional distance has an arbitrary starting point so horizontal alignment is not true, but vertical differences are true.

The thalweg elevation of each cross-section was plotted against longitudinal distance and the slope of the channel was obtained by linear regression, yielding S = 0.0032 (Figure 43). The measured mean discharge of 0.016 m^3s^{-1} was utilized as a steady flow condition at the injection site, x = 0 m. The downstream boundary condition was determined by the known water line elevation at 90 m (477.215 m). The model geometry was calibrated by adjusting the Manning's

roughness coefficients (n) at each cross-section in order to match the observed water levels (Figure 44).

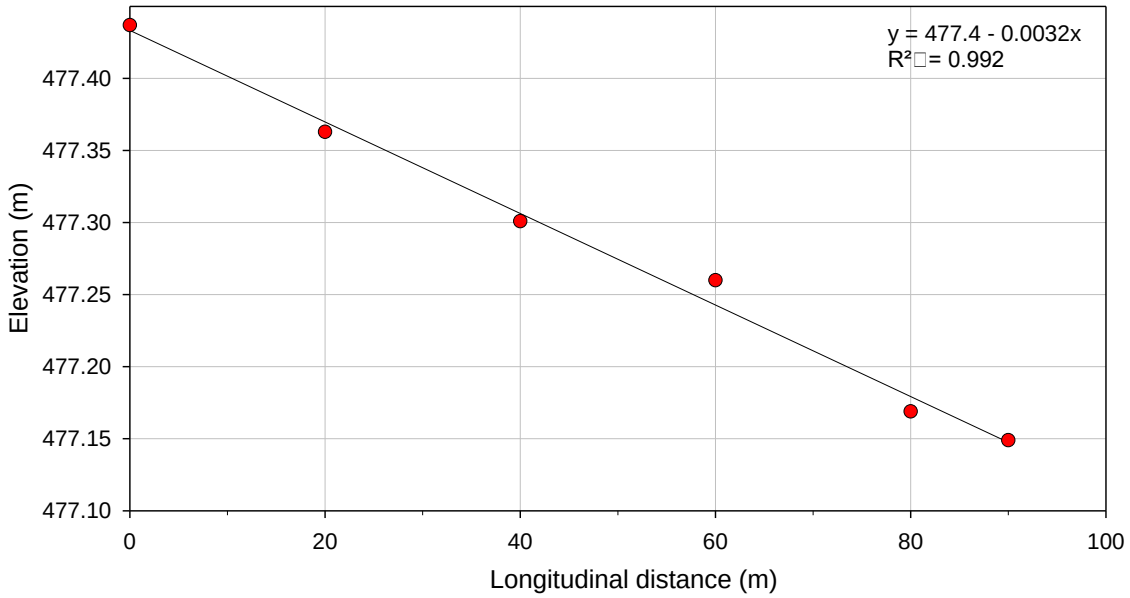

Figure 43. Thalweg slope surveyed in the semi-natural channel.

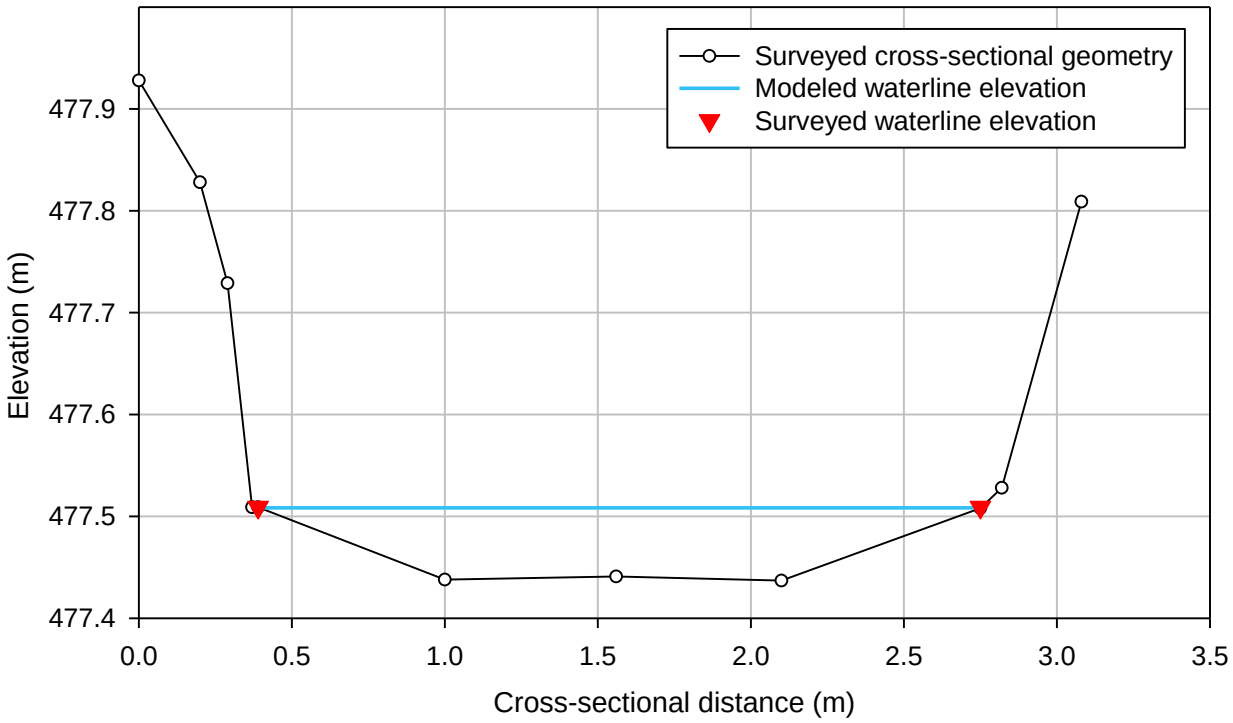

Figure 44. Example of a semi-natural cross-section calibrated on HEC-RAS (x = 0 m).

The calibrated Manning coefficients varied between 0.05 and 0.065, which are in the typical range for sluggish reaches of natural streams with some weeds and stones (Chow 1959). The largest difference between a surveyed and modeled waterline elevation was 1.05 cm at cross-section 3, therefore, the model calibration was accepted (Table 30, Figure 45). Cross-section 2 was surveyed during a different discharge; therefore, it was not utilized to calibrate the waterline elevation.

Table 30. Observed and modeled waterline elevations in the semi-natural channel.

Location (m)	**Cross-section number**	**Observed/interpolated waterline elevation (m)**	**Modeled waterline elevation (m)**	**$\|\Delta E\|$ (cm)**
0	1	477.509	477.508	0.09
20	2	-	477.437	-
40	3	477.379	477.390	1.05
60	4	477.343	477.343	0.02
80	5	477.248	477.249	0.12
90	6	477.215	477.216	0.09

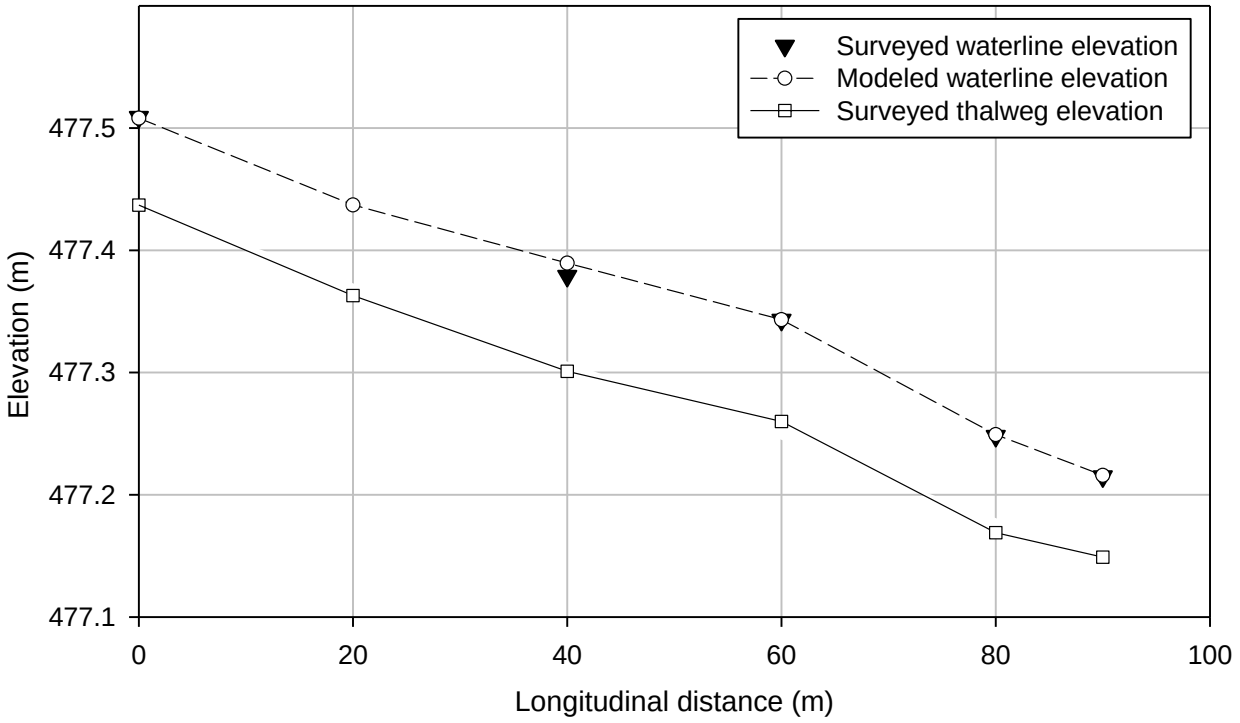

Figure 45. Thalweg and waterline elevations in the semi-natural channel.

The velocity varied between 0.10 and 0.16 ms^{-1}, producing an average of 0.13 ms^{-1} (Table 31). The flow depth, width, and area were very consistent over the reach, with averages of 0.05 m, 2.50 m, and 0.13 m^2, respectively. The average modeled thalweg slope, 0.0031, agrees well with the surveyed slope of the channel, 0.0032.

Table 31. Summary of hydraulic conditions for the semi-natural channel model.

Location (m)	n	Velocity (ms^{-1})	Flow depth (m)	Top width (m)	Flow area (m^2)	Shear velocity (ms^{-1})	Friction slope	Froude number
0	0.050	0.13	0.05	2.35	0.12	0.03	0.0024	0.19
20	0.060	0.16	0.04	2.33	0.10	0.05	0.0065	0.24
40	0.060	0.10	0.06	2.68	0.17	0.03	0.0014	0.12
60	0.065	0.16	0.05	2.20	0.10	0.05	0.0058	0.23
80	0.060	0.14	0.04	2.74	0.12	0.05	0.0054	0.19
90	0.060	0.12	0.05	2.69	0.14	0.04	0.0030	0.16
Average		0.13	0.05	2.50	0.13	0.04	0.0041	0.19

The results from the model were processed according to the methodology described in 3.3 in order to obtain a spatially-weighted average for the sub-reach within which a cross-section is located (Table 32). These results will be utilized in further calculations to investigate dispersion characteristics and sediment transport mode.

Table 32. Spatially weighted average of the hydraulic model results for each sampling location in the semi-natural channel.

Location (m)	Velocity (ms^{-1})	Flow Depth (m)	Top width (m)	Flow area (m^2)	Shear velocity (ms^{-1})	Friction slope	Froude number
20	0.15	0.05	2.34	0.11	0.04	0.0054	0.22
40	0.14	0.05	2.42	0.12	0.04	0.0053	0.20
60	0.14	0.05	2.43	0.13	0.04	0.0051	0.19
80	0.14	0.05	2.44	0.12	0.04	0.0052	0.20
90	0.14	0.05	2.47	0.12	0.04	0.0053	0.19

4.3.3. Concentration curves

Conductivity was recorded at three locations or more during all runs (Appendix D). During runs SNC-1 and SNC-2 two of the conductivity sensors did not record any data. During run SNC-3, the probe located at 20 m LB did not record data.

4.3.3.1. Recovery rates

With the exception of the experimentally truncated curves, all the curves were defined based on the truncation criterion of 1.2 x log (t_{peak}). The sodium chloride recovery rates varied between 86% and 152% during the three runs (Table 33). During run SNC-1, the recovery rates based on the measured discharge (0.016 m^3s^{-1}) were approximately 150% at all three sampling locations, indicating that this discharge value may be an overestimation for this run taken early in the day. On the other hand, during runs SNC-2 and SNC-3, the recoveries were approximately 100%, except for the curve at 20 m RB during run SNC-3, which was 143%. Given that the discharge measurements were conducted after the end of the sodium chloride injections, the discharge might have increased between runs SCN-1 and SNC-2/3. In this regard, it is notable that this channel is located in an agricultural area where irrigation pumps upstream often cycle on and off during the growing season.

At 20 m downstream of the injection line during run SNC-3, there was a large difference in recovery rates between the center (106%) and the right bank of the channel (143%), as well as in the peak recovery, which was almost 2 times larger in the center of the channel (Figure 46). Despite the similar recovery rates at 60 m downstream of the injection line, particularly during run SNC-2, the peak concentration was much larger on the left bank of the channel than the right bank, indicating that the sodium chloride was unequally mixed laterally, despite laterally uniform injection. During run SCN-1, the peak concentration at 90 m downstream of the injection was slightly larger than the peak concentration at 80 m, also suggesting that the sodium chloride was not evenly distributed in the lateral direction, given that the peak concentration is expected to decrease in the downstream direction.

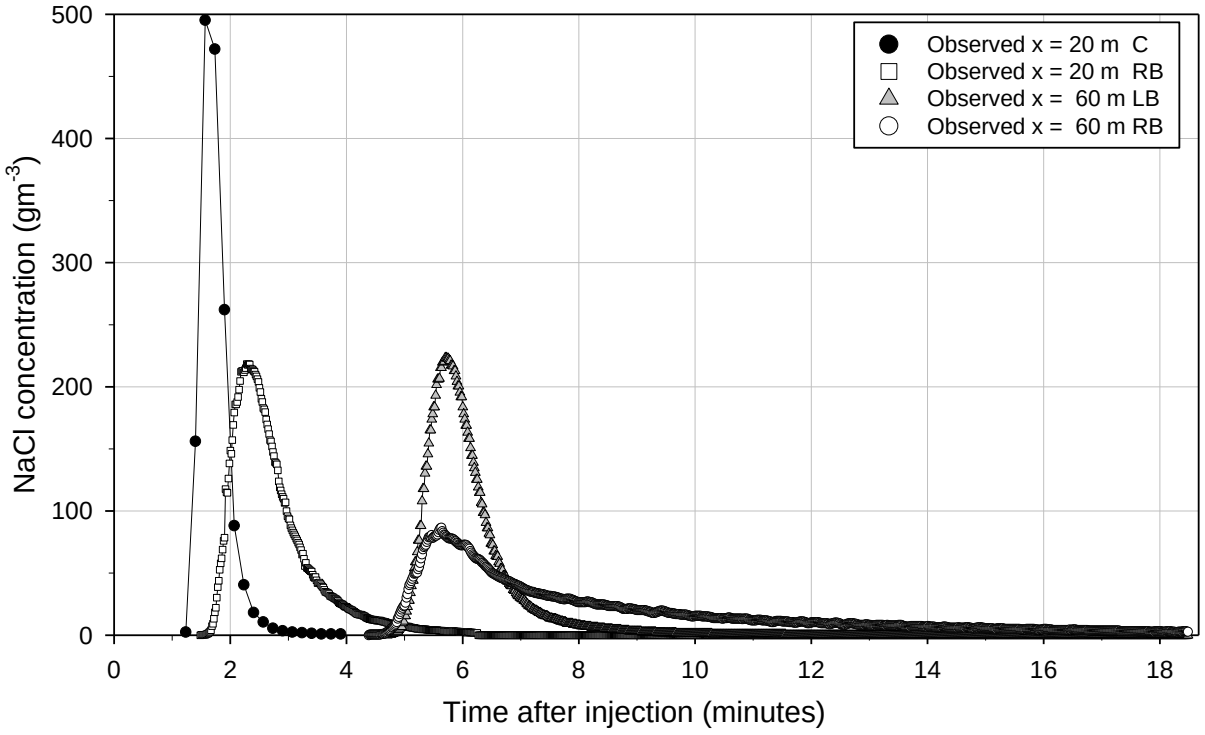

Figure 46. Sodium chloride concentration curves during run SNC-3. Note differences in response curves depending on measurement location in the transverse direction.

Table 33. Sodium chloride concentration curves on the semi-natural channel. T = truncation criterion; ET = experimental truncation; BC = return to background; "–" indicates no data because there was no probe at that location for the run or data was not recorded.

Run	Location (m)	RR (%)	R_{peak} (%)	End defined by
SNC-1	20 C	-	-	-
	40 C	-	-	-
	60 C	146	1.5	ET
	80 C	147	0.5	ET
	90 C	152	0.5	ET
SNC-2	20 LB	-	-	-
	20 C	-	-	-
	20 RB	102	1	T
	60 LB	97	1	T
	60 RB	95	0.5	T
SNC-3	20 LB	-	-	-
	20 C	106	3.5	T
	20 RB	143	2	T
	60 LB	86	1	ET
	60 RB	116	0.5	T

4.3.3.2. Advection velocity

The centroid velocity varied between 0.10 ms^{-1} and 0.19 ms^{-1}, while the peak velocity varied between 0.11 ms^{-1} and 0.21 ms^{-1}, with the fastest velocities observed during run SNC-3 (Table 34). The peak velocity was greater (2-32%) than the centroid velocity during all runs (Figure 47). At 20 m downstream of the injection line, the curve at the center of the channel arrived faster than the one on the right bank. The peak velocities on the left and right banks at 60 m downstream of the injection line were very similar during runs SNC-1 and SNC-2, increasing slightly during run SNC-3.

Table 34. Centroid and peak velocities of the sodium chloride concentration curves in the semi-natural channel.

Run	Location (m)	$\bar{U}_{centroid}$ (ms^{-1})	$\bar{U}_{peak}$ (ms^{-1})	$\bar{U}_{peak} - \bar{U}_{centroid}$ (ms^{-1})
SNC-1	20 C	-	-	-
	40 C	-	-	-
	60 C	0.13	0.15	0.02

	80 C	0.10	0.15	0.05
	90 C	0.11	0.15	0.04
SNC-2	20 LB	-	-	-
	20 C	-	-	-
	20 RB	0.10	0.11	0.01
	60 LB	0.13	0.14	0.01
	60 RB	0.10	0.15	0.05
SNC-3	20 LB	-	-	-
	20 C	0.19	0.21	0.02
	20 RB	0.12	0.15	0.03
	60 LB	0.16	0.18	0.02
	60 RB	0.12	0.18	0.06

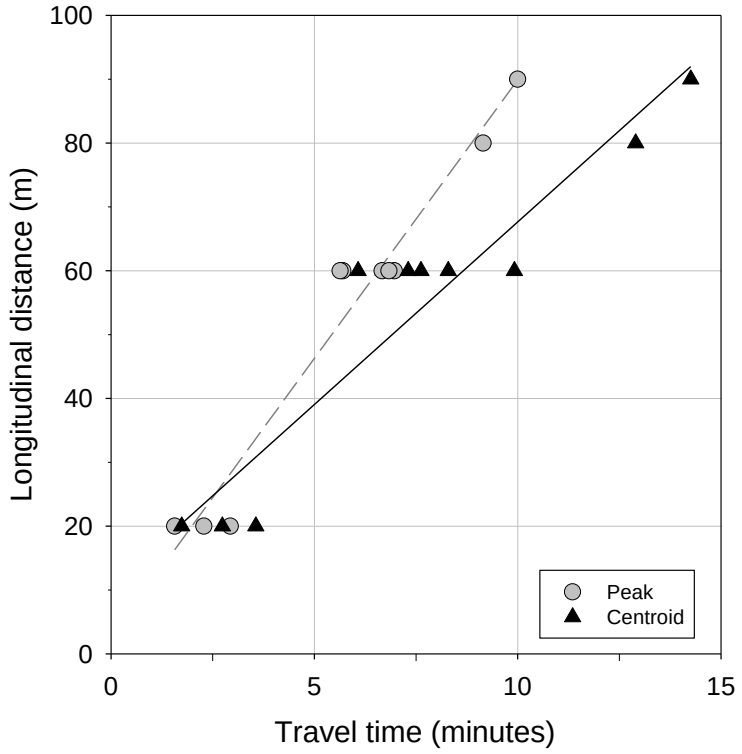

Figure 47. Travel times (peak and centroid) of sodium chloride concentration curves in the semi-natural channel.

4.3.4. Dispersion

The sodium chloride concentration curves measured at the same locations during runs SNC-2 and SNC-3 were normalized by their respective peak concentrations (Figure 48) in order to compare the dispersion process. The curves show that the plumes during run SNC-2 had longer rising limbs and delayed peaks in comparison to those during run SNC-3. This could be a result of the injection process, which was not exactly instantaneous but involved simultaneously inverting and submerging the trough to rinse it out, a process that took at least 2-5 seconds. Nevertheless, this would not explain the approximately 1-minute delay in peak concentrations between the two runs. The plume of run SNC-3 was faster than the plume of run SNC-2 at the three sampling locations, as indicated by the centroid and peak velocities shown in Table 34. Timestamps were checked for all instruments, and instrumental error does not appear to be the explanation. Thus, the differences in plume response are accepted as real since no other reasonable explanations are apparent. The temptation to shift the curves by approximately one minute to achieve better alignment was therefore resisted. Despite these differences, the trailing limbs of the curves were similar in geometry and duration during both runs.

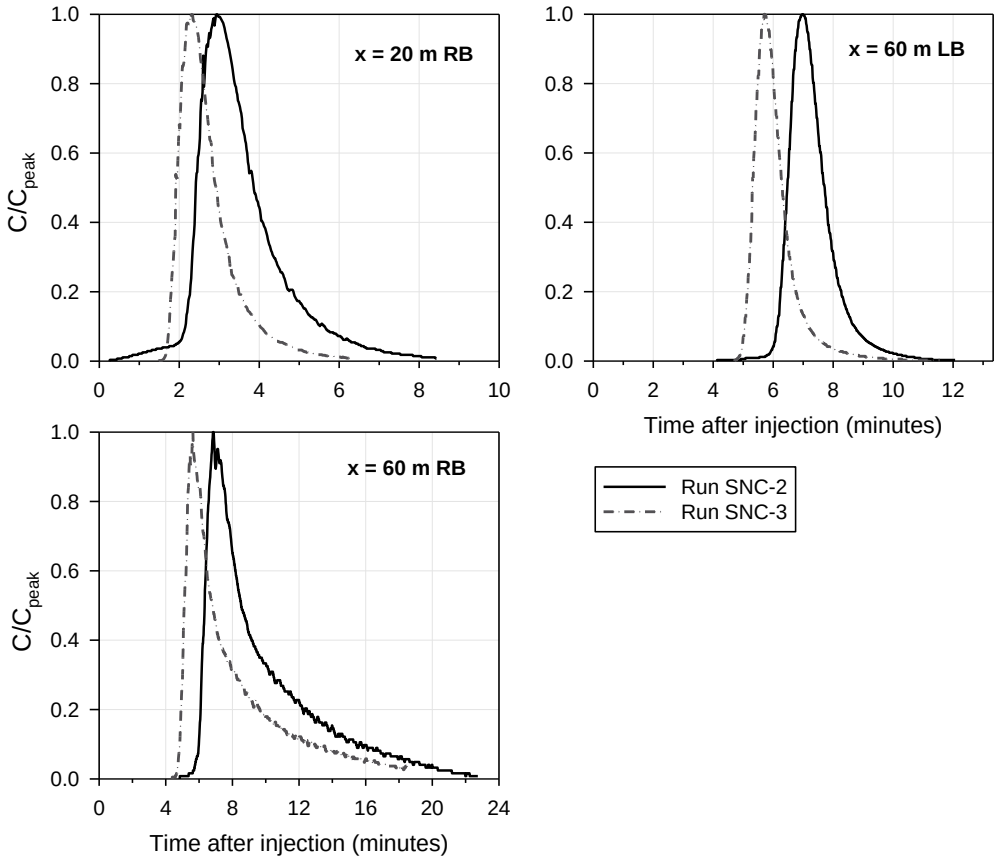

Figure 48. Normalized sodium chloride curves in the semi-natural channel (note the scale change on the x-axis).

The advective zone length estimates based on Equation 65 for the semi-natural channel varied between 4 and 1571 m (Table 35). Similar to the concrete channel case, it is difficult to judge whether measurements were taken within the advective zone or not. Therefore, the tracer data were analyzed to define which sampling locations were located in the advective or the equilibrium zones.

Table 35. Advective zone length estimates in the semi-natural channel based on the minimum and maximum empirical coefficients reported in the literature (Rutherford 1994; Sharma and Ahmad 2014).

β	**E_y (m^2s^{-1})**	**α**	**L_x (m)**
0.13	0.0003	0.2	314
		1	1571
4.65	0.0094	0.2	9
		1	44

The Hayami solution of the one-dimensional ADE (64) was utilized to estimate a longitudinal dispersion coefficient for each sodium chloride injection. The results indicate that a single longitudinal dispersion coefficient was not capable of reproducing the concentrations observed at the different sampling locations (Table 36), i.e., the sampling locations were located in the advective zone. Given that the sodium chloride concentrations were not evenly distributed across the channel width, the longitudinal dispersion coefficients obtained on the left and right banks of the channel were very different. On average, the difference between the values obtained for the left bank and right bank during runs SNC-2 and SNC-3 was 85%. The coefficients obtained for the left bank of the channel were all very small, yielding large Peclet numbers. The coefficients obtained on the right bank, however, yielded Peclet numbers between 1.60 and 4.68.

Table 36. Longitudinal dispersion coefficients estimated using the Hayami analytical solution fit on the sodium chloride concentration curves observed in the natural channel and the respective Peclet numbers.

Location (m)	**K_x**			**Pe**		
	SNC-1	**SNC-2**	**SNC-3**	**SNC-1**	**SNC-2**	**SNC-3**
20 C	-	-	0.01	-	-	27.0
20 RB	-	0.22	0.08	-	1.60	4.68
60 LB	-	0.03	0.02	-	12.6	18.9
60 C	0.03	-	-	10.01	-	-
60 RB	-	0.21	0.13	-	1.62	2.62
80 C	0.22	-	-	1.55	-	-
90 C	0.16	-	-	2.16	-	-

The average flow velocity was not capable of reproducing the start of the concentration curves at 20 m downstream of the injection line the center or the right bank of the channel (Figure 49). At 60 m downstream, however, the average flow velocity was able to reproduce the start of the curve on the right bank of the channel only. It is clear from the obtained concentration curves that the sodium chloride was not evenly mixed laterally in the study reach; therefore, the advection zone length is likely larger than that 90 m and the curves obtained should not be compared with modeled cross-sectional averaged concentrations.

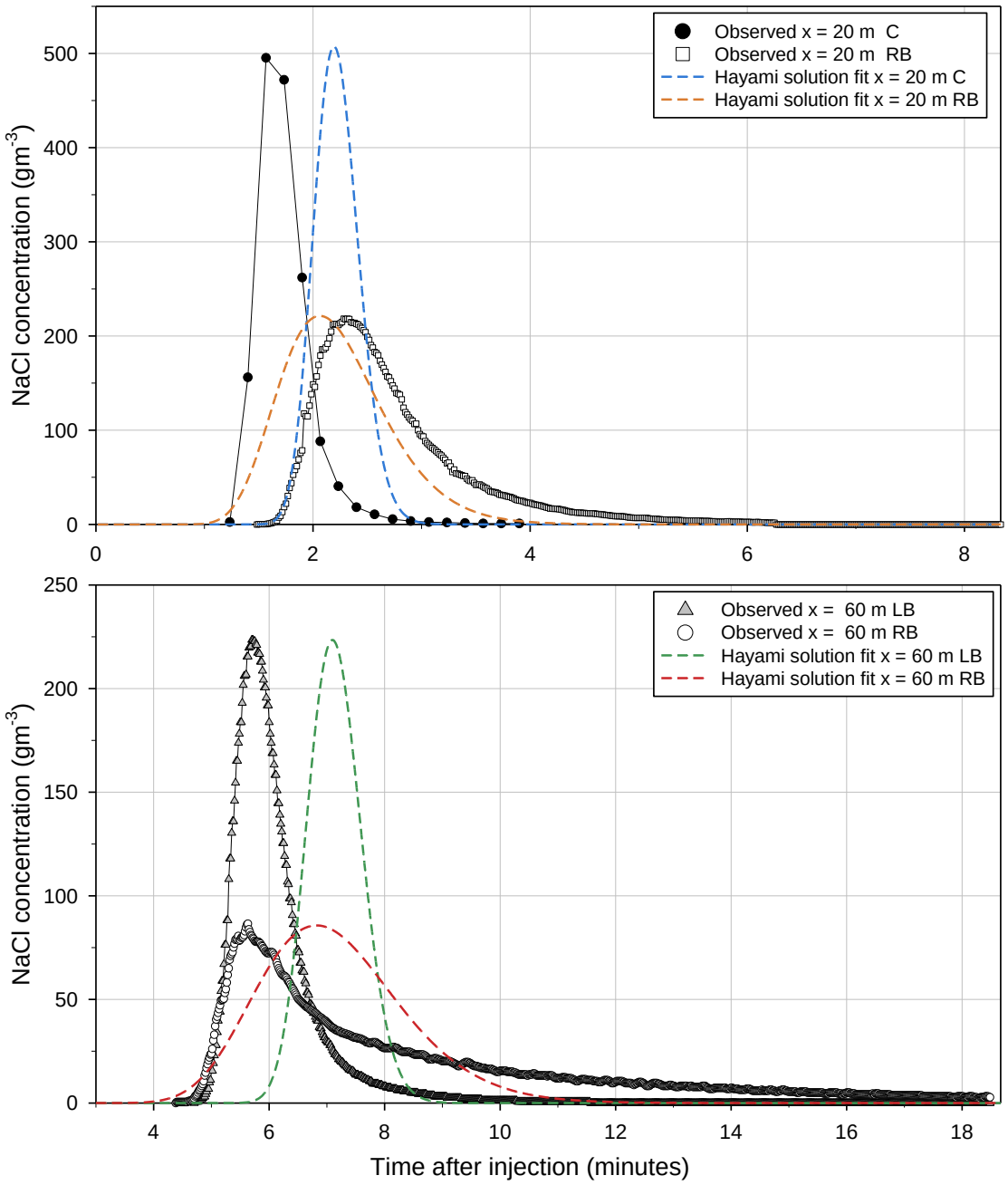

Figure 49. Observed versus predicted sodium chloride curves utilizing the Hayami analytical solution of the one-dimensional ADE in the semi-natural channel (run SNC-3) (note the scale change on both axes).

4.4.Natural channel

4.4.1. Discharge

During runs NC-1.1 to NC-1.3, the discharge was measured (by FLNRORD personnel) using an acoustic Doppler flow meter, yielding 0.093 m^3s^{-1}. No discharge measurements were taken during runs NC-2.1 to NC-2.6. The discharge on both days was estimated for each sodium chloride concentration curve (before truncation) utilizing the salt dilution method. During runs NC-1.1 to NC-1.3, conductivity returned to the background at all sampling locations. The average discharge obtained with the salt dilution method was 0.104 m^3s^{-1}, which agrees reasonably well with the measured discharge (Table 37).

Table 37. Summary of discharge values estimated through the salt dilution method for runs NC-1 to NC-3.

Run	Location (m)	Estimated discharge (m^3s^{-1})
NC-1.1	36 LB	-
	36 C	0.099
	36 RB	0.093
	49.6 LB	0.112
	49.6 LB	0.103
NC-1.2	36 LB	-
	36 C	0.101
	36 RB	0.099
	49.6 LB	0.103
	49.6 LB	0.107
NC-1.3	36 LB	-
	36 C	0.108
	36 RB	0.129
	49.6 LB	0.090
	49.6 LB	0.104
Average		0.104
CV (%)		10

CV = coefficient of variation (standard deviation/average).

During runs NC-2.1 to NC-2.6, the conductivity returned to the background value during all runs, except run NC-2.6, which were not included in the calculations for the salt dilution method.

The discharge varied between 0.031 and 0.048 m^3s^{-1}, yielding an average of 0.038 m^3s^{-1} (Table 38).

Table 38. Summary of discharge values estimated through the salt dilution method for runs NC-2.1 to NC-2.6.

Run	Location (m)	Estimated discharge (m^3s^{-1})
NC-2.1	36 LB	0.037
	36 C	0.040
	36 RB	0.048
NC-2.2	36 LB	0.030
	36 C	0.032
	36 RB	0.043
NC-2.3	49.6 LB	0.041
	49.6 C	0.038
	49.6 RB	0.037
NC-2.4	36 C	0.031
	92 C	0.033
	222 RB	0.031
NC-2.5	36 C	-
	92 C	0.042
	127.9 LB	0.045
NC-2.6	36 C	0.043[ET]
	92 C	0.046 [ET]
	127.9 LB	0.045 [ET]
Average		0.039
CV (%)		15

ET = experimental truncation; CV = coefficient of variation (standard deviation/average).

4.4.2. HEC-RAS hydraulic model

Sixteen cross-sections were surveyed in the field (Appendix E) and were utilized as the basis for the channel geometry on HEC-RAS (Table 39, Figure 50). The total length of the modeled reach was approximately 347 m with a thalweg slope of approximately S = 0.006 (Figure 51).

Table 39. Geometry input for the HEC-RAS model of the natural channel.

Distance from the injection line (m)	Cross-section number
-23.2	1
0	2
12.5	3
22	4
36	5
49.6	6
65	7
73.3	8
92	9
107.1	10
115.9	11
127.9	12
162.9	13
207.3	14
222	15
323.5	16

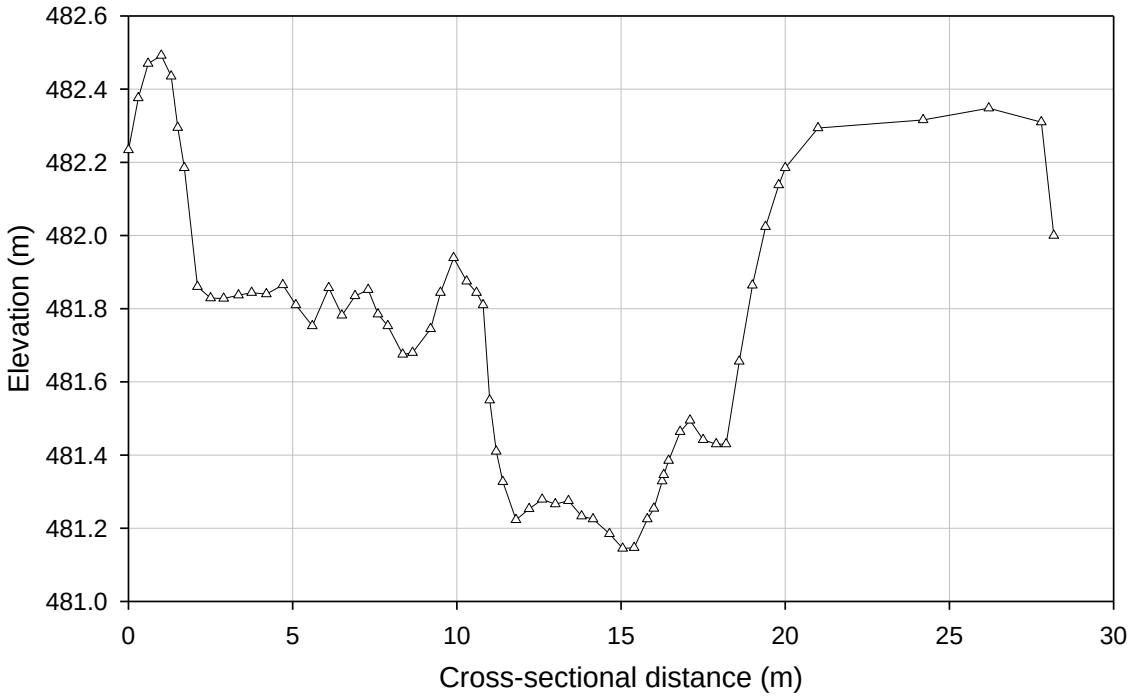

Figure 50. Example of a cross-section surveyed on the natural channel at 73.3 m downstream of the injection line.

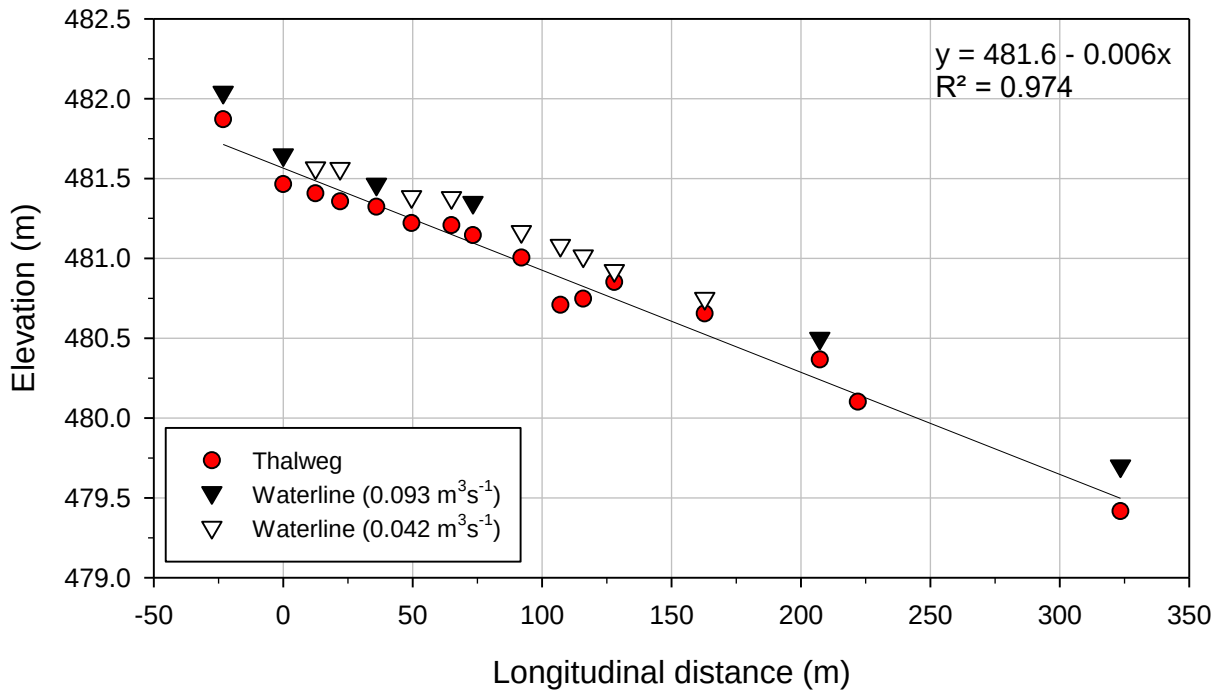

Figure 51. Thalweg and waterline elevations surveyed in the natural channel (longitudinal distance from the injection line).

Two profiles (discharges and waterline elevations) were utilized to calibrate the HEC-RAS model of the natural channel. The first profile corresponds to the conditions during runs NC-1.1 to NC-1.3. The measured discharge of 0.093 m^3s^{-1} was utilized as a steady flow condition at cross-section 1. At cross-section 14, a portion of the discharge was lost to a side-channel because of a minor breach in the levee containing the main flow. The side channel flowed through the semi-natural channel described in the previous section. Therefore, the discharge of the semi-natural channel (0.016 m^3s^{-1}), which corresponded to 18% of the total discharge, was subtracted from the measured discharge in the main channel, yielding a discharge of 0.077 m^3s^{-1} for the downstream section of the main channel between cross-sections 14 and 16. The downstream boundary condition was determined by the known waterline elevation at cross-section 16, which was 479.7 m. The model was calibrated by adjusting the Manning's roughness coefficients (n) at each cross-section in order to match the observed waterline elevations for both discharges (Figure 52). The calibrated Manning coefficients varied between 0.06 and 0.18.

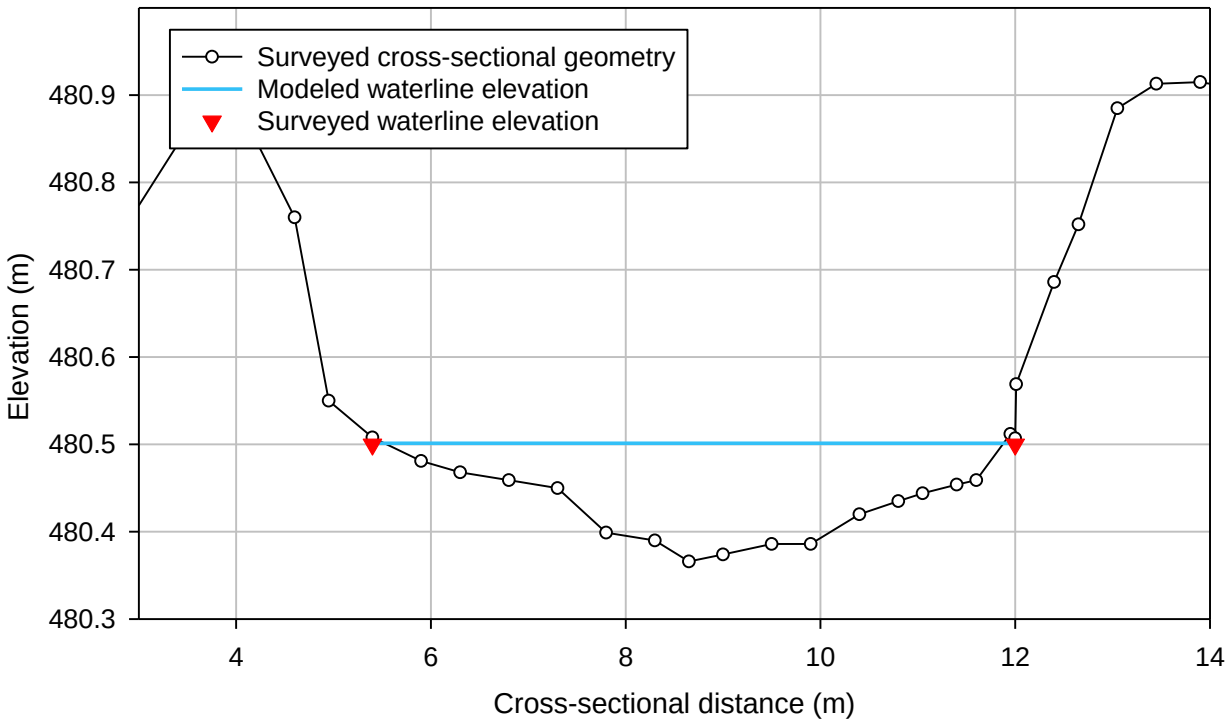

Figure 52. Example of a natural channel cross-section calibrated on HEC-RAS (x = 207.3 m, Q = 0.093 m^3s^{-1}).

For Q = 0.093 m^3s^{-1}, the largest difference between a surveyed and modeled waterline elevation was 2 cm at cross-section 14 (well within measurement uncertainty), therefore, the model calibration was accepted (Table 40).

Table 40. Observed and modeled waterline elevations in the natural channel (Q = 0.093 m^3s^{-1}).

Location (m)	**Cross-section number**	**Observed waterline elevation Q = 0.093 m^3s^{-1} (m)**	**Modeled waterline elevation (m)**	**$\|\Delta E\|$ (cm)**
-23.2	1	482.040	482.042	0.2
0	2	481.648	481.663	1.5
12.5	3	-	481.618	-
22	4	-	481.592	-
36	5	481.464	481.470	0.60
49.6	6	-	481.431	-
65	7	-	481.392	-

Location (m)	Cross-section number	Observed waterline elevation Q = 0.093 m^3s^{-1} (m)	Modeled waterline elevation (m)	|ΔE| (cm)
73.3	8	481.350	481.334	1.6
92	9	-	481.228	-
107.1	10	-	481.141	-
115.9	11	-	481.093	-
127.9	12	-	480.989	-
162.9	13	-	480.775	-
207.3	14	480.500	480.520	2.0
222	15	-	480.231	-
323.5	16	479.700	479.700	BC

BC = boundary condition.

Table 41 provides a summary of the hydraulic conditions in the natural channel for Q = 0.093 m^3s^{-1}. The channel-averaged velocity varied between 0.09 and 0.24 ms^{-1}, producing an average of 0.18 ms^{-1}. The flow depth, width, and area averages are 0.11 m, 4.90 m, and 0.54 m^2, respectively. The Froude number shows that the flow was subcritical (Fr < 1).

Table 41. Summary of hydraulic conditions for the natural channel model (Q = 0.093 m^3s^{-1}).

Location (m)	n	Velocity (ms^{-1})	Flow Depth (m)	Top width (m)	Flow area (m^2)	Shear velocity (ms^{-1})	Froude number
-23.2	0.15	0.21	0.12	3.52	0.44	0.14	0.19
0	0.15	0.20	0.10	4.6	0.48	0.13	0.19
12.5	0.08	0.14	0.15	4.19	0.65	0.05	0.12
22	0.10	0.17	0.13	4.23	0.53	0.08	0.15
36	0.17	0.18	0.10	5.47	0.53	0.14	0.18
49.6	0.08	0.13	0.16	4.71	0.75	0.04	0.10
65	0.10	0.19	0.08	5.99	0.50	0.09	0.21
73.3	0.08	0.19	0.10	4.88	0.49	0.07	0.19
92	0.12	0.17	0.11	5.28	0.58	0.11	0.13
107.1	0.10	0.19	0.15	3.38	0.50	0.08	0.16
115.9	0.08	0.24	0.13	3	0.39	0.09	0.21
127.9	0.09	0.22	0.07	5.91	0.42	0.10	0.26
162.9	0.06	0.19	0.09	5.7	0.49	0.05	0.21
207.3	0.18	0.13	0.09	6.73	0.60	0.11	0.14
222	0.15	0.22	0.08	4.17	0.35	0.16	0.24
323.5	0.14	0.09	0.14	6.58	0.89	0.06	0.07
Average	-	0.18	0.11	4.90	0.54	0.09	0.17

The second profile corresponds to the conditions during runs NC-2.1 to NC-2.6. The average discharge estimated based on the salt dilution method (Q = 0.038 m^3s^{-1}) was utilized as a steady flow condition input at cross-section 1. The discharge was reduced to Q = 0.031 m^3s^{-1} for the section between cross-sections 14 and 16, following the same proportion loss to the side channel as with the first profile. The downstream boundary condition was determined by the normal depth of flow based on the average surveyed thalweg slope (S = 0.006).

Given that no discharge measurements were taken on the second day of experiments and the uncertainties related to the discharge obtained by the salt dilution method, the model was fine-tuned by adjusting the discharge input to minimize the error between the modeled and observed waterline elevations, while maintaining the calibrated Manning's roughness coefficients fixed. The discharge that provided the best agreement was 0.042 m^3s^{-1} (Table 42).

Table 42. Observed and modeled waterline elevations in the natural channel (Q = 0.042 m^3s^{-1}).

Location (m)	**Cross-section number**	**Observed waterline elevation Q = 0.042 m^3s^{-1} (m)**	**Modeled waterline elevation (m)**	**$\|\Delta E\|$ (cm)**
-23.2	1	-	481.994	-
0	2	-	481.602	-
12.5	3	481.567	481.565	0.2
22	4	481.563	481.547	1.7
36	5	-	481.412	-
49.6	6	481.386	481.377	0.9
65	7	481.380	481.346	3.4
73.3	8	-	481.290	-
92	9	481.168	481.140	2.8
107.1	10	481.081	481.067	1.4
115.9	11	481.015	481.039	2.4
127.9	12	480.924	480.946	2.2
162.9	13	480.75	480.739	1.1
207.3	14	-	480.449	-
222	15	-	480.230	-
323.5	16	-	479.599	-

Table 43 provides a summary of the hydraulic conditions in the natural channel for Q = 0.042 m^3s^{-1}. The velocity varied between 0.08 and 0.21 ms^{-1}, producing an average of 0.15 ms^{-1}. The

flow depth, width, and area averages are 0.08 m, 3.71 m, and 0.30 m^2, respectively. The Froude number shows that the flow was subcritical (Fr < 1).

Table 43. Summary of hydraulic conditions for the natural channel model (Q = 0.042 m^3s^{-1}).

Location (m)	n	Velocity (ms^{-1})	Flow Depth (m)	Top width (m)	Flow area (m^2)	Shear velocity (ms^{-1})	Froude number
-23.2	0.15	0.15	0.09	3.20	0.28	0.11	0.16
0	0.15	0.18	0.08	3.03	0.23	0.13	0.21
12.5	0.08	0.10	0.11	3.86	0.43	0.04	0.09
22	0.10	0.12	0.09	3.90	0.35	0.06	0.13
36	0.17	0.19	0.05	4.22	0.22	0.16	0.26
49.6	0.08	0.08	0.11	4.43	0.50	0.03	0.08
65	0.10	0.15	0.07	3.92	0.27	0.08	0.19
73.3	0.08	0.15	0.06	4.58	0.29	0.06	0.19
92	0.12	0.15	0.09	2.92	0.27	0.11	0.16
107.1	0.10	0.14	0.16	1.87	0.30	0.06	0.11
115.9	0.08	0.17	0.11	2.24	0.24	0.06	0.17
127.9	0.09	0.21	0.05	4.22	0.20	0.10	0.31
162.9	0.06	0.14	0.07	4.67	0.31	0.04	0.17
207.3	0.18	0.19	0.05	3.90	0.19	0.17	0.27
222	0.15	0.10	0.08	4.16	0.34	0.07	0.11
323.5	0.14	0.10	0.08	4.31	0.35	0.07	0.11
Average	-	0.15	0.08	3.71	0.30	0.08	0.17

The results from the model were processed according to the methodology described in 3.3 in order to obtain a spatially-weighted average for the sub-reach within which a cross-section was located (Table 44 and 45). These results will be utilized in further calculations to investigate dispersion characteristics and sediment transport mode.

Table 44. Spatially weighted average of the hydraulic model results for each sampling location in the natural channel (Q = 0.093 m^3s^{-1}).

Location (m)	Velocity (ms^{-1})	Flow Depth (m)	Top width (m)	Flow area (m^2)	Shear velocity (ms^{-1})	Friction slope	Froude number
12.5	0.17	0.13	4.40	0.56	0.09	0.0098	0.16
22	0.16	0.13	4.32	0.57	0.08	0.0069	0.15
36	0.17	0.13	4.52	0.56	0.09	0.0090	0.15
49.6	0.16	0.13	4.68	0.58	0.09	0.0093	0.15
65	0.16	0.12	4.84	0.59	0.08	0.0085	0.15
73.3	0.17	0.12	4.91	0.58	0.08	0.0084	0.16
92	0.17	0.12	4.94	0.57	0.08	0.0082	0.16

Location (m)	Velocity (ms^{-1})	Flow Depth (m)	Top width (m)	Flow area (m^2)	Shear velocity (ms^{-1})	Friction slope	Froude number
107.1	0.17	0.12	4.85	0.57	0.09	0.0081	0.16
115.9	0.17	0.12	4.73	0.56	0.09	0.0079	0.16
127.9	0.18	0.12	4.70	0.54	0.09	0.0080	0.17
162.9	0.18	0.11	4.94	0.52	0.08	0.0081	0.18
207.3	0.18	0.11	5.21	0.53	0.08	0.0082	0.18
222	0.18	0.10	5.23	0.52	0.09	0.0091	0.18

Table 45. Spatially weighted average of the hydraulic model results for each sampling location in the natural channel (Q = 0.042 m^3s^{-1}).

Location (m)	Velocity (ms^{-1})	Flow Depth (m)	Top width (m)	Flow area (m^2)	Shear velocity (ms^{-1})	Friction slope	Froude number
12.5	0.14	0.10	3.45	0.33	0.08	0.0116	0.15
22	0.13	0.10	3.63	0.36	0.07	0.0076	0.13
36	0.14	0.09	3.80	0.33	0.08	0.0161	0.16
49.6	0.14	0.08	3.94	0.34	0.09	0.0194	0.16
65	0.13	0.09	4.00	0.35	0.08	0.0159	0.15
73.3	0.13	0.08	4.03	0.34	0.08	0.0149	0.16
92	0.14	0.08	3.97	0.33	0.08	0.0138	0.16
107.1	0.14	0.09	3.75	0.32	0.08	0.0129	0.16
115.9	0.14	0.09	3.62	0.32	0.08	0.0122	0.16
127.9	0.14	0.09	3.58	0.31	0.08	0.0122	0.16
162.9	0.15	0.08	3.77	0.30	0.08	0.0120	0.18
207.3	0.15	0.08	3.88	0.29	0.08	0.0163	0.19
222	0.15	0.08	3.89	0.28	0.09	0.0175	0.19

4.4.3. Concentration curves

During runs NC-1.1 to NC-1.3, conductivity was recorded at four out of the five sampling locations (Appendix F). Turbidity was recorded at all five sampling locations during each of the three runs. The turbidity curve recorded at 49.6 m on the right bank of the channel during run NC-1.3 was contaminated by sunlight, and it was not included in the results. During runs NC-2.1 to NC-2.6, conductivity was recorded at all three sampling stations (Appendix F). Some of the turbidity measurements, however, were affected by sensors malfunction and/or sunlight interference. OBS sensor 735 did not record data during any of the runs; OBS sensor 1437 did not record any data during run NC-2.3; sunlight affected sensor 10181 during run NC-2.4, and sensors

735 to 1437 during run NC-2.6. Nevertheless, there were several high-quality measurements during the experimental period, lasting two days.

4.4.3.1. Runs NC-1.1 to NC-1.3 ($Q = 0.093\ m^3s^{-1}$)

4.4.3.1.1. Recovery rates

During runs NC-1.1 to NC-1.3, eight (8) of the sodium chloride curves returned to the background level whereas four (4) others were ended by the truncation criterion (Table 46). Most of the suspended sediment curves were ended by the truncation criterion, except for the two curves at 49.6 m downstream of the injection line during run NC-1.1, which were experimentally truncated. Figure 53 shows two of the sodium chloride and suspended sediment curves obtained during run NC-1.2.

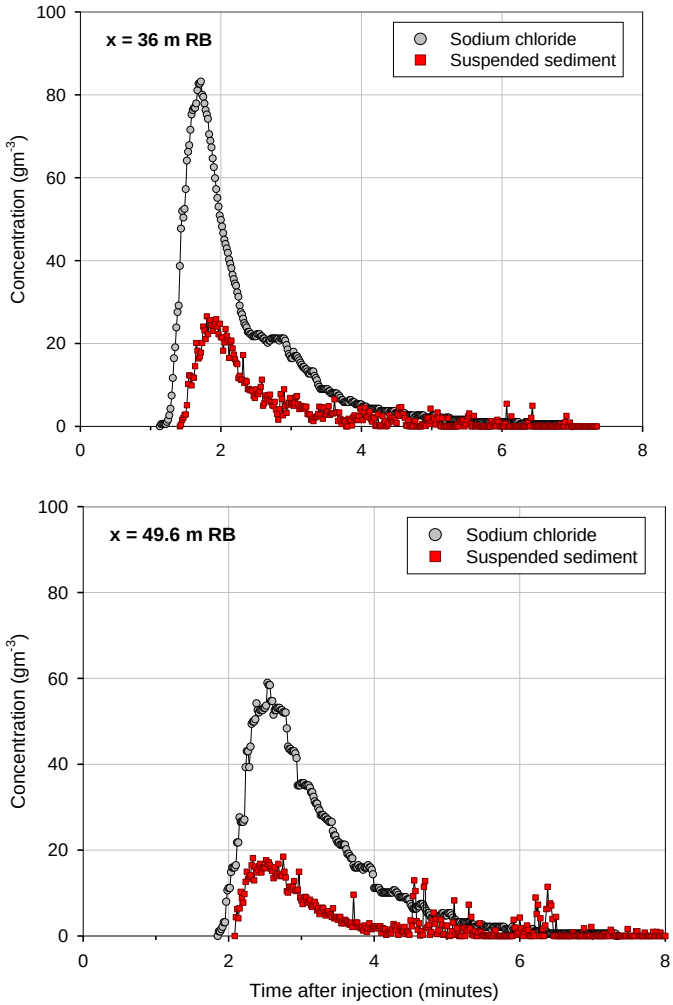

Figure 53. Concentration curves during run NC-1.2.

The average sodium chloride recovery was 90%, varying between 72% and 103% (Table 46). Figure 54 shows that at 36 m downstream of the injection line, the sodium chloride concentration curves on the center and the right bank of the channel were very similar, suggesting even lateral mixing. As the suspended sediment concentration curves demonstrated, however, the plumes shifted to the left bank of the channel, yielding larger concentrations at this location compared to the center and right bank. At 49.6 m downstream of the injection line, although the recovery rates were similar, the peak concentrations were approximately 30% larger on the right bank of the channel.

Table 46. Summary of the sodium chloride and sediment concentration curves obtained on the natural channel (Q = 0.093 m^3s^{-1}). T = truncation criterion; ET = experimental truncation; BC = return to background; "–" indicates no data because there was no probe at that location for the run or data was not recorded.

Run	Location (m)	Sodium chloride			Sediment			
		RR (%)	R_{peak} (%)	End defined by	Particle size (mm)	RR (%)	R_{peak} (%)	End defined by
NC-1.1	12.5 LB	-	-	-	<0.075	77	3.0	T
	12.5 C	-	-	-		55	3.5	
	12.5 RB	-	-	-		42	3.5	
	36 LB	-	-	-		55	0.7	
	36 C	93	1.5	T		36	0.6	
	36 RB	97	1.5	T		41	0.7	
	49.6 LB	82	0.7	BC		35	0.4	ET
	49.6 RB	90	1.1	BC		33	0.5	
NC-1.2	12.5 LB	-	-	-	0.075-0.125	32	1.5	T
	12.5 C	-	-	-		37	2	
	12.5 RB	-	-	-		23	1	
	36 LB	-	-	-		18	<0.5	
	36 C	92	1.7	BC		16	<0.5	
	36 RB	94	1.5	T		14	<0.5	
	49.6 LB	90	0.8	BC		12	<0.5	
	49.6 RB	87	1.1	BC		14	<0.5	
NC-1.3	12.5 LB	-	-	-	0.125-0.25	20	1	T
	12.5 C	-	-	-		24	1.5	
	12.5 RB	-	-	-		3	<0.5	
	36 LB	-	-	-		11	<0.5	
	36 C	86	1.7	BC		9	<0.5	
	36 RB	72	1.4	T		7	<0.5	
	49.6 LB	103	1	BC		6	<0.5	
	49.6 RB	90	1.2	BC		-	-	-

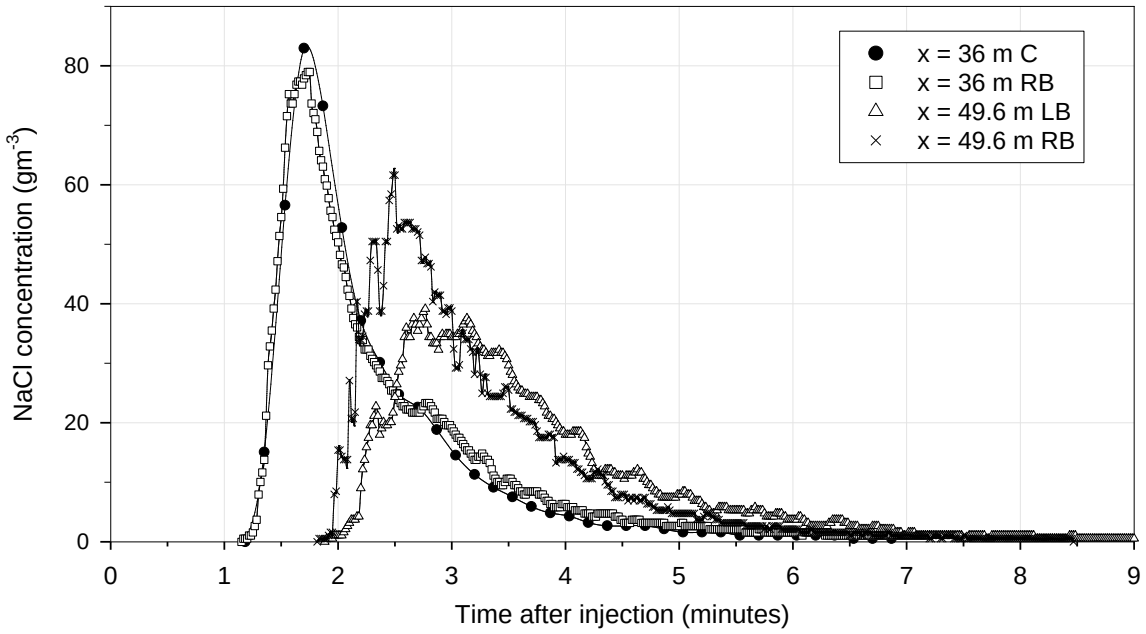

Figure 54. Sodium chloride plumes during run NC-1.1.

The suspended sediment recoveries were again dependent on particle size (Figure 55). The finest fraction (<0.075 mm), corresponding to the very fine sand and silt-clay particles, had approximately 35% recovery at 49.6 m downstream of the injection line. The recovery rates decreased to approximately 10% or less for the 0.075-0.125 mm and 0.125-0.25 mm fractions, respectively. Likewise, the peak recoveries also decreased with increasing particle size at all sampling locations.

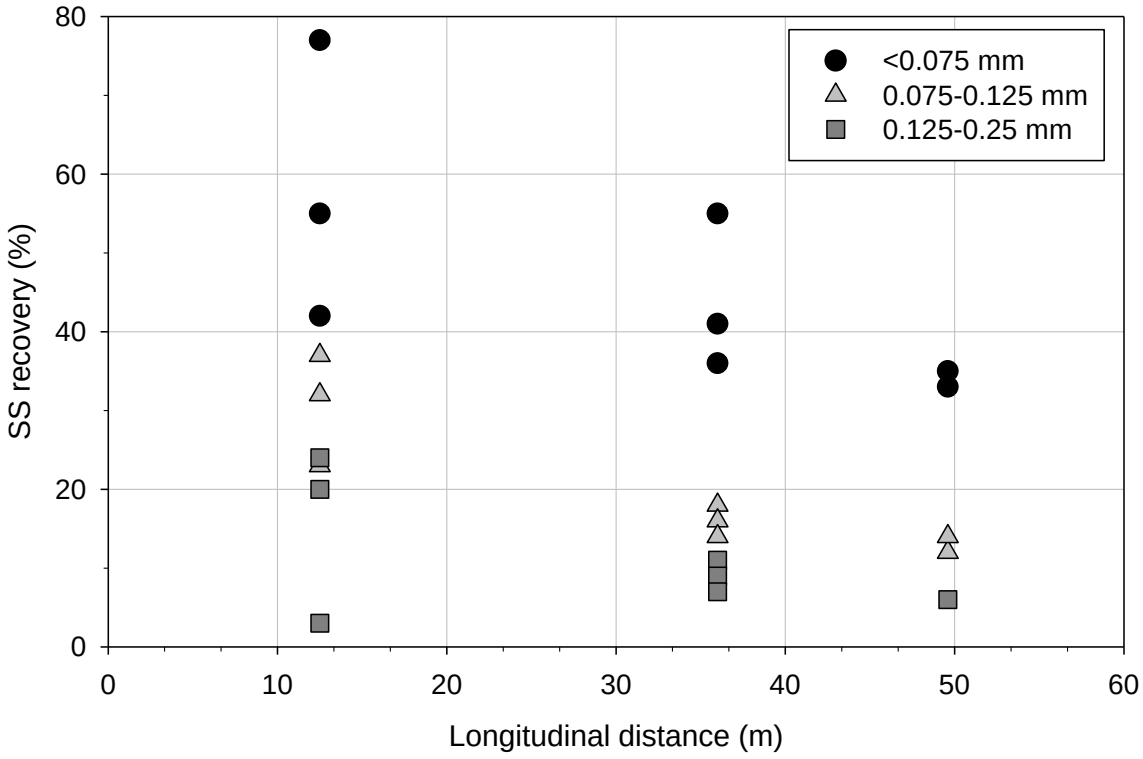

Figure 55. Suspended sediment recovery rates in the natural channel (Q = 0.093 m^3s^{-1}).

The surveyed cross-sections at 12.5 m, 36 m, and 49.6 m show that the thalweg was located on the left bank at 12.5 m, and started to shift towards the right bank of the channel at 36 m. This behavior was visually observed during the field experiments, where the plume was seen moving toward the left bank immediately after injection. As a consequence, the largest concentrations and plume velocities are observed on the center, left bank, and right bank at 12.5 m, 36 m, and 49.6 m, respectively.

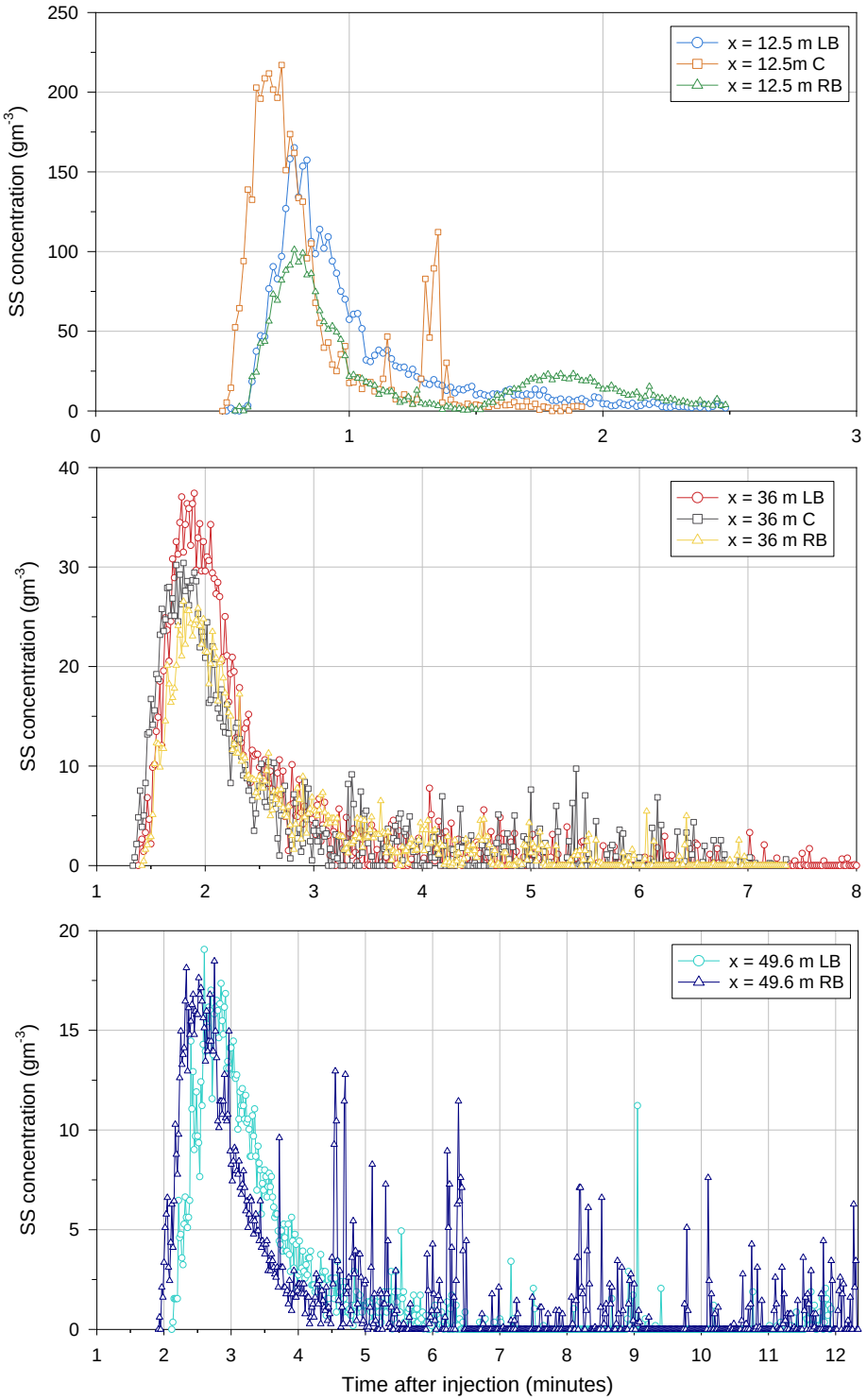

Figure 56. Suspended sediment plumes: lateral mixing at 12.5 m, 36 m, and 49.6 m downstream of the injection point during run NC-1.2 (note the scale change on both axes).

4.4.3.1.2. Advection velocity

Despite the variations between runs, the centroid and peak travel times were linearly related to distance (Figure 57). There is a large degree of scatter about the arrival times at fixed stations downstream of the injection line, on the order of about 1 minute. These differences show that the plume was being distorted by lateral shear velocity while moving downstream, consequently arriving at different times on the center, left bank, and right bank of the channel.

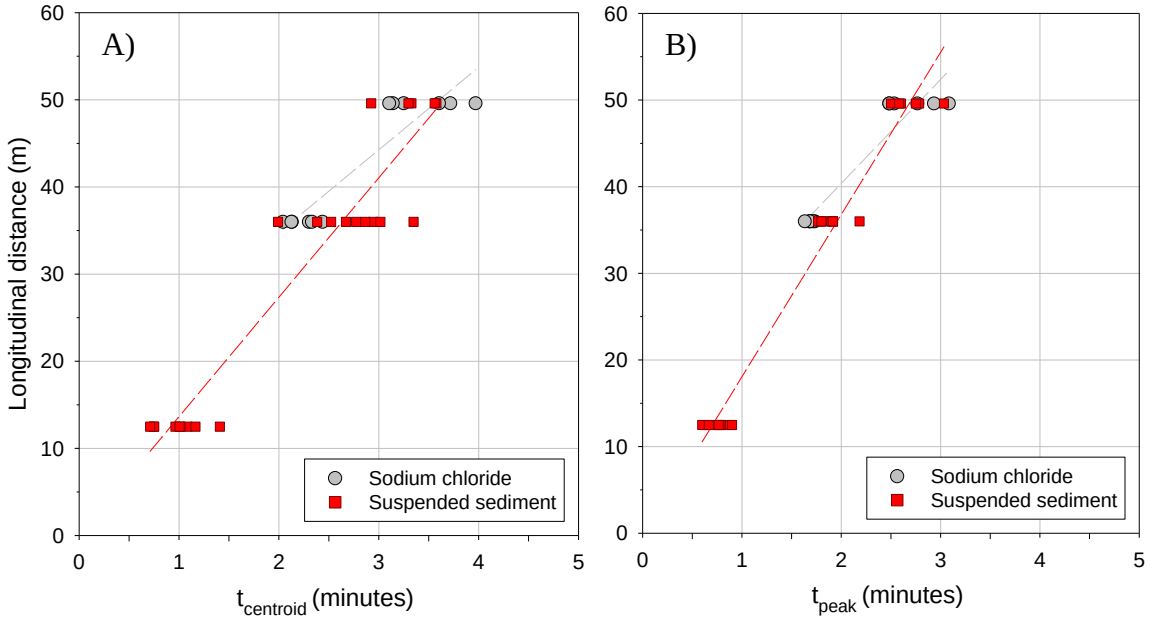

Figure 57. Travel time of the concentration curves in the natural channel (Q = 0.093 m^3s^{-1}). A) Centroid travel times; B) Peak travel times.

The velocities of the peaks for sodium chloride were 18-29% faster than the centroid velocities (Table 47). This shows that the front part of the plume travelled faster than the center of mass. This is confirmed by the positive skewness of the concentration curves. The differences between centroid and peak velocities were similar at all four sampling locations, indicating similar skewness of the concentration curves. Both the peak and centroid velocities were faster than the modeled average flow velocity (0.17 ms^{-1}).

Table 47. Centroid and peak velocities of sodium chloride in the natural channel (Q = 0.093 m^3s^{-1}).

Location (m)	U (ms^{-1})	NC-1.1	NC-1.2	NC-1.3	Average	CV (%)
36 C	$\bar{U}_{centroid}$	0.26	0.28	0.29	0.28	2
	$\bar{U}_{peak}$	0.35	0.35	0.35	0.35	0
	$\bar{U}_{peak}$ - $\bar{U}_{centroid}$	0.09	0.07	0.06	0.07	2
36 RB	$\bar{U}_{centroid}$	0.25	0.26	0.28	0.26	2
	$\bar{U}_{peak}$	0.35	0.35	0.37	0.35	1
	$\bar{U}_{peak}$ - $\bar{U}_{centroid}$	0.1	0.09	0.09	0.09	1
49.6 LB	$\bar{U}_{centroid}$	0.22	0.23	0.21	0.22	1
	$\bar{U}_{peak}$	0.3	0.28	0.27	0.28	2
	$\bar{U}_{peak}$ - $\bar{U}_{centroid}$	0.08	0.05	0.06	0.06	2
49.6 RB	$\bar{U}_{centroid}$	0.25	0.26	0.27	0.25	1
	$\bar{U}_{peak}$	0.33	0.33	0.33	0.33	0
	$\bar{U}_{peak}$ - $\bar{U}_{centroid}$	0.08	0.07	0.06	0.08	1

CV = coefficient of variation (standard deviation/average).

Likewise, the peak velocity of the suspended sediment curves was larger than the centroid velocity at all sampling locations (Table 48). However, in the case of suspended sediment, the variation was much larger, from 6% to 55%. This can be attributed to the influence of the suspended sediment concentration fluctuations on the centroid velocity calculations using the temporal moments.

Table 48. Centroid and peak velocities of suspended sediment in the natural channel (Q = 0.093 m^3s^{-1}).

Run	Location (m)	$\bar{U}_{centroid}$ (ms^{-1})	$\bar{U}_{peak}$ (ms^{-1})	$\bar{U}_{peak}$ - $\bar{U}_{centroid}$ (ms^{-1})
NC-1.1	12.5 LB	0.19	0.28	0.09
	12.5 C	0.28	0.32	0.04
	12.5 RB	0.15	0.24	0.09
	36 LB	0.18	0.31	0.13
	36 C	0.20	0.34	0.14
	36 RB	0.22	0.33	0.14
	49.6 LB	0.23	0.30	0.07
	49.6 RB	0.25	0.33	0.08
NC-1.2	12.5 LB	0.21	0.27	0.06
	12.5 C	0.28	0.35	0.07
	12.5 RB	0.18	0.27	0.09
	36 LB	0.25	0.32	0.06
	36 C	0.30	0.33	0.03

Run	Location (m)	$\bar{U}_{centroid}$ (ms^{-1})	$\bar{U}_{peak}$ (ms^{-1})	$\bar{U}_{peak}$ - $\bar{U}_{centroid}$ (ms^{-1})
	36 RB	0.24	0.33	0.10
	49.6 LB	0.23	0.32	0.09
	49.6 RB	0.28	0.30	0.02
NC-1.3	12.5 LB	0.22	0.27	0.06
	12.5 C	0.29	0.31	0.02
	12.5 RB	0.21	0.23	0.02
	36 LB	0.20	0.27	0.08
	36 C	0.21	0.31	0.10
	36 RB	0.22	0.31	0.09
	49.6 LB	0.25	0.27	0.02
	49.6 RB	-	-	-
Average	12.5 LB	0.21	0.27	0.07
	12.5 C	0.28	0.33	0.04
	12.5 RB	0.18	0.25	0.07
	36 LB	0.21	0.30	0.09
	36 C	0.24	0.33	0.09
	36 RB	0.23	0.32	0.11
	49.6 LB	0.24	0.30	0.06
	49.6 RB	-	-	-
CV (%)	12.5 LB	7	2	25
	12.5 C	2	6	58
	12.5 RB	17	8	61
	36 LB	17	9	40
	36 C	23	5	62
	36 RB	5	4	24
	49.6 LB	5	8	60
	49.6 RB	-	-	-

CV = coefficient of variation (standard deviation/average).

4.4.3.2. Runs NC-2.1 to NC-2.6 (Q = 0.042 m^3s^{-1})

4.4.3.2.1. Recovery rates

During runs NC-2.1 to NC-2.6, 14 out of the 18 sodium chloride curves returned to the background or were defined by the truncation criterion. Experimental truncation occurred for the curves at207 m and 222 m downstream of the injection line during run NC-2.4 and the curves during run NC-2.6 (Table 49). 23 out of the 34 suspended sediment plumes were defined by the

truncation criterion, while 11 had experimental truncation, particularly at long distances downstream of the injection line. Figure 58 shows the sodium chloride and suspended sediment curves obtained at 92 m downstream of the injection line during run NC-2.5.

Recovery for sodium chloride varied between 92% and 136%. Peak recoveries were very consistent between runs, decreasing in the downstream direction from 1.3% at 36 m to 0.1% at 222 m.

Table 49. Summary of the sodium chloride and sediment concentration curves obtained in the natural channel (Q = 0.042 m^3s^{-1}). T = truncation criterion; ET = experimental truncation; BC = return to background; "–" indicates no data because there was no probe at that location for the run or data was not recorded.

Run	Location (m)	Sodium chloride			Particle size (mm)	Sediment		
		RR (%)	R_{peak} (%)	End defined by		RR (%)	R_{peak} (%)	End defined by
NC-2.1	36 LB	88	1.0	BC	0.075-0.125	-	-	T
	36 C	103	1.2	T		17	0.25	
	36 RB	109	1.3	T		20	0.27	
	49.6 LB	-	-	-		19	0.16	
	49.6 C	-	-	-		15	0.17	
	49.6 RB	-	-	-		14	0.14	
	65 LB	-	-	-		8	0.05	
	65 RB	-	-	-		11	0.10	
NC-2.2	36 LB	98	0.9	BC	0.125-0.25	-	-	T
	36 C	125	1.2	T		11	0.30	
	36 RB	135	1.2	T		12	0.29	
	49.6 LB	-	-	-		13	0.23	
	49.6 C	-	-	-		11	0.20	
	49.6 RB	-	-	-		14	0.21	
	65 LB	-	-	-		6	0.05	ET
	65 RB	-	-	-		8	0.11	
NC-2.3	36 LB	-	-	-	0.25-0.5	-	-	
	36 C	-	-	-		10	0.39	T
	36 RB	-	-	-		10	0.61	
	49.6 LB	113	0.7	BC		-	-	
	49.6 C	116	0.8	T		8	0.18	T
	49.6 RB	114	0.6	T		9	0.17	ET
	65 LB	-	-	-		4	0.09	ET
	65 RB	-	-	-		6	0.14	T

Run	Location (m)	Sodium chloride			Particle size (mm)	Sediment		
		RR (%)	R_{peak} (%)	End defined by		RR (%)	R_{peak} (%)	End defined by
NC-2.4	12.5	-	-	-	<0.075	-	-	-
	36	128	1.3	T		37	0.6	T
	49.6	-	-	-		29	0.3	
	73.3	-	-	-		22	0.1	ET
	92	126	0.4	BC		13	0.07	T
	107	-	-	-		-	-	-
	207	-	-	-		6	0.02	ET
	222	136	0.1	ET		5	0.02	ET
NC-2.5	12.5	-	-	-	0.075-0.125	-	-	-
	36	96	1.3	T		16	0.24	T
	49.6	-	-	-		14	0.14	
	73.3	-	-	-		9	0.06	
	92	100	0.4	T		8	0.04	
	107	-	-	-		-	-	-
	115.9	-	-	-		7	0.03	ET
	127.9	101	0.2	BC		6	0.02	
NC-2.6	12.5	-	-	-	0.125-0.25	-	-	-
	36	98	1.3	ET		-	-	-
	49.6	-	-	-		-	-	-
	73.3	-	-	-		-	-	-
	92	92	0.4	ET		-	-	-
	107	-	-	-		-	-	-
	115.9	-	-	-		4	0.02	ET
	127.9	94	0.2	ET		3	0.02	

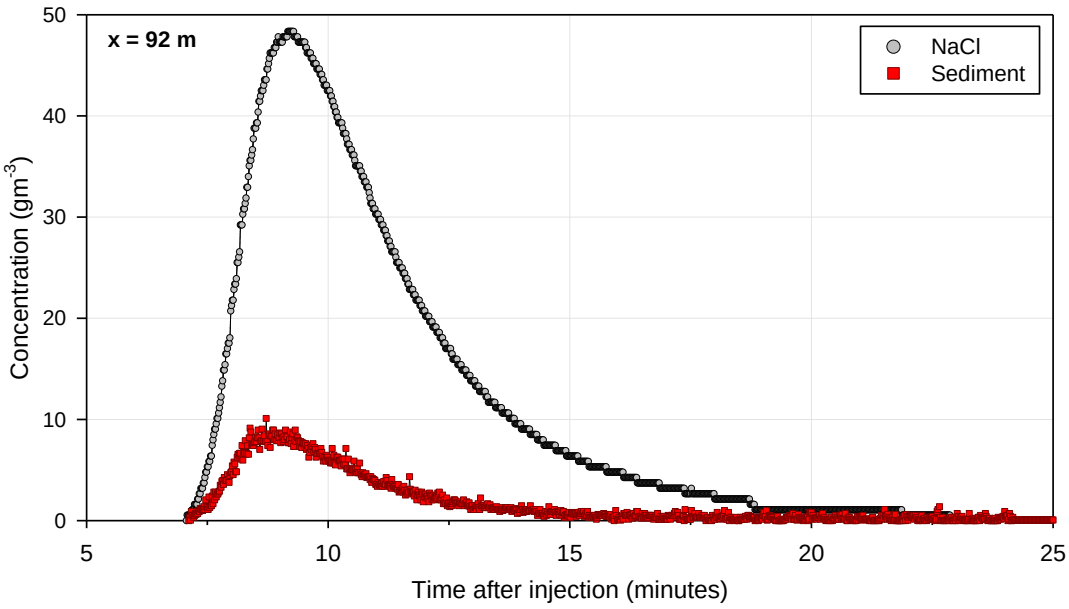

Figure 58. Concentration curves observed at 92 m downstream of the injection during run NC-2.5.

Recovery for suspended sediment decreased in the downstream direction (Figure 59). For the finest fraction (<0.075 mm), the recovery decreased from 37% at 36 m to approximately 4% at 207 m. For the 0.125-0.25 mm size range, a similar recovery of 4% was observed at 115.9 m downstream, indicating more rapid loss due to settling.

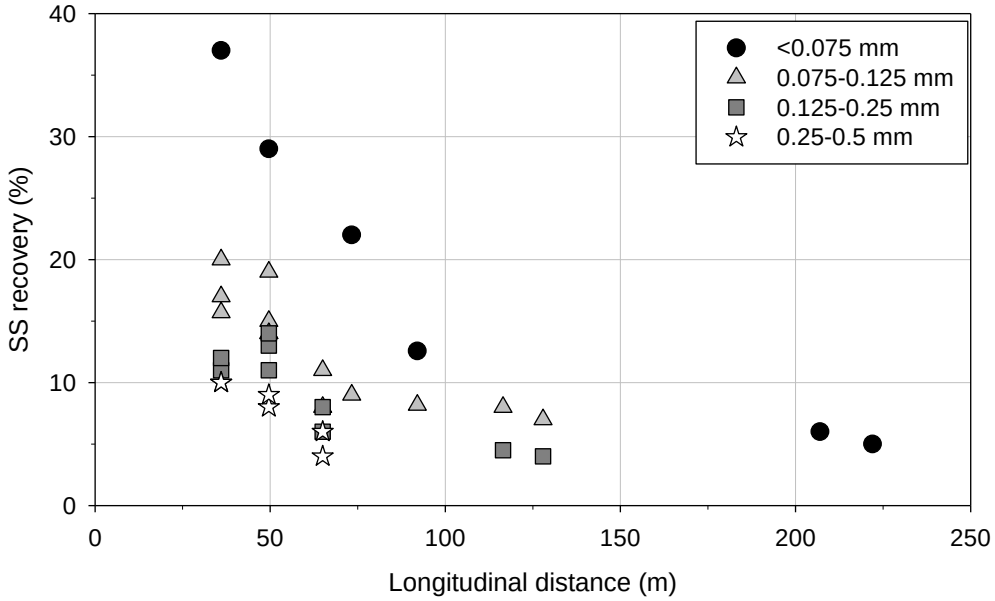

Figure 59. Suspended sediment recovery rates in the natural channel (Q = 0.042 m^3s^{-1}).

4.4.3.2.2. Advection velocity

Overall, the centroid and peak travel times of the sodium chloride plumes were very similar at all sampling locations (Figure 60). The travel time increased nonlinearly over the study reach, indicating that the mean flow velocity decreased somewhere between 150 m and 220 m downstream of the injection line.

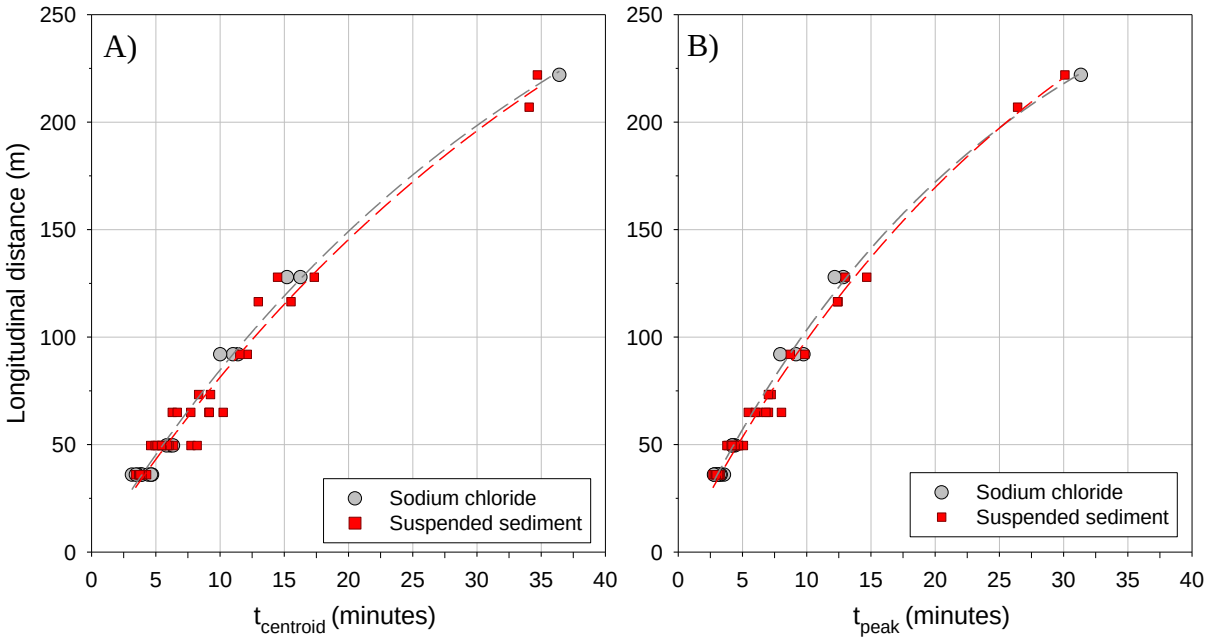

Figure 60. Travel time of the concentration curves in the natural channel (Q = 0.042 m^3s^{-1}). A) Centroid travel times; B) Peak travel times.

The peak velocity was larger (13-32%) than the centroid velocity during all runs (Table 50). The difference between the centroid velocity and the modeled average flow velocity (0.14 ms^{-1}) decreases in the downstream direction, becoming very similar at 92 m and 127.9 m downstream of the injection line. At 222 m, the centroid and peak velocities decrease to 0.10 and 0.12 ms^{-1}, respectively. The peak velocities of the suspended sediment curves were also larger than the centroid velocities at all sampling locations. Similar to runs NC-1.1 to NC-1.3, the differences between the peak and centroid velocities of the curves are much larger than the differences for the sodium chloride curves, from 6% to 46%.

Table 50. Centroid and peak velocities of sodium chloride and suspended sediment in the natural channel ($Q = 0.042\ m^3s^{-1}$).

Run	Location (m)	Sodium chloride			Suspended sediment		
		$\bar{U}_{centroid}$	$\bar{U}_{peak}$	$\bar{U}_{peak} - \bar{U}_{centroid}$	$\bar{U}_{centroid}$	$\bar{U}_{peak}$	$\bar{U}_{peak} - \bar{U}_{centroid}$
		(ms^{-1})					
NC-2.1	36 LB	0.16	0.20	0.04	-	-	-
	36 C	0.16	0.21	0.05	0.18	0.22	0.04
	36 RB	0.15	0.21	0.06	0.16	0.21	0.05
	49.6 LB	-	-	-	0.11	0.20	0.09
	49.6 C	-	-	-	0.18	0.21	0.03
	49.6 RB	-	-	-	0.17	0.22	0.05
	65 LB	-	-	-	0.17	0.20	0.03
	65 RB	-	-	-	0.12	0.15	0.03
NC-2.2	36 LB	0.13	0.17	0.04	-	-	-
	36 C	0.14	0.19	0.05	0.15	0.19	0.04
	36 RB	0.13	0.18	0.05	0.14	0.18	0.04
	49.6 LB	-	-	-	0.13	0.18	0.05
	49.6 C	-	-	-	0.14	0.18	0.04
	49.6 RB	-	-	-	0.10	0.16	0.06
	65 LB	-	-	-	0.11	0.13	0.02
	65 RB	-	-	-	0.14	0.17	0.03
NC-2.3	36 LB	-	-	-	-	-	-
	36 C	-	-	-	0.16	0.20	0.04
	36 RB	-	-	-	0.15	0.19	0.04
	49.6 LB	0.13	0.19	0.06	-	-	-
	49.6 C	0.14	0.20	0.06	0.16	0.20	0.04
	49.6 RB	0.14	0.20	0.06	0.14	0.18	0.04
	65 LB	-	-	-	0.12	0.16	0.04
	65 RB	-	-	-	0.16	0.18	0.02
NC-2.4	12.5	-	-	-	-	-	-
	36	0.14	0.19	0.05	0.16	0.19	0.03
	49.6	-	-	-	0.15	0.19	0.04
	73.3	-	-	-	0.13	0.17	0.04
	92	0.12	0.16	0.04	0.13	0.16	0.03
	107	-	-	-	-	-	-
	207	-	-	-	0.10	0.13	0.03
	222	0.10	0.12	0.02	0.11	0.12	0.01
NC-2.5	12.5	-	-	-	-	-	-
	36	0.17	0.20	0.03	0.16	0.20	0.04
	49.6	-	-	-	0.15	0.20	0.05
	73.3	-	-	-	0.15	0.17	0.02

Run	Location (m)	Sodium chloride			Suspended sediment		
		$\bar{U}_{centroid}$	$\bar{U}_{peak}$	$\bar{U}_{peak} - \bar{U}_{centroid}$	$\bar{U}_{centroid}$	$\bar{U}_{peak}$	$\bar{U}_{peak} - \bar{U}_{centroid}$
		(ms^{-1})					
	92	0.14	0.17	0.03	0.14	0.18	0.04
	107	-	-	-	-	-	
	115.9	-	-	-	0.12	0.16	0.04
	127.9	0.13	0.17	0.04	0.12	0.15	0.03
NC-2.6	12.5	-	-	-	-	-	-
	36	0.17	0.22	0.05	-	-	-
	49.6	-	-	-	-	-	-
	73.3	-	-	-	-	-	-
	92	0.15	0.19	0.04	-	-	-
	107	-	-	-	-	-	-
	115.9	-	-	-	0.15	0.16	0.01
	127.9	0.14	0.17	0.03	0.15	0.16	0.01
Average	36 LB	0.16	0.20	0.05	-	-	-
	36 C	-	-	-	0.16	0.20	0.04
	36 RB	-	-	-	0.15	0.19	0.04
	49.6 LB	-	-	-	-	-	-
	49.6 C	-	-	-	0.16	0.20	0.04
	49.6 RB	-	-	-	0.14	0.19	0.05
	65 LB	-	-	-	0.13	0.16	0.03
	65 RB	-	-	-	0.14	0.17	0.03
	92	0.14	0.17	0.04	-	-	-
CV (%)	36 LB	9	6	19	-	-	-
	36 C	-	-	-	7	6	12
	36 RB	-	-	-	7	8	13
	49.6 LB	-	-	-	-	-	-
	49.6 C	-	-	-	13	8	16
	49.6 RB	-	-	-	26	16	20
	65 LB	-	-	-	24	22	33
	65 RB	-	-	-	14	9	22
	92	11	9	16	-	-	-

CV = coefficient of variation (standard deviation/average).

The lateral concentration measurements show that the start, duration, and tails of the curves are similar at 36 m and 49.6 m downstream of the injection line, for both sodium chloride and suspended sediment (Figures 61, 62, and 63). At 36 m the sodium chloride curves were very similar between the center and the right bank of the channel, with the center arriving slightly faster. The same behavior was observed with the suspended sediment curves. The sodium chloride curve on

the left bank, however, had a smaller peak concentration and slower arrival time. At 49.6 m, the plumes arrived slightly faster at the center of the channel, where the largest peak concentrations were observed, followed by the left and then the right bank. At 65 m the curves are very different between the left and right banks of the channel. The plumes arrived faster on the right bank of the channel during all three runs. Despite the recovery rates being similar, the peak concentration was approximately 50% larger on the right bank than on the left bank.

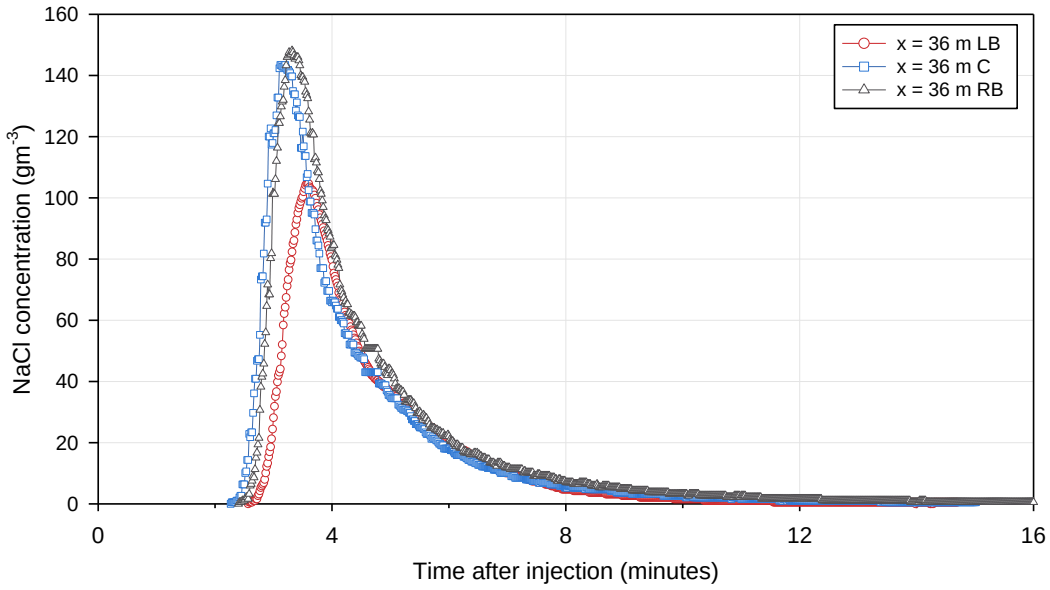

Figure 61. Sodium chloride concentration at 36 m downstream of the injection line during run NC-2.2.

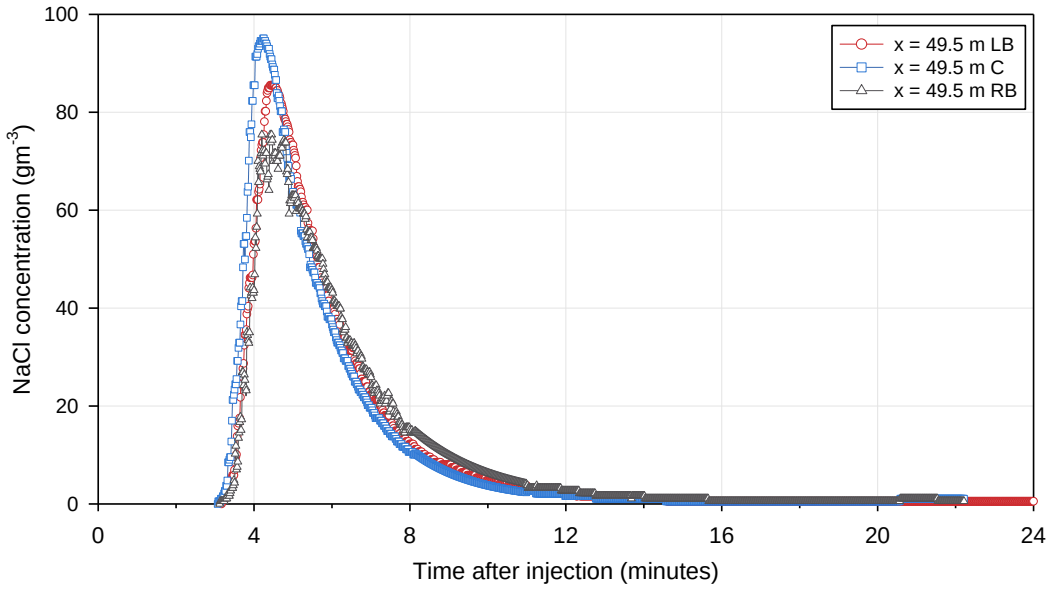

Figure 62. Sodium chloride concentration at 49.6 m downstream of the injection line during run NC-2.3.

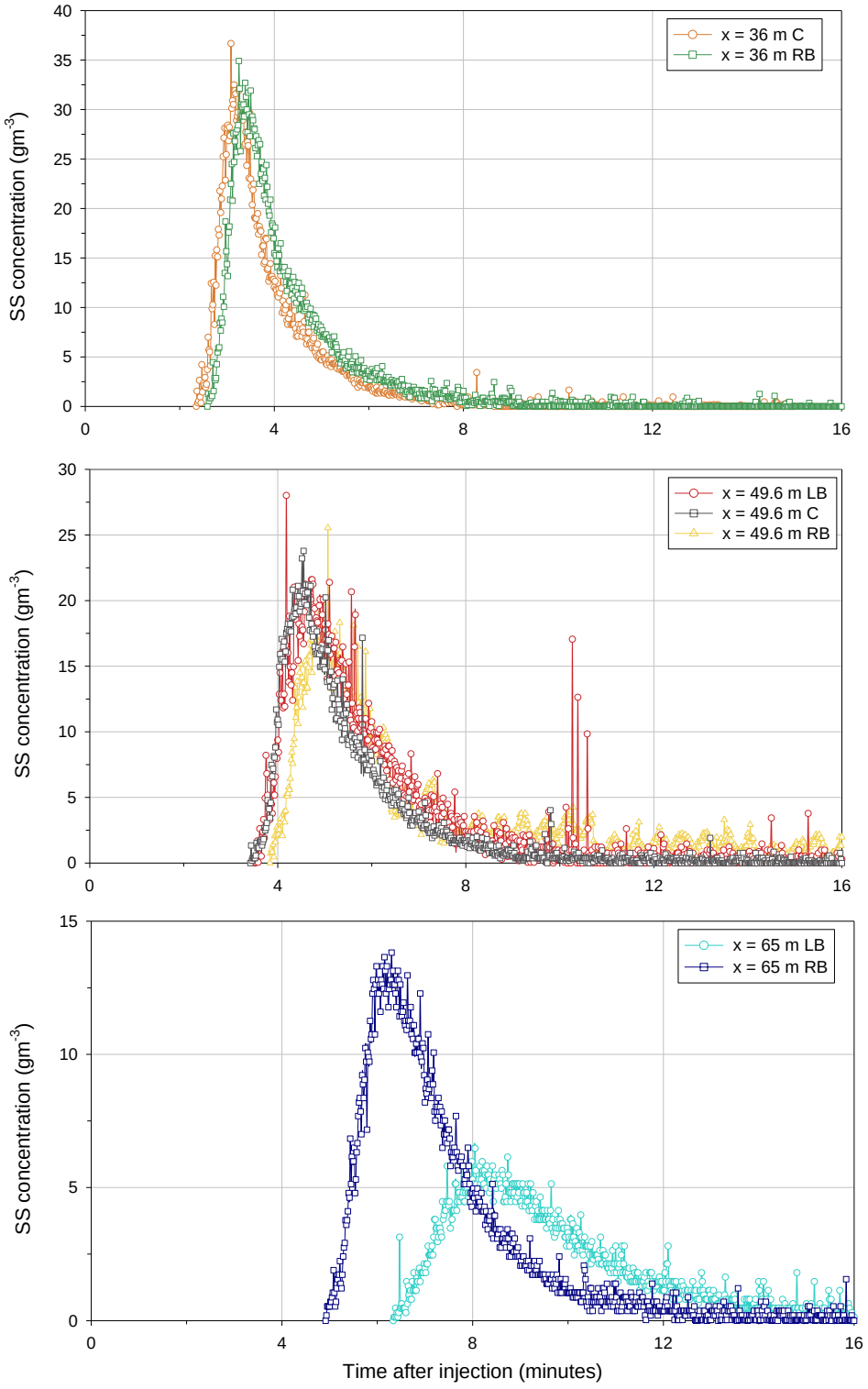

Figure 63. Suspended sediment (0.125-0.25 mm) concentration during run NC-2.2 (note the scale change on both axes).

4.4.4. Dispersion

4.4.4.1. Advective zone length and longitudinal dispersion coefficient

4.4.4.1.1. Runs NC-1.1 to NC-1.3 ($Q = 0.093\ m^3s^{-1}$)

The sodium chloride concentration curves were normalized by their respective peak concentrations (Figure 64). The graphs show that there was a high degree of consistency among all three runs, indicating that dispersion processes were similar.

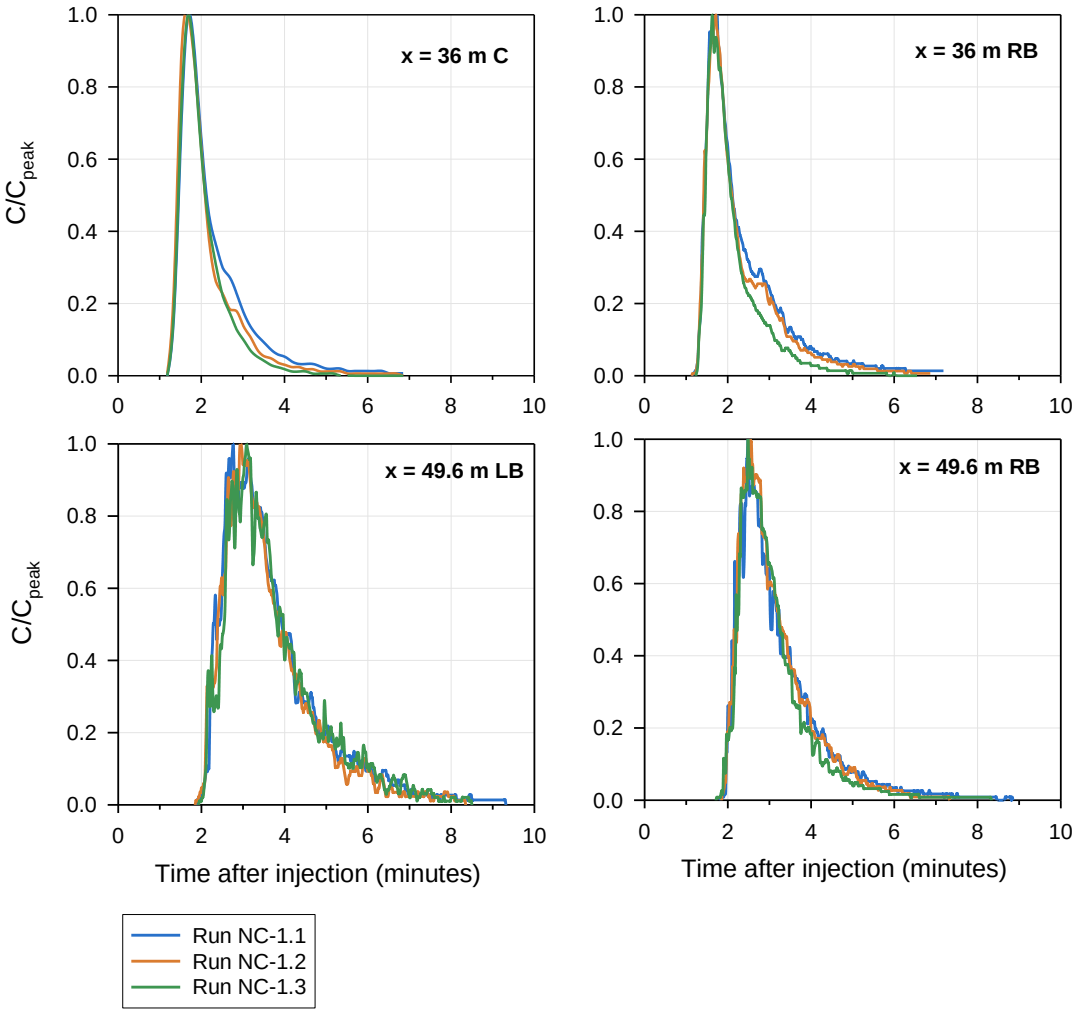

Figure 64. Normalized sodium chloride curves for runs NC-1.1 to NC-1.3.

Unfortunately, the advective zone length estimates based on Equation 65 varied between 11 and 2034 m (Table 51), so it is difficult to judge whether measurements were taken within the advective zone or not. Therefore, as it was done in the concrete and semi-natural channels, the

tracer data were analyzed to define which sampling locations were located in the advective or the equilibrium zones.

Table 51. Estimates of the advective zone length in the concrete channel based on the minimum and maximum empirical coefficients reported in the literature (Rutherford 1994; Sharma and Ahmad 2014).

β	**E_y (m^2s^{-1})**	**α**	**L_x (m)**
0.13	0.0012	0.2	407
		1	2034
4.65	0.0442	0.2	11
		1	57

The Hayami solution of the one-dimensional ADE (64) was utilized to estimate a longitudinal dispersion coefficient value for each sodium chloride injection. Unfortunately, this proved difficult because the average flow velocity was not capable of reproducing the start and peak times of the plumes (Figure 65) suggesting that the observations were made in the advective zone. Thus, instead of the mean flow governing the transport of the plume, most of the sodium chloride was carried in the faster flow of the thalweg. The calculated Peclet numbers were all very large (>10), confirming that advection dominated over dispersion at these locations (Table 52). Therefore, it is clear that the advection zone length is longer than 49.6 m for the estimated discharge conditions, $Q = 0.093\ m^3s^{-1}$, and it is not reliable to estimate an equilibrium longitudinal dispersion coefficient based on these runs.

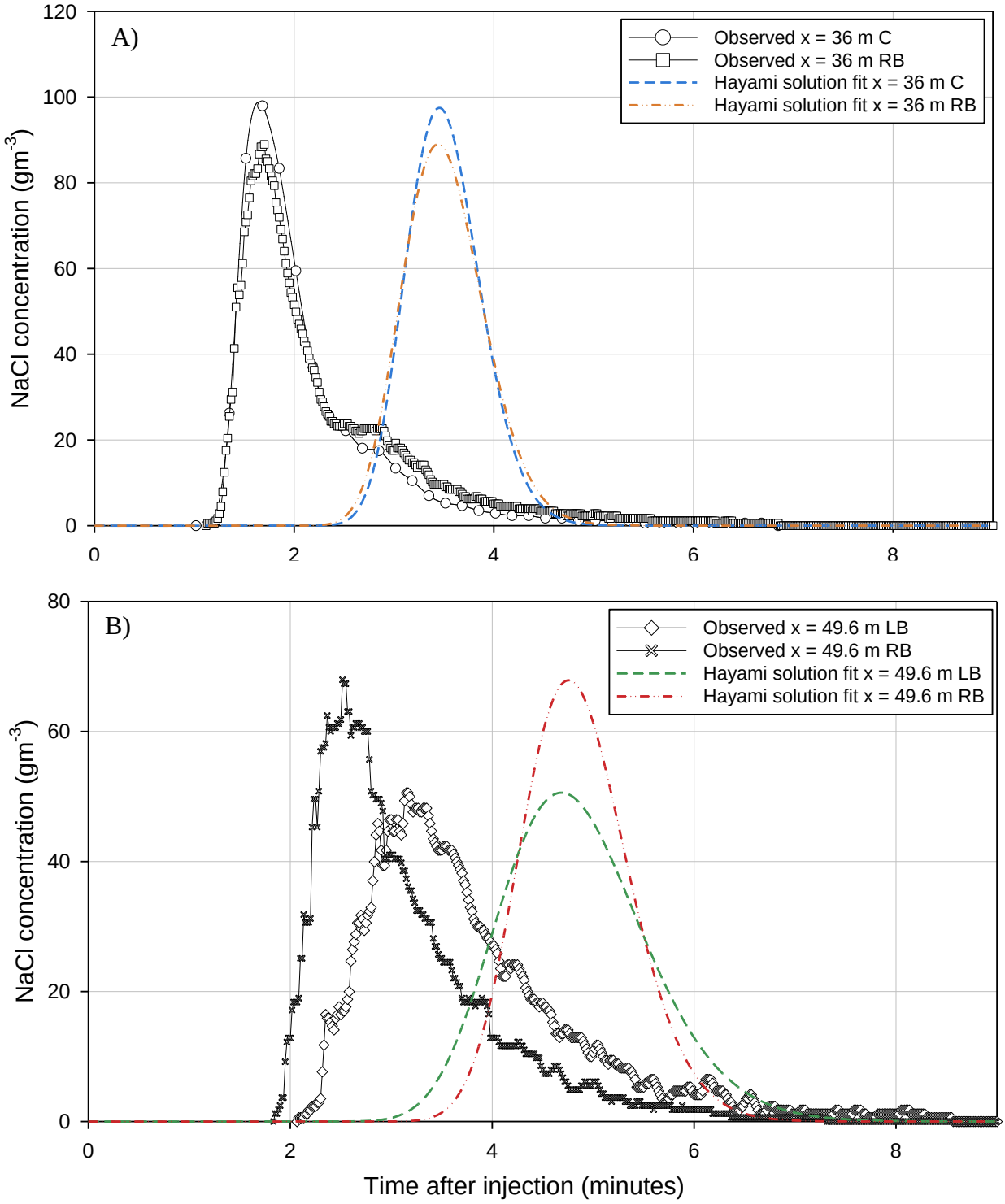

Figure 65. Modeled sodium chloride curves utilizing the Hayami solution fit based on the peak concentration versus observed data (run NC-1.2) (note the scale change on the y-axis). A) 36 m downstream of the injection line; B) 49.6 m downstream of the injection line.

Table 52. Longitudinal dispersion coefficients estimated using the Hayami analytical solution fit on the sodium chloride concentration curves observed in the natural channel and the respective Peclet numbers.

Location (m)	K_x					Pe				
	NC-1	NC-2	NC-3	Average	CV (%)	NC-1	NC-2	NC-3	Average	CV (%)
36 C	0.04	0.03	0.03	0.03	17	19	22	23	21	10
36 RB	0.05	0.04	0.03	0.04	25	16	19	23	19	18
49.6 LB	0.10	0.09	0.12	0.10	15	7	8	6	7	14
49.6 RB	0.05	0.05	0.05	0.5	0	15	15	15	15	0

CV = coefficient of variation (standard deviation/average).

4.4.4.1.2. Runs NC-4 to NC-6 (Q = 0.042 m^3s^{-1})

The sodium chloride concentration curves were normalized by their respective peak concentrations (Figure 66). The graphs show that the plume during run NC-2.6 was slightly faster than previous runs at all sampling locations. This was also the case for the sediment plumes. Despite differences in travel time, the shapes of the curves were similar at each sampling location indicating that the dispersion processes were similar during all the runs.

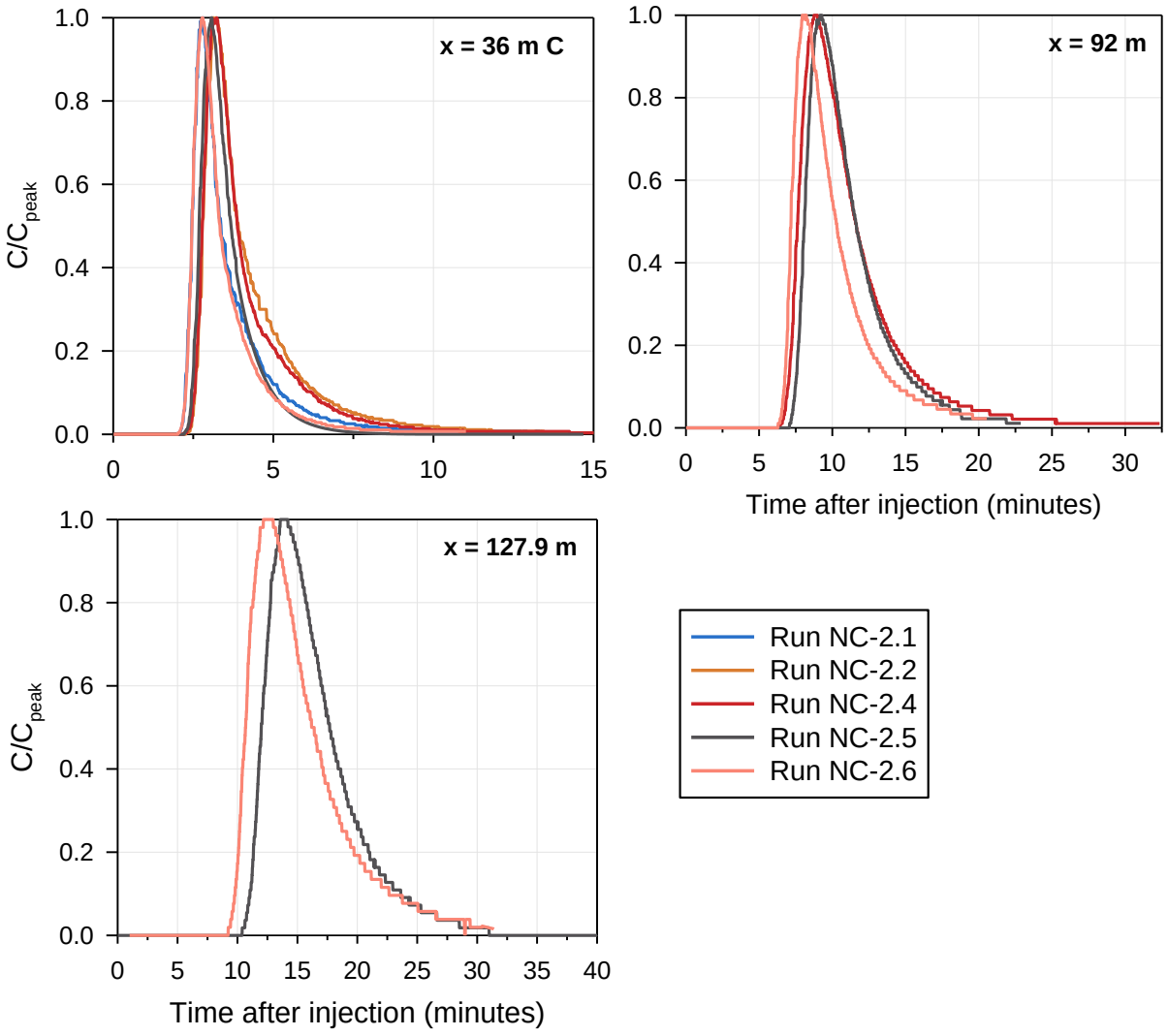

Figure 66. Normalized sodium chloride curves during runs NC-2.1 and NC-2.6 (note the scale change on the x-axis).

The estimates of the advective zone length obtained with Equation 65 varied between 7 and 1302 m (Table 53), so it is difficult to judge whether measurements were taken within the advective zone or not. Therefore, the tracer data were analyzed to define which sampling locations were located in the advective or the equilibrium zones.

Table 53. Estimates of the advective zone length in the concrete channel based on the minimum and maximum empirical coefficients reported in the literature (Rutherford 1994; Sharma and Ahmad 2014).

β	E_y (m^2s^{-1})	α	L_x (m)
0.13	0.0009	0.2	260
		1	1302

β	E_y (m^2s^{-1})	α	L_x (m)
4.65	0.0312	0.2	7
		1	36

The Hayami solution of the one-dimensional ADE (64) was utilized to estimate the longitudinal dispersion coefficient for each sodium chloride injection following the methodology introduced in 3.5. The results indicate that a single longitudinal dispersion coefficient is not capable of reproducing the concentrations observed at all three sampling locations, given that the values increased by approximately two orders of magnitude between the upstream and the farthest downstream sampling locations. The longitudinal dispersion coefficient increases in the downstream direction (Figures 67 and 68). The average flow velocity underestimates both, the start time and peak time at 36 m downstream of the injection. At 92 and 127.9 m, the average flow velocity has a better agreement with the centroid velocity of the curves. The longitudinal dispersion coefficient increases, on average, from <0.1 m^2s^{-1} to 0.17 m^2s^{-1} at 92 m downstream of the injection, and again to 0.31 m^2s^{-1} at 127.9 m. At 222 m (run NC-2.4), the average flow velocity overestimated the arrival of the plume by over 16 minutes (Figure 67). Both plumes, sodium chloride and suspended sediment, were moving at a velocity slower than the average flow velocity at this section, suggesting that the characteristics of the flow have changed between 127.9 m and 207/222 m. With the average flow velocity, the longitudinal dispersion coefficient required to replicate the observed peak would be 1.6 m^2s^{-1}.

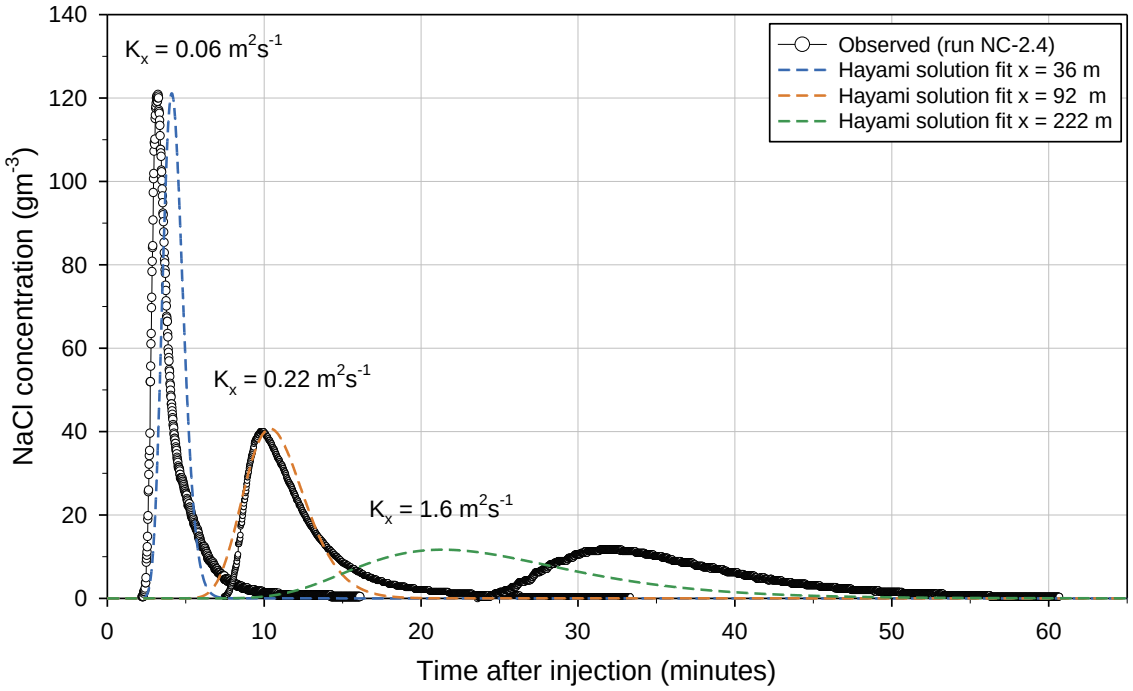

Figure 67. Longitudinal dispersion coefficients obtained for the sodium chloride curves utilizing the Hayami analytical solution of the one-dimensional ADE (run NC-2.4).

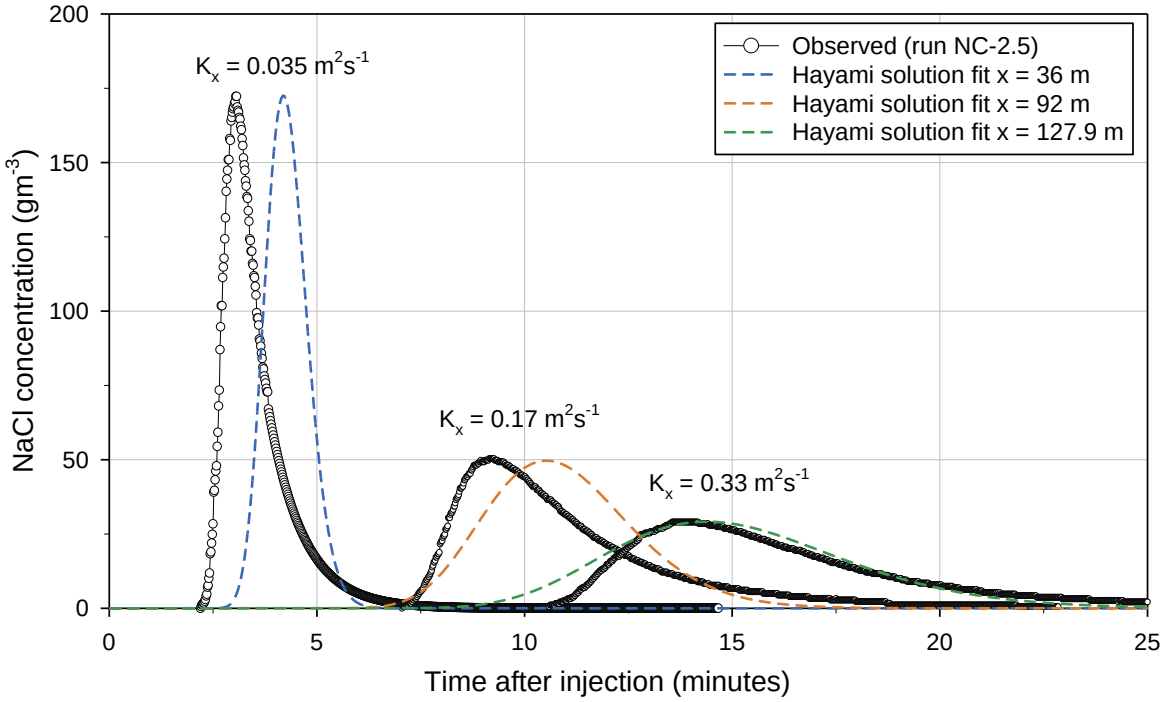

Figure 68. Longitudinal dispersion coefficients obtained for the sodium chloride curves utilizing the Hayami analytical solution of the one-dimensional ADE (run NC-2.5).

Table 54. Longitudinal dispersion coefficients estimated using the Hayami analytical solution fit on the concentration curves observed in the natural channel (Q = 0.042 m^3s^{-1}).

Location (m)	K_x (m^2s^{-1})							
	NC-2.4	NC-2.5	NC-2.6	NC-2.7	NC-2.8	NC-2.9	Average	CV (%)
36 LB	-	-	-	0.05	0.08	-	-	-
36 C	0.06	0.04	0.04	0.04	0.07	-	0.05	30
36 RB	-	-	-	0.05	0.08	-	-	-
49.6 LB	-	-	-	-	-	0.12	-	-
49.6 C	-	-	-	-	-	0.10	-	-
49.6 RB	-	-	-	-	-	0.16	-	-
92	0.22	0.16	0.13	-	-	-	0.17	26
127.9	-	0.33	0.31	-	-	-	-	-
222	1.6	-	-	-	-	-	-	-

CV = coefficient of variation (standard deviation/average).

The Peclet number decreases from approximately 10 at 36 m downstream of the injection line, to approximately 1.7 at 127.9 m, suggesting that advection and dispersion have reached equilibrium at this location. The Peclet number further decreases to 0.4 at 222 m, however, the average flow velocity obtained from the hydraulic model does not seem capable of reproducing the advection velocity of the plume at this location. The modeled peak time starts approximately 10 minutes before the observed peak during run NC-2.4, while during runs NC-2.5 and NC-2.6 the differences are of less than a minute. Therefore, the apparent longitudinal dispersion coefficient is not correct.

Table 55. Peclet numbers calculated based on the apparent longitudinal dispersion coefficient values obtained for the natural channel.

Location (m)	Pe							
	NC-4	NC-5	NC-6	NC-7	NC-8	NC-9	Average	CV (%)
36 LB	-	-	-	9.9	9.9	-	-	-
36 C	8.6	15.2	14.8	12.1	12.6	-	11.7	33
36 RB	-	-	-	11.6	10.9	-	-	-
49.6 LB	-	-	-	-	-	6.6	-	-
49.6 C	-	-	-	-	-	7.8	-	-
49.6 RB	-	-	-	-	-	7.1	-	-
92	2.5	3.5	4.3	-	-	-	3.4	27
127.9	-	1.5	1.6	-	-	-	-	-
222	0.4	-	-	-	-	-	-	-

CV = coefficient of variation (standard deviation/average).

Based on the results shown in Table 55, it will be assumed that the first three sampling locations (36 m, 49.6 m, and 92 m) are located within the advective zone because the average Pe > 2.5. The concentration curves measured at these locations cannot be utilized to provide reliable estimates of the longitudinal dispersion coefficient, and neither can the curves be compared with modeled curves. Only the observed data located at 127.9 m can be used to estimate the longitudinal dispersion coefficient using the Hayami solution (66). Other methods to estimate the longitudinal dispersion coefficient, such as the method of moments and the routing procedure, cannot be utilized because there is only one observation location.

4.4.4.2. Suspended sediment

In order to determine if sediment particles were carried in suspension, the sediment transport mode was estimated based on the Rouse Number. The analysis was conducted utilizing the average results for shear velocity and flow depth from the HEC-RAS model. The results demonstrate that the flow was capable of carrying all the studied particle sizes in suspension, therefore, the ADE approach should be applicable to model the concentration curves (Table 56).

Table 56. Sediment transport mode classification in the natural channel.

Run	Sediment size (mm)	Estimated D_{50} (mm)	Water temperature (°C)	ω (ms^{-1})	Rouse number	$u_*\omega^{-1}$	Mode of sediment transport
NC-1.1	<0.075	0.063	18.5	0.0017	0.05	53.57	Suspension
NC-1.2	0.075-0.125	0.097		0.0022	0.06	40.99	
NC-1.3	0.125-0.25	0.177		0.0031	0.08	29.50	
NC-2.1	0.075-0.125	0.097	15.1	0.0023	0.07	35.40	
NC-2.2	0.125-0.250	0.177		0.0031	0.10	25.47	
NC-2.3	0.250-0.500	0.354		0.0044	0.14	18.00	
NC-2.4	<0.075	0.063		0.0017	0.05	46.26	
NC-2.5	0.075-0.125	0.097		0.0023	0.07	35.40	
NC-2.6	0.125-0.25	0.177		0.0031	0.10	25.47	

A comparison between the concentration curves of sodium chloride and suspended sediment normalized by their respective peak concentrations at 36 m, 92 m, and 127.9 m downstream of the injection, shows that the curves have essentially the same start time and peak times (Figure 69). At 36 m, the sodium chloride and suspended sediment curves had similar shapes for the duration

of the time series. However, the concentrations of suspended sediment in the tail decreased in comparison to sodium chloride, suggesting that some sediment settling or transient storage had occurred upstream.

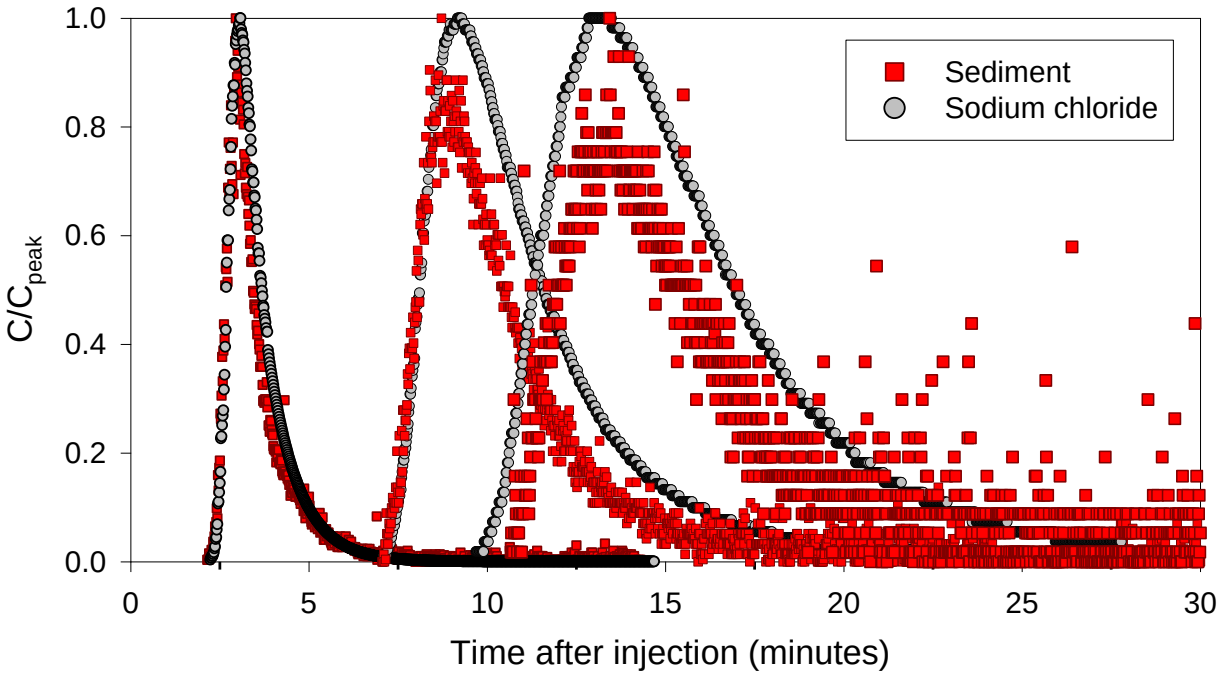

Figure 69. Normalized concentration curves of sodium chloride and sediment measured at 36 m, 92 m, and 127.9 m downstream of the injection line in the natural channel (run NC-2.5).

The shapes of the normalized curves indicate that sediment particle dispersion was similar to the dispersion of sodium chloride. Therefore, the equilibrium longitudinal dispersion coefficients estimated based on the sodium chloride concentration curves were applied to model the suspended sediment injections. The suspended sediment settling rates were obtained utilizing the Hayami solution of the one-dimensional ADE with a settling rate (102) on the curves located at 127.9 m, initially. The specific longitudinal dispersion coefficients for each run rather than the average one were utilized for this process in order to eliminate errors related to this parameter while obtaining the settling rates. The settling rates were adjusted by trial and error in order to provide the closest agreement with the total recovered mass observed for each run while maintaining the longitudinal dispersion coefficient fixed. The estimated settling rates were calculated based on the methodology described on 3.3.2. The results show that the longitudinal dispersion coefficient and the settling

rate are also capable of predicting the curves located at 115.9 m well. This indicates that the equilibrium zone started somewhere between 92 m and 115.9 m downstream of the injection line. The observed settling rate increased slightly with increased particle size between runs NC-2.4 and NC-2.5 (Table 57). The fact that a single settling rate is capable of predicting the curves at 115.9 m and 127.9 m in the natural channel might suggest that the settling rate became a constant in the equilibrium zone, as indicated by the theory. However, given the proximity of the two sampling locations, it is also possible that there was just not enough time for the settling rate to change between 115.9 m and 127.9 m. The estimated settling rates were calculated using Equation 101. Similar to the concrete channel, for all runs, the observed settling rates are smaller than the estimated values, which means that the sediment was settling at a slower rate than estimated or that previously deposited particles were being resuspended by the flow, reducing the net sediment loss (Figure 70).

Table 57. Settling rates (observed and estimated) according to sediment size in the natural channel (Q = 0.042 m^3s^{-1}).

Run	Location (m)	Sediment size (mm)	Estimated D_{50} (mm)	Estimated settling rate (s^{-1})	Observed settling rate (s^{-1})	Estimated - observed (s^{-1})
NC-2.5	115.9	0.075-0.125	0.097	0.028	0.0033	0.025
	127.9					
NC-2.6	115.9	0.125-0.25	0.177	0.039	0.0040	0.035
	127.9					

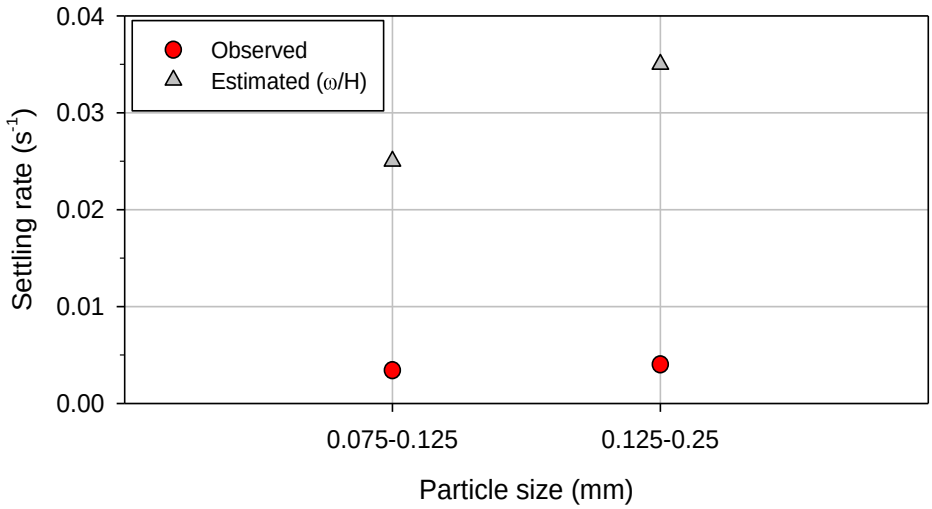

Figure 70. Observed and estimated settling rates of suspended sediment according to particle size in the natural channel (Q = 0.042 m^3s^{-1}).

The observed and estimated settling rates were applied to model the suspended sediment injections (Figure 71). Based on the estimated settling rates, the modeled curves would have zero concentration at 115.9 m. Similar to the concrete channel results, this was clearly not the case, suggesting that the use of estimated settling rates for problems of plume dispersion is an unreliable approach.

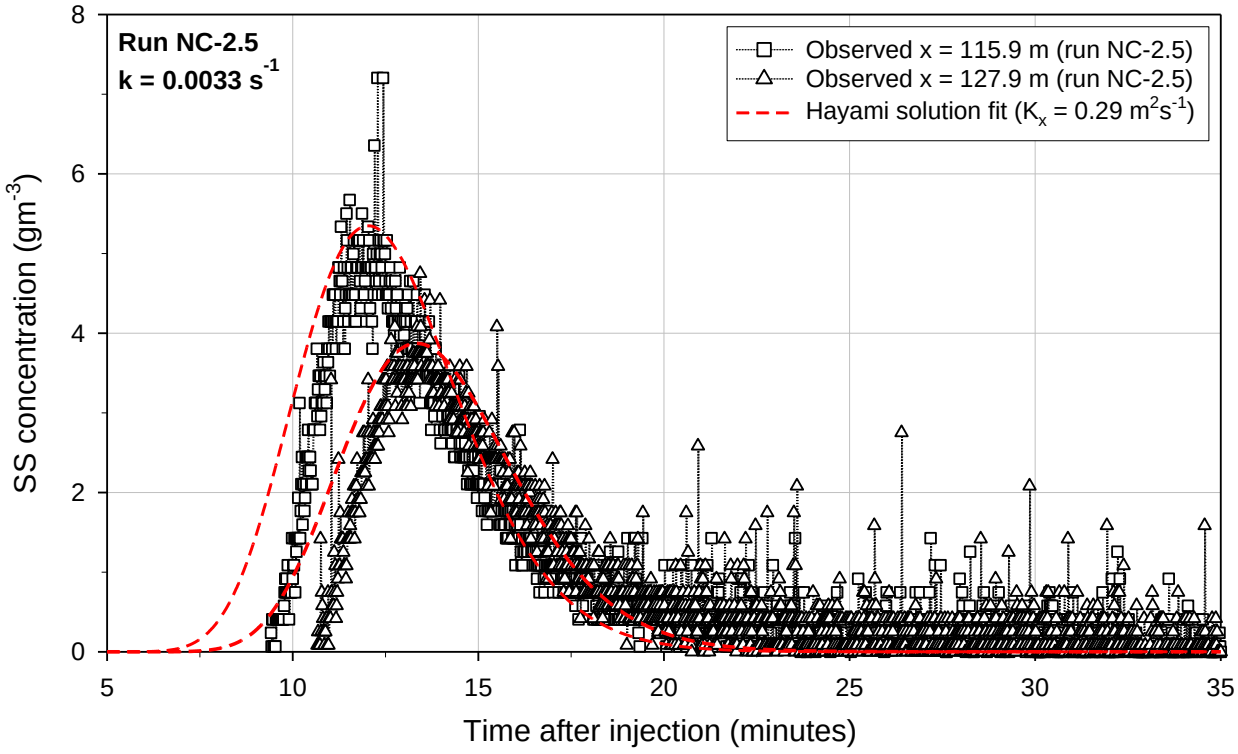

Figure 71. Suspended sediment concentration curves: observed data versus modeled curves utilizing the longitudinal dispersion coefficients determined by the Hayami solution fit and the observed settling rate (run NC-2.5).

4.4.4.3. Quantifying the accuracy of predictive formulas for K_x

All of the 26 predictive formulas in Table 1 were utilized to estimate the longitudinal dispersion coefficient based on the average characteristics of the flow (Table 43). The sinuosity factor for the reach between the injection line and 127.9 m downstream for the formula of Sahay (2013) was estimated as Si = 1.54. The maximum value was estimated by formula 2 from Kashefipour and Falconer (2002), K_x = 19.9 m^2s^{-1}. On the other hand, the smallest value was predicted by the Ribeiro et al. (2010) formula, where K_x = 0.01 m^2s^{-1}.

Table 58. Longitudinal dispersion coefficients for the natural channel estimated from predictive formulas ($Q = 0.042\ m^3s^{-1}$).

Reference	**K_x**
Ribeiro et al. (2010)	0.01
Seo & Cheong (1998)	0.02
Elder (1959)	0.04
Deng et al. (2001)	0.04
McQuivey and Keefer (1974)	0.06
Taylor (1954)	0.07
Disley et al. (2015)	0.07
Sattar & Gharabaghi (2015) (Formula 1)	0.10
Parker (1961)	0.19
Kashefipur & Falconer (2002) (Formula 1)	0.23
Devens (2006)	0.25
Fischer (1975)	0.38
Alizadeh et al. (2017)	0.39
Kashefipur & Falconer (2002) (Formula 2)	0.43
Li et al. (2013)	0.62
Sahay (2013)	0.84
Wang and Huai (2016)	0.92
Wang et al (2017)	0.96
Zeng & Huai (2014)	0.96
Sahay & Dutta (2009)	0.99
Etemad-Shahidi and Taghipour (2012)	1.55
Sattar & Gharabaghi (2015) (Formula 2)	1.90
Liu (1977)	2.71
Oliveira et al. (2017)	3.51
Iwasa & Aya (1991)	3.61
Koussis & Mirassol (1998)	6.84

The estimated longitudinal dispersion coefficients were applied to the Hayami analytical solution (64) to predict the sodium chloride curves at 127.9 m downstream of the injection location (Figure 72). The results show that 11 out of the 26 formulas tested overestimated the concentration, while the remainder underestimated the concentration.

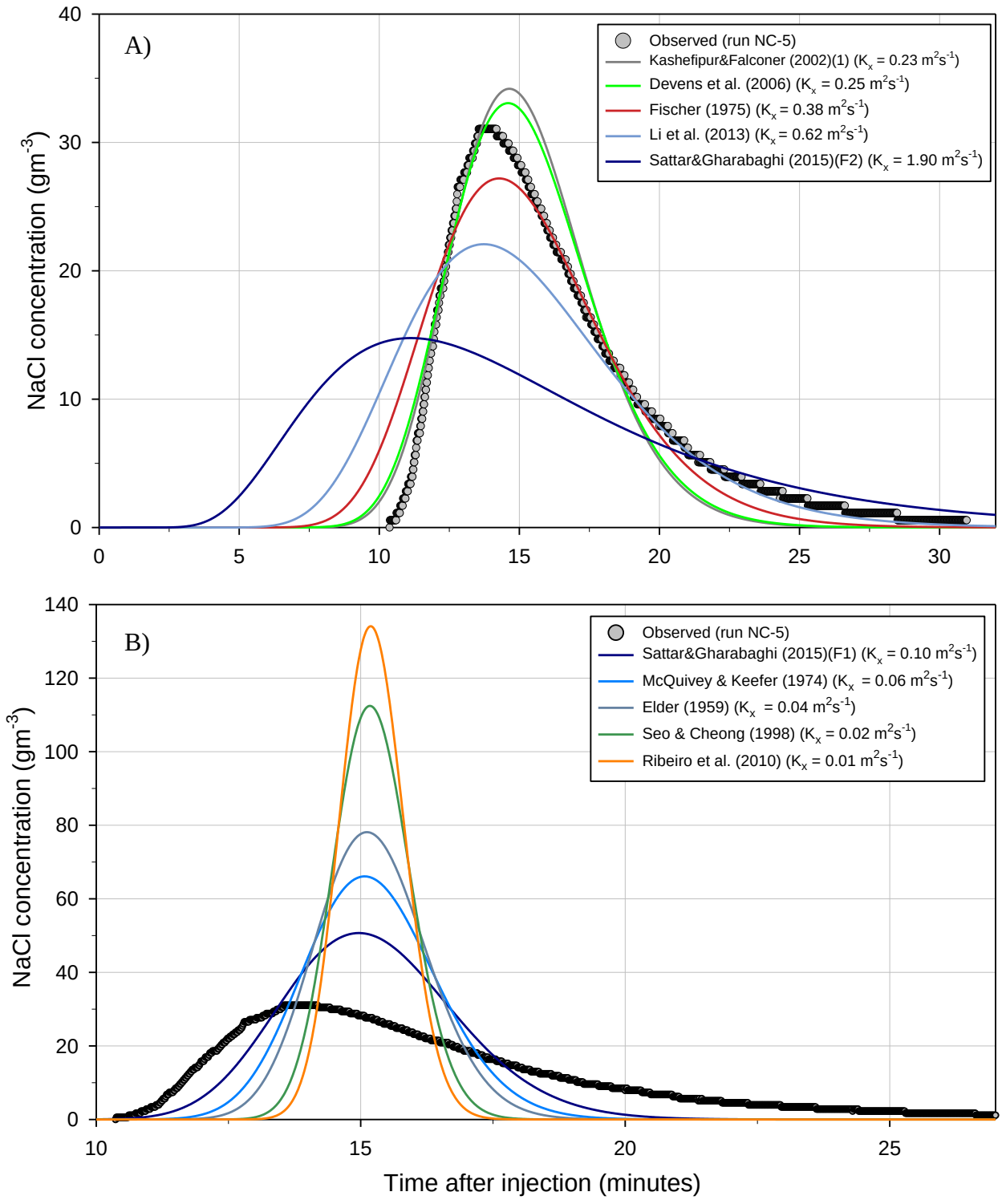

Figure 72. Modeled concentration curves utilizing the longitudinal dispersion coefficients obtained from predictive formulas (note the change in scale on the axes). A) Coefficients that underestimated the peak concentration; B) Coefficients that overestimated the peak concentration.

Chapter 5: Discussion

The overarching purpose of the thesis research was to better understand the dynamics of sediment plume dispersion in small streams. Two primary hypotheses were proposed. The first was with regard to the applicability of the one-dimensional ADE with a sink term to model suspended sediment dispersion in small channels. Four sub-questions were proposed in case the alternative hypothesis, that the one-dimensional ADE with a sink term is capable of reproducing observed suspended sediment plumes with ±50% accuracy, was considered. The sub-questions were established to investigate: (i) the importance of the sink term in simulating suspended sediment plume dispersion; (ii) the locations where the one-dimensional ADE applied in the studied reaches; (iii) the importance of the lateral velocity and concentration gradients; and (iv) the importance of transient storage effects. The second hypothesis was related to the applicability of the predictive formulas for the longitudinal dispersion coefficient to small channels. The results presented in Chapter 4 provide the basis for the synthesis and discussion in this chapter, which ultimately leads to the acceptance or rejection of the null hypotheses.

5.1. Modeling suspended sediment dispersion in small channels with the one-dimensional ADE

In Chapter 4, it was shown that one-dimensional ADE appears to be applicable to model suspended sediment dispersion in small channels (see Figures 40 and 71). These results lead to a consideration of the alternative hypothesis (H1a), which suggests that the one-dimensional ADE with a sink term is capable of reproducing observed suspended sediment plumes to an acceptable degree of accuracy. Specifically, the next section will examine the alternative hypothesis H1a as well as the sub-questions established in Chapter 1.

5.1.1. Assessing the accuracy of the one-dimensional ADE in the equilibrium zone

The first research question was with respect to the degree of accuracy that the one-dimensional ADE is able to reproduce suspended sediment plumes. The sodium chloride data were utilized to parameterize the longitudinal dispersion coefficient because sodium chloride is a soluble substance, and assumed to be conservative (i.e., no settling or decay). The sodium chloride curves

sampled in the equilibrium zone were compared with the observed data to provide some insight into the general accuracy of the one-dimensional ADE in small channels. The longitudinal dispersion coefficients obtained from the sodium chloride data were then utilized to model the sediment injections.

5.1.1.1. Sodium chloride

The modeled sodium chloride concentration curves were compared with the observed data utilizing the relative percent error (Equation 123). Three parameters were utilized to evaluate the accuracy of the model: the peak time, start time, and duration of the curves. Since the peak concentration was utilized to obtain the longitudinal dispersion coefficient through a best-fit analysis, this parameter was not considered in the assessment of the accuracy of one-dimensional ADE in the equilibrium zone.

For the concrete and the natural channels, the modeled and observed start and peak times were very similar for all runs (Table 59). For 9 of 11 runs, there was excellent agreement (± 25% accuracy) between measured and modeled curves. The observed curves were consistently more skewed than the modeled curves, with the observed curves starting slightly later than the modelled curves but the observed peaks arriving slightly earlier than the modeled peaks. The percentage errors in peak time and start time were slightly smaller in the concrete channel than for the natural channel, indicating that the heterogeneity of the natural channel (e.g., vegetation, gravel bars, meandering thalweg, etc.) can lead to additional complications in the advection-dispersion process, reducing the goodness of fit to the theoretical model.

Plume duration was predicted with the least accuracy for both channel types, with consistent underestimation in 10 out of 11 runs. The modeled curves did not reproduce the long tails of the observed curves, and therefore, the observed duration is longer than modeled. The long tails are a common feature of observed data and have been reported on several previous studies. Taylor (1954) and Elder (1959) attributed the long tails to tracer storage in the boundary layer when working with pipe flow and a laboratory flume, respectively. On natural channels, however, the most common causes include i) the effects of velocity shear in the advective zone that have not disappeared yet, as reported by Rutherford (1994), and ii) transient storage effects (Launay et al. 2015; Rutherford 1994; Schmid 2002). Launay et al. (2015), for example, also observed some

skewness in curves from fluorescent tracers in a concrete channel, where transient storage is unlikely to occur. Hence, not all skewness on data from natural channels should be attributed to transient storage effects.

Table 59. Relative error between the modeled and observed sodium chloride concentration curves in the concrete and natural channels (equilibrium zone).

Run	Location (m)	Relative error (%) $\frac{\text{Modeled value} - \text{observed value}}{\text{Observed value}}$				Level of agreement
		C_{peak}	t_{peak}	t_{start}	Duration	
CC-1	370.15	0	3	-5	-13	E
CC-2		-	-	-	-	-
CC-3		0	3	-7	-21	E
CC-4		0	4	-5	-25	E
CC-5		0	3	-7	-55	F
CC-6		0	3	-7	6	E
CC-7		0	2	-12	-47	G
CC-8		0	4	-8	-43	G
CC-9		0	3	-8	-40	G
NC-2.4	222	72	-24	-35	-39	F
NC-2.5	127.9	0	6	-26	-61	F
NC-2.6^{ET}	127.9	0	19	-15	-14	E

Run NC-2.4 was particularly unusual in the lack of fit between modeled and observed curves. Applying the average equilibrium longitudinal dispersion coefficient of the natural channel (K_x = 0.32 m^2s^{-1}) to run NC-2.4, leads to an overestimation of 72% of the peak concentration at 222 m downstream of the injection line. Even though this sampling location is located in the equilibrium zone according to the analysis conducted in 4.4.4.1.2, the average flow velocity decreased between 127.9 m and 222 m. This was the section of the stream where some of the flow was diverted through the levee and into a side channel. In addition to the loss of discharge from the main channel, there were many roughness elements such as woody debris, vegetation, and gravel bars that decreased the flow velocity in this section (Figure 72). The reach averaged velocity used in the model did not accommodate this increased roughness, thus yielding a poor fit.

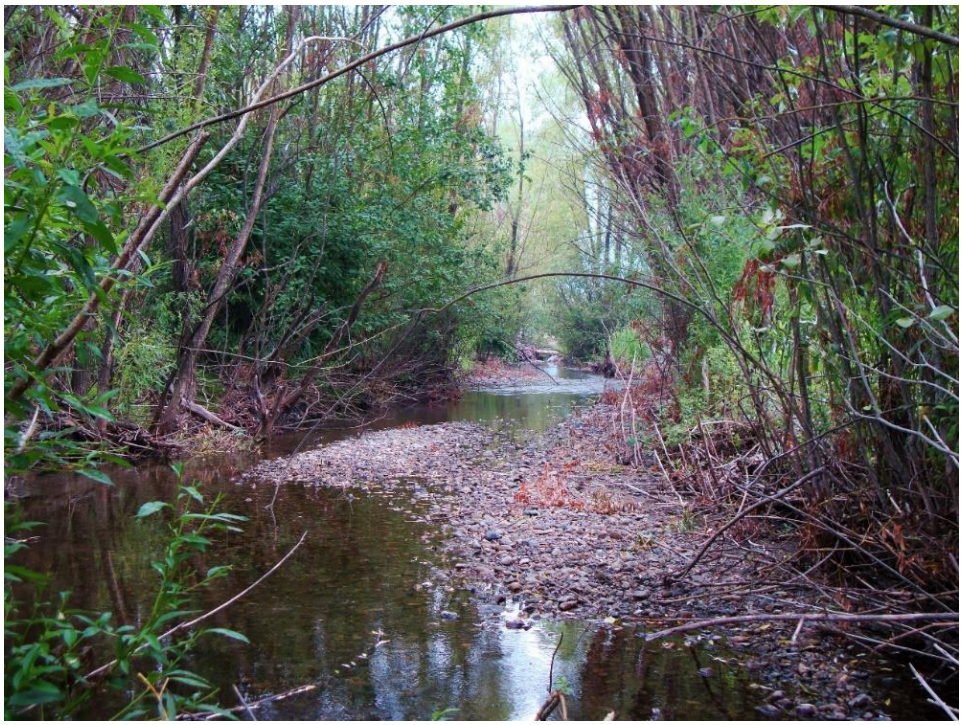

Figure 73. Natural channel view near cross-section 14 (222 m), looking upstream.

The relative errors shown in Table 59 suggest that the one-dimensional ADE is able to provide good results in small channels if a correct value of the longitudinal dispersion coefficient is coupled to robust estimates of the average flow velocity in the channel. The peak concentrations and the initial part of the curves can be modeled with excellent accuracy while the trailing limbs of the curves cannot. Similar results have been reported in the literature. Ani et al. (2009) found that, based on a calibrated model, the peaks were the best-predicted parameter, while the trailing limbs were the least well-predicted parameter.

These results suggest that, despite its limitations, the one-dimensional ADE is capable of providing accurate results in small natural channels without the inclusion of extra terms to account for transient storage, as it has been suggested previously in the literature (e.g., Ani et al. 2009; Karwan and Saiers 2009; Launay et al. 2015). However, if accurate predictions of plume duration are required, the results suggest that a more robust model is necessary in order to reproduce the skewness and long tails of the plumes. The duration of the plumes is particularly important when assessing water quality for aquatic biota (Bilotta and Brazier 2008), given that a certain

concentration over a short time might not be detrimental for the organisms, but smaller concentrations during long periods of time might.

5.1.1.2. Suspended sediment

The equilibrium longitudinal dispersion coefficients obtained from the sodium chloride curves were used in the subsequent analysis of the suspended sediment plumes. Settling rates were determined from the suspended curves sampled in the equilibrium zone (see Table 27 and 57). The resulting error analysis between modeled and observed curves is summarized in Table 60.

The one-dimensional ADE was capable of predicting the peak concentration, peak time, and start time of the observed suspended sediment curves in the concrete and natural channels with excellent to good agreement (Table 60).

Table 60. Relative error between the modeled and observed suspended sediment concentration curves in the concrete and natural channels.

Run	Location (m)	Relative error (%) $\frac{\text{Modeled value} - \text{observed value}}{\text{Observed value}}$			Level of agreement
		C_{peak}	t_{peak}	t_{start}	
CC-1	370.15	-	-	-	-
CC-2		-8	1	-3	E
CC-3		15	2	-1	E
CC-4		4	5	-4	E
CC-5		3	2	-8	E
CC-6		0	2	-7	E
CC-7		-3	0	-9	E
CC-8		30	-1	-5	G
CC-9		21	-1	-8	E
NC-2.5	115.9	-26	-2	-31	G
NC-2.5	127.9	-19	-1	-30	G
NC-2.6	115.9	-24	12	23	E
NC-2.6	127.9	-32	18	-1	G

Part of the error in the peak concentration values might be associated with the dynamics of suspended sediment transport in turbulent flows. The interaction between the settling tendency of

the particles and the flow turbulence that sustains them in suspension is likely to be spatially random and variable from one run to another. This would be particularly true in the natural channel, which may explain why the peak concentration was consistently underestimated in the natural channel, but not in the concrete channel. Similar to the sodium chloride plumes, the observed peak times were slightly faster than the modeled, and the observed suspended sediment plumes started later compared to the modeled ones. Also, the errors in peak time and start time were slightly smaller in the concrete channel.

Although the exact duration of the suspended sediment curves could not be determined reliably, the tails of the plumes can be visually compared with the tails of the sodium chloride curves. The results from the concrete channel showed that the sediment plumes from particles up to 0.125-0.25 mm in size had very similar tails as the sodium chloride (Figure 38). This indicates that skewness caused by the shear and any possible transient storage was similar for the sediment particles and the sodium chloride. For the fractions 0.25-0.5 mm and 0.5-1 mm, however, the plumes had tails that were more pronounced than the sodium chloride (i.e., normalized concentrations above the normalized sodium chloride concentrations). This might suggest i) the development of more pronounced concentration gradients in the case of coarser particles, where a larger volume of particles is moving closer to bed in comparison with the sodium chloride, which is dissolved in fluid and supposedly evenly distributed in the vertical direction, and ii) the fact that sediment particles previously deposited on the bed were being resuspended from bed or moving in saltation, hence also being measured by the turbidity sensors. Similar results have been reported by Sayre and Chang (1968), who reported longer tails on coarser particles (53-62 μm) plumes than on fine particles plumes (<44 μm) when analyzing dispersion on a laboratory flume. According to them, the absence of more pronounced tails on the plumes from fine particles suggests that the turbulence levels were sufficient to prevent the establishment of a negative concentration gradient. The sink term in the one-dimensional ADE is simply a removal term utilized to account for the net loss of sediment particles from the flow and it assumes uniform concentration in the vertical direction as well as no resuspension of the particles. Therefore, the consideration of such factors might be an option to increase the accuracy of tail prediction on suspended sediment plumes.

The use of the one-dimensional ADE to model suspended dispersion assumes that sediment particles have the same velocity as the fluid at a point (Sayre and Chang 1968). However, this is

not particularly true given that non-soluble particles will suffer the effects of drag (i.e., fluid resistance) (Julien 2010). As a consequence, the velocities of the particles are smaller than the velocity of the fluid. This drag effect tends to increase with increasing particle size. The calculated travel times for the sodium chloride and suspended sediment plumes, however, were very similar on both channels (Table 21,22, 47, 48, and 50). Hence, the relative errors for the travel times of the sediment plumes were in the same range as the sodium chloride (±25%) and in the same range for all size fractions studied. This suggests that the drag effects on the study particle sizes were not sufficient to decrease the accuracy of the one-dimensional ADE in comparison to a soluble substance, such as sodium chloride, under the study flow conditions. Sayre and Chang (1968) reported slightly larger travel times for silt size particles (glass beads and natural silt between 53-62 μm) in comparison to the mean flow calculated velocities. However, based on the presented data, the differences were in the range of a few seconds (up to 10 s) and could have been related to measurement uncertainty.

Previous studies have focused on assessing the one-dimensional ADE to model the transport of only very fine particles, where settling is not significant to require the inclusion of a sink term in the one-dimensional ADE. As mentioned in Chapter 2, Sayre and Chang (1968) analyzed dispersion of particles up to 62 μm in size in a laboratory flume, while Karwan and Saiers (2009) focused on the dispersion of titanium dioxide (TiO_2) particles (0.45 μm) in a mountain stream. These results demonstrate that the ADE can also be utilized to model the dispersion of somewhat coarser particles (<0.075 mm to 1 mm) with relatively good agreement with the inclusion of a sink term. Furthermore, the results confirm that longitudinal dispersion coefficients obtained from measurements using a soluble substance, such as sodium chloride, can be applied to the modeling of suspended sediment plumes as long as particle settling is taken into account. Sayre and Chang (1968) and Karwan and Saiers (2009) also compared the dispersion of the particles with the dispersion of a soluble conservative substance and concluded that the dispersion processes were similar.

Overall, these results provide support for rejecting the null hypothesis (H1o) and accepting the alternative hypothesis (H1a), which states that the one-dimensional ADE is capable of predicting the suspended sediment dispersion with at least 50% accuracy as long as the correct parameters are applied to the model.

5.1.2. Particle settling and the sink term

The main difference between the dispersion processes of sodium chloride (a conservative tracer) and suspended sediment (a non-conservative substance) is the potential for loss during transport. For particularly coarse (heavy) materials, there are additional complications having to do with fluid drag and the fact that particle velocities are slower than fluid velocities, but these will be ignored here. Suspended sediment particles have the tendency to settle and be deposited on the channel bed, where they may rest temporarily or permanently. The dynamics of particle settling and resuspension in turbulent flows are important, but not generally considered when applying the one-dimensional ADE to plume dynamics. Sub-question 1.1 was directed at the importance of the sink term when simulating suspended sediment plume dispersion.

The observed suspended sediment recovery rates at 370.15 m downstream of the injection line in the concrete channel (Figure 74) demonstrated that, under the flow conditions of the experiments, only the fine sediment (<0.075 mm) was able to stay in suspension with minimum loss downstream. With increasing particle size, sediment settling was more pronounced. The fraction of sediment that settled on the bed may have been transported as bedload (below the sensing zone of the OBS sensors) or have become trapped in cracks or the bottom roughness elements of the concrete channel as transient storage. In the natural channel, only the finest fraction had recoveries larger than 50% (during Q = 0.093 m^3s^{-1}) (Figure 75A). During Q = 0.042 m^3s^{-1}, no recoveries over 40% were observed (Figure 75B). In the context of water quality management for multiple-use watersheds, these results suggest that fine particles (<0.075 mm – 0.125 mm) are of greatest concern when dealing with suspended sediment plumes under similar flow conditions. Coarser particles settled much faster, even in the concrete channel, which had a large advection velocity, uniform geometry, and minimum transient storage zones when compared to the other channels. These results are, of course, largely dependent on the flow conditions.

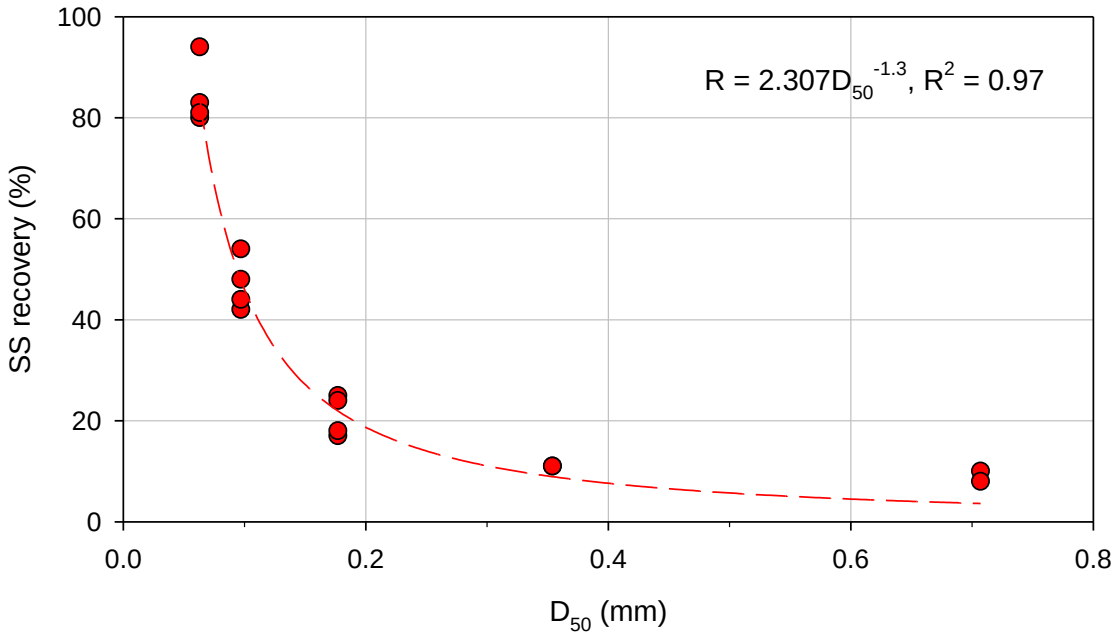

Figure 74. Suspended sediment recovery rates versus D_{50} at 370.15 m downstream of the injection line in the concrete channel.

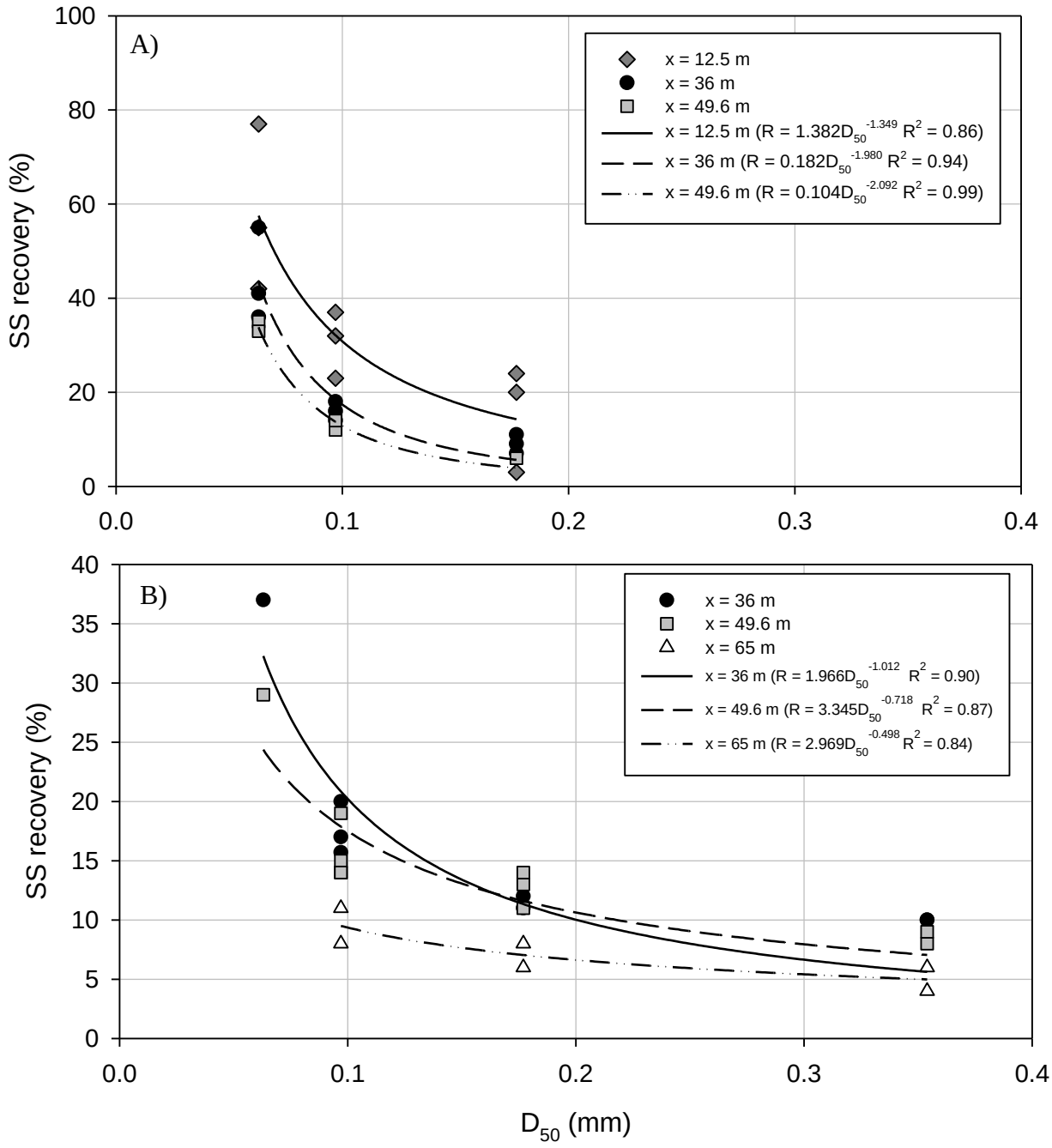

Figure 75. Suspended sediment recovery rates versus D_{50} at different locations downstream of the injection line in the natural channel. A) Q = 0.093 m^3s^{-1}; B) Q = 0.042 m^3s^{-1}.

The curve fitted for the concrete channel consists of measurements conducted in the equilibrium zone (370.15 m downstream of the injection line). The curves fitted for the natural channel include measurements conducted in the advective zone (12.5 m – 65 m downstream the

injection line), given that there were only two (or one) sampling points on each of the remaining locations (including the equilibrium zone). Even so, in both channels, the relationship between the recovery rates and particle size (D_{50}) for a certain location was best described by a power relation. This suggests that the suspended sediment settling mechanism was similar on both channels and it is not affected by the nature of dispersion processes in the advective zone relative to the equilibrium zone.

In the natural channel, the suspended sediment recovery rates for the finest size fractions (<0.075 mm and 0.125-0.25 mm) decreased exponentially with downstream distance under both discharges (Figure 76). A similar result was obtained by Sayre and Chang (1968) while analyzing the dispersion of fine particles (up to 62 μm) in a flume.

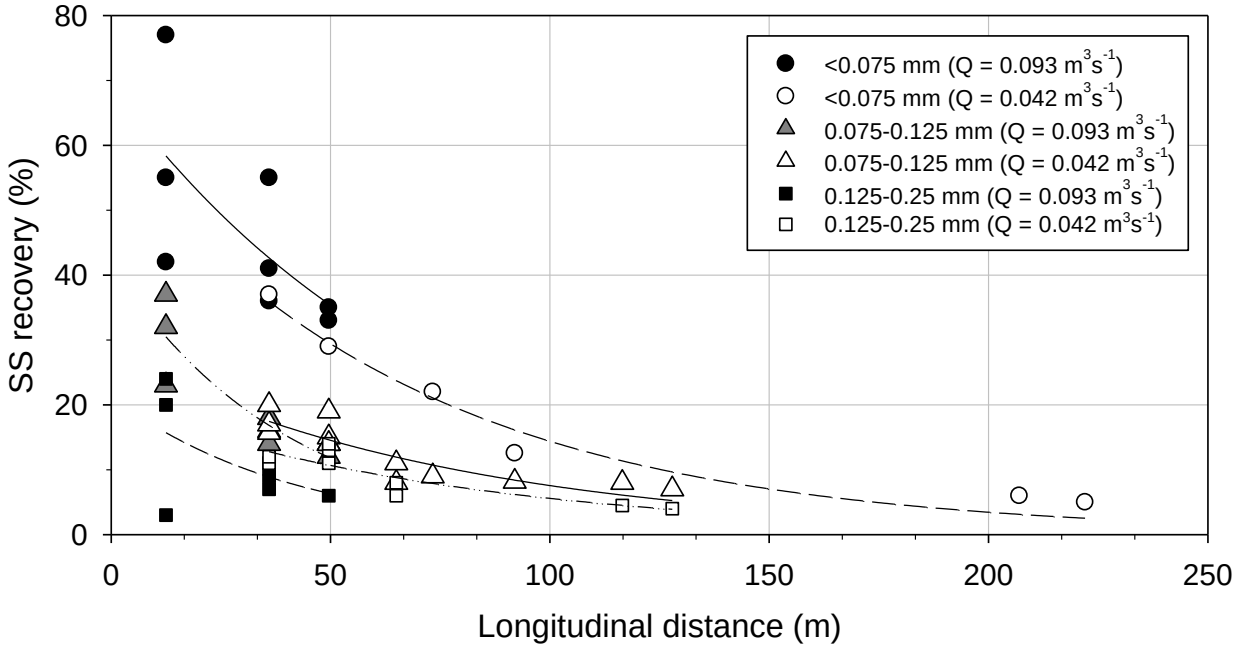

Figure 76. Suspended sediment recovery rates in the natural channel.

For the smallest size fraction (<0.075 mm), the percent recovery was greater for the larger discharge, as would be expected given that the mean flow velocity and turbulence intensity were greater. However, for the slightly coarser fractions (0.075 mm up to 0.25 mm), the recovery rates during Q = 0.042 m^3s^{-1} were similar or larger than the ones observed during Q = 0.093 m^3s^{-1} (Figure 76). There are only a few locations where the data overlap, so this may not be a significant trend. But one potential explanation for this is the fact that the OBS sensors were installed closer

to the bed during Q = 0.042 m^3s^{-1} because of limited water depth. Thus, they would have sampled coarser particles moving closer to the bed in saltation or intermittent bed load.

Several studies in the literature have suggested the use of $k = \omega/H$ and the use of settling velocities from still fluids in order to account for sediment settling when using the advection-dispersion equation (e.g., Chou et al. 2018; Douillet et al. 2001; Göransson et al. 2012; Palu and Julien 2019). The results from this research, however, suggest that such estimated settling rates are not a reliable approach. The percent recovery of suspended sediment provided the basis upon which to estimate an observed settling rate for each plume sampled in the equilibrium zone, as shown in Tables 27 and 57. In both channels (concrete and natural), the estimated settling rates were larger than the observed (Figure 77 and 78). A possible explanation for this is that formulas for the settling velocity of sediment such as the one from Dietrich (1982) are commonly obtained for still fluids. Therefore, they do not account for the turbulent diffusion that can bring settling particles up again. Furthermore, in both channels, the difference between the observed and estimated settling rate increased with increasing particle size. This suggests that the effects of turbulence maintaining particles in suspension or bringing particles up from the bed is more important in the case of coarser particles, which are prone to settle faster.

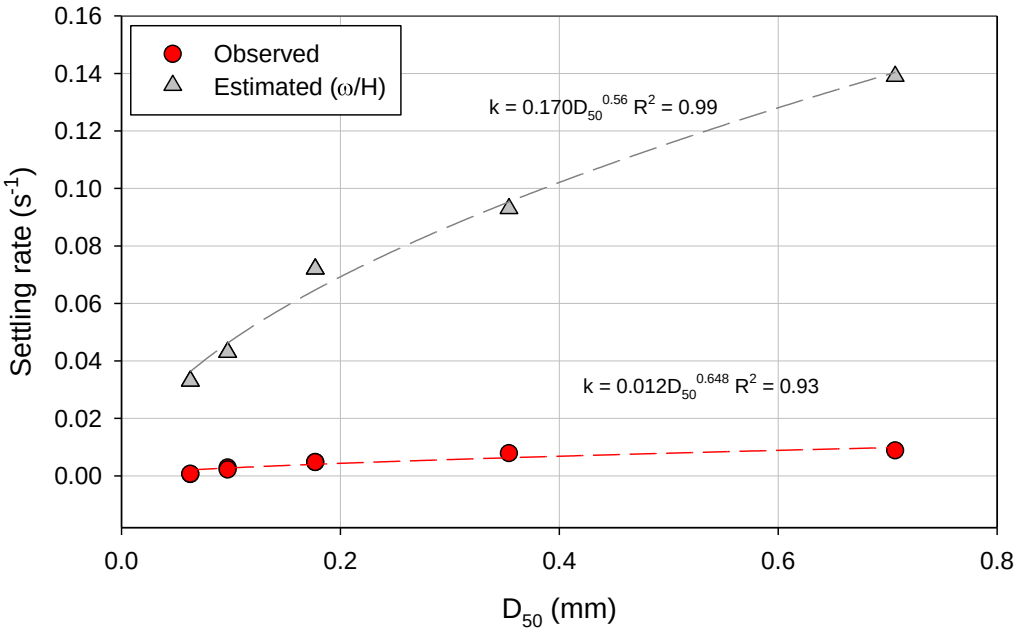

Figure 77. Settling rates versus D_{50} in the concrete channel.

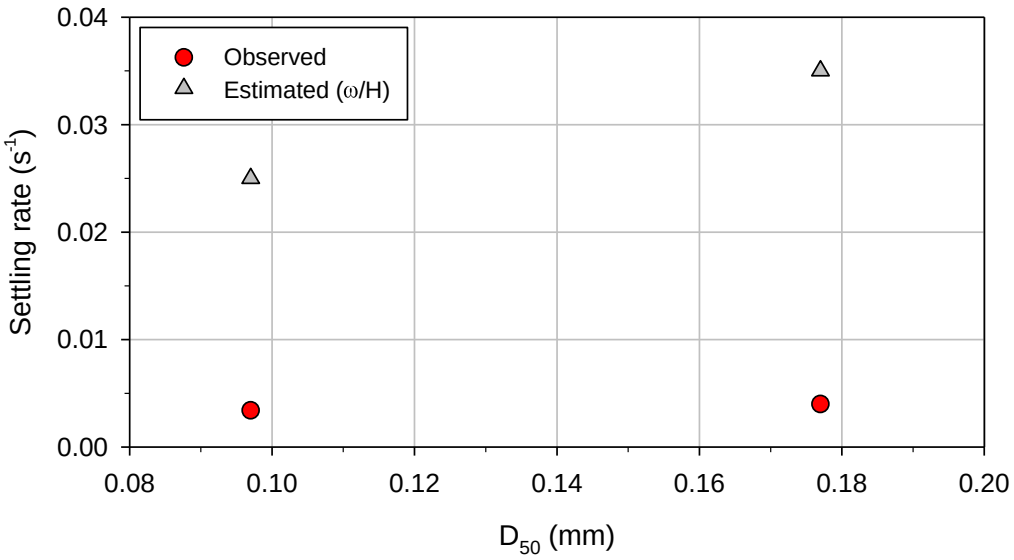

Figure 78. Settling rates versus D_{50} in the natural channel.

Data from the concrete channel indicates that the relationship between the observed settling rates and particle size (D_{50}) can be well described by a power relation, similar to the estimated rates. The rate of increase of settling rate with particle size is faster for the observed data than for the predicted settling rates based on equations for settling velocity in still fluids. However, it is important to highlight that the largest errors are associated with the coarsest fractions, so these power relations are uncertain and not universal.

The implication of the use of such estimated settling rates is an underestimation of the suspended sediment concentration. When dealing with drinking water safety, underprediction of concentration or turbidity levels can lead to reduced efficiency in water treatments such as disinfection and filtration (World Health Organization 2017) and potentially water disease outbreaks (Allen et al. 2008). In the concrete channel, based on the estimated settling rates for the fines fraction (<0.075 mm), the modeled concentration would have returned to background at approximately 330 m downstream of the injection. However, the observed data demonstrated that more than 80% of the injected particles were still in the flow at 370.15 m downstream of the injection. A similar result can be obtained for the coarser fractions. In the case of particles of size 0.5-1 mm, the modeled concentration would have returned to background at approximately 100 m downstream of the injection, while the observed data showed a 10% recovery at 370.15 m. These

results demonstrate that the settling rate term is essential to get correct in order to model suspended sediment dispersion, particularly for coarser fractions.

5.1.3. Applicability of the one-dimensional ADE in the advective zone

Sub-question 1.2 was directed at understanding whether the one-dimensional ADE was applicable everywhere along the studied reaches, especially in the advective zone. Strictly, the ADE for turbulent flows only applies in the equilibrium zone where it is assumed that the longitudinal dispersion coefficient becomes constant. This is well established in the literature, as reviewed in Chapter 2. However, practical applications of the one-dimensional ADE to real-world problems often lead to situations where the model is applied indiscriminately. Therefore, it is useful to understand the potential error associated with mis-applying the ADE to the advective zone. To the author's knowledge, no previous studies have done so.

5.1.3.1. One-dimensional advective zone length

Close to the injection, a transverse tracer line such as the one utilized in these experiments is distorted by the lateral velocity profile, as mentioned by Rutherford (1994). As a consequence, different parts of the plume move with different velocities according to their distance from the banks (or alternatively, the thalweg). This velocity shear induces lateral concentration gradients, that in turn, lead to turbulent diffusion. Eventually, the transverse mixing by turbulent diffusion counteracts the effects of velocity shear, and the plume becomes more evenly distributed in the lateral direction. The distance required for an "equilibrium" to be achieved determines the length of the advective zone.

Assessment of the length of the advective zone is essential for knowing if a sampling location is appropriate for estimating where equilibrium longitudinal dispersion coefficients can be obtained. Given the difficulties in obtaining detailed velocity field data to determine the length of the advective zone, most studies rely on equations such as Equation 65 developed by Fischer (1967). Equation 65 has two empirical coefficients that yield a large range of values, over several orders of magnitude. This large uncertainty regarding the advective zone length can lead to underestimation or overestimation of the longitudinal dispersion coefficients. In the concrete

channel, for example, the range was from 13 m to 2310 m, whereas, the observed data suggest that the advective zone length was between 139.95 m and 370.15 m. Similar results were obtained for the natural channel ($Q = 0.042$ m^3s^{-1}). The range was from 7 m to 1302 m for the empirical relations, while the observed data indicate that the advective zone ended between 92 m and 115.9 m. In both cases, the observed advective zone lengths were within the values estimated by Equation 65 with an α/β ratio between 0.22 and 1.54. For the semi-natural channel and the natural channel ($Q = 0.093$ m^3s^{-1}), all measurement locations were in the advective zone, therefore, it was not possible to estimate its length. For both, the concrete and natural channels, if the smaller estimates of the advective zone length had been utilized, all sampled curves would have been interpreted as being located in the equilibrium zone. However, if the larger estimates had been utilized, none of the measured data would have been judged to be in the equilibrium zone. These results demonstrate the importance of assessing the measured data with regard to sampling location in order to determine which stations are in the equilibrium zone and can provide reliable estimates of the longitudinal dispersion coefficient.

The Peclet number was the most useful parameter to identify which sampling locations were in the advective or the equilibrium zone, but this method requires *a posteriori* assessment. Specifically, estimates of the dispersion coefficient must be available. According to the Peclet number analysis, the fastest downstream balance between advection and dispersion was achieved in the natural channel, likely due to a range of natural roughness sources that induce mixing (e.g., meandering thalweg, undercut banks, large grain size on the bed). In contrast, the concrete channel was much smoother hydraulically, and the large flow velocity ensured that advection was dominant.

In the semi-natural and natural channels, the closer the plumes were to the equilibrium zone, the better was the fit with average flow velocity (e.g., Figure 49 and 68). This suggests that evaluating plume velocities in relation to the average velocity might also be a good indicator of the transition between advective and equilibrium zone conditions. In contrast, in the concrete channel, the average flow velocity was able to predict the curves start and peak times even in the advective zone. This is likely due to the uniform geometry of the concrete channel, hence, the similar nature of velocity profiles throughout the study reach.

The relation developed by Fischer (1967) (Equation 65) suggests that the advective zone length decreases with decreasing flow velocity and width. As the flow width decreases, the distance that the particles have to travel to sample the entire flow regime also decreases, reducing the length of the advective zone. Furthermore, while larger velocities can promote lateral mixing, they also increase the relative importance of advection, hence, increasing the length of the advective zone. In the natural channel, although it was not possible to determine the length of the advective zone during Q = 0.093 m^3s^{-1}, the results suggest that the advective length zone followed this relation when the discharge decreased from 0.093 m^3s^{-1} to 0.042 m^3s^{-1}. At 36 m and 49.6 m downstream of the injection, the differences between the observed and modeled t_{peak} and t_{start} decreased by approximately 50% as the discharge decreased from 0.093 m^3s^{-1} to 0.042 m^3s^{-1}.

5.1.3.2. Assessing the accuracy of the one-dimensional ADE in the advective zone

The one-dimensional ADE was applied to model the sodium chloride injections utilizing the average flow velocity from the hydraulic model results. The longitudinal dispersion coefficient was adjusted by trial and error in order to provide the best-fit value for each concentration curve based on the peak concentration. Finally, the sampling locations were classified as being in the advective or equilibrium zones according to the Peclet number. The longitudinal dispersion coefficients obtained in the equilibrium zones were utilized to model concentration at the upstream locations, which were located in the advective zone, to analyze the errors in comparison to the observed data. The relative errors to observed data were calculated and classified according to the methodology described in 3.5.

In the concrete channel (Table 65) at 80.75 m downstream of the injection, all observed curves had a fair agreement with observed data, while at 139.95 m seven out of eight runs had good agreement with observed data, and one run (CC-4) had fair agreement. In the natural channel (Table 62), all runs had fair agreement with observed data at 36 m, and good agreement with observed data at 49.6 m and 92 m.

Table 61. Relative errors of the modeled concentration curves calculated with the longitudinal dispersion coefficient from the equilibrium zone in the concrete channel.

Run	Location (m)	Relative error (%) Modeled value − observed value / Observed value				Final classification
		C_{peak}	t_{peak}	t_{start}	Duration	
CC-1	80.75	-61	-2	-33	31	F
CC-2		-65	-3	-37	46	F
CC-3		-58	-3	-35	46	F
CC-4		-63	0	-34	44	F
CC-5		-63	0	-38	59	F
CC-6		-62	-2	-36	44	F
CC-7		-64	-5	-45	78	F
CC-8		-59	-2	-37	46	F
CC-9		-62	-2	-33	41	F
CC-1	139.95	-50	0	-24	-	G
CC-2		-45	1	-27	-2	G
CC-3		-44	1	-29	-2	G
CC-4		-52	2	-27	87	F
CC-5		-48	1	-28	2	G
CC-6		-40	0	-27	-8	G
CC-7		-49	-2	-34	12	G
CC-8		-	-	-	-	-
CC-9		-39	-1	-27	-5	G

Table 62. Relative errors of the modeled concentration curves calculated with the longitudinal dispersion coefficient from the equilibrium zone in the natural channel.

Run	Location (m)	Relative error (%) Modeled value − observed value / Observed value				Final classification
		C_{peak}	t_{peak}	t_{start}	Duration	
NC-2.1	36	-54	18	-50	-8	F
NC-2.1		-58	27	-45	-3	F
NC-2.1		-57	24	-48	-4	F
NC-2.2		-43	0	-57	-9	F
NC-2.2		-47	14	-51	-13	F
NC-2.2		-45	7	-54	-21	F
NC-2.4		-51	10	-50	-20	F

Run	Location (m)	Relative error (%) Modeled value − observed value / Observed value				Final classification
		C_{peak}	t_{peak}	t_{start}	Duration	
NC-2.5		-63	15	-51	-19	F
NC-2.6		-61	28	-43	21 ET	F
NC-2.3		-35	17	-40	-40	G
NC-2.3	49.6	-40	22	-39	-34	G
NC-2.3		-26	23	-39	-34	G
NC-2.4		-14	4	-35	-36	G
NC-2.5	92	-27	11	-32	-35	G
NC-2.6		-32	28	-22	15 ET	G

ET = experimental truncation

The results from both the concrete channel and the natural channel have similar trends indicating that the farther downstream (closer to the equilibrium zone), the better the results (Figures 79 and 80). This is particularly true for the peak concentration. These results are a reflection of the relative importance of advection over dispersion in the advective zone. Initially, advection dominates over dispersion, but as the plumes move downstream, the relative importance of dispersion increases. The plumes start to spread out more, and peak concentrations decrease faster, at rates that are closer to the equilibrium zone rate.

The peak times had excellent agreement with observed data in 29 out of 32 cases. Since the peak time is mainly governed by the advection velocity, which was a fixed variable in this analysis, this parameter was modeled with good agreement (±50% accuracy) in all runs, regardless of the value of the longitudinal dispersion coefficient. Start time and plume duration had mixed results in terms of performance regardless of location, particularly in the natural channel.

The start time was consistently underestimated in both channels. This reflects the larger skewness of the observed curves in comparison to the predicted ones. In the case of the concrete channel, this was mainly caused by the effects of lateral velocity shear. Additional skewness caused by transient storage in the natural channel might have been responsible for the larger errors observed during some of the runs.

In the concrete channel, the duration of the plumes was constantly overestimated at 80.75 m, indicating that the plumes were much shorter than predicted by the model. This reflects the large relative importance of advection over dispersion in the advective zone. At 139.95 m, most plumes had excellent agreement with the observed duration, indicating that at a certain point where the importance of dispersion increases, the duration of the observed plumes becomes closer to the modeled. The exception was the plume obtained during run CC-4, which had a much shorter duration than the others. This case will be treated as an unexplained outlier since all the other runs had very similar durations. In contrast, the duration of the plumes in the natural channel was underpredicted in all runs (with the exception of the experimentally truncated plume at 92 m during run NC-2.6). This indicates that the plumes in the natural channel had much longer tails than the ones in the concrete channel, even close to the injection line. This analysis also reaffirms the finding that the advective zone length in the concrete channel was much longer than in the natural channel. At 49.6 m and 92 m downstream of the injection in the natural, the runs had good agreement with the observed data, while at 80.95 m in the concrete channel the data had only fair agreement with observed data.

This analysis suggests that modeling errors of approximately ±100% will occur in the advective zone. This is particularly important in the case of the peak concentration, which is consistently underestimated in the advective zone. Trusting model results without consideration of the advective zone can lead to unforeseen concentration values close to the pollutant source. In the context of water quality predictions, this could lead to problems such as decreased efficiency in water treatments, and detrimental effects on the aquatic biota.

In cases where the advective zone length is not known in advance, model simulations for locations close to the injection point should account for such potential error.

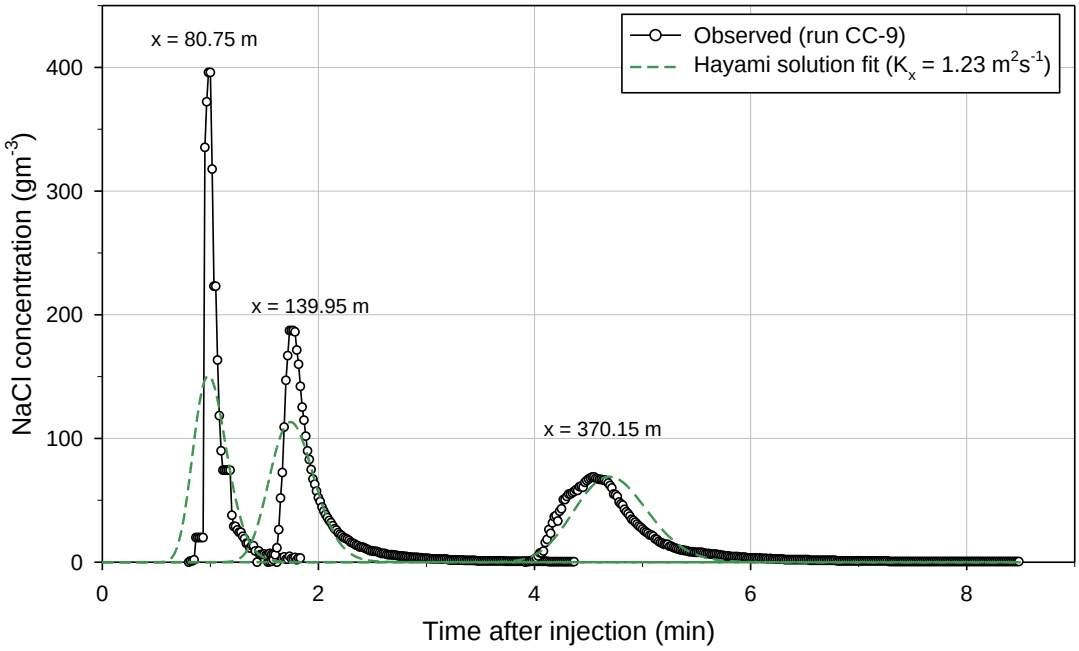

Figure 79. Modeled concentration curves in the concrete channel based on the equilibrium longitudinal dispersion coefficient. Sampling locations x = 80.75 m and x = 139.95 m were located in the advective zone, and x = 370.15 m was located in the equilibrium zone.

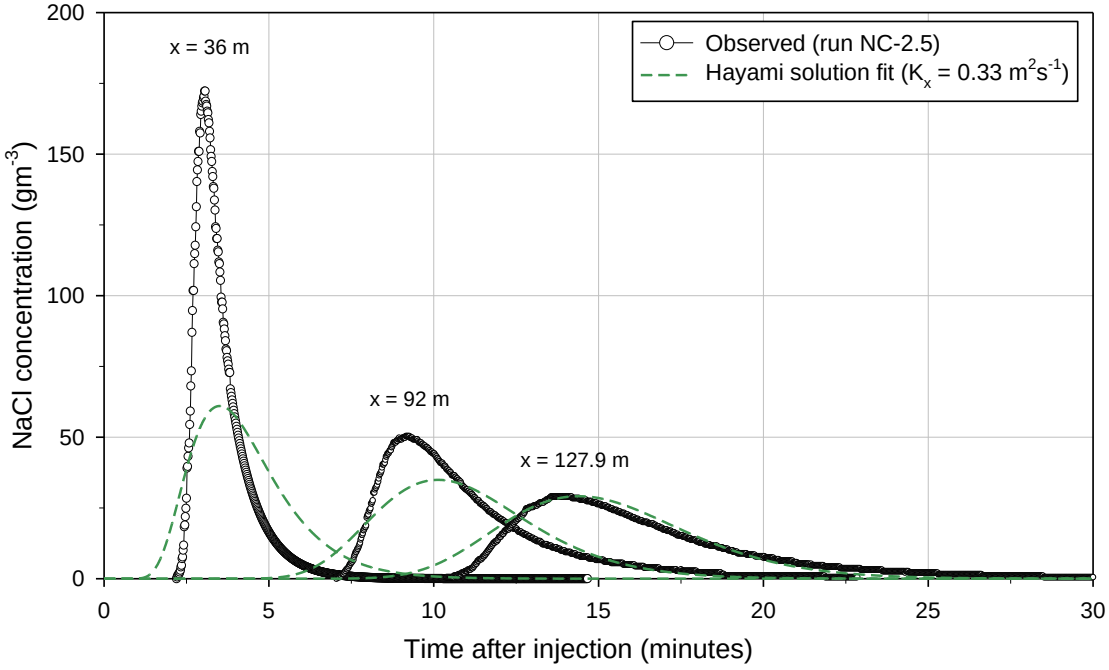

Figure 80. Modeled concentration curves in the natural channel based on the equilibrium longitudinal dispersion coefficient. Sampling locations x = 36 m and x = 92 m were located in the advective zone, and x = 127.9 m was located in the equilibrium zone.

5.1.4. Lateral velocity gradients and transient storage

Sub-questions 1.3 and 1.4 were directed at the importance of lateral gradients in velocity and suspended sediment concentration as well as transient storage effects when using a one-dimensional ADE approach. Lateral velocity shear and transient storage have overlapping effects on plume dispersion in the sense that both can alter advection velocity and lead to lateral concentration gradients; therefore, they will be discussed simultaneously in this section.

Given the different degrees of complexity of the studied channels, it was hypothesized that the simplest channel, the concrete channel, would be the least affected by lateral velocity gradients and transient storage. On the other hand, complexities such as roughness elements, non-uniform banks, vegetation, and obstacles, in the semi-natural and natural channels were expected to increase the heterogeneity of the lateral velocity profiles and effects of transient storage, leading to larger lateral concentration gradients and data variability in general.

5.1.4.1. Lateral velocity profiles

A comparison between transverse velocity profiles in the three channels (Figure 81-83), helps to highlight the effects of lateral shear velocity and transient storage. Although the profiles were measured under different discharges or at locations other than the tracer sampling locations, they help to illustrate the characteristics of each channel. The velocity profile of the concrete channel was measured during Q = 0.698 m^3s^{-1}. It has a fairly uniform distribution, with slower velocities near the side walls, and faster velocities towards the center, resembling a theoretical lateral velocity profile. Two profiles were measured in the semi-natural channel after the tracer experiments were concluded. One of the profiles is fairly uniform, similar to the concrete channel, while the second shows very slow velocities near the left bank, increasing towards the right bank, despite the greater depth on the left side of the channel. Such a profile would cause the plume near the left bank to travel more slowly than at the center or right bank, thereby increasing the effect of lateral shear velocity. The profile in the natural channel during (Q = 0.093 m^3s^{-1}) was obtained upstream of the injection line location, where the flow was slightly deeper. The profile reveals much larger variations in velocity over the cross-section, including a back-water zone with negative velocities that may lead to transient storage. Overall it can be seen that the complexity increases from the concrete channel to the natural channel, which can affect dispersion processes.

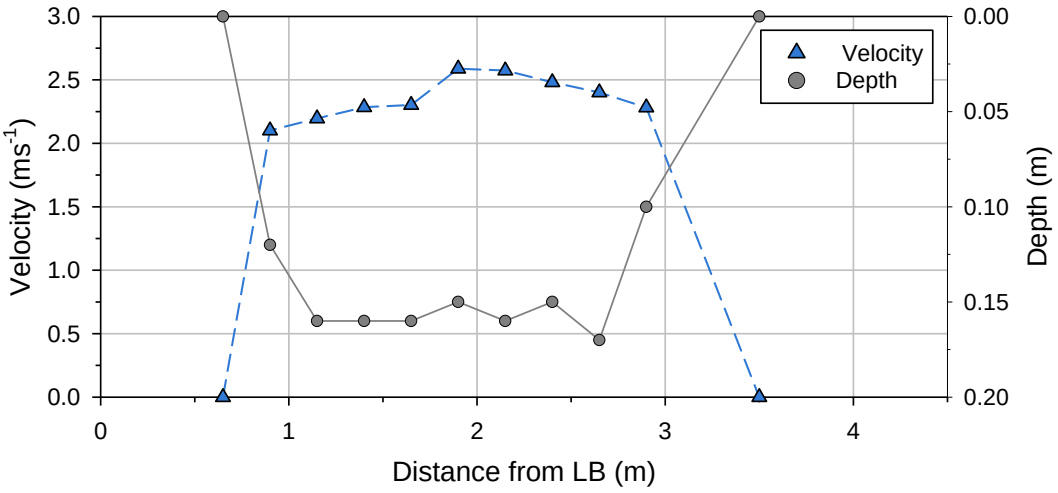

Figure 81. Lateral velocity profile from the concrete channel (Q = 0.698 m^3s^{-1}).

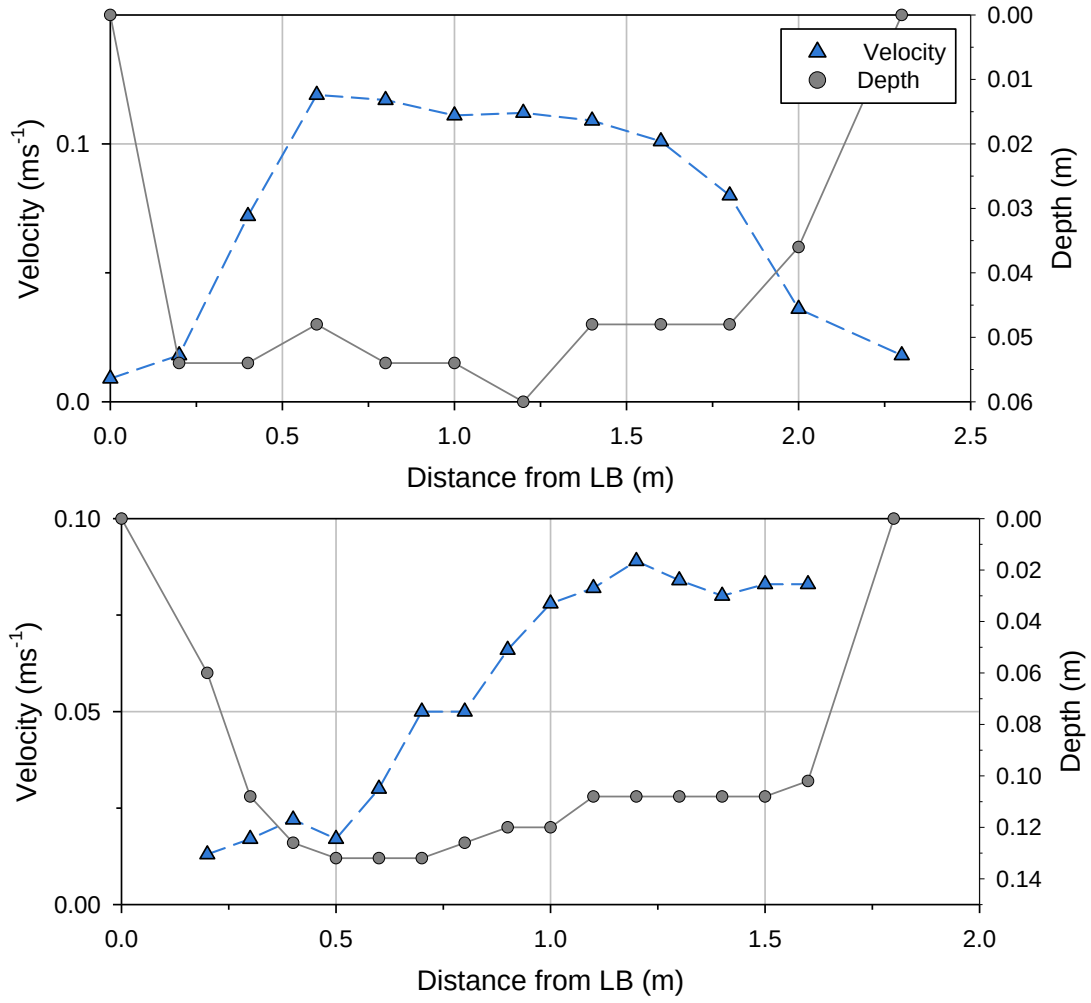

Figure 82. Lateral velocity profiles from the semi-natural channel (Q = 0.16 m^3s^{-1}).

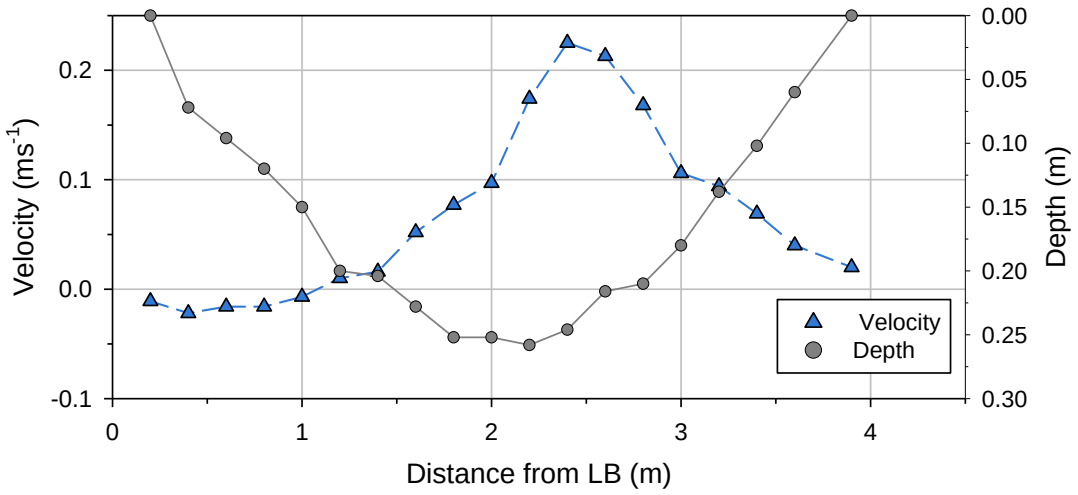

Figure 83. Lateral velocity profile from the natural channel (Q = 0.093 m^3s^{-1}).

5.1.4.2. Lateral concentration gradients

Although sodium chloride is considered a conservative tracer, recovery rates other than 100% are commonly observed during tracer experiments (Nordin and Sabol 1974; Rutherford 1994; Schmadel et al. 2010; Singh et al. 2010). A primary reason for this is that lateral mixing may not have been fully achieved at the measurement location. Because the measured concentration values are multiplied by the total discharge of the cross-section, the recovery rates will be greater (or lesser) than 100% if the tracer concentration is not even over the cross-sectional area. Only when the tracer is uniformly mixed across the channel will the recovery rates approximate 100% using this method. Transient storage of tracer may also yield recoveries smaller 100% if the stored tracer is not released within the measurement interval. Furthermore, as mentioned in Chapter 2, Rutherford (1994) reported that in the case of instantaneous injections, such as the ones used in this study, there will always be concentration gradients caused by lateral velocity shear even in the far-field.

In the concrete channel, recovery rates of generally more than 100% suggest that the line injections were being distorted by the lateral velocity profile, leading to lateral concentration gradients until at least 139.95 m downstream (Table 63). At 370.15 m, in contrast, the cross-sectional measurements yielded very similar concentration curves, indicating that turbulent

diffusion was able to counteract the effects of lateral velocity shear and promote more even lateral mixing.

Table 63. Relative cross-sectional differences for the suspended sediment curves obtained at 370.15 m downstream of the injection in the concrete channel.

Run	Sediment size (mm)	Location (m)	Relative difference (%) $\frac{\text{Observed value C} - \text{observed value RB}}{\text{Observed value RB}}$			
			R	C_{peak}	t_{peak}	t_{start}
CC-1	<0.075	370.15	-	-	-	-
CC-2			13	3	0	3
CC-3			-1	-3	-1	1
CC-4	0.075-0.125		-4	0	-2	0
CC-5			-10	6	-5	-2
CC-6	0.125-0.25		1	8	-1	-1
CC-7			-4	-9	-2	3
CC-8	0.25-0.5		7	15	-6	2
CC-9	0.5-1		24	36	11	-1

In the semi-natural channel, the plumes had large (>100%) differences in lateral concentration at 20 m and 60 m downstream of the injection line (Table 64). Despite the similar recoveries at 20 m, part of the plume arrived faster at the center probe than on the right bank, suggesting that the plume was being distorted by the lateral velocity profile. At 60 m, the part of the plume on the right bank had smaller peaks and longer tails, but similar arrival times as the left bank. This could have been a consequence of the slower velocities on the right bank, possibly combined with transient storage zones.

Table 64. Relative cross-sectional differences for sodium chloride curves obtained in the semi-natural channel.

Run	Location (m)	Relative difference (%) $\frac{\text{Observed value LB or C} - \text{observed value RB}}{\text{Observed value RB}}$				
		R	C_{peak}	t_{peak}	t_{start}	Duration
SNC-2	60 LB	3	165	2	-15	-56
SNC-3	60 LB	-26	158	1	7	-51
SNC-3	20 C	-26	122	-80	-77	-59

In the natural channel, the lateral concentration gradients decreased in the downstream direction (Table 65). The largest differences occurred very close to the injection line, at 12.5 m, demonstrating the effects of the lateral velocity shear distorting the plume close to the injection. There was also large variability between runs. The presence of non-uniformities, such as gravel bars, vegetation, and obstacles in the flow likely created slightly different conditions between runs, affecting suspended sediment dispersion and settling.

Table 65. Relative cross-sectional differences for the sodium chloride and suspended sediment curves obtained in the natural channel.

Run	Location (m)	Relative difference (%) Observed value LB or C − observed value RB / Observed value RB								
		Sodium chloride					Sediment			
		R	C_{peak}	t_{peak}	t_{start}	Duration	R	C_{peak}	t_{peak}	t_{start}
NC-1.1	12.5 LB	-	-	-	-	-	83	-15	-13	-15
	12.5 C	-	-	-	-	-	31	-2	-25	-28
	36 LB	-	-	-	-	-	35	20	5	13
	36 C	-4	10	-2	17	-9	-11	-12	-4	8
	49.6 LB	8	-31	11	4	12	6	-15	11	11
NC-1.2	12.5 LB	-	-	-	-	-	40	63	0	3
	12.5 C	-	-	-	-	-	61	114	-17	-24
	36 LB	-	-	-	-	-	23	41	6	-2
	36 C	-1	10	-2	3	-4	11	15	0	-6
	49.6 LB	4	-26	25	13	19	-14	3	-5	2
NC-1.3	12.5 LB	-	-	-	-	-	486	299	-15	-15
	12.5 C	-	-	-	-	-	575	478	-26	-33
	36 LB	-	-	-	-	-	55	40	14	1
	36 C	20	1	3	8	24	24	16	0	-5
	49.6 LB	15	-33	24	13	17	-	-	-	-
NC-2.1	36 LB	-15	-7	5	5	4	-	-	-	-
	36 C	-6	2	-2	-5	-2	-16	-8	-6	-5
	49.6 LB	-	-	-	-	-	34	13	11	5
	49.6 C	-	-	-	-	-	3	21	3	-3
	65 LB	-	-	-	-	-	-30	-55	29	23
NC-2.2	36 LB	-21	-3	8	7	-14	-	-	-	-
	36 C	-8	5	-6	-6	-9	-9	5	-5	-9
	49.6 LB	-	-	-	-	-	-5	10	-17	-6
	49.6 C	-	-	-	-	-	-21	-7	-10	-11
	65 LB	-	-	-	-	-	-33	-53	28	30
NC-2.3	36 LB	-3	14	5	2	11	-	-	-	-

Run	Location (m)	Relative difference (%) $\frac{\text{Observed value LB or C} - \text{observed value RB}}{\text{Observed value RB}}$								
		Sodium chloride					Sediment			
		R	C_{peak}	t_{peak}	t_{start}	Duration	R	C_{peak}	t_{peak}	t_{start}
	36 C	2	24	1	0	0	-2	-36	-9	-23
	49.6 LB	-	-	-	-	-	-	-	-	-
	49.6 C	-	-	-	-	-	-14	12	-12	-8
	65 LB	-	-	-	-	-	-31	-37	14	31

The lateral gradients in the concrete channel and natural channel (runs NC-2.1 to NC-2.3) were similar despite the fact that the natural channel sampling locations were much closer to the injection. Comparing the lateral concentration gradients between the semi-natural channel and natural channel at similar distances downstream, the largest gradients occurred in the semi-natural channels. This again indicates that the greatest and fastest equilibrium between advection velocity and dispersion occurred in the natural channel.

The analysis of the total duration of the sodium chloride curves in relation to the peak time for the truncation criterion in 4.1 (Table 13, Figure 27) revealed that the skewness of the curves (tail length) increased with increased channel complexity. Part of this increase can be attributed to the effects of transient storage on the dispersion of the plumes. As a consequence, the centroid velocities of the curves were slower than the peak velocities in all channels, demonstrating that most of the mass of the plume was concentrated after the peak. The relative differences between the sodium chloride peak and centroid velocities were much larger in the semi-natural channel (2-32%) and in the natural channel (13-32%) than in the concrete channel (2-10%), again showing that the shortest tails occurred in the concrete channel.

5.2. Applicability of formulas for predicting the longitudinal dispersion coefficients to small channels

The second hypothesis was with regard to the applicability of formulas for predicting longitudinal dispersion coefficient to small channels. Twenty-six predictive formulas (Table 3) for the longitudinal dispersion coefficient were evaluated for applicability to small channels. Each of them was applied using the guidelines recommended in the original publications. The predicted

coefficients were then compared to the dispersion coefficients obtained from the best-fit average value using the Hayami solution applied to measured sodium-chloride plumes in both the concrete channel and natural channel. Relative errors were calculated according to Equation 123. Afterward, the predicted coefficients were utilized to model the sodium chloride injections, and the modeled curves were compared with the observed data acquired in the equilibrium zone. Again, the relative errors were calculated according to Equation 123.

None of the formulas was able to yield accurate predictions of the longitudinal dispersion coefficient in both the concrete and natural channels, although some formulas performed well in one or the other. The majority (19 out of 26 formulas) of the formulas overestimated the value of the longitudinal dispersion coefficient in the concrete channel (Figure 84) as well as the natural channel (15 out of 26 formulas) (Figure 85). The relative errors ranged from -100% (underestimation) to greater than 1000% (overestimation) in a few cases. Note that the limit on underestimation is -100% given the way the relative error is constructed (i.e., predicted minus measured), whereas there is no upper limit on overestimation.

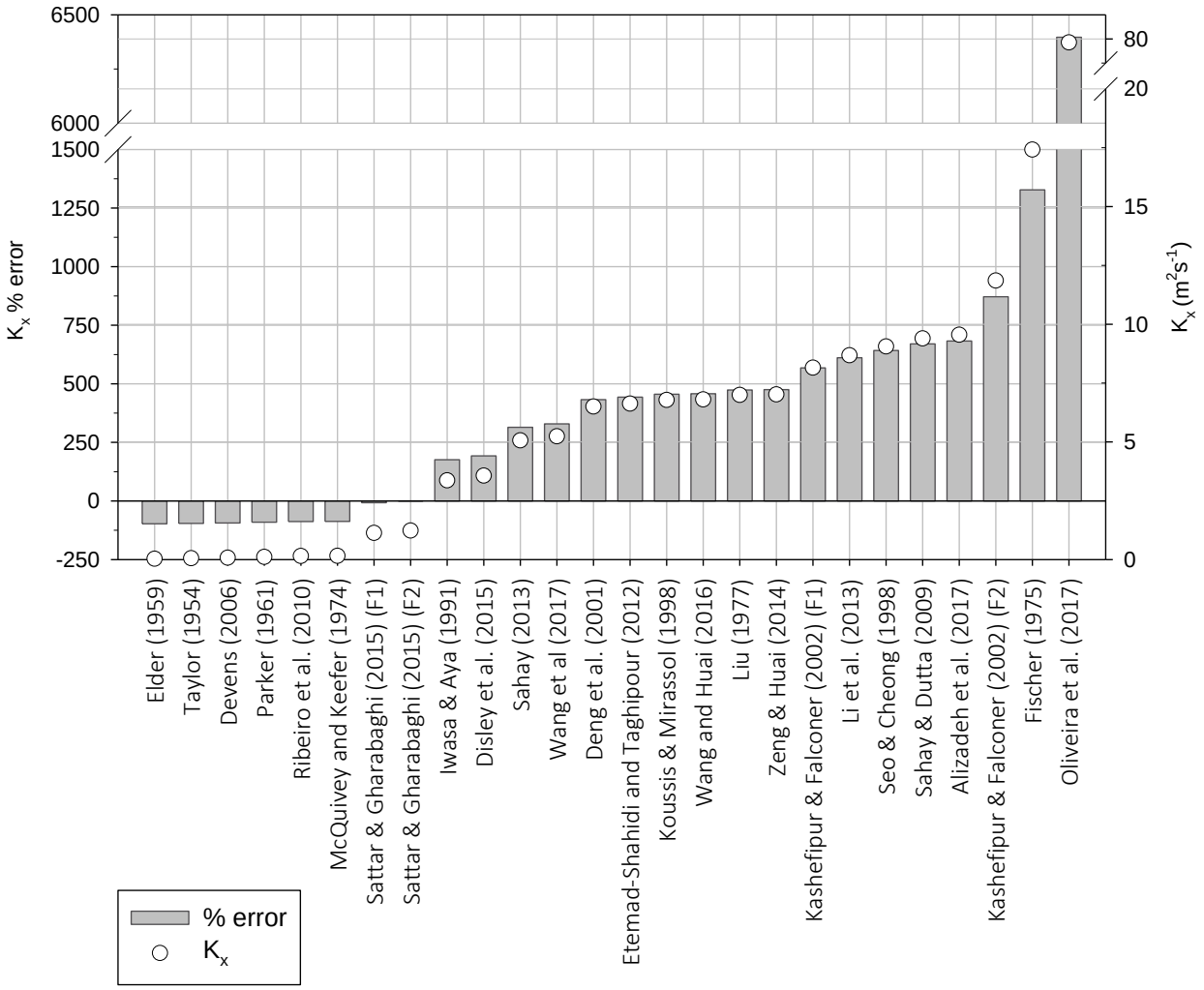

Figure 84. Percent error of the longitudinal dispersion coefficient value obtained with the predictive formulas when compared with the best-fit average value from the Hayami solution for the concrete channel.

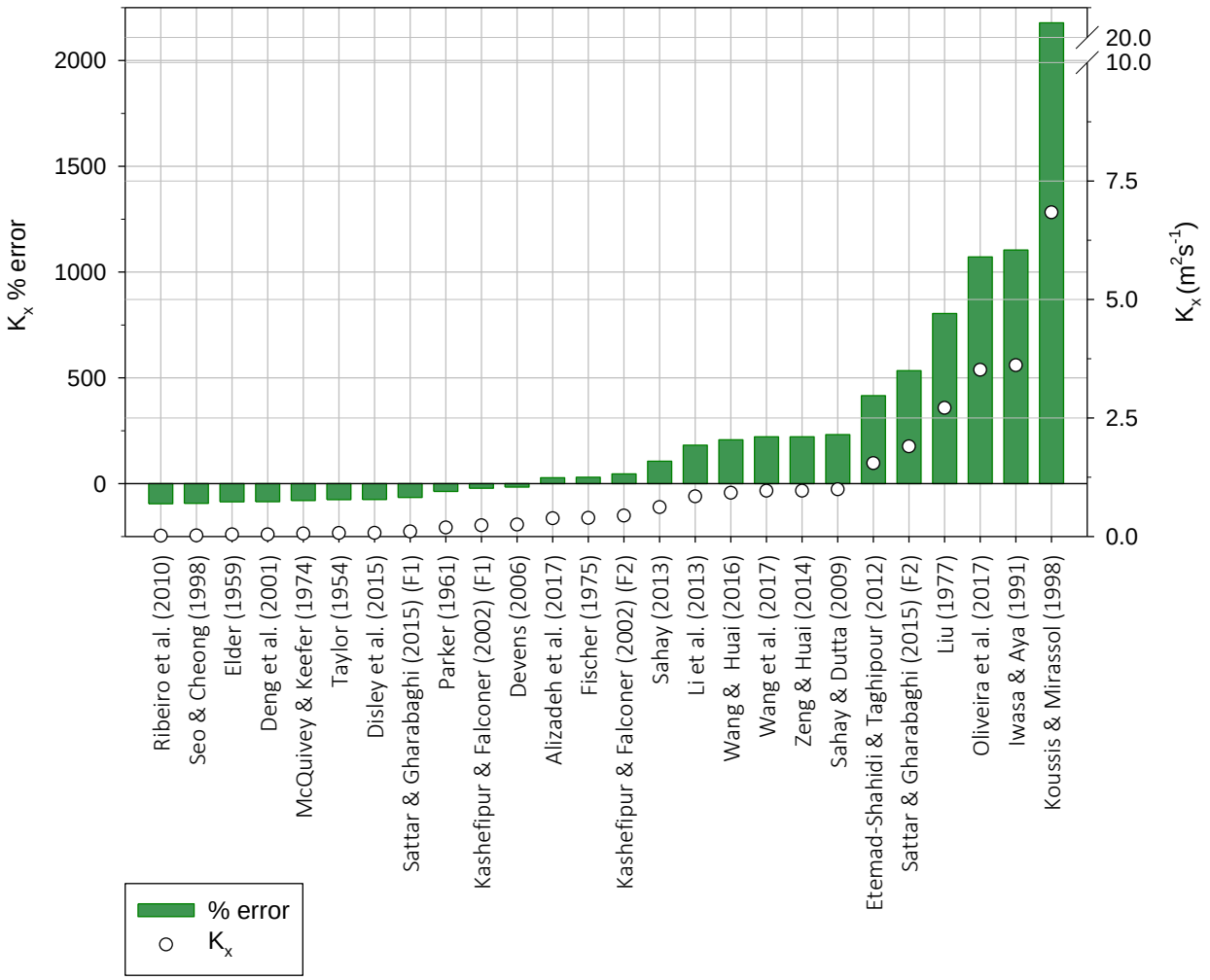

Figure 85. Percent error of the longitudinal dispersion coefficient value obtained with the predictive formulas when compared with the best-fit average value from the Hayami solution for the natural channel.

Based on a simple comparison of the value of the longitudinal dispersion coefficient, eight of the formulas underestimated the longitudinal dispersion coefficient in both channels: Taylor (1954), Elder (1959), Parker (1961), McQuivey and Keefer (1974), Kashefipour and Falconer (2002) (F2), Devens (2006), Ribeiro et al. (2010), and Sattar and Gharabaghi (2015) (F1). Fourteen formulas overestimated the longitudinal dispersion coefficient in both channels: Oliveira et al. (2017), Iwasa and Aya (1991), Koussis and Mirassol (1998), Zeng and Huai (2014), Liu (1977), Etemad-Shahidi and Taghipour (2012), Sahay (2013), Wang et al. (2017), Alizadeh et al. (2017), Sattar and Gharabaghi (2015) (F2), Li et al. (2013), Sahay and Dutta (2009), and Fischer (1975). Four formulas overestimated the coefficient in the concrete channel but underestimated them in

the natural channel: Seo and Cheong (1998), Kashefipour and Falconer (2002) (F1), Deng et al. (2001), and Disley et al. (2015). No similarities were found between these formulas except that all four have a coefficient >1 for the $\bar{U}/u_*$ ratio and that their calibrating data sets included the data set from Seo and Cheong (1998). However, this was true for other formulas analyzed.

Each of the 26 longitudinal dispersion coefficients predicted for the concrete and the natural channels was utilized to model the sodium chloride injections. The modeled curves were compared with the observed data acquired in the equilibrium zone as shown in Figure 41 and 72. Four parameters of the concentration curves were analyzed in order to determine the accuracy of the predicted formulas: peak concentration, peak time, start time, and duration of the plume. The relative errors between the modeled and observed curves were estimated for each run (Appendices G and H) according to the methodology described in 3.6. The average results for the concrete and natural channel are shown in Figure 86 and Figure 87, respectively.

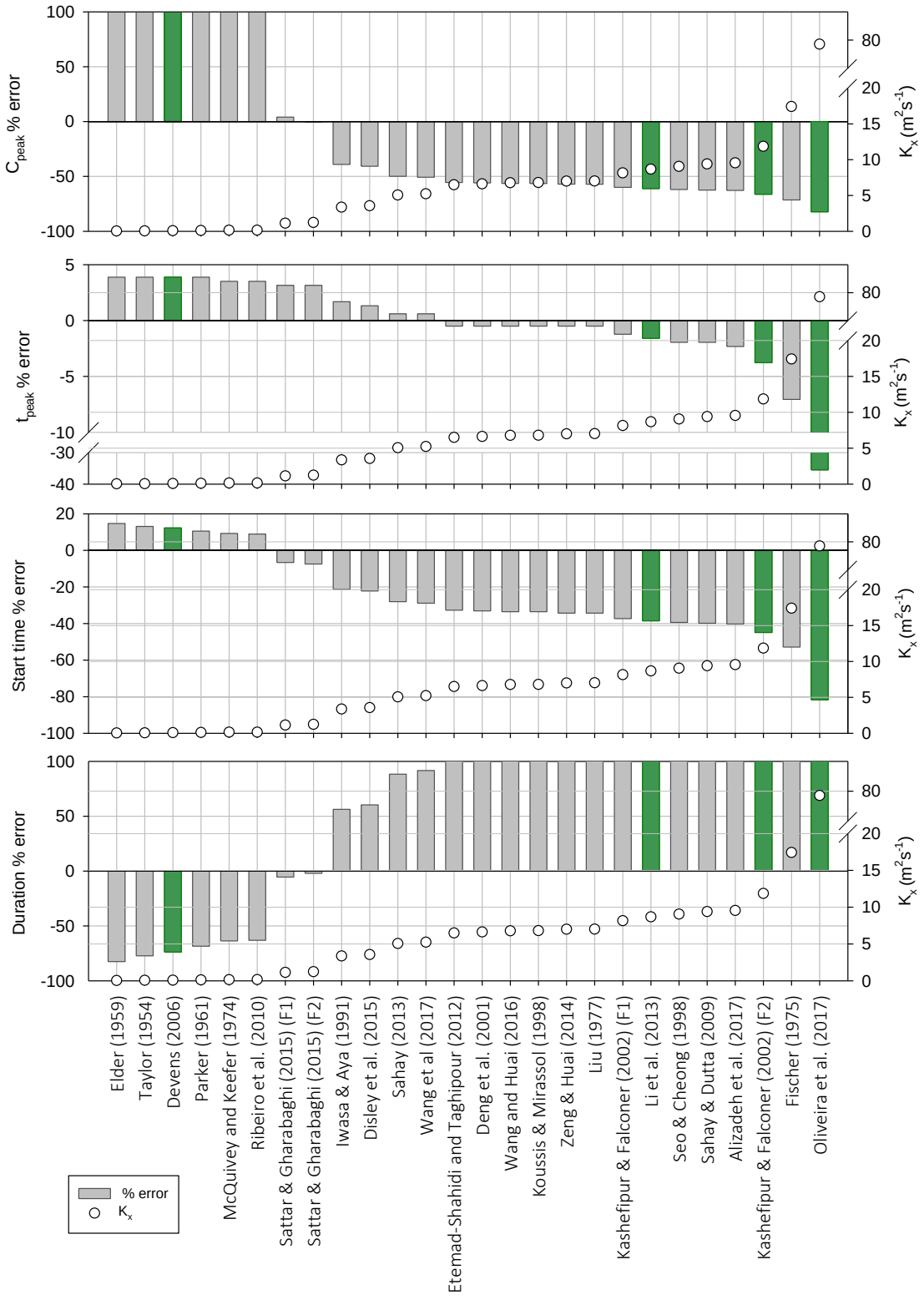

Figure 86. Relative error and longitudinal dispersion coefficient according to predictive formulas in the concrete channel. Errors larger than 100% are not shown for better scaling. The green bars show the best predictors for the natural channel for comparison.

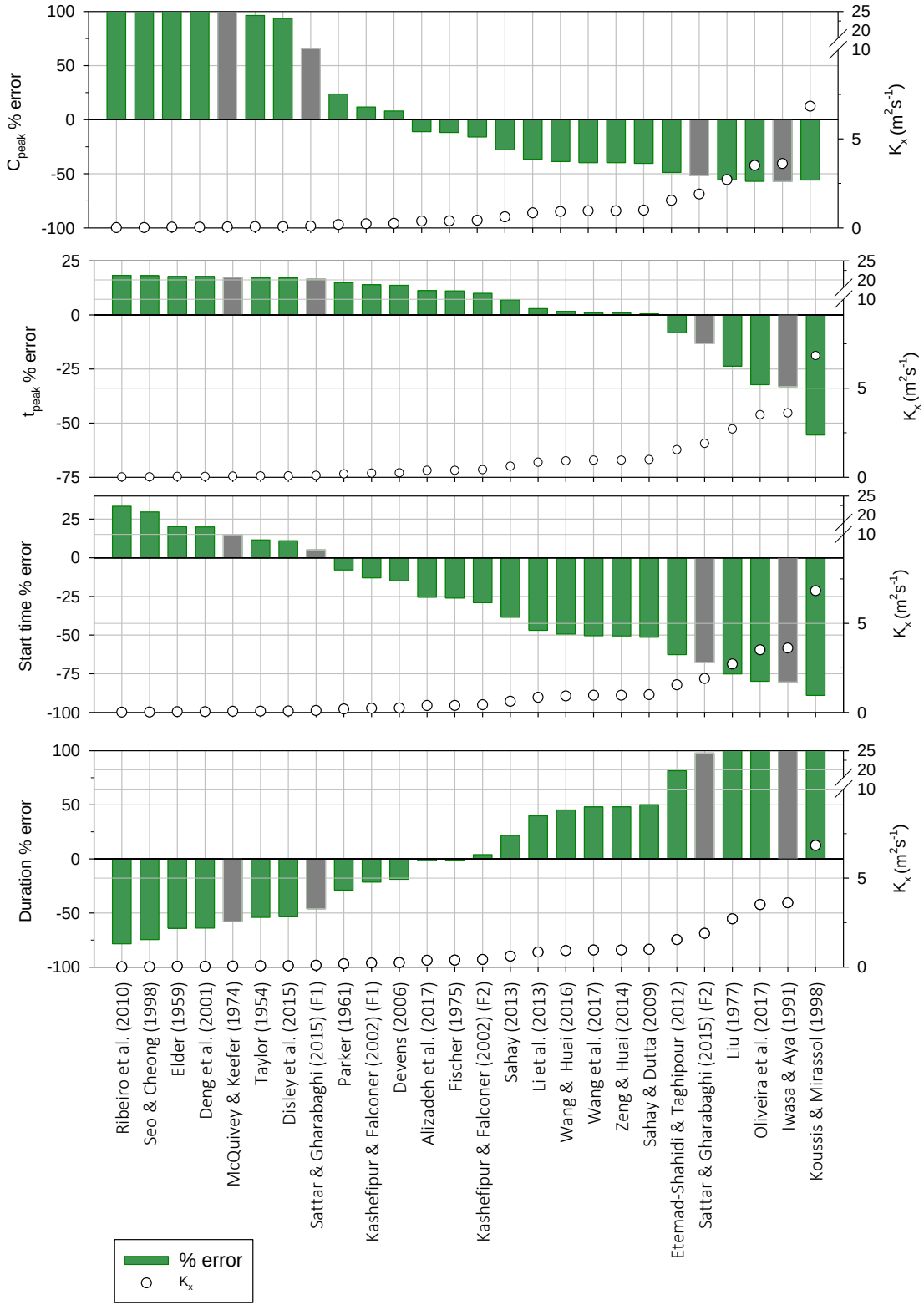

Figure 87. Relative error and longitudinal dispersion coefficient according to predictive formulas in the natural channel. Errors larger than 100% are not shown for better scaling. The grey bars show the best predictors for the concrete channel for comparison.

In the concrete channel, the two formulas by Sattar and Gharabaghi (2015) had excellent agreement with the observed data (Table 66). The models were capable of predicting the peak concentration, peak time, start time, and duration of the curve with less than 10% absolute error. The formulas by Iwasa and Aya (1991), Disley et al. (2015), Sahay (2013), and Wang et al. (2017) were classified as providing fair agreement to the observed data. All the remaining formulas were classified as providing poor agreement with the observed data, particularly due to the errors in the duration parameter.

Table 66. Relative error according to predictive formulas in the concrete channel.

Reference	K_x	Relative % error $\frac{\text{Modeled value} - \text{observed value}}{\text{Observed value}}$				Level of agreement
		C_{peak}	t_{peak}	t_{start}	Duration	
Elder (1959)	0.03	506	4	15	-83	P
Taylor (1954)	0.06	365	4	13	-77	P
Devens (2006)	0.08	299	4	12	-74	P
Parker (1961)	0.11	228	4	11	-68	P
McQuivey and Keefer (1974)	0.15	183	4	9	-64	P
Ribeiro et al. (2010)	0.15	180	4	9	-63	P
Sattar & Gharabaghi (2015) (F1)	1.13	4	3	-7	-5	E
Sattar & Gharabaghi (2015) (F2)	1.23	0	3	-7	-2	E
Iwasa & Aya (1991)	3.36	-39	2	-21	56	F
Disley et al. (2015)	3.56	-41	1	-22	60	F
Sahay (2013)	5.06	-50	1	-28	88	F
Wang et al (2017)	5.23	-51	1	-29	92	F
Etemad-Shahidi and Taghipour (2012)	6.50	-56	0	-33	111	P
Deng et al. (2001)	6.62	-56	0	-33	113	P
Wang and Huai (2016)	6.77	-56	0	-34	115	P
Koussis & Mirassol (1998)	6.80	-56	0	-34	116	P
Zeng & Huai (2014)	6.99	-57	0	-34	118	P
Liu (1977)	7.01	-57	0	-34	119	P
Kashefipur & Falconer (2002) (F1)	8.15	-60	-1	-37	134	P
Li et al. (2013)	8.67	-61	-2	-39	141	P
Seo & Cheong (1998)	9.05	-62	-2	-39	146	P
Sahay & Dutta (2009)	9.39	-62	-2	-40	149	P

Reference	K_x	Relative % error $\frac{\text{Modeled value} - \text{observed value}}{\text{Observed value}}$				Level of agreement
		C_{peak}	t_{peak}	t_{start}	Duration	
Alizadeh et al. (2017)	9.55	-63	-2	-40	151	P
Kashefipur & Falconer (2002) (F2)	11.85	-66	-4	-45	177	P
Fischer (1975)	17.42	-71	-7	-53	229	P
Oliveira et al. (2017)	79.26	-82	-35	-82	520	P

In the natural channel, the formulas by Devens (2006) and Kashefipour and Falconer (2002) (F1) had the best performance (excellent agreement), with all four parameters predicted with 25% or less absolute error (Table 67). The formulas from Parker (1961), Fischer (1975), Alizadeh et al. (2017), Kashefipour and Falconer (2002) (F2), Li et al. (2013), Sahay (2013), Wang and Huai (2016), and Wang et al. (2017) were classified as having good agreement with the observed data. All the remaining formulas (16) were classified as having fair or poor agreement with the observed data, including the two formulas by Sattar and Gharabaghi (2015), which performed best in the concrete channel.

Table 67. Relative error according to the predictive formula in the natural channel.

Reference	K_x	Relative % error $\frac{\text{Modeled value} - \text{observed value}}{\text{Observed value}}$				Level of agreement
		C_{peak}	t_{peak}	t_{start}	Duration	
Ribeiro et al. (2010)	0.01	338	18	33	-78	P
Seo & Cheong (1998)	0.02	267	18	30	-75	P
Elder (1959)	0.04	155	18	20	-64	P
Deng et al. (2001)	0.04	154	18	20	-64	P
McQuivey and Keefer (1974)	0.06	116	17	15	-58	P
Taylor (1954)	0.07	96	17	12	-54	F
Disley et al. (2015)	0.07	94	17	11	-53	F
Sattar & Gharabaghi (2015) (F1)	0.10	66	17	5	-46	F
Parker (1961)	0.19	24	15	-8	-29	G
Kashefipur & Falconer (2002) (F1)	0.23	12	14	-13	-21	E
Devens (2006)	0.25	8	14	-15	-19	E

Reference	K_x	Relative % error $\frac{\text{Modeled value} - \text{observed value}}{\text{Observed value}}$				Level of agreement
		C_{peak}	t_{peak}	t_{start}	Duration	
Fischer (1975)	0.38	-11	11	-26	-2	G
Alizadeh et al. (2017)	0.39	-12	11	-26	-1	G
Kashefipur & Falconer (2002) (F2)		-16	10	-29	4	G
Li et al. (2013)	0.62	-28	7	-38	22	G
Sahay (2013)	0.84	-37	3	-47	40	G
Wang and Huai (2016)	0.92	-39	2	-49	45	G
Wang et al. (2017)	0.96	-40	1	-50	48	G
Zeng & Huai (2014)	0.96	-40	1	-51	48	F
Sahay & Dutta (2009)	0.99	-40	0	-51	50	F
Etemad-Shahidi and Taghipour (2012)	1.55	-49	-8	-63	81	F
Sattar & Gharabaghi (2015) (F2)	1.90	-52	-13	-68	98	F
Liu (1977)	2.71	-55	-24	-75	129	P
Oliveira et al. (2017)	3.51	-57	-32	-80	153	P
Iwasa & Aya (1991)	3.61	-57	-33	-80	156	P
Koussis & Mirassol (1998)	6.84	-56	-55	-89	221	P

None of the formulas were able to predict the dispersion process on both channels with excellent or good agreement. However, the two formulas from Sattar and Gharabaghi (2015) had the smallest absolute relative errors when considering both channels (Figure 88). A graph of the peak concentration relative errors is able to show this, given that the times are well predicted in both cases, and the duration is closely related to the peak concentration.

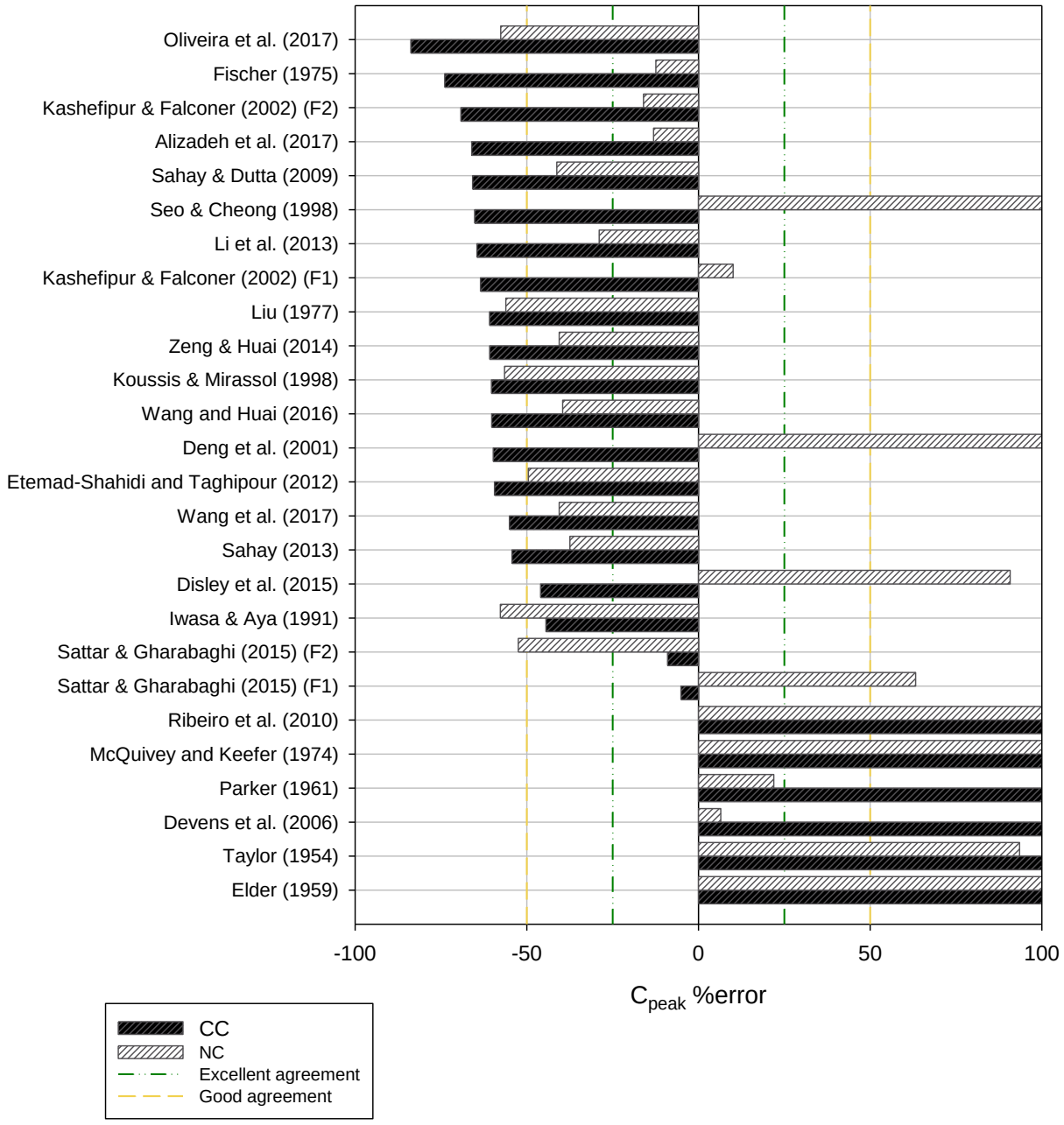

Figure 88. Peak concentration relative error for the concrete and natural channels.

A key observation from this analysis is that the peak concentration predictions had large variation on both channels. This parameter is of extreme importance for water quality predictions. In the case of turbidity (mainly caused by suspended sediment in water), for example, if the level is above certain limits it will trigger boil advisory alerts and adjustments to the drinking water treatment processes. Furthermore, most formulas yield overestimations of the longitudinal

dispersion coefficient, hence, underestimations of the peak. Several other studies in the literature have reached a similar conclusion (e.g., Ahsan 2008; Camacho Suarez et al. 2019; Carr 2007; Devens 2006). This is of relevance to regulatory compliance because it suggests that the probability of a modeler choosing, at random, a formula that will underestimate the peak concentration is greater than choosing a formula that will predict the exact or larger concentrations.

The peak time was the parameter predicted with the best accuracy and consistency on both channels. In the concrete channel, 25 out of 26 formulas yielded excellent agreement with observed peak times, while in the natural channel 22 out of 26. El Kadi Abderrezzak et al. (2015) also observed small percent errors for the prediction of peak times (average of 5%) while analyzing data from a laboratory flume. As mentioned in 5.1.3, since the peak time is mainly governed by the advection velocity, which was a fixed variable in this analysis, this parameter is not affected to any significant degree by the value of the longitudinal dispersion coefficient. The range of relative error for the peak time in the concrete channel (-35% to 4%) was smaller than the range of error on the natural channel (-83% to 18%), suggesting that the non-uniformities in a natural channel may increase the error in the prediction of travel times.

In both channels, the errors for start time of the plume from time of injection were slightly larger than the errors obtained for peak time. The reason for this is that the peak time is largely dependent only on the advection velocity whereas the start of the plume depends on both advection of the center of mass of the plume and dispersion or spreading of the plume. Interestingly, the formulas that were able to predict the peak concentration with less than 25% absolute error all underestimated the start times of the curves given that the one-dimensional ADE produces curves that are less skewed than the observed curves. These formulas also had the smallest error for the duration of the plume. As the spread of the plume increases the peak decreases, therefore, these two variables are closely related.

The duration predictions had the largest errors among the four parameters. However, as has already been established in the literature and confirmed based on the analysis conducted in 5.1.1.1, observed data from real channels have much longer tails than predicted by the one-dimensional ADE model. Therefore, part of the error in the duration parameter is associated with the general lack of agreement with the one-dimensional model and not necessarily linked to the longitudinal dispersion coefficient values. Furthermore, since the peak and duration are closely related, accurate

peak concentration predictions will lead to accurate duration predictions, therefore, this parameter does not require as much attention.

The error analysis for the predictive formulas applied to the concrete channel and natural channel indicates that the null hypothesis, that none of the available formulas are applicable to small streams, should be rejected. Therefore, it is reasonable to conclude that there is at least one predictive formula capable of estimating the longitudinal dispersion coefficient in small channels with better than ±50% accuracy, although none of the formulas had good agreement on both study channels.

The use of the percent error in relation to observed data allows a clear comparison of which formulas underestimate or overestimate the longitudinal dispersion coefficient and the characteristics of the concentration curves. This information is particularly important in the context of water quality predictions for drinking water safety. Camacho Suarez et al. (2019) also mentioned this in the context of environmental standards, after comparing several efficiency criteria for the predictive formulas of the longitudinal dispersion coefficient.

Although it cannot be stated for certain the reason some of the formulas performed better than others, some inferences can be drawn. As mentioned in 2.3.1, in the case of empirical formulas, it seems reasonable to expect that they should apply to channels that are similar to those represented in the data set to calibrate the formula. A cursory analysis of the parameters utilized to derive each formula pointed to the general lack of data on small channels in comparison to medium-sized and large channels as discussed in 2.3.1. The hydraulic characteristics of the studied channels (Table 68) were compared with the results of the cursory analysis from 2.3.1. The values of width and flow depth of the studied channels are not well represented in the data sets (Figure 89). It is also important to highlight that none of the calibration data sets include supercritical flow conditions (Fr > 1), which was the case for the concrete channel.

Table 68. Hydraulic reach-averaged characteristics for the studied channels where the longitudinal dispersion coefficient was estimated.

Channel	Q (m^3s^{-1})	A (m^2)	W (m)	H (m)	U (ms^{-1})	u_* (ms^{-1})	W/H	$\bar{U}/u_*$	Fr
Concrete channel	0.143	0.11	2.27	0.05	1.30	0.11	45	12	1.87

Channel	Q (m^3s^{-1})	A (m^2)	W (m)	H (m)	U (ms^{-1})	u_* (ms^{-1})	W/H	$\bar{U}/u_*$	Fr
Natural channel	0.042	0.28	3.89	0.08	0.15	0.09	50	2	0.19

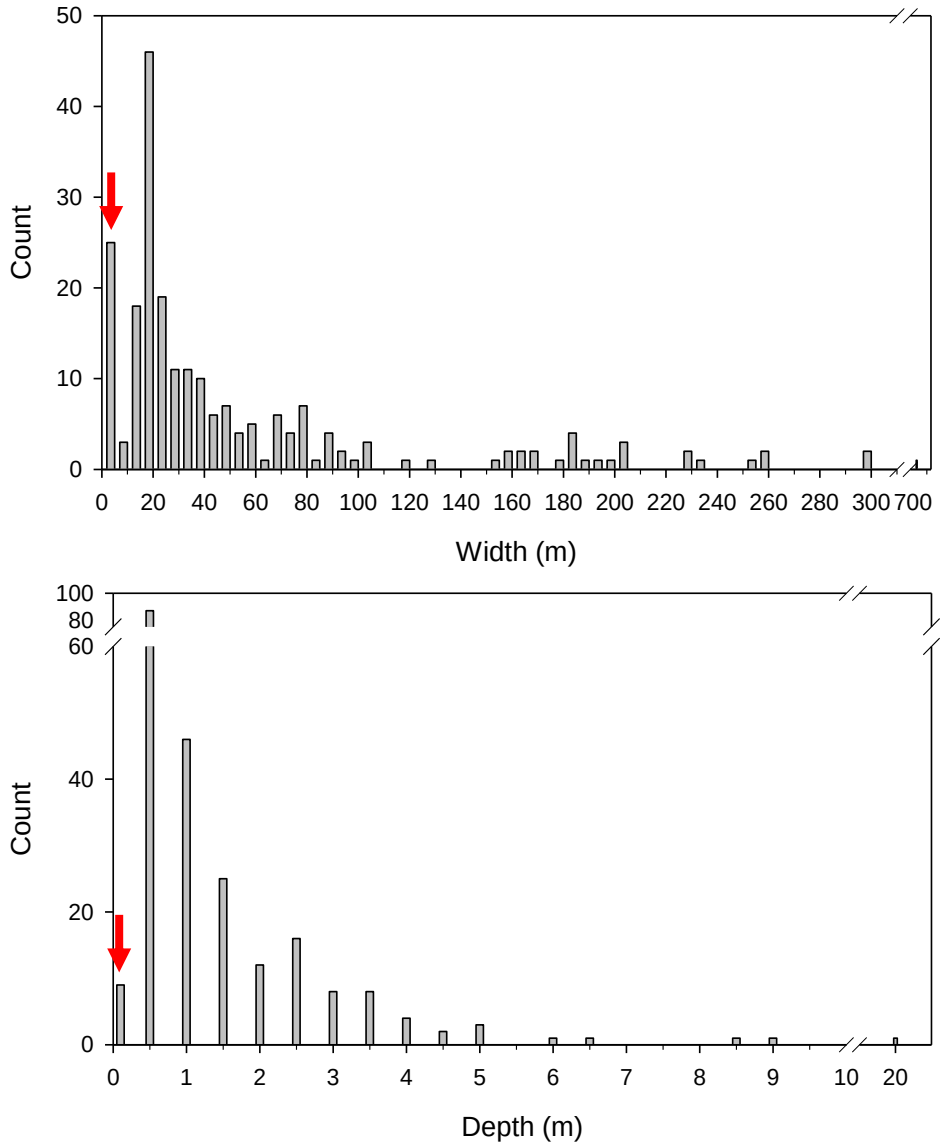

Figure 89. Frequency distribution of the data utilized to calibrate the empirical formulas for the longitudinal dispersion coefficient in Table 1. A) Width frequency distribution; B) Depth frequency distribution. The red arrows indicate the ranges corresponding to channels in this study.

However, the data sets utilized to calibrate the empirical formulas include channels with similar W/H and $\bar{U}/u_*$ ratios as the ones obtained for the concrete and natural channels (Table 68, Figure 90), as well as similar velocity and shear velocity values. This analysis suggests that having similar W/H and $\bar{U}/u_*$ ratios as the medium and large channels utilized for the calibration of the empirical formulas does not necessarily result in accurate predictions of the longitudinal dispersion coefficient in small channels.

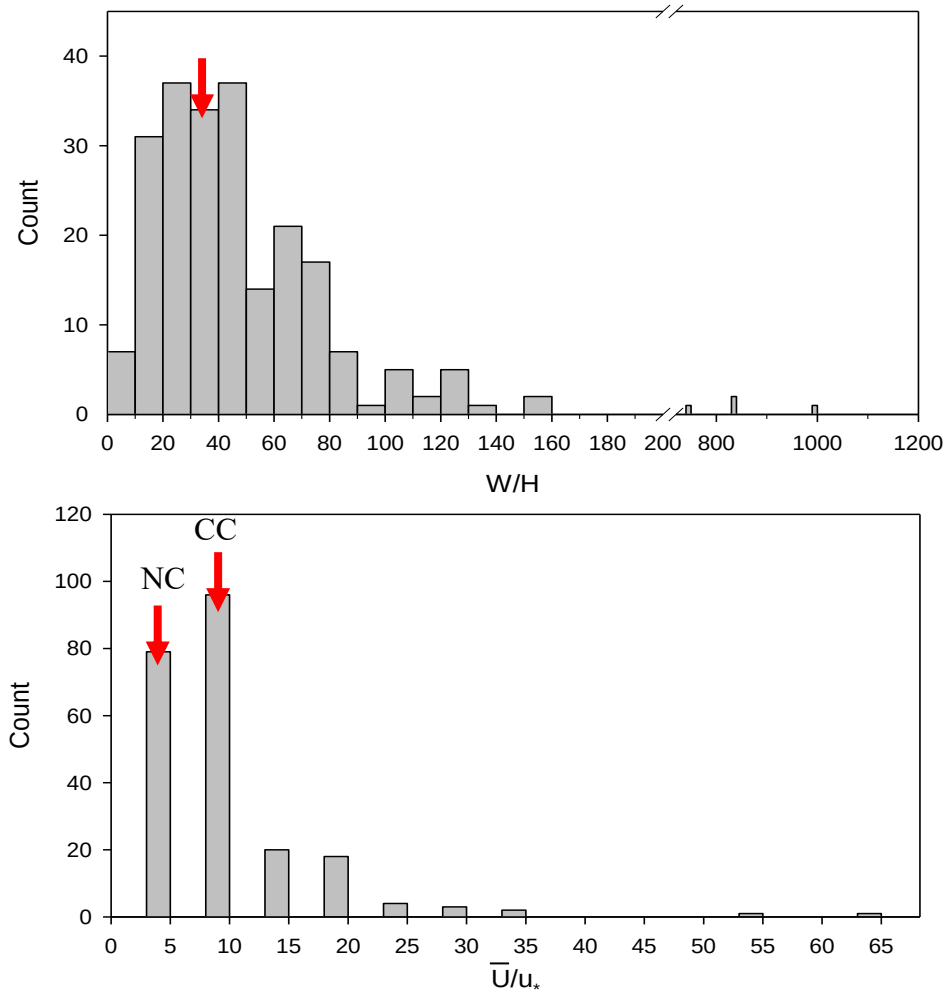

Figure 90. Frequency distribution of the data utilized to calibrate the empirical formulas for the longitudinal dispersion coefficient in Table 1. A) W/H frequency distribution; B) U/u_* frequency distribution. The red arrows indicate the ranges corresponding to channels in this study.

The formula from Devens (2006) had excellent agreement when predicting the natural channel longitudinal dispersion coefficient. This formula was calibrated based on data solely from channels with similar characteristics to the natural channel. The formula from Iwasa and Aya (1991) has been calibrated utilizing a large number of data points from laboratory flumes, which are not as complex as natural channels. This might explain the good agreement of this formula with the concrete channel data. The formula from Oliveira et al. (2017), despite having been calibrated using data solely from streams with similar width and shear velocity ranges as the concrete channel and the natural channel did not perform well in both channels. The calibration data included streams with larger flow depth (average of 0.57 m), which reduces the influence of the surface roughness on the dispersion process. Moreover, although the velocities are in the same range as the natural channel, they are much slower than the average concrete channel data, which could explain why this formula had larger errors in the concrete channel than the natural channel.

Other formulas such as Alizadeh et al. (2017), Disley et al. (2015), Etemad-Shahidi and Taghipour (2012), and Sattar and Gharabaghi (2015) have at least one data point acquired in small channels. However, they had very different results between channels, with some working really well in the concrete channel, but not the in natural channel, leading to the conclusion that either the calibration data set was not the major contributing factor in this case or that only a few data points from small channels in the data set will not increase the accuracy of the formulas for use with small channels. A good example of the first case are the formulas by Deng et al. (2001) and Li et al. (2013), which have been calibrated using the data set, but have yielded very different results on both channels. The formula of Deng et al. (2001) overestimated the concentration in the natural channel and underestimated in the concrete channel, while the formula of Li et al. (2013) underestimated the concentration on both channels. Furthermore, the formula of Deng et al. (2001) was developed to include the effects of lateral dispersion in the longitudinal dispersion coefficient. However, its performance was better on the concrete channel, where the lateral velocity profile was more uniform than in the natural channel. On the other hand, the formula by Sahay and Dutta (2009), which has been reportedly better at predicting longitudinal dispersion coefficients in large channels (Sahay and Dutta 2009), did not perform well on both channels, underestimating the peak concentration.

Given the uniform geometry of the concrete channel, it is reasonable to expect that theoretical formulas would work well in the concrete channel. However, most of them had large prediction errors. While the formulas from Elder (1959), Parker (1961), and Taylor (1954) largely overestimated the peak concentration and underestimated the duration of the curve, the formulas from Fischer (1975) and Liu (1977) underestimated the peak concentration and overestimated the duration of the curve. The formula from Elder (1959) also had large errors on both the natural channel. Several other studies have reported similar results. Launay et al. (2015) and Devens (2006) compared the values estimated by the formula with optimized values obtained from field experiments in medium and small channels, respectively. In both cases, the formula underestimated the observed values of the longitudinal dispersion coefficient. Seo and Cheong (1998) compared the values predicted by the formula of Elder (1959) against a data set with 59 data points from 26 medium and large rivers and also obtained a similar result. El Kadi Abderrezzak et al. (2015), on the contrary, compared 10 predicted formulas developed between 1959 and 2002, and reported that the formula of Elder (1959) had the best agreement with observed longitudinal dispersion coefficients from a laboratory flume. This formula was derived assuming flow in a channel with infinite width (Elder 1959), therefore, it does not consider the effect of transverse shear on the dispersion process (Fischer 1966; Rutherford 1994). In most natural channels, transverse shear is far more important in the dispersion process than vertical shear. The results from this research and previous studies suggest that this formula is not applicable to model dispersion in natural channels. The formula from Taylor (1954) was developed for pipe flows, therefore, it is expected that it should not provide good results in open-flows. Finally, based on the literature review conducted during this research, the formula by Parker (1961) has not been included in any previous studies regarding the accuracy of the longitudinal dispersion coefficient.

In contrast, the theoretical formulas by Parker (1961) and Fischer (1975), yielded good agreement with observed data in the natural channel. This is contrary to what has been reported in previous studies based on medium and large rivers. El Kadi Abderrezzak et al. (2015), Launay et al. (2015), and Seo and Cheong (1998), for example, reported that the formula of Fischer (1975) overestimated the longitudinal dispersion in field cases. Devens (2006) analyzed the accuracy of the formula by Fischer (1975) in two small streams and obtained errors from -99% to 1050% in relation to observed values of the longitudinal dispersion coefficient. While relative errors between ±50% were observed for one flow condition, much larger errors were obtained for the same stream,

under different flow conditions. These results highlight the importance of analyzing predictions by the same formula under different flow conditions, in order to determine if the results can be replicated.

Some of the formulas include the Froude number in the parameterization of the dispersion coefficient. The Froude number is closely related to the presence of lateral velocity gradients. Large Froude numbers lead to less variation in the lateral velocity distribution, therefore, little shear-induced dispersion and smaller values of the longitudinal dispersion coefficient (Fischer et al. 1979; Rutherford 1994). As a consequence, an increase in the slope or velocity of the flow leads to smaller longitudinal dispersion coefficients and vice-versa. None of the formulas other than Disley et al. (2015) and Sattar and Gharabaghi (2015) include the Froude number. Furthermore, the flow conditions in the concrete channel were supercritical on the day of the experiments. However, none of the predictive formulas were calibrated using data from supercritical flows.

The formulas by Sattar and Gharabaghi (2015), showed the best performance for the concrete channel. Both formulas have coefficients that vary according to the characteristics of the flow (Table 69) (all other formulas have fixed coefficients that depend on the characteristics of the calibration). Once the Froude number is larger than 0.5 for formula 1 (and the value $0.514Fr^{0.516}$ is larger than $0.5 + \frac{\bar{U}}{u_*}0.42^{\bar{U}/u_*}$, for formula 2), the exponent on W/H becomes negative. This means that with Fr < 1, W is more important than H, whereas, with Fr > 1, H is more important than W. In other words, the relative width is positively related to the longitudinal dispersion coefficient in sub-critical flows, and negatively related to the longitudinal dispersion coefficient in super-critical flows. For the concrete channel, the exponents were negative on both formulas (-1.37 for formula 1, and -0.21 for formula 2).

Table 69. Formulas of Sattar and Gharabaghi (2015).

Formula 1	$K_x = Hu_*(2.9 \times 4.6^{\sqrt{Fr}})\left(\frac{\bar{U}}{u_*}\right)^{1+\sqrt{Fr}}\left(\frac{W}{H}\right)^{0.5-Fr} Fr^{0.5}$
Formula 2	$K_x = Hu_* 8.45\left(\frac{\bar{U}}{u_*}\right)^{1.65}\left(\frac{W}{H}\right)^{0.5-0.514Fr^{0.516}+\frac{\bar{U}}{u_*}0.42^{\bar{U}/u_*}}$

The formula by Disley et al. (2015), which includes the inverse of the Froude number, yielded good agreement with the observed data in the concrete channel, but only fair agreement with data in the natural channel. The formula of McQuivey and Keefer (1974) was developed strictly for Fr < 0.5. This could explain the poor level of agreement produced in the concrete channel, although this formula also yielded poor predictions in the natural channel, which had Fr < 0.5, underestimating the longitudinal dispersion coefficient. The analyses conducted by Seo and Cheong (1998) and Devens et al. (2010) have also suggested that this formula underestimates the value of the longitudinal dispersion coefficient in small streams.

The effects of surface roughness are larger in wide, shallow channels (i.e., large W/H ratios), such as the ones studied here, than in narrow, deep channels. Five out of the seven formulas that had good agreement with observed data in the natural channel had a coefficient for the $\bar{U}/u_*$ ratio larger than 1 (Alizadeh et al. 2017; Fischer 1975; Li et al. 2013; Sahay 2013; Wang and Huai 2016). Furthermore, none of these formulas had good agreement with data in the concrete channel, which could be related to the smaller importance of surface roughness in a smooth concrete bed. Although there was no proportional relationship between the value of this specific coefficient and the level of agreement of the formula, this might reinforce the importance of the surface roughness ratio parameter in the case of natural channels. In contrast, three formulas that also have a coefficient larger than 1 for the $\bar{U}/u_*$ ratio (Oliveira et al. 2017; Sahay and Dutta 2009; Seo and Cheong 1998) had either poor or fair agreement with data on both channels, which points out to the importance of the other coefficients in the formula as well.

The two formulas from Kashefipour and Falconer (2002) had good performance in the natural channel, being able to predict the peak concentration with excellent accuracy. Devens (2006) analyzed the accuracy of one of these formulas (F2) and also observed good agreement with data from small channels. Combined with the results from this research, the results from Devens (2006) suggest that this formula might also be a good predictor for small channels in subcritical flows, given that both formulas had large errors in the concrete channel. According to Kashefipour and Falconer (2002), F1 had better performance in channels with W/H > 50, while F2 had better performance in channels with W/H < 50. The natural channel had a W/H = 50, which could explain why both formulas had very similar results. The formulas by Liu (1977) and Koussis and Rodríguez-Mirsasol (1998) had similar performances on both channels. Devens (2006) also

observed a similar result when assessing their accuracy on small channels. Both of these formulas have been developed based on the formula by Fischer (1975), suggesting that their structures do not fully include represent dispersion in small channels. Finally, the formula of Seo and Cheong (1998) also had a worse performance than the F2 by Kashefipour and Falconer (2002) on the analysis conducted by Devens (2006). These similarities point out a general consistency of the performance of these formulas in small channels.

Overall, the error range reported in this research is much larger than previous errors reported in the literature, which are often within ±100% (e.g., Camacho Suarez et al. 2019; El Kadi Abderrezzak et al. 2015; Kashefipour and Falconer 2002). This is likely partially related to the lack of representation of small channels in the calibrating data sets. For example, Camacho Suarez et al. (2019) assessed the accuracy of six formulas (Deng et al. 2001; Disley et al. 2015; Etemad-Shahidi and Taghipour 2012; Wang et al. 2017; Wang and Huai 2016; Zeng and Huai 2014) and found that all formulas would be equally suitable when predicting the longitudinal dispersion coefficient for a channel with average width, depth, and slope of 16.4 m, 0.7 m, 0.005, respectively.

In conclusion, the accuracy of the predictive formulas will largely vary according to the characteristics of the stream of interest. This is largely influenced by the calibration data set in the case of empirical formulas, but also by the structure of the formula (fixed or variable coefficients). For the concrete channel, the Froude number was the deciding factor, while in the natural channel, one of the best formulas was the one that was calibrated using data similar to the natural channel. At the same time, very different theoretical formulas and formulas containing no empirical data from small channels also performed well in the natural channel, making it extremely difficult to draw a conclusion regarding which parameters have more influence on the longitudinal dispersion coefficient. Further analysis of the accuracy of such formulas is necessary to determine if they can be indeed applied to small channels as these results suggest. In general, it appears that, without conducting an assessment of the formulas in the stream of interest, the best approach to predicting longitudinal dispersion coefficients is to utilize formulas that were calibrated under similar flow and channel conditions as the stream of interest. These results also suggest that the development of more specific formulations rather than “universal” formulas based on very diverse data sets might be more beneficial for accurate water quality predictions.

Chapter 6: Conclusion and recommendations

6.1. Conclusions

The main objective of this research was to better understand the dynamics of sediment plume dispersion in small streams with a view towards mitigating the potential negative impacts of turbidity-based events on water quality.

The first research question addressed the accuracy of the one-dimensional ADE when predicting suspended sediment dispersion in small channels. The findings of this research indicate that the advection-dispersion of fine-grained sediment ($d<0.075$ mm), travelling predominantly in the suspension mode, was similar to that of sodium chloride. Based on the longitudinal dispersion coefficients derived from the sodium chloride plumes, the one-dimensional ADE was able to predict the peak concentration, start time, and peak time of suspended sediment plumes with good levels of agreement (±50% error) for both the uniform concrete channel as well as the natural channel.

The coarse grain sizes were less reliably modeled because of the greater relative importance of particle settling. The formula commonly utilized to estimate the settling rate always overestimated the actual settling rates in both channels, leading to an underestimation of the concentration. This is likely due to the fact that settling velocities of particles are commonly estimated in still fluids and do not account for the turbulence that keeps particles in suspension or re-entrains particles from the bed.

Although the suspended sediment plumes do not behave strictly according to the theoretical Fickian model, the observed data demonstrate that the relative importance of advection decreases in the downstream direction, while the importance of turbulent diffusion and lateral shear increases, leading to a better balance as is expected in the equilibrium zone. These results suggest that, with the correct coefficients obtained sufficiently far downstream of the injection point, the one-dimensional ADE can be utilized to model suspended sediment dispersion of particles (at least up to 1 mm in size) with reasonable accuracy. However, obtaining the correct values for the coefficients remains a challenge, especially if no field data are available.

In the advective zone, immediately downstream of injection, the results of the one-dimensional ADE are less accurate although in the range of ±100%. When the length of the

advective zone is not known, this margin of error should be built into the model predictions. This is particularly important in the case of the peak concentration, which is typically greater than the value predicted by models in the advective zone, and therefore may lead to unforeseen water quality management problems. The results also demonstrated the importance of assessing the measured data with regard to sampling location in order to determine whether sampling stations are located in the equilibrium zone, where reliable estimates of the longitudinal dispersion coefficient can be obtained.

Cross-sectional concentration differences are rarely measured in tracer studies and it is usually assumed that after a certain distance downstream, measured concentrations will reflect the cross-sectionally averaged concentration. The lateral mixing measurements in this study have suggested, however, that there will always be lateral cross-sectional differences in concentrations caused by the lateral velocity profile and by transient storage. This was particularly evident because lateral injections rather than slug injections were used in this study. Therefore, it is important to bear in mind that concentration values modeled with the one-dimensional ADE represent the average cross-sectional concentration, and that larger or smaller concentrations are likely to occur in real streams depending on horizontal position.

The second research question concerned the applicability of formulas for predicting the longitudinal dispersion coefficients to small channels. This thesis is the most comprehensive comparison to date between predictive formulas for the longitudinal dispersion coefficient, including the application of the predicted coefficients to model concentration curves and a cursory analysis of the calibrating data sets. Twenty-six formulas were evaluated and compared based on the relative error against observed data in small channels. The findings demonstrate that the predictive accuracy of the formulas is extremely variable. The longitudinal dispersion coefficient includes the non-uniformities of the channels and it is very unique; therefore, it is difficult for formulas to capture the large heterogeneity of mixing processes in a single predictor. Given the general absence of small channels in the empirical data that were utilized for the calibration of these formulas, most of them are not capable of predicting the dispersion process in small channels with less than ±50% error. None of the formulas analyzed were capable of replicating the observed data trends in both the concrete channel and the natural channel with excellent or good agreement. In the context of water quality assessments in small streams, it is advisable to look for a formula

that has been calibrated utilizing data solely from streams with similar characteristics, in order to assure high levels of accuracy, as was demonstrated by the results for the natural channel. Otherwise, it is suggested that the two formulas from Sattar and Gharabaghi (2015) should be utilized, since they had the best performance overall, being able to predict the concentrations with the largest accuracy on both channels. Furthermore, the results from this research indicate that it might be beneficial to develop formulas for the longitudinal dispersion coefficients that are more case-specific and can assure high levels of accuracy, instead of the common approach of developing "universal" formulas with large degrees of uncertainty.

This research has also introduced a novel truncation criterion for concentration curves that takes into consideration the dispersion characteristics of the stream of interest. This criterion does not depend on a percentage of the peak concentration; therefore, it can be applied to curves where the tails have concentration fluctuations and do not return to the background value. Furthermore, this criterion accounts for the skewness of the curves commonly observed in field data. The fact that some of the measured concentration curves were located in the advective zone had some implications for the results. Part of the skewness of the curves, caused by velocity shear in the advective zone, decreases in the downstream direction. As a consequence, the ratio log (T_{start})/log ($t_{start-peak}$) decreased in the downstream direction. The analysis of log (T_{start})/log ($t_{start-peak}$) versus distance suggests that the ratio might be reaching a constant value in the equilibrium zone, however, more measurements in this region would be necessary to confirm this hypothesis. The average log (T_{start})/log ($t_{start-peak}$) value obtained is likely larger than the average value that would be obtained if only curves in the equilibrium zone had been measured. Furthermore, when applied to curves in the equilibrium zone, this average value might be overestimating the duration of the curves. A similar conclusion can be drawn for the log ($T_{injection}$)/log($t_{injection-peak}$) ratios. Therefore, if one has curves measured in both the advective and equilibrium zones, the injection time is certainly the preferred reference time. Further analysis is required in order to determine which reference time is more appropriate if the curves are measured only in the equilibrium zone.

Conclusions here apply to the specific flow conditions studied and likely for channels with similar geometry characteristics. Nevertheless, the results and analyses conducted in this research

can serve as a practical guide to engineers and scientists that do not have access to tracer data when modeling suspended sediment dispersion in small streams.

6.2.Future research

Based on the findings of this research, the following topics would be fruitful avenues for future work on longitudinal dispersion:

- The results suggest that the lateral velocity profiles play an important role, particularly in the advective zone. Given the shallow flow depths of the studied channels, lateral velocity profiles could not be measured in the sampling locations. Flow conditions allowing, lateral velocity profiles should be measured to increase the understanding of the effects of velocity shear on concentration gradients. Hence, a better understanding of the causes of the long tails on the observed data.
- Lateral line injections were conducted in order to help induce lateral mixing and decrease the length of the advection zone. It is known, however, that the advective zone length is longer for point sources. A comparison between point and lateral injections in small channels could help improve predictions for the advection length as well as the effects of lateral velocity shear on a point source.
- The equilibrium longitudinal coefficients reported in this thesis were obtained under only one discharge in each of the channels. Experiments could be conducted in a single channel but under different flow conditions to investigate the effects of different hydraulic parameters on the longitudinal dispersion coefficient in small channels.
- Flume experiments can be utilized to investigate the dispersion processes in a highly controllable environment that does not have the heterogeneities of natural channels. The relation between parameters of the flow (depth, discharge, slope, velocity) and the characteristics of the concentration curves (recovery, peak, and travel times), as well as the settling rate, could be investigated.

Bibliography

Ahmad, Z. (1997). “Longitudinal dispersion of conservative pollutants in open channels.” Thapar Institute of Engineering and Technology.

Ahsan, N. (2008). “Estimating the Coefficient of Dispersion for a Natural Stream.” *World Academy of Science, Engineering and Technology*, (20), 131–135.

Alizadeh, M. J., Ahmadyar, D., and Afghantoloee, A. (2017). “Improvement on the existing equations for predicting longitudinal dispersion coefficient.” *Water Resources Management*, Springer, 31(6), 1777–1794.

Allen, M. J., Brecher, R. W., Copes, R., Hrudey, S. E., and Payment, P. (2008). *Turbidity and Microbial Risk in Drinking Water*. *Ministerial Technical Advisory Committee*.

Ani, E. C., Wallis, S., Kraslawski, A., and Agachi, P. S. (2009). “Development, calibration and evaluation of two mathematical models for pollutant transport in a small river.” *Environmental Modelling and Software*, 24, 1139–1152.

Atkinson, T. C., and Davis, P. M. (2000). “Longitudinal dispersion in natural channels: 1. Experimental results from the River Severn, U.K.” *Hydrology and Earth System Sciences*, 4(3), 345–353.

Barnett, A. G. (1983). “Exact and approximate solutions of the advection-diffusion equation.” *Proceedings of the 20th IAHR Congress*, Moscow, 180–190.

Benedini, M. (2011). “Water quality models for rivers and streams. State of the art and future perspectives.” *European water*, 34(1), 27–40.

Benettin, P., Rinaldo, A., and Botter, G. (2013). “Kinematics of age mixing in advection-dispersion models.” *Water Resources Research*, 49, 8539–8551.

Bilotta, G. S., and Brazier, R. E. (2008). “Understanding the influence of suspended solids on water quality and aquatic biota.” *Water Research*, 42(12), 2849–2861.

Bottacin-Busolin, A. (2017). “Non-Fickian dispersion in open-channel flow over a porous bed.” *Water Resources Research*, 53, 7426–7456.

Camacho Suarez, V. V., Schellart, A. N. A., Brevis, W., and Shucksmith, J. D. (2019).

"Quantifying the impact of uncertainty within the longitudinal dispersion coefficient on concentration dynamics and regulatory compliance in rivers." *Water Resources Research*, 55, 4393–4409.

Carr, M. L. (2007). "An efficient method for measuring the dispersion coefficient in rivers." University of Illinois.

Chanson, H. (2004). *Environmental hydraulics of open channel flows*. *Elsevier All Access Books, Books24x7*, Elsevier Ltd., Amsterdam, Boston.

Chatwin, P. C. (1971). "On the interpretation of some longitudinal dispersion experiments." *Journal of Fluid Mechanics*, 48(4), 689–702.

Chau, K. (2000). "Transverse mixing coefficient measurements in an open rectangular channel." *Advances in Environmental Research*, 4, 287–294.

Cheong, T. S., and Seo, I. W. (2003). "Parameter estimation of the transient storage model by a routing method for river mixing processes." *Water Resources Research*, 39(4), 1074-n/a.

Chou, Y.-J., Nelson, K. S., Holleman, R. C., Fringer, O. B., Stacey, M. T., Lacy, J. R., Monismith, S. G., and Koseff, J. R. (2018). "Three-Dimensional Modeling of Fine Sediment Transport by Waves and Currents in a Shallow Estuary." *Journal of Geophysical Research: Oceans*, 123(6), 4177–4199.

Chow, V. Te. (1959). *Open-channel hydraulics*. McGraw-Hill, New York.

Cushman, J. H., and O'Malley, D. (2015). "Fickian dispersion is anomalous." *Journal of Hydrology*, 531, 161–167.

Demetracopoulos, A. C., and Stefan, H. G. (1983). "Transverse mixing in wide and shallow river: case study." *Journal of Environmental Engineering*, 109(3), 685–699.

Deng, Z.-Q., Singh, V. P., Fellow, ASCE, and Bengtsson, L. (2001). "Longitudinal dispersion coefficients in straight rivers." *Journal of Hydraulic Engineering*, 127(11), 919–927.

Devens, J. A. (2006). "Quantificação do coeficiente de dispersão longitudinal em pequenos cursos d'água naturais com uso de traçador ambientalmente neutro." Universidade Federal de Ouro Preto.

Devens, J., Junior, A., Silva, G., and Giorgetti, M. (2010). “Modelos Empíricos e Semi-Empíricos para a Obtenção do Coeficiente de Dispersão Longitudinal de Pequenos Cursos de Água.” *Revista Brasileira de Recursos Hídricos*, 15(1), 75–88.

Dietrich, W. E. (1982). “Settling velocity of natural particles.” *Water Resources Research*, 18(6), 1615–1626.

Disley, T., Gharabaghi, B., Mahboubi, A. A., and Mcbean, E. A. (2015). “Predictive equation for longitudinal dispersion coefficient.” *Hydrological Processes*, 29(2), 161–172.

Douillet, P., Ouillon, S., and Cordier, E. (2001). “A numerical model for fine suspended sediment transport in the southwest lagoon of New Caledonia.” *Coral Reefs*, 20(4), 361–372.

Downing, J. (2008a). “Effects of Light Absorption and Scattering in Water Samples on OBS Measurements.” *Campbell Scientific Application Note*, 2Q-Q.

Downing, J. (2008b). “Effects of Sediment Size on OBS Measurements.” *Campbell Scientific Application Note*, 2Q-T.

Drummond, J. D., Covino, T. P., Aubeneau, A. F., Leong, D., Patil, S., Schumer, R., and Packman, A. I. (2012). “Effects of solute breakthrough curve tail truncation on residence time estimates: A synthesis of solute tracer injection studies.” *Journal of Geophysical Research*, 117, 1–11.

Duarte, A. A. L. S., and Boaventura, R. A. R. (2008). “Dispersion modelling in rivers for water sources protection, based on tracer experiments. Case studies.” *2nd International Conference on Waste Management, Water Pollution, Air Pollution, Indoor Climate (WWAI’08)*, 205–210.

Elder, J. W. (1959). “The dispersion of marked fluid in turbulent shear flow.” *Journal of Fluid Mechanics*, 5(4), 544–560.

Elhadi, N., Harrington, A., Hill, I., Lau, Y. L., and Krishnappan, B. G. (1984). “River mixing - A state-of-the-art report.” *Canadian Journal of Civil Engineering*, 11, 585–609.

Etemad-Shahidi, A., and Taghipour, M. (2012). “Predicting longitudinal dispersion coefficient in natural streams using M5’ model tree.” *Journal of Hydraulic Engineering*, 138(6), 542–554.

Fick, A. (1995). “On liquid diffusion.” *Journal of Membrane Science*, (Reprinted from the London, Edinburgh, and Dublin Philosophical Magazine and Journal of Science, Vol. 10, p.30-39,

1855), 100(1), 33–38.

Fischer, H. B. (1966). “Longitudinal dispersion in laboratory and natural streams.” *California Institute of Technology*, Report No.KH-R-12.

Fischer, H. B. (1967). “The mechanics of dispersion in natural streams.” *Journal of the Hydraulics Division*, 93(6), 187–216.

Fischer, H. B. (1968). “Dispersion predictions in natural streams.” *Journal of the Sanitary Engineering Division*, 94(5), 927–944.

Fischer, H. B. (1973). “Longitudinal dispersion and turbulent mixing in open-channel flow.” *Annual Review of Fluid Mechanics*, 5, 59–78.

Fischer, H. B. (1975). “Discussion of simple method for predicting dispersion in streams by Raul S. McQuivey and Thomas N. Keefer.” *Journal of the Environmental Engineering Division*, 101(3), 453–455.

Fischer, H. B., List, E. J., Koh, R. C. Y., Imberger, J., and Brooks, N. H. (1979). *Mixing in inland and coastal waters*. Academic Press, INC.

Van Genuchten, M. T., Leij, F. J., Skaggs, T. H., Toride, N., Bradford, S. A., and Pontedeiro, E. M. (2013). “Exact analytical solutions for contaminant transport in rivers 1. The equilibrium advection-dispersion equation.” *Journal of Hydrology and Hydromechanics*, 61(2), 146–160.

Göransson, G., Larson, M., Bendz, D., and Åkesson, M. (2012). “Mass transport of contaminated soil released into surface water by landslides (Göta River, SW Sweden).” *Hydrology and Earth System Sciences*, 16(7), 1879–1893.

Guymer, I. (1998). “Longitudinal dispersion in sinuous channel with changes in shape.” *Journal of Hydraulic Engineering*, 124(1), 33–40.

Holley, E. R., Siemons, J., and Abraham, G. (1972). “Some Aspects Of Analyzing Transverse Diffusion In Rivers.” *Journal of Hydraulic Research*, 10(1), 27–57.

Iwasa, Y., and Aya, S. (1991). “Predicting longitudinal dispersion coefficient in open-channel flows.” *Proceedings of the International Symposium on Environmental Hydraulics*, Hong Kong, 505–510.

Ji, Z. G. (2008). *Hydrodynamics and water quality: modeling rivers, lakes, and estuaries*. Wiley-Interscience, Hoboken, N.J.

Jiménez, J. A., and Madsen, O. S. (2003). "A simple formula to estimate settling velocity of natural sediments." *Journal of Warterway, Port, Coastal and Ocean Engineering*, 129(2), 70–78.

Julien, P. Y. (2010). *Erosion and sedimentation*. Cambridge University Press, Cambridge; New York.

El Kadi Abderrezzak, K., Ata, R., and Zaoui, F. (2015). "One-dimensional numerical modelling of solute transport in streams: the role of longitudinal dispersion coefficient." *Journal of Hydrology*, 527, 978–989.

Karwan, D. L., and Saiers, J. E. (2009). "Influences of seasonal flow regime on the fate and transport of fine particles and a dissolved solute in a New England stream." *Water Resources Research*, 45(11), 1–9.

Kashefipour, S. M., and Falconer, R. A. (2002). "Longitudinal dispersion coefficients in natural streams." *Water Research*, 36, 1596–1608.

Kim, D. (2012). "Assessment of longitudinal dispersion coefficients using Acoustic Doppler Current Profilers in large river." *Journal of Hydro-environment Research*, 6, 29–39.

Koussis, A. D., and Rodríguez-Mirasol, J. (1998). "Hydraulic estimation of dispersion coefficient for streams." *Journal of Hydraulic Engineering*, 124(3), 317–320.

Koussis, A. D., Saenz, M. A., and Tollis, I. G. (1983). "Pollution routing in streams." *Journal of Hydraulic Engineering*, 109(12), 1636–1651.

Launay, M., Le Coz, J., Camenen, B., Walter, C., Angot, H., Dramais, G., Faure, J. B., and Coquery, M. (2015). "Calibrating pollutant dispersion in 1-D hydraulic models of river networks." *Journal of Hydro-environment Research*, 9, 120–132.

Leibundgut, C., Maloszewski, P., Külls, C., and Kulls, C. (2009). *Tracers in Hydrology*. Wiley-Blackwell, Chichester, West Sussex, UK;Hoboken, NJ.

Li, X., Liu, H., and Yin, M. (2013). "Differential evolution for prediction of longitudinal dispersion coefficients in natural streams." *Water Resources Management*, 27, 5245–5260.

Liu, H. (1977). “Predicting dispersion coefficients of streams.” *Journal of the Environmental Engineering Division*, 103(1), 56–69.

Liu, H., and Cheng, A. H. D. (1980). “Modified Fickian model for predicting dispersion.” *Journal of the Hydraulics Division*, 106(6), 1021–1040.

Luo, J., Cirpka, O. A., and Kitanidis, P. K. (2006). “Temporal-moment matching for truncated breakthrough curves for step or step-pulse injection.” *Advances in Water Resources*, 29, 1306–1313.

Magazine, M. K., Pathak, S. K., and Pande, P. K. (1988). “Effect of bed and side roughness on dispersion in open channels.” *Journal of Hydraulic Engineering*, 114(7), 766–782.

Van Mazijk, A., and Veling, E. J. M. (2005). “Tracer experiments in the Rhine Basin: evaluation of the skewness of observed concentration distributions.” *Journal of Hydrology*, 307, 60–78.

McQuivey, R. S., and Keefer, T. N. (1974). “Simple method for predicting dispersion in streams.” *Journal of the Environmental Engineering Division*, 100(4), 977–1011.

Moore, R. D. D. (2005). “Slug injection using salt in solution.” *Streamline Watershed Management Bulletin*, 8(2), 1–6.

Nordin, C. F. J., and Sabol, G. V. (1974). *Empirical data on longitudinal dispersion in rivers*. *Water Resources Investigations*, Washington, DC.

“Okanagan Basin Water Board.” (2019). *Community Water Forum – November 19, 2019*, <https://www.obwb.ca/community-water-forum-november-19-2019/> (Nov. 19, 2019).

Oliveira, V. V. de, Mateus, M. V., Gonçalves, J. C. D. S. I., Utsumi, A. G., and Giorgetti, M. F. (2017). “Prediction of the longitudinal dispersion coefficient for small watercourses.” *Acta Scientiarum. Technology*, 39(3), 291–299.

Palu, M. C., and Julien, P. Y. (2019). “Modeling the sediment load of the Doce River after the Fundão tailings dam collapse, Brazil.” *Journal of Hydraulic Engineering*, 145(5), 05019002-1–14.

Pannone, M. (2017). “An analytical model of Fickian and non-Fickian dispersion in evolving-scale log-conductivity distributions.” *Water*, 9(10), 1–17.

Parker, F. L. (1961). “Eddy diffusion in reservoirs and pipelines.” *Journal of the Hydraulics Division*, 87(3), 151–171.

Ribeiro, C. B. M., da Silva, D. D., Soares, J. H. P., and Guedes, H. A. S. (2010). “Development and validation of an equation to estimate longitudinal dispersion coefficient in medium-sized rivers.” *Engenharia Sanitaria e Ambiental*, 15(4), 393–400.

Roberts, P. J. W., and Webster, D. R. (2002). “Turbulent Diffusion.” *Environmental Fluid Mechanics: Theories and Applications*, American Society of Civil Engineers, Reston, VA.

Rouse, H. (1937). “Modern conceptions of the mechanics of fluid turbulence.” *Transactions of the American Society of Civil Engineers*, 102(1), 463–505.

Rutherford, J. C. (1994). *River Mixing*. Wiley, New York.

Sahay, R. R. (2013). “Predicting longitudinal dispersion coefficients in sinuous rivers by genetic algorithm.” *Journal of Hydrology and Hydromechanics*, 61(3), 214–221.

Sahay, R. R., and Dutta, S. (2009). “Prediction of longitudinal dispersion coefficients in natural rivers using genetic algorithm.” *Hydrology Research*, 40(6), 544–552.

Sattar, A. M. A., and Gharabaghi, B. (2015). “Gene expression models for prediction of longitudinal dispersion coefficient in streams.” *Journal of Hydrology*, 524, 587–596.

Sayre, W. W. (1969). “Dispersion of silt particles in open channel flow.” *Journal of the Hydraulics Division*, 95(3), 1009–1040.

Sayre, W. W. (1973). “Transport and dispersion of fluvial sediments. Some mathematical models and their verification by tracer methods.” *Tracer techniques in sediment transport*, International Atomic Energy Agency, Vienna, 49–68.

Sayre, W. W. (1975). *Dispersion of mass in open-channel flow*. *Hydrology Papers*, Colorado State University.

Sayre, W. W., and Chang, F. M. (1968). “A Laboratory Investigation of the Open Channel Dispersion Processes for Dissolved, Suspended, and Floating Dispersants.” *U.S. Geological Survey Professional Paper*, 433-E, E1–E71.

Schmadel, N. M., Neilson, B. T., and Stevens, D. K. (2010). “Approaches to estimate uncertainty

in longitudinal channel water balances." *Journal of Hydrology*, 394, 357–369.

Schmid, B. H. (2002). "Persistence of skewness in longitudinal dispersion data: can the dead zone model explain it after all?" *Journal of Hydraulic Engineering*, 128(9), 848–854.

Schnoor, J. L. (1996). *Environmental modeling: fate and transport of pollutants in water, air, and soil*. Wiley, New York.

Seo, W., and Cheong, T. S. (1998). "Predicting longitudinal dispersion coefficient in natural streams." *Journal of Hydraulic Engineering*, 124(1), 25–32.

Shahrabadi, A., Kamalipour, M., and Jamialahmadi, M. (2016). "A new method for reducing the numerical dispersion in mathematical modeling of miscible injection process." *Energy Sources, Part A: Recovery, Utilization and Environmental Effects*, 38(7), 928–934.

Sharma, H., and Ahmad, Z. (2014). "Transverse mixing of pollutants in streams: a review." *Canadian Journal of Civil Engineering*, 41(5), 472–482.

Singh, S., Ahmad, Z., and Kothyari, U. C. (2010). "Mixing coefficients for longitudinal and vertical mixing in the near field of a surface pollutant discharge." *Journal of Hydraulic Research*, 48(1), 91–99.

Taylor, G. (1922). "Diffusion by continuous movements." *Proceedings of the London Mathematical Society*, S2-20(1), 196–212.

Taylor, G. (1954). "The dispersion of matter in turbulent flow through a pipe." *Proceedings of the Royal Society A: Mathematical, Physical and Engineering Sciences*, 223(1155), 446–468.

Valentine, E. M., and Wood, I. R. (1979). "Experiments in longitudinal dispersion with dead zones." *Journal of the Hydraulics Division*, 105(HY8), 999–1016.

Velísková, Y., Halaj, P., Sokáč, M., and Bárek, V. (2014). "Pollution spread analysis in the Malá Nitra River by using of 1-D model." *Acta Horticulturae et Regiotectuare*, 17(2), 38–42.

Wallis, S. G., Bonardi, D., and Silavwe, D. D. (2014). "Solute transport routing in a small stream." *Hydrological Sciences Journal*, 59(10), 1894–1907.

Wallis, S. G., and Manson, J. R. (2004). "Methods for predicting dispersion coefficients in rivers." *Proceedings of the Institution of Civil Engineers - Water Management*, 157(VM3), 131–141.

Wallis, S., and Manson, J. R. (2005). “On the theorerical prediction of longitudinal dispersion coefficients in a compound channel.” *Water Quality Hazards and Dispersion of Pollutants*, W. Czernuszenko and P. M. Rowiński, eds., Springer, New York, NY, 69–84.

Wang, Y. F., Huai, W. X., and Wang, W. J. (2017). “Physically sound formula for longitudinal dispersion coefficients of natural rivers.” *Journal of Hydrology*, 544, 511–523.

Wang, Y., and Huai, W. (2016). “Estimating the longitudinal dispersion coefficient in straight natural rivers.” *Journal of Hydraulic Engineering*, 142(11), 04016048-1–11.

World Health Organization. (2017). “Water quality and health - Review of turbidity: Information for regulators and water suppliers.” *Who/Fwc/Wsh/17.01*, 10.

Zeng, Y. H., and Huai, W. X. (2014). “Estimation of longitudinal dispersion coefficient in rivers.” *Journal of Hydro-environment Research*, 8, 2–8.

Appendices

Appendix A

Surveyed geometry data from the concrete channel.

Table A 1. Surveyed cross-sections in the concrete channel.

Distance from injection line							
15.7 m		**42.50 m**		**75.70 m**		**139.95 m**	
Distance from LB (m)	Elevation (m)	Distance from LB (m)	Elevation (m)	Distance from LB (m)	Elevation (m)	Distance from LB (m)	Elevation (m)
0.00	428.601	2.74	426.146	0.00	427.213	0.00	425.806
1.44	427.615	3.00	426.115	1.88	425.981	1.90	424.572
2.54	426.835	3.30	426.095	2.59	425.511	2.71	424.053
2.74	426.725	3.60	426.054	2.75	425.411	2.75	424.020
3.14	426.675	3.73	426.023	3.28	425.341	3.05	424.000
3.64	426.575	4.00	426.069	3.77	425.321	3.34	423.935
4.24	426.685	4.30	426.097	4.33	425.361	3.54	423.953
4.99	426.715	4.60	426.113	4.97	425.401	3.85	423.979
5.24	426.837	4.90	426.141	5.19	425.511	4.05	423.980
6.04	427.443	5.06	426.143	5.86	425.946	4.42	423.970
7.70	428.594	7.70	427.872	7.70	427.211	4.62	423.988
						4.99	424.022
						5.00	424.023
						5.90	424.612
						7.70	425.779

Table A 2. Thalweg and waterline survey.

Distance from injection line (m)	**Thalweg elevation (m)**	**Distance from injection line (m)**	**Waterline elevation (m) ($Q = 0.698\ m^3s^{-1}$)**
0	427.057	0	427.187
4	426.907	4	427.087
8	426.817	8	427.022
8.25	426.812	12	426.917
12	426.727	16	426.827
20	426.577	20	426.742
24	426.507	24	426.677
27.05	426.458	28	426.542
28	426.427	32	426.482
32	426.331	36	426.389
36	426.257	40	426.332
40	426.182	45.37	426.239
42.5	426.023	49.37	426.089
45.37	426.044	53.37	426.047
49.37	425.967	57.37	426.002
53.37	425.851	61.37	425.969
57.37	425.807	65.37	425.896
61.625	425.554	69.37	425.842

Distance from injection line (m)	Thalweg elevation (m)	Distance from injection line (m)	Waterline elevation (m) ($Q = 0.698\ m^3s^{-1}$)
77.37	425.387	73.37	425.607
79.37	425.347	77.37	425.547
80.65	425.112	79.37	425.547
81.37	425.297	81.37	425.477
85.37	425.187	85.37	425.447
89.37	425.097	89.37	425.297
93.37	425.057	93.37	425.227
97.37	424.997	97.37	425.167
103.75	424.709		
128.05	424.245		
139.5	423.980		
165.15	423.479		
190.8	422.976		
265	421.433		
297.9	420.806		
329.6	420.149		

Appendix B

Sodium chloride and suspended sediment concentration curves measured in the concrete channel.

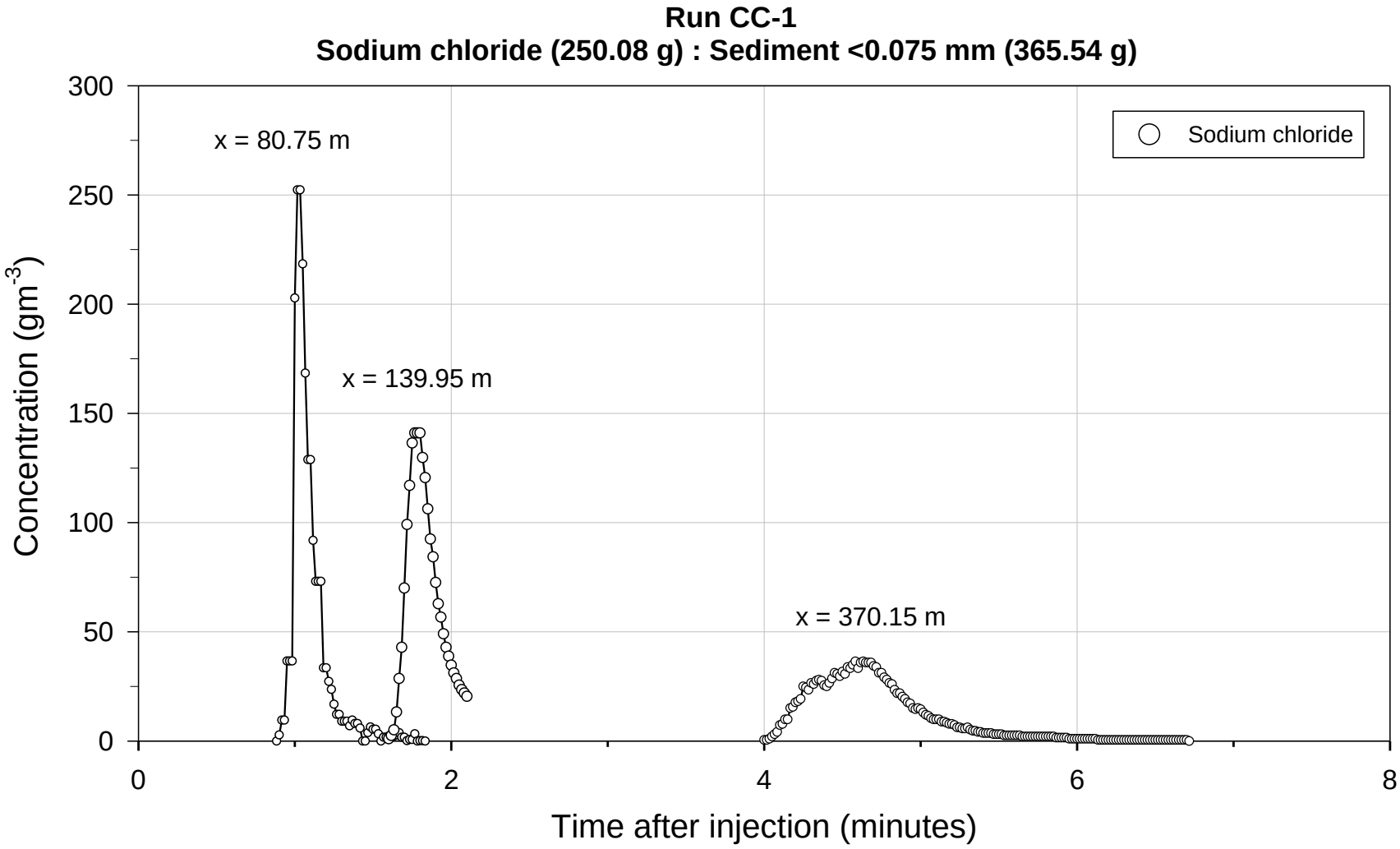

Figure B 1. Sodium chloride and suspended sediment concentration during run CC-1.

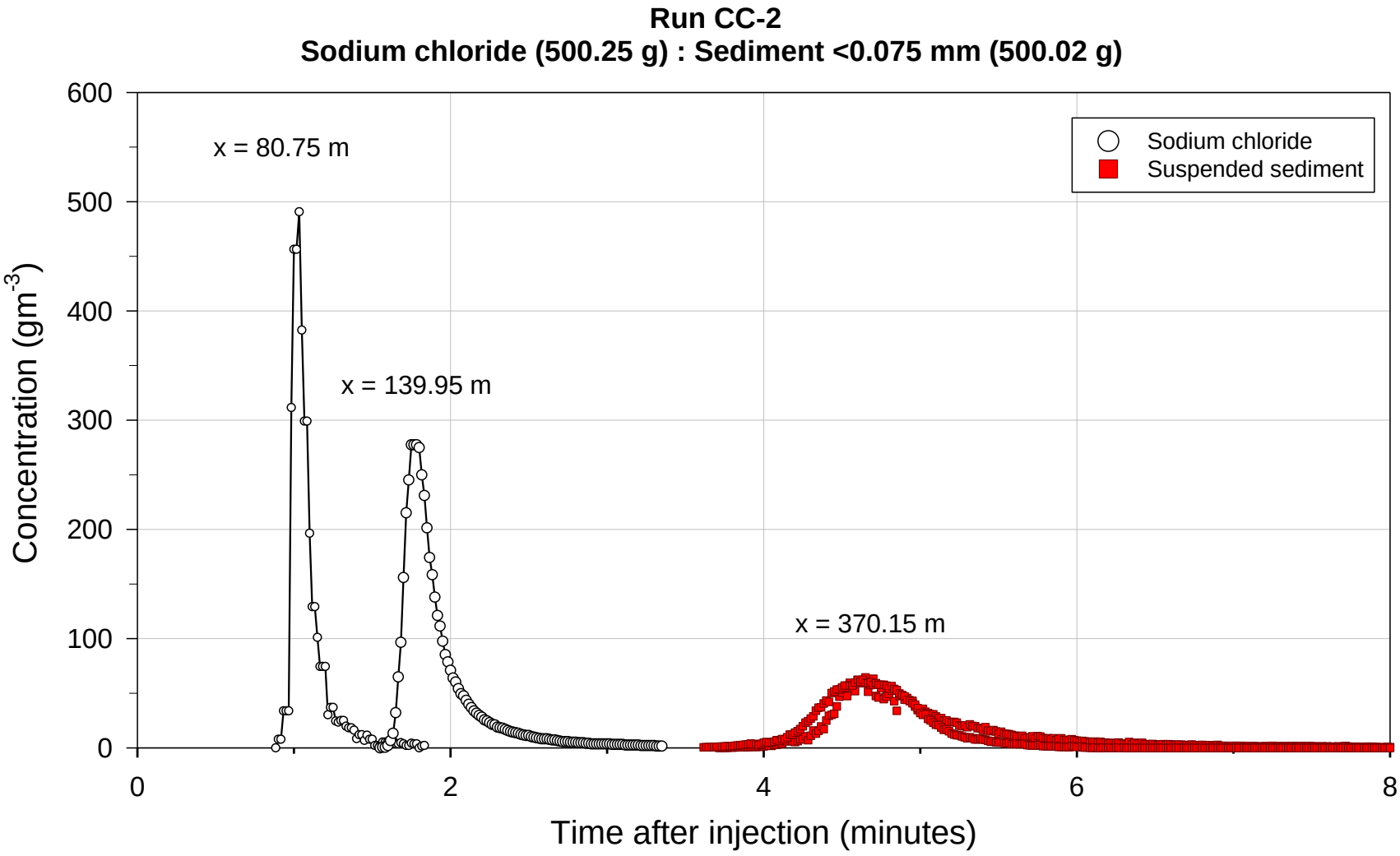

Figure B 2. Sodium chloride and suspended sediment concentration during run CC-2.

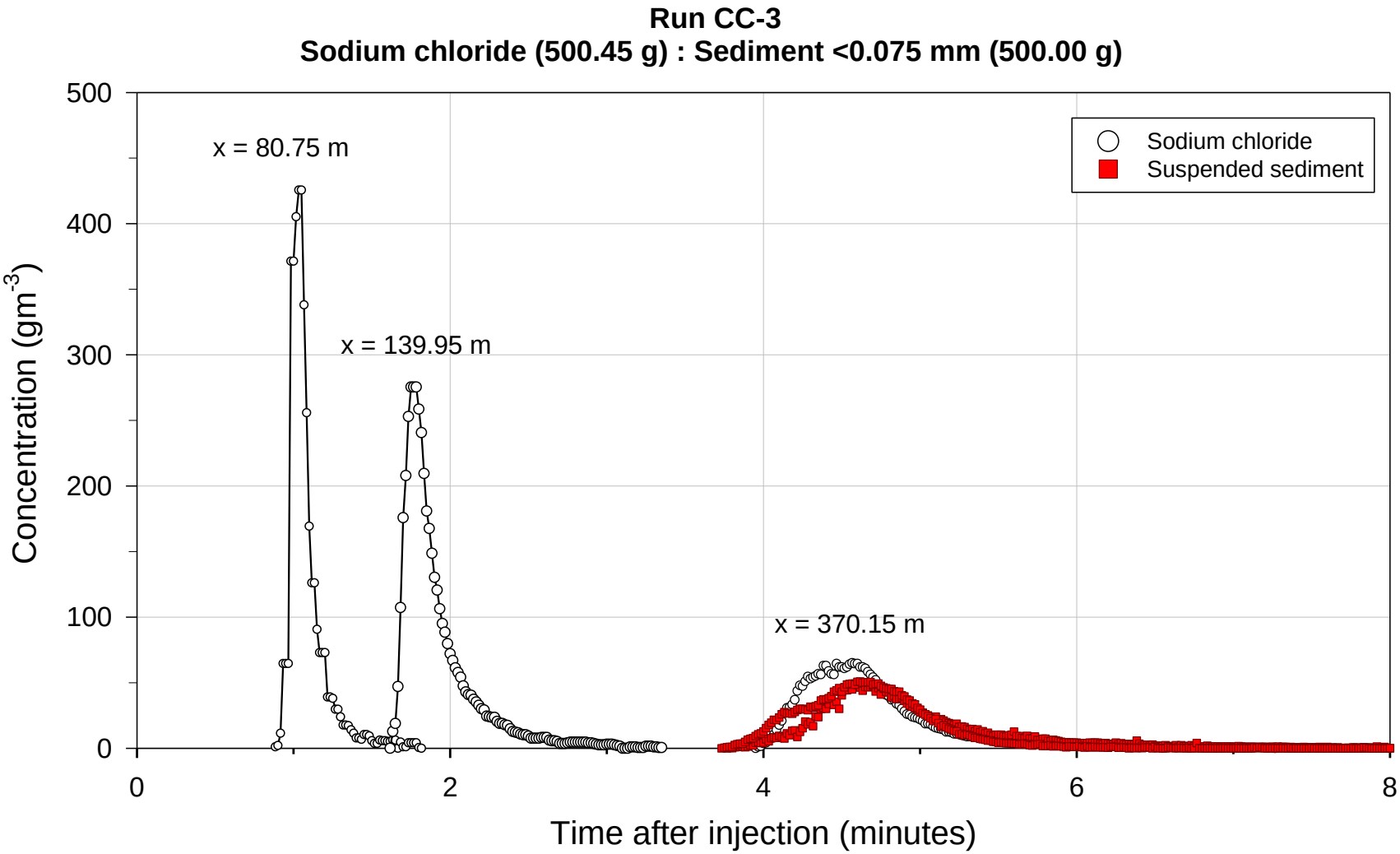

Figure B 3. Sodium chloride and suspended sediment concentration during run CC-3.

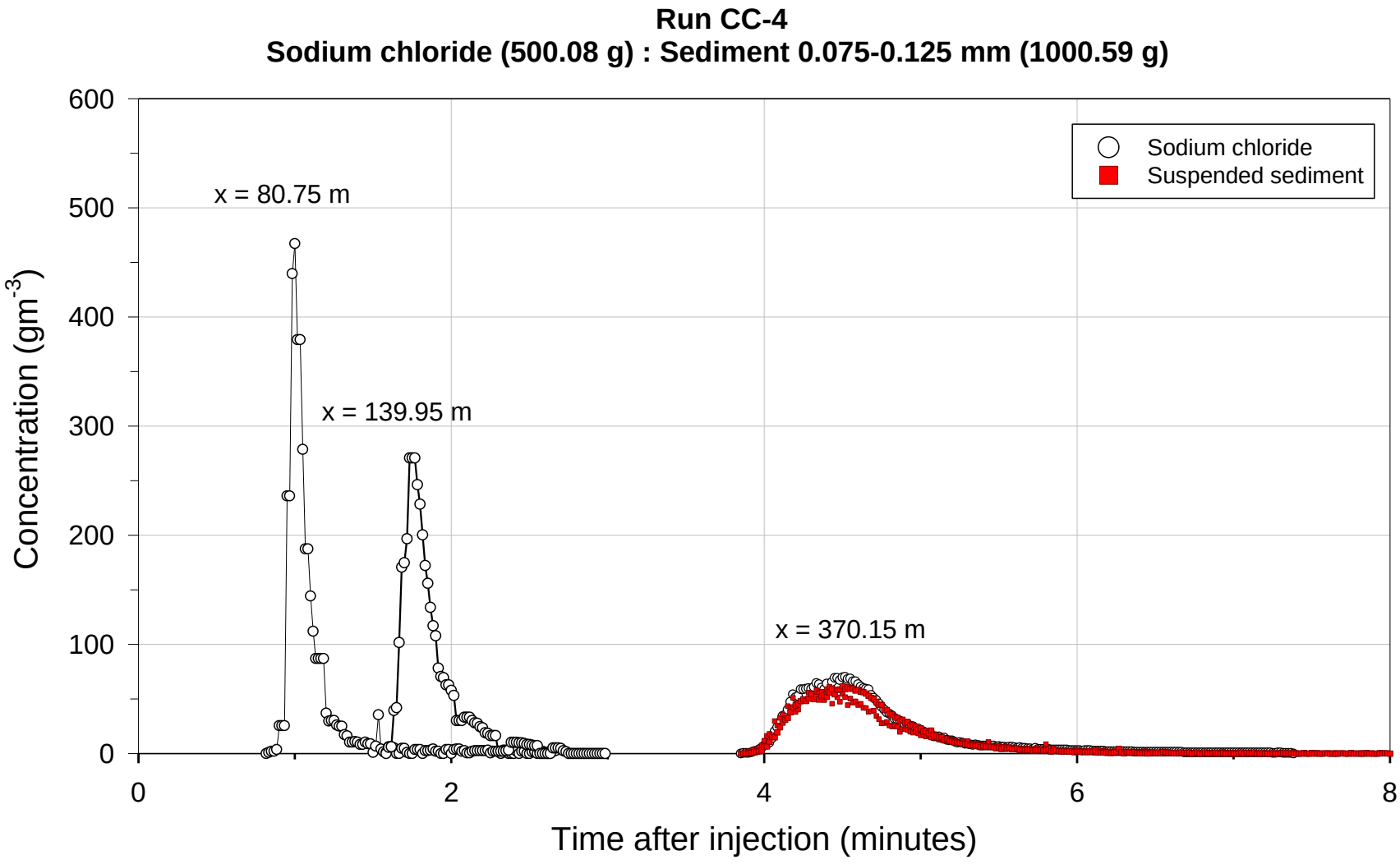

Figure B 4. Sodium chloride and suspended sediment concentration during run CC-4.

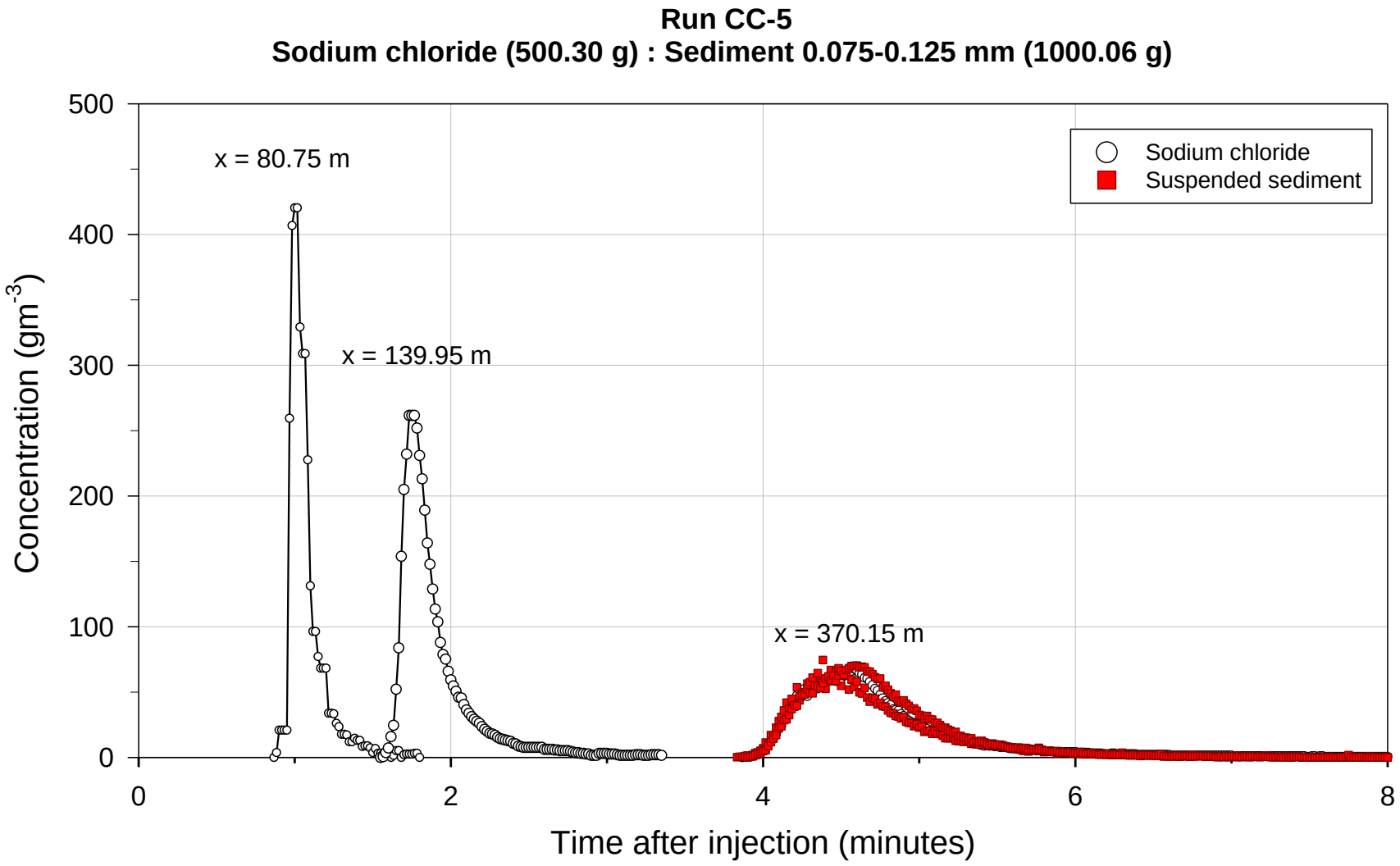

Figure B 5. Sodium chloride and suspended sediment concentration during run CC-5.

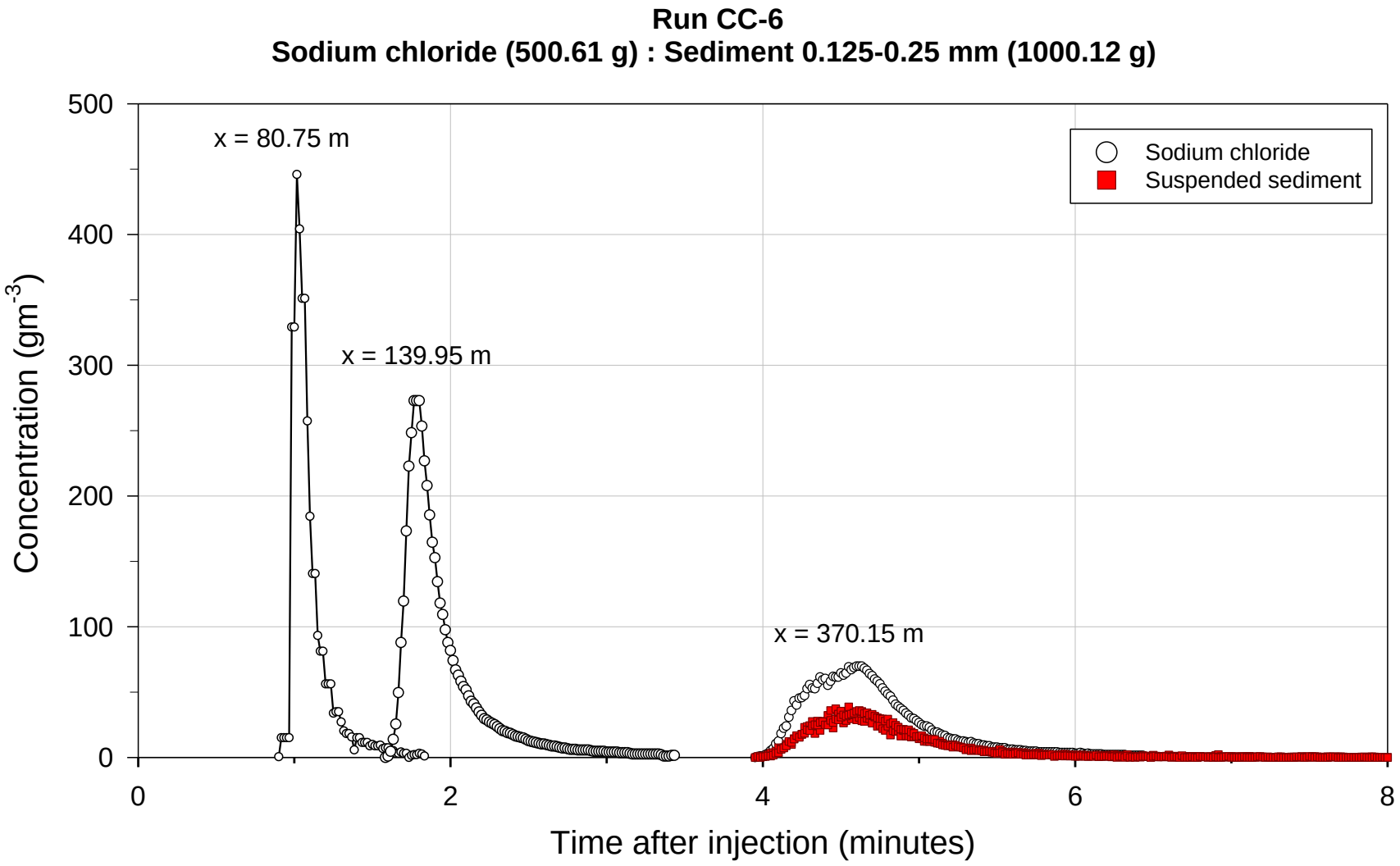

Figure B 6. Sodium chloride and suspended sediment concentration during run CC-6.

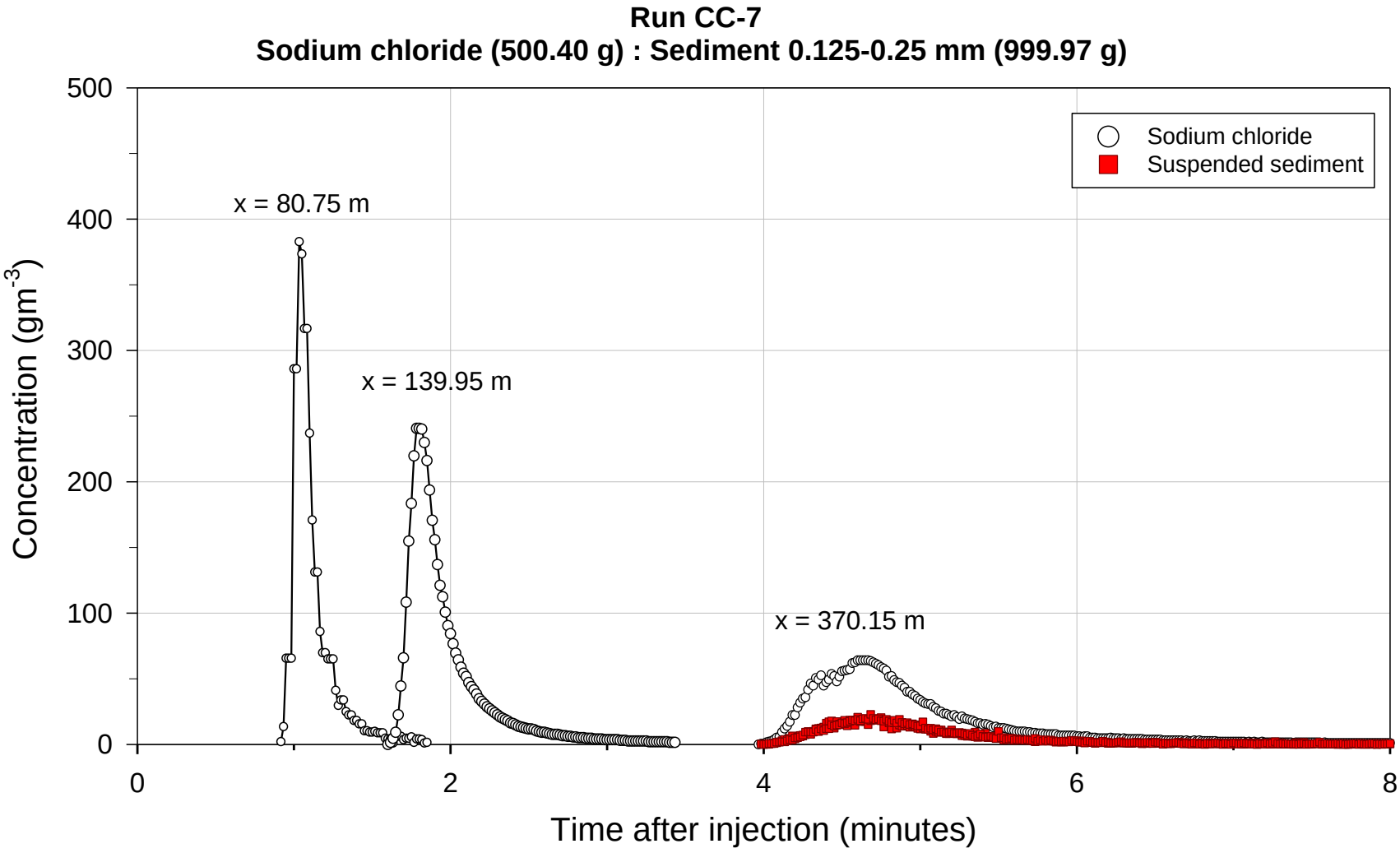

Figure B 7. Sodium chloride and suspended sediment concentration during run CC-7.

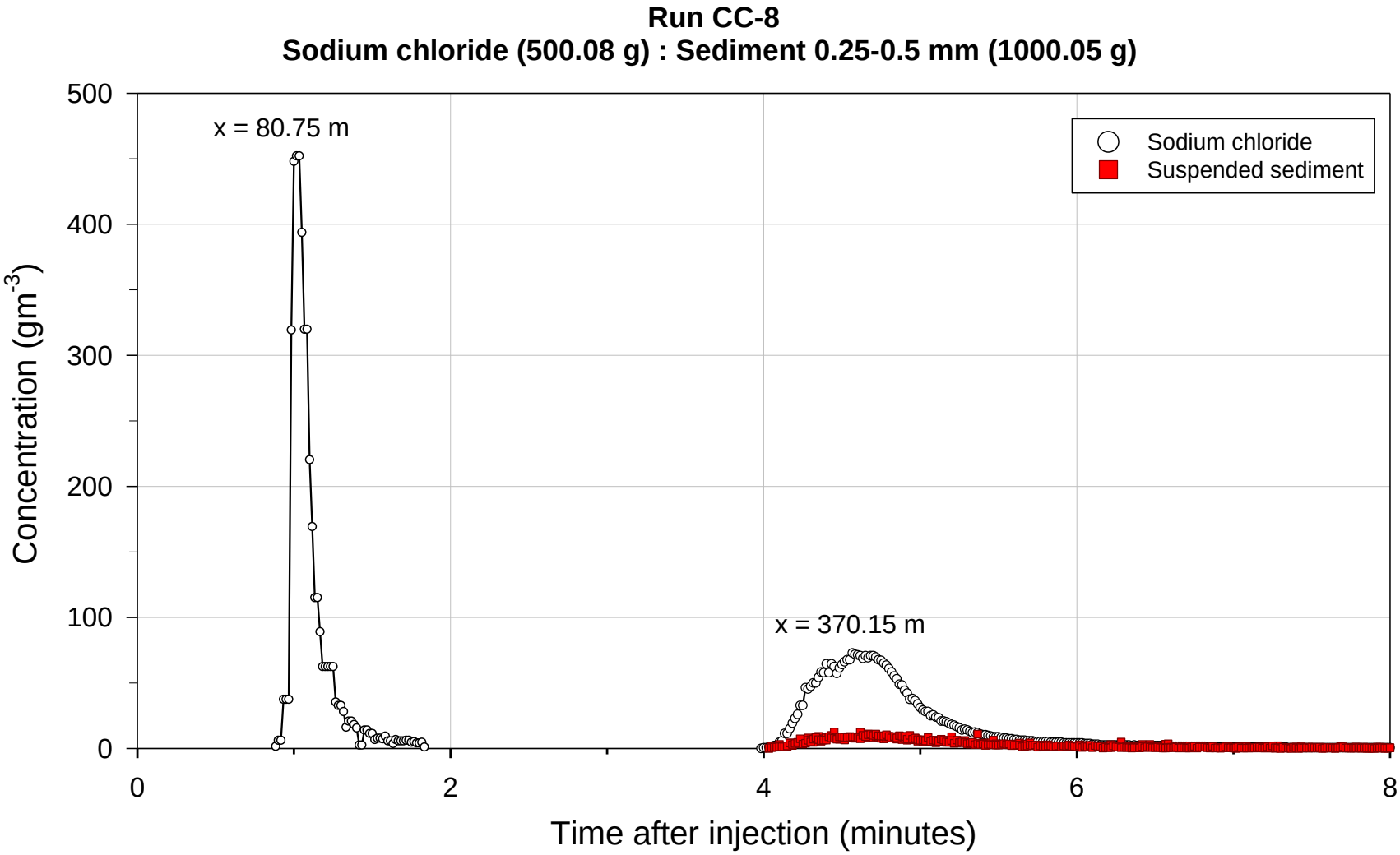

Figure B 8. Sodium chloride and suspended sediment concentration during run CC-8.

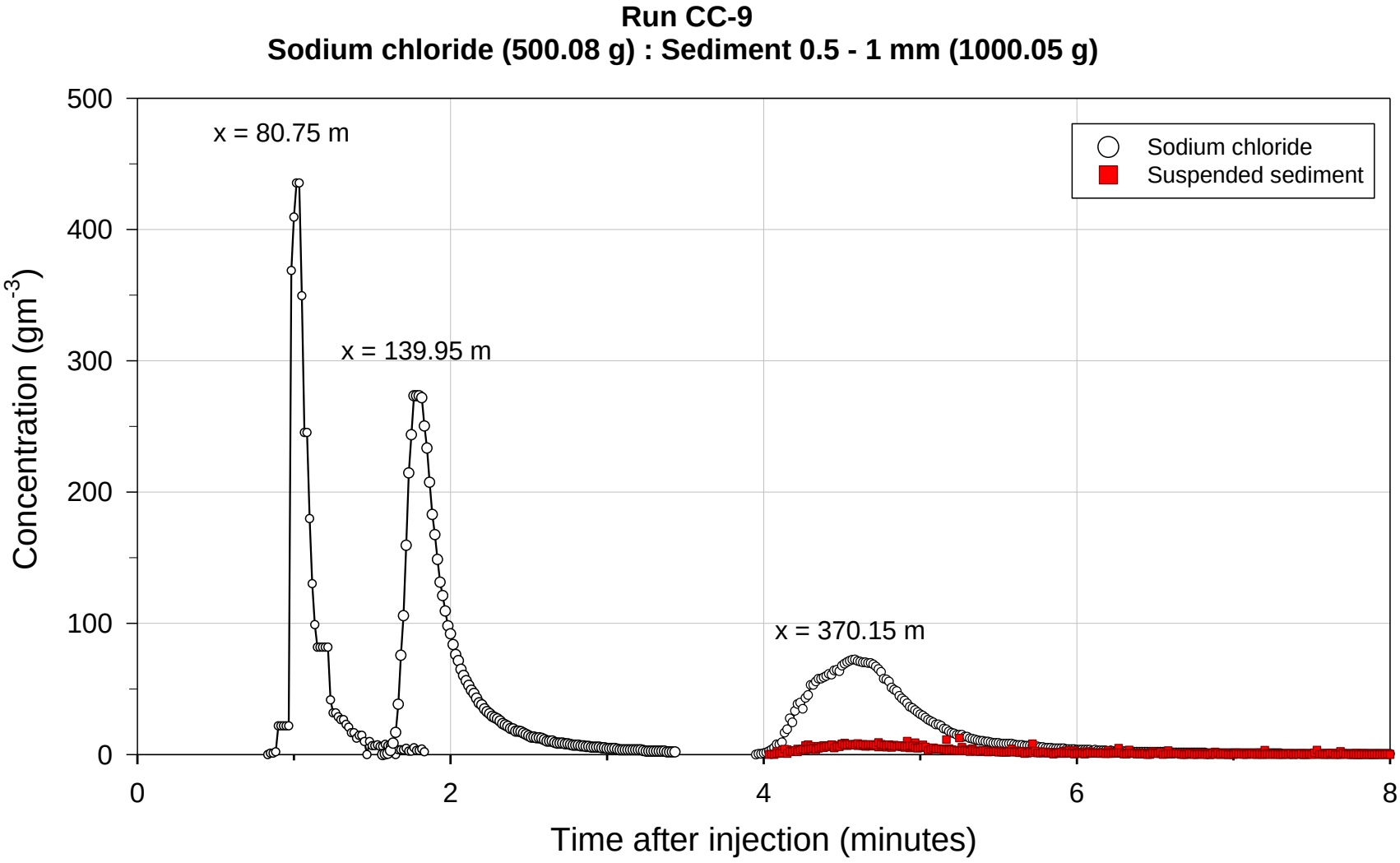

Figure B 9. Sodium chloride and suspended sediment concentration during run CC-9.

Appendix C

Surveyed geometry data for the semi-natural channel.

Table C 1. Surveyed cross-sections in the semi-natural channel.

Distance from the injection line					
0 m		**20 m**		**40 m**	
Distance from LB (m)	Elevation (m)	Distance from LB (m)	Elevation (m)	Distance from LB (m)	Elevation (m)
0.00	477.928	0.00	477.755	0.00	477.835
0.20	477.828	0.50	477.714	0.79	477.730
0.29	477.729	1.00	477.523	1.01	477.386
0.37	477.509	1.54	477.401	1.07	477.378
0.39	477.509	2.60	477.363	1.50	477.301
1.00	477.438	3.87	477.396	2.20	477.302
1.56	477.441	4.30	477.761	2.90	477.320
2.10	477.437	4.70	477.937	3.61	477.380
2.75	477.508	5.30	478.037	3.69	477.388
2.82	477.528			3.85	477.707
3.08	477.809				
Distance from the injection line					
60 m		**80 m**		**90 m**	
Distance from LB (m)	Elevation (m)	Distance from LB (m)	Elevation (m)	Distance from LB (m)	Elevation (m)
0.00	477.905	0.00	477.438	0.00	477.928
0.31	477.779	0.59	477.328	0.45	477.689
0.50	477.610	0.78	477.248	0.64	477.452
1.11	477.340	0.93	477.229	0.81	477.241
1.14	477.340	1.10	477.226	0.91	477.216
1.60	477.260	1.40	477.190	1.30	477.159
2.41	477.297	1.98	477.169	1.99	477.149
3.04	477.310	2.65	477.203	2.95	477.149
3.32	477.346	2.96	477.228	3.55	477.215
3.45	477.350	3.05	477.230	3.60	477.215
3.97	477.379	3.47	477.240	3.95	477.608
4.55	477.354	4.30	477.688		
4.85	477.810	5.10	478.231		

Table C 2. Thalweg and waterline surveyed in the semi-natural channel.

Distance from injection line (m)	**Thalweg elevation (m)**	**Waterline elevation (m)**
0	477.437	477.509
20	477.363	-
40	477.301	477.379
60	477.260	477.343
80	477.169	477.248
90	477.149	477.215

Appendix D

Sodium chloride plumes measured in the semi-natural channel.

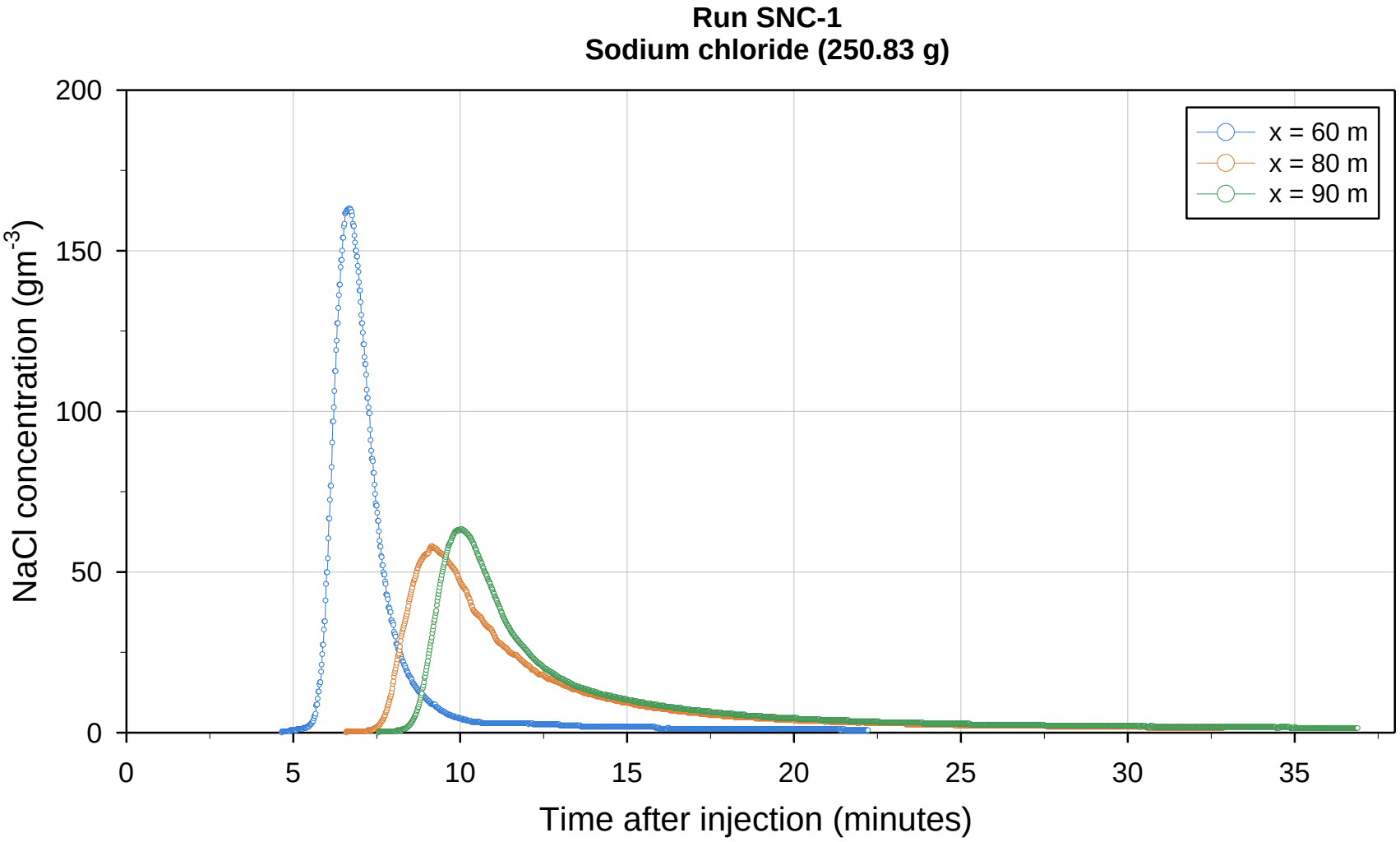

Figure D 1. Sodium chloride concentration during run SNC-1.

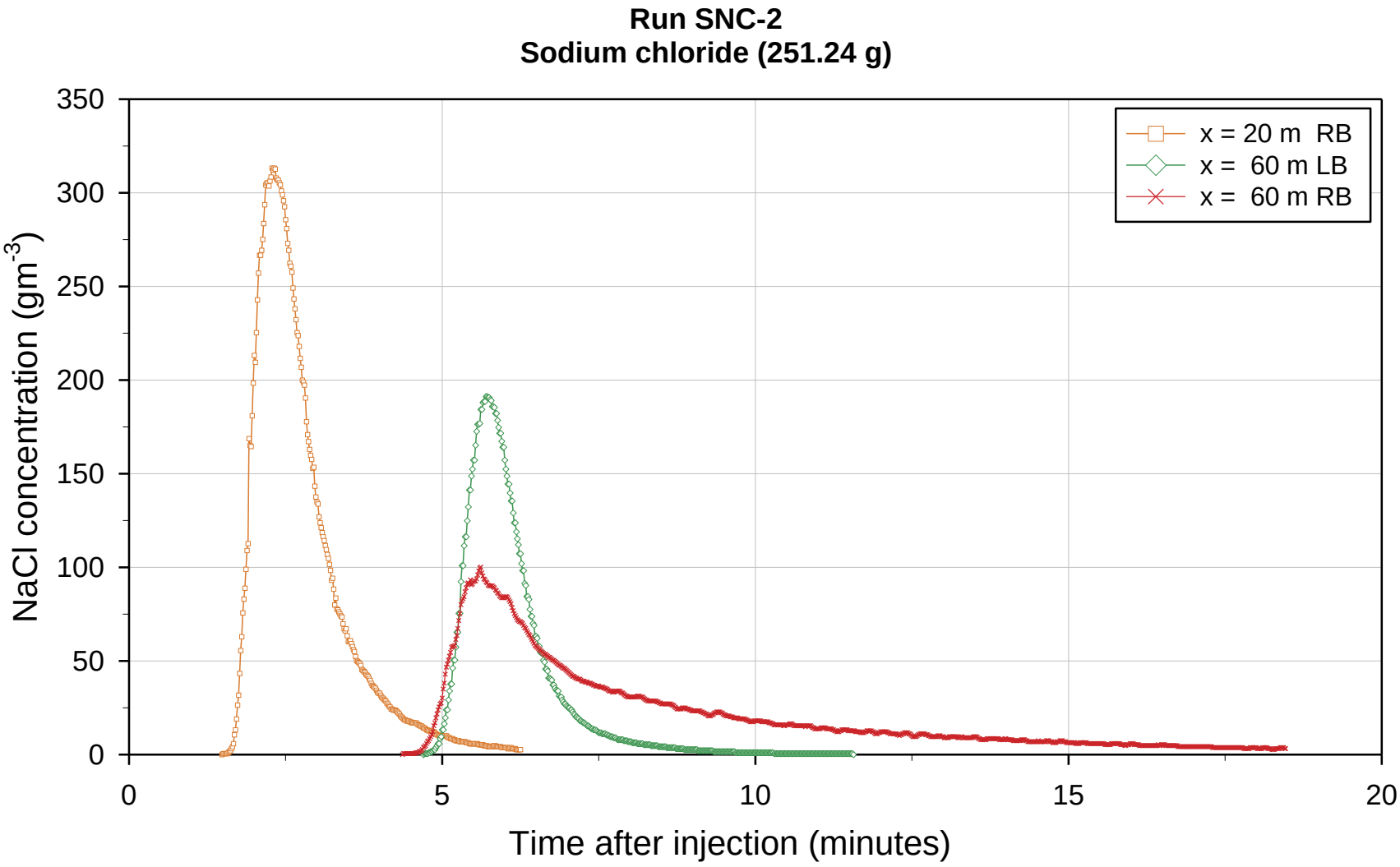

Figure D 2. Sodium chloride concentration during run SNC-2.

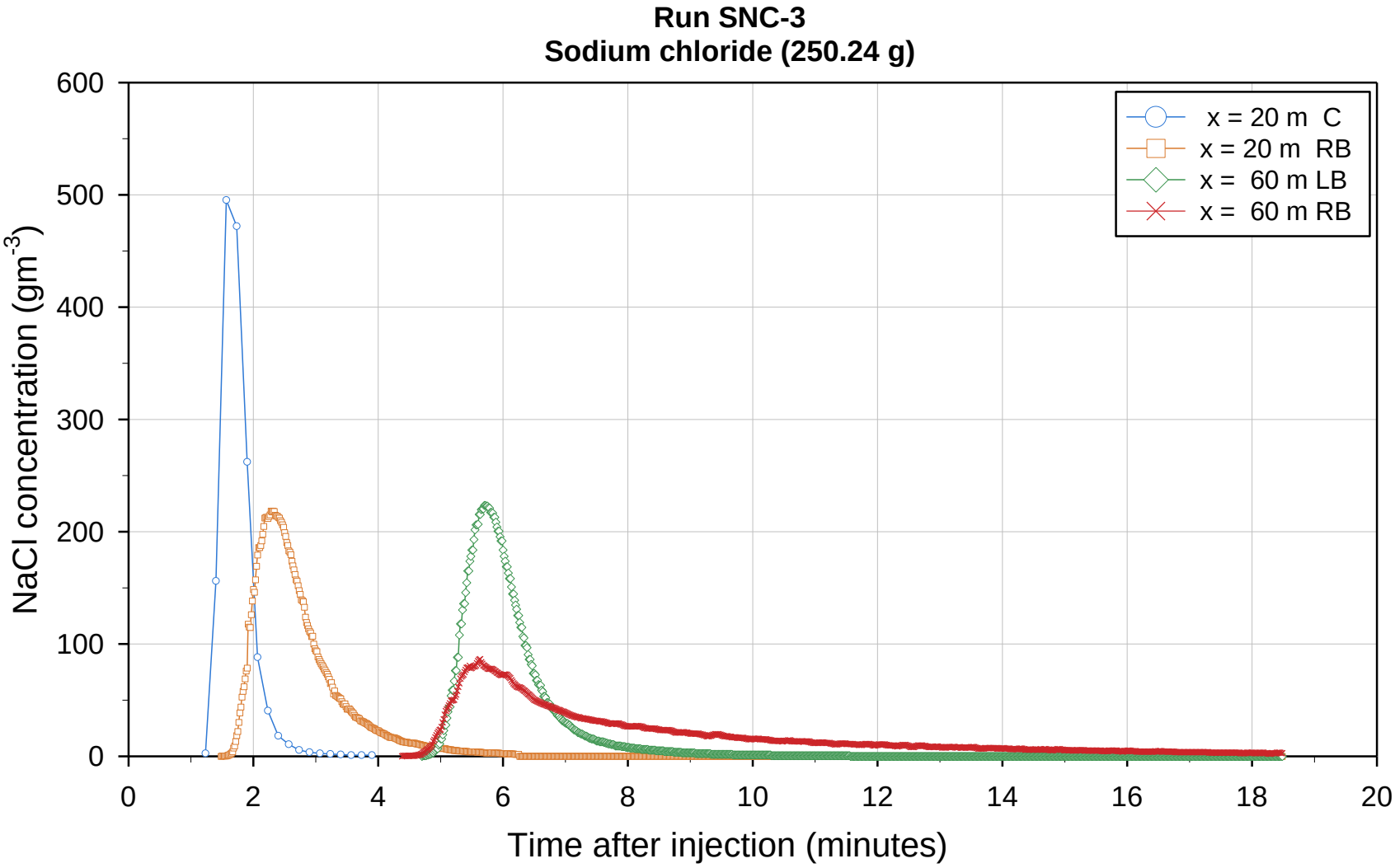

Figure D 3. Sodium chloride concentration during run SNC-3.

Appendix E

Surveyed geometry data for the natural channel.

Table E 1. Cross-sections surveyed in the natural channel (table 1/4).

Distance from the injection line							
-23.2 (m)		**0 (m)**		**12.5 (m)**		**22 (m)**	
Distance from LB (m)	Elevation (m)	Distance from LB (m)	Elevation (m)	Distance from LB (m)	Elevation (m)	Distance from LB (m)	Elevation (m)
0.00	483.000	0.00	482.606	0.00	482.351	0.00	482.393
0.50	482.851	0.40	482.694	0.15	482.290	0.50	482.443
0.75	482.770	0.80	482.683	0.40	482.138	0.75	482.217
1.10	482.716	1.10	482.654	0.50	482.055	1.00	482.137
1.40	482.665	1.40	482.563	0.70	481.722	1.10	481.729
1.50	482.671	1.80	482.464	0.95	481.567	1.40	481.680
1.75	482.641	2.00	482.378	1.30	481.442	2.00	481.563
2.00	482.671	2.35	482.264	1.50	481.407	2.50	481.494
2.20	482.713	2.80	482.353	1.95	481.417	3.00	481.450
2.50	482.631	3.20	482.387	2.50	481.423	3.50	481.460
2.80	482.631	3.70	482.388	3.00	481.425	4.00	481.453
3.05	482.471	4.10	482.365	3.45	481.419	4.50	481.485
3.30	482.501	4.50	482.373	3.90	481.475	5.00	481.453
3.85	482.661	5.00	482.334	4.40	481.513	5.50	481.377
4.30	482.541	5.20	482.303	4.85	481.570	5.70	481.357
4.90	482.621	5.50	482.314	5.00	481.615	5.80	481.415
5.40	482.580	5.80	482.284	5.50	481.640	6.05	481.567
5.90	482.470	6.10	482.242	6.00	481.691	6.40	481.830
6.40	482.459	6.45	482.194	6.50	481.738	6.70	482.120
6.95	482.511	6.70	482.314	6.90	481.772	7.00	482.315
7.50	482.541	7.10	482.314	7.20	481.860	7.60	482.653
8.00	482.541	7.30	482.333	7.70	481.885	8.10	482.831
8.70	482.468	7.70	482.283	8.20	481.978	9.05	482.845
9.30	482.371	8.00	482.284	9.05	482.083		
10.00	482.521	8.40	482.214				
10.30	482.601	8.80	482.294				
11.00	482.661	9.20	482.334				
11.60	482.714	9.65	482.264				
12.20	482.751	10.00	482.334				
12.75	482.770	10.15	482.353				
13.30	482.697	10.45	482.154				
14.00	482.720	10.70	481.973				
14.60	482.751	10.85	481.819				
15.00	482.674	11.15	481.834				
15.30	482.451	11.50	481.644				
15.60	482.201	11.65	481.624				
15.80	482.072	12.05	481.602				
16.00	482.040	12.30	481.643				
16.40	481.940	12.60	481.593				
16.80	481.901	12.80	481.619				
17.20	481.880	13.00	481.599				
17.50	481.881	13.33	481.575				
17.80	481.889	13.50	481.563				
18.10	481.892	13.75	481.525				

Distance from the injection line							
-23.2 (m)		**0 (m)**		**12.5 (m)**		**22 (m)**	
Distance from LB (m)	Elevation (m)	Distance from LB (m)	Elevation (m)	Distance from LB (m)	Elevation (m)	Distance from LB (m)	Elevation (m)
18.40	481.871	14.05	481.493				
18.70	481.929	14.40	481.483				
19.00	481.901	14.70	481.465				
19.30	481.960	15.00	481.48				
19.49	482.040	15.30	481.514				
19.75	482.071	15.50	481.544				
20.00	482.170	15.80	481.57				
20.50	482.161	16.00	481.648				
21.00	482.188	16.30	481.714				
21.70	482.150	16.55	481.788				
22.20	482.141	17.10	481.794				
22.55	482.120	17.50	481.764				
22.70	482.137	17.80	481.724				
22.95	482.041	18.00	481.714				
23.30	482.085	18.25	481.773				
23.65	482.070	18.50	482.013				
24.00	482.121	18.95	482.164				
24.30	482.080	19.30	482.223				
24.31	482.076	19.65	482.214				
24.35	482.150	20.00	482.113				
24.45	482.191	20.25	482.064				
24.50	482.281	20.65	482.114				
24.85	482.299	21.00	482.101				
25.05	482.608	21.45	482.212				
25.40	482.691	21.80	482.306				
25.65	482.903	22.20	482.344				
25.80	483.087	22.80	482.353				
27.50	483.071	23.15	482.363				
29.97	483.059	23.60	482.394				
		24.00	482.363				
		24.50	482.368				
		25.50	482.863				
		29.60	482.775				
		30.00	482.641				
		30.12	482.532				
		31.08	482.11				

Table E 2. Cross-sections surveyed in the natural channel (table 2/4).

Distance from injection line (m)							
36 (m)		**49.6 (m)**		**65 (m)**		**73.3 (m)**	
Distance from LB (m)	Elevation (m)	Distance from LB (m)	Elevation (m)	Distance from LB (m)	Elevation (m)	Distance from LB (m)	Elevation (m)
0	482.433	0	481.9415	0	482.0125	0	482.234
0.45	482.601	0.2	481.8225	0.5	482.0245	0.3	482.376
0.85	482.614	0.3	481.3855	1	481.9475	0.6	482.47
1.1	482.628	0.6	481.2425	1.5	481.8525	1	482.492
1.4	482.585	1	481.2205	2	481.5875	1.3	482.435

Distance from injection line (m)							
36 (m)		**49.6 (m)**		**65 (m)**		**73.3 (m)**	
Distance from LB (m)	Elevation (m)	Distance from LB (m)	Elevation (m)	Distance from LB (m)	Elevation (m)	Distance from LB (m)	Elevation (m)
1.6	482.526	1.4	481.2505	2.3	481.5775	1.5	482.295
1.7	482.407	1.95	481.2805	2.4	481.3805	1.7	482.185
1.9	482.286	2.55	481.2585	2.75	481.3055	2.1	481.86
2.2	482.073	3.1	481.2335	3.3	481.2335	2.5	481.829
2.6	482.043	3.65	481.2305	3.8	481.2375	2.9	481.828
3	482.086	4	481.2685	4.15	481.2075	3.35	481.837
3.3	482.115	4.4	481.3155	4.7	481.2425	3.75	481.844
3.6	482.001	4.8	481.3855	5.15	481.3055	4.2	481.84
3.8	481.983	5.2	481.4765	5.4	481.3175	4.7	481.865
4.1	482.114	5.3	481.7155	5.9	481.3265	5.1	481.81
4.3	482.161	5.5	481.9125	6.6	481.3505	5.6	481.753
4.6	482.034	6	481.9125	6.75	481.3655	6.1	481.857
4.9	481.883	6.4	481.9135	7.3	481.3705	6.5	481.782
5.05	481.775	6.8	481.9815	8	481.3705	6.9	481.835
5.5	481.752	7.25	482.0135	8.4	481.3925	7.3	481.852
5.95	481.703			8.6	481.4375	7.6	481.785
6.08	481.651			8.85	481.7725	7.9	481.753
6.5	481.774			9.25	481.9205	8.35	481.675
6.7	482.133					8.65	481.68
6.85	481.814					9.2	481.745
7.15	481.771					9.5	481.844
7.35	481.875					9.9	481.939
8	482.104					10.3	481.875
8.1	481.973					10.6	481.844
8.4	481.938					10.8	481.81
8.55	481.879					11	481.55
8.85	481.703					11.2	481.41
9.1	481.794					11.4	481.327
9.5	481.781					11.8	481.223
9.75	481.727					12.2	481.253
10.1	481.723					12.6	481.279
10.55	481.783					13	481.266
10.9	481.873					13.4	481.275
11.25	481.944					13.8	481.233
11.7	482.019					14.15	481.225
12.2	482.124					14.65	481.185
12.6	482.183					15.05	481.145
13.1	482.174					15.4	481.147
13.6	482.204					15.8	481.225
14	482.124					16	481.254
14.4	482.203					16.25	481.329
14.8	482.186					16.3	481.346
15.1	482.214					16.45	481.385
15.4	482.201					16.8	481.464
15.7	482.133					17.1	481.495
15.9	481.683					17.5	481.442
16.05	481.464					17.9	481.43
16.06	481.314					18.2	481.43
16.3	481.294					18.6	481.656
16.6	481.334					19	481.864

Distance from injection line (m)							
36 (m)		**49.6 (m)**		**65 (m)**		**73.3 (m)**	
Distance from LB (m)	Elevation (m)	Distance from LB (m)	Elevation (m)	Distance from LB (m)	Elevation (m)	Distance from LB (m)	Elevation (m)
16.9	481.384					19.4	482.024
17.1	481.398					19.8	482.138
17.4	481.424					20	482.185
17.75	481.419					21	482.294
18.15	481.424					24.2	482.316
18.45	481.404					26.2	482.348
18.7	481.403					27.8	482.31
19	481.398					28.18	482
19.3	481.391						
19.6	481.354						
19.9	481.343						
20.2	481.323						
20.45	481.325						
20.8	481.335						
21.05	481.343						
21.2	481.361						
21.35	481.413						
21.4	481.425						
21.5	481.464						
21.65	481.517						
21.95	481.723						
22.25	481.825						
22.6	481.883						
22.85	482.008						
23.35	482.059						
24	482.086						
24.2	482.193						
24.7	482.503						
24.9	482.64						
25.15	482.704						
25.5	482.724						
25.8	482.644						
28	482.532						
29.18	482.385						

Table E 3. Cross-sections surveyed in the natural channel (table 3/4).

Distance from the injection line (m)							
92 (m)		**107.1 (m)**		**115.9 (m)**		**127.9 (m)**	
Distance from LB (m)	Elevation (m)	Distance from LB (m)	Elevation (m)	Distance from LB (m)	Elevation (m)	Distance from LB (m)	Elevation (m)
0.00	481.649	0.00	481.882	0.00	481.637	0.00	481.332
0.50	481.624	0.50	481.862	0.50	481.660	0.35	481.306
1.00	481.629	1.00	481.867	0.85	481.442	0.70	481.257
1.25	481.721	1.50	481.867	0.95	481.157	1.10	481.203
1.50	481.172	1.90	481.742	1.50	481.154	1.35	481.018
1.60	481.019	2.00	481.357	2.00	481.302	1.70	480.955
1.90	481.002	2.30	481.339	2.20	481.317	1.80	480.955

Distance from the injection line (m)							
92 (m)		**107.1 (m)**		**115.9 (m)**		**127.9 (m)**	
Distance from LB (m)	Elevation (m)	Distance from LB (m)	Elevation (m)	Distance from LB (m)	Elevation (m)	Distance from LB (m)	Elevation (m)
2.20	480.979	2.70	481.292	2.80	481.222	2.00	480.980
2.40	481.004	3.00	481.227	3.30	481.227	2.45	481.004
2.70	481.011	3.30	481.201	3.80	481.154	2.85	481.002
3.10	481.049	3.70	481.169	4.45	481.115	3.35	480.962
3.40	481.064	4.20	481.126	5.00	481.054	3.50	480.959
3.90	481.089	4.60	481.105	5.25	481.027	3.90	480.943
4.30	481.124	5.00	481.097	5.50	480.992	4.30	480.927
4.70	481.168	5.50	481.072	6.00	480.948	4.80	480.933
5.10	481.198	5.80	480.977	6.10	480.875	5.40	480.887
5.60	481.229	5.80	480.985	6.30	480.847	5.80	480.886
6.00	481.223	6.00	480.937	6.70	480.855	6.20	480.906
6.50	481.216	6.20	480.883	7.00	480.867	6.75	480.937
7.00	481.234	6.40	480.883	7.20	481.002	7.00	480.954
7.50	481.351	7.05	480.829	7.50	481.064	7.30	480.924
7.70	481.449	7.35	480.914	7.70	481.105	7.40	480.852
7.90	481.746	7.40	481.142	8.00	481.234	7.70	480.800
8.30	481.656	7.60	481.537	8.35	481.347	7.95	480.812
8.80	481.423	7.80	481.447	8.60	481.395	8.15	480.856
9.30	481.446	8.00	481.577	8.70	481.605	8.25	480.934
9.70	481.479	8.50	481.467	8.90	481.462	8.26	480.924
		8.85	481.554	9.20	481.579	8.27	481.087
		9.20	481.604	9.50	481.685	8.55	481.367
		9.40	482.251			8.75	481.371
		9.75	482.252			9.15	481.575
						9.25	481.567
						9.60	481.934
						10.75	481.931
						13.10	481.828
						16.20	481.662

Table E 4. Cross-sections surveyed in the natural channel (table 4/4).

Distance from injection line (m)							
162.9 (m)		**207.3 (m)**		**222 (m)**		**323.5 (m)**	
Distance from LB (m)	Elevation (m)	Distance from LB (m)	Elevation (m)	Distance from LB (m)	Elevation (m)	Distance from LB (m)	Elevation (m)
0.00	481.530	0.00	480.894	0.00	480.885	0.00	480.782
0.50	481.490	1.00	480.865	0.00	480.779	0.50	480.817
1.00	481.350	1.80	480.799	0.50	481.077	1.50	480.799
1.50	481.175	2.25	480.642	1.20	481.032	2.40	480.826
2.00	481.153	3.60	480.879	1.80	481.040	2.90	480.704
2.70	481.217	4.10	480.871	2.70	480.979	3.25	480.555
3.30	481.192	4.60	480.760	3.50	480.957	3.75	480.304
4.00	481.090	4.95	480.550	4.05	481.059	4.30	479.944
4.30	480.785	5.40	480.508	4.70	480.727	4.95	479.804
4.40	480.610	5.90	480.481	5.10	480.347	5.00	479.754
4.70	480.530	6.30	480.468	5.80	480.127	5.25	479.656
5.30	480.590	6.80	480.459	6.30	480.147	5.45	479.584

Distance from injection line (m)							
162.9 (m)		**207.3 (m)**		**222 (m)**		**323.5 (m)**	
Distance from LB (m)	Elevation (m)	Distance from LB (m)	Elevation (m)	Distance from LB (m)	Elevation (m)	Distance from LB (m)	Elevation (m)
5.30	480.620	7.30	480.450	6.80	480.102	5.60	479.510
5.60	480.730	7.80	480.399	7.30	480.155	6.00	479.484
6.10	480.795	8.30	480.390	7.80	480.159	6.30	479.480
6.70	480.810	8.65	480.366	8.20	480.127	6.75	479.518
7.30	480.780	9.00	480.374	8.30	480.142	6.95	479.494
7.80	480.755	9.50	480.386	8.50	480.127	7.10	479.518
8.30	480.715	9.90	480.386	8.75	480.159	7.35	479.479
8.80	480.707	10.40	480.420	9.30	480.155	7.55	479.458
9.40	480.710	10.80	480.435	9.60	480.207	7.80	479.461
9.90	480.720	11.05	480.444	9.75	480.305	8.00	479.504
10.30	480.683	11.40	480.454	10.00	480.709	8.10	479.525
10.70	480.680	11.60	480.459	10.50	481.035	8.20	479.500
11.10	480.655	11.95	480.512	11.20	481.393	8.50	479.554
11.40	480.763	12.00	480.507	12.00	481.248	9.00	479.595
11.80	480.833	12.01	480.569	12.50	481.227	9.50	479.613
12.30	480.919	12.40	480.686	13.00	481.203	10.00	479.677
12.60	481.045	12.65	480.752	13.50	481.249	10.45	479.704
13.00	481.271	13.05	480.885	14.00	481.510	10.90	479.683
13.50	481.314	13.45	480.913	14.70	481.350	11.40	479.812
		13.90	480.915	15.40	481.247	11.45	479.798
		14.40	480.905	16.00	481.207	11.95	479.861
		14.85	480.885	17.00	481.202	12.30	479.902
				18.00	481.203	12.60	479.890
				19.00	481.151	12.90	479.699
				20.00	481.032	12.95	479.717
						13.15	479.555
						13.30	479.518
						13.65	479.572
						13.87	479.702
						14.45	479.888
						14.80	480.076
						15.26	479.867

Table E 5. Surveyed thalweg and waterline elevations in the natural channel.

Distance from injection (m)	**Thalweg elevation (m)**	**Waterline elevation (m) Q = 0.093 m^3s^{-1}**	**Waterline elevation (m) Q = 0.042 m^3s^{-1}**
-23.2	481.871	482.040	-
0	481.465	481.648	-
12.5	481.406	-	481.567
22	481.356	-	481.563
36	481.323	481.464	-
49.6	481.220	-	481.386
65	481.207	-	481.380
73.3	481.145	481.350	-
92	481.004	-	481.168
107.1	480.709	-	481.081
115.9	480.747	-	481.015

Distance from injection (m)	Thalweg elevation (m)	Waterline elevation (m) $Q = 0.093\ m^3s^{-1}$	Waterline elevation (m) $Q = 0.042\ m^3s^{-1}$
127.9	480.852	-	480.924
162.9	480.655	-	480.750
207.3	480.366	480.500	-
222	480.102	-	-
323.5	479.416	479.700	-

Appendix F

Sodium chloride and suspended sediment plumes measured in the natural channel.

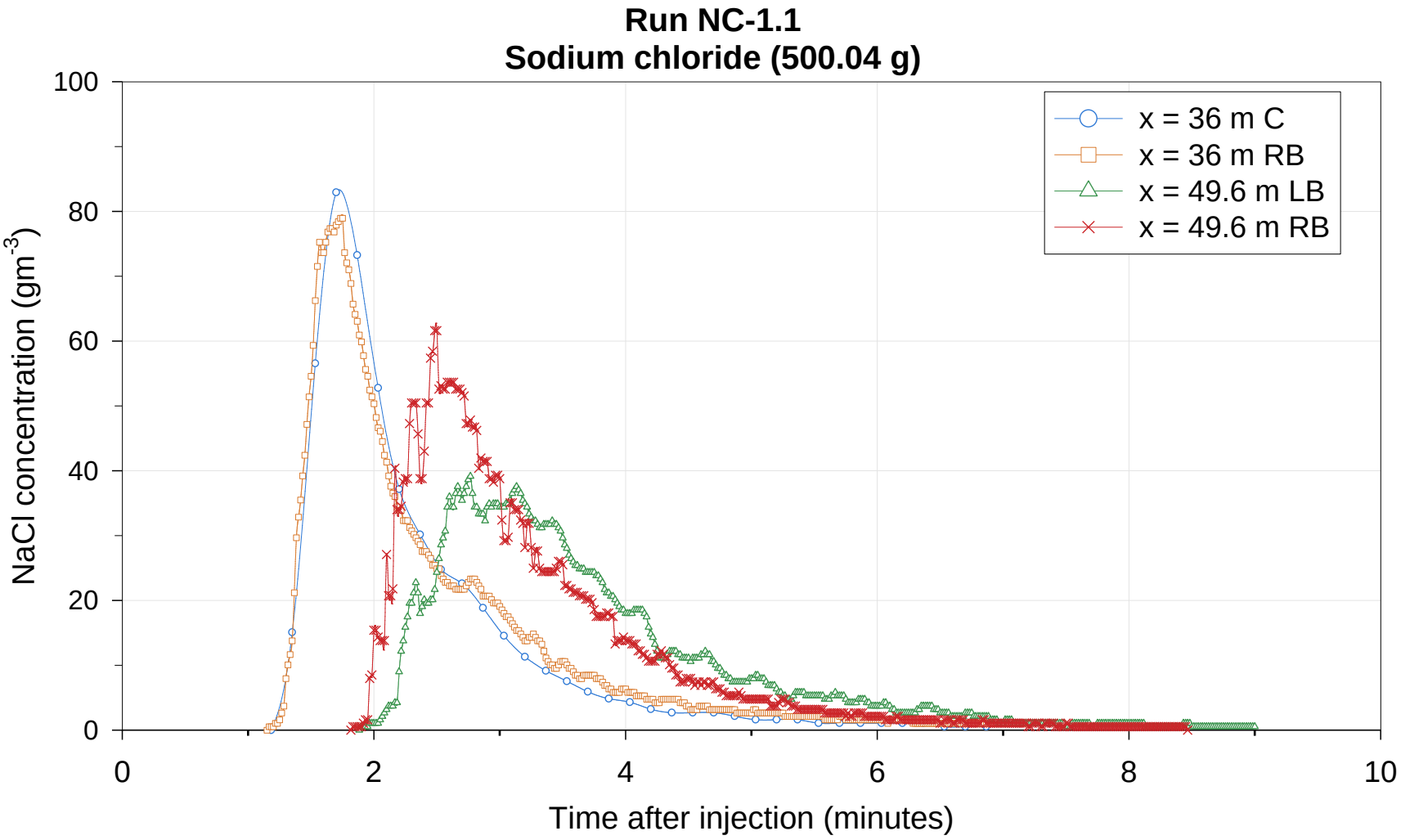

Figure F 1. Sodium chloride concentration during run NC-1.1.

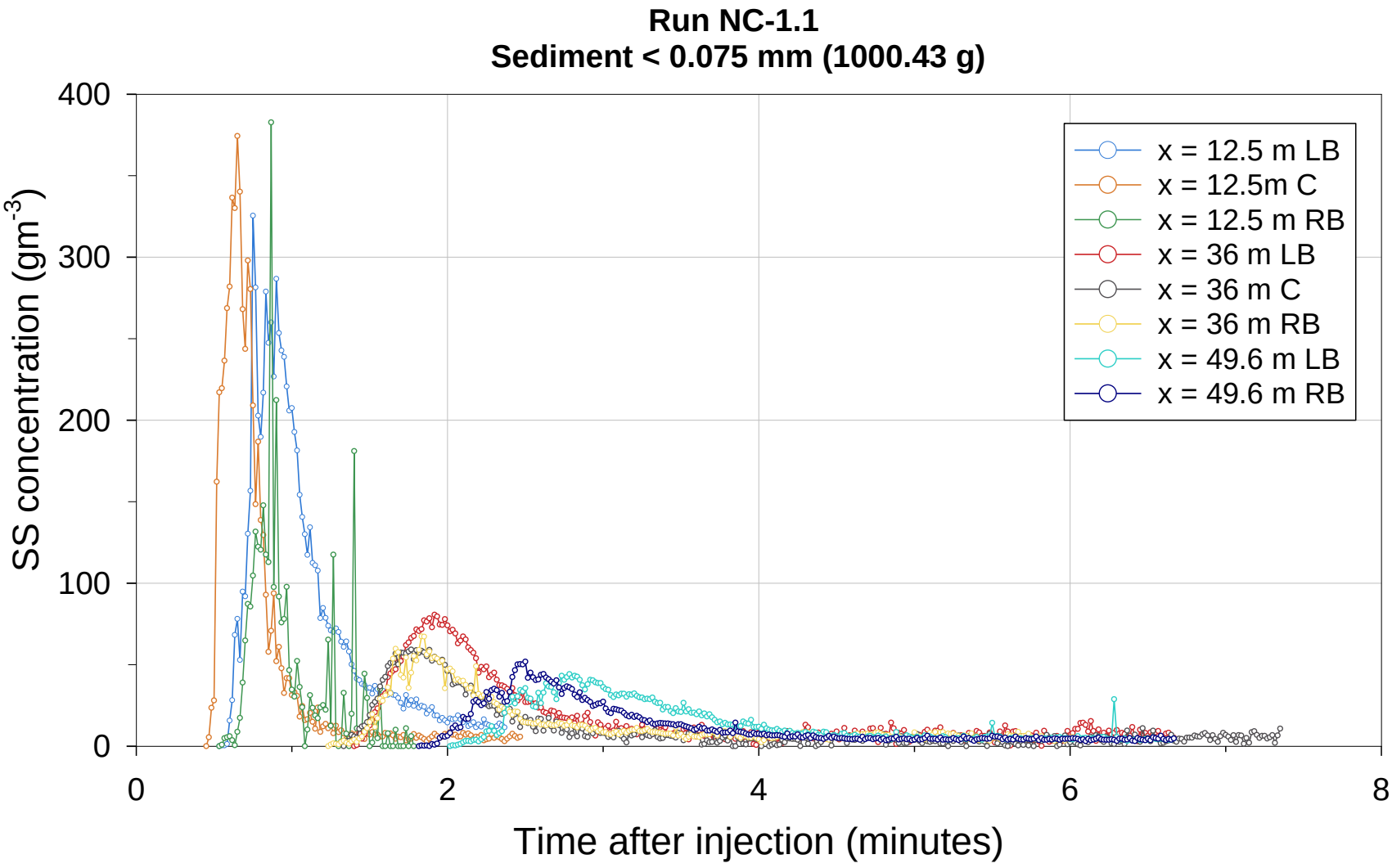

Figure F 2. Suspended sediment concentration during run NC-1.1.

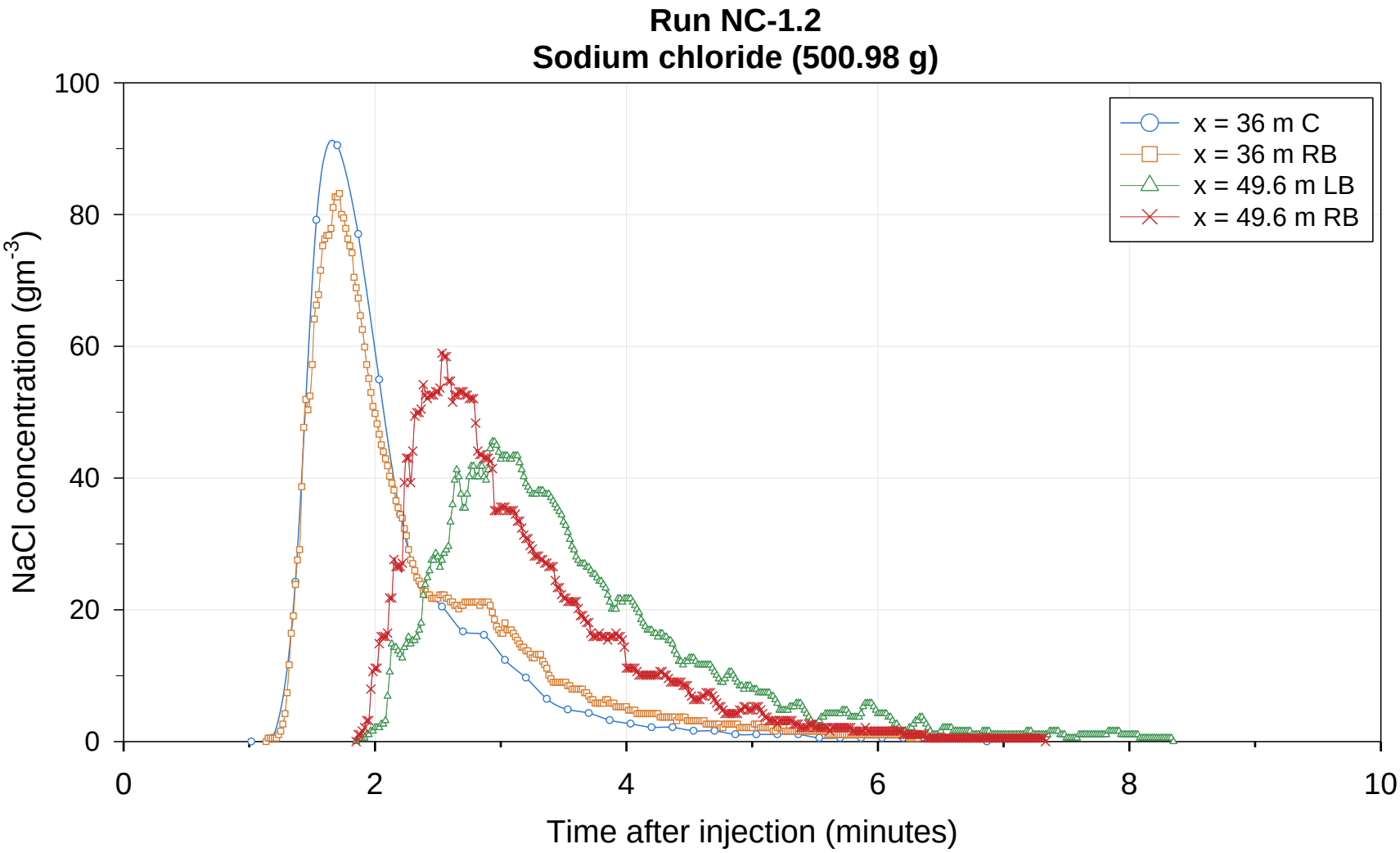

Figure F 3. Sodium chloride concentration during run NC-1.2.

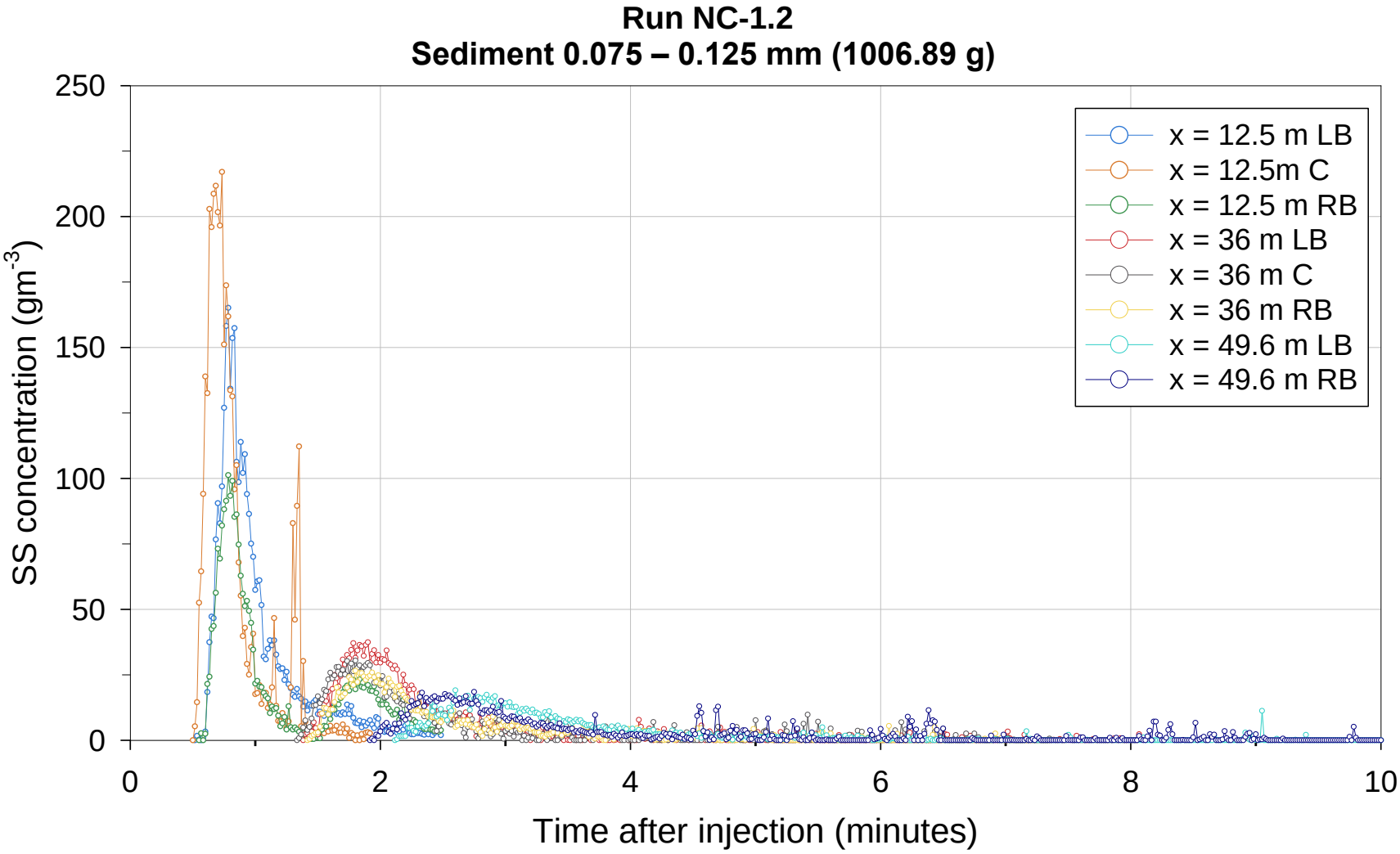

Figure F 4. Suspended sediment concentration during run NC-1.2.

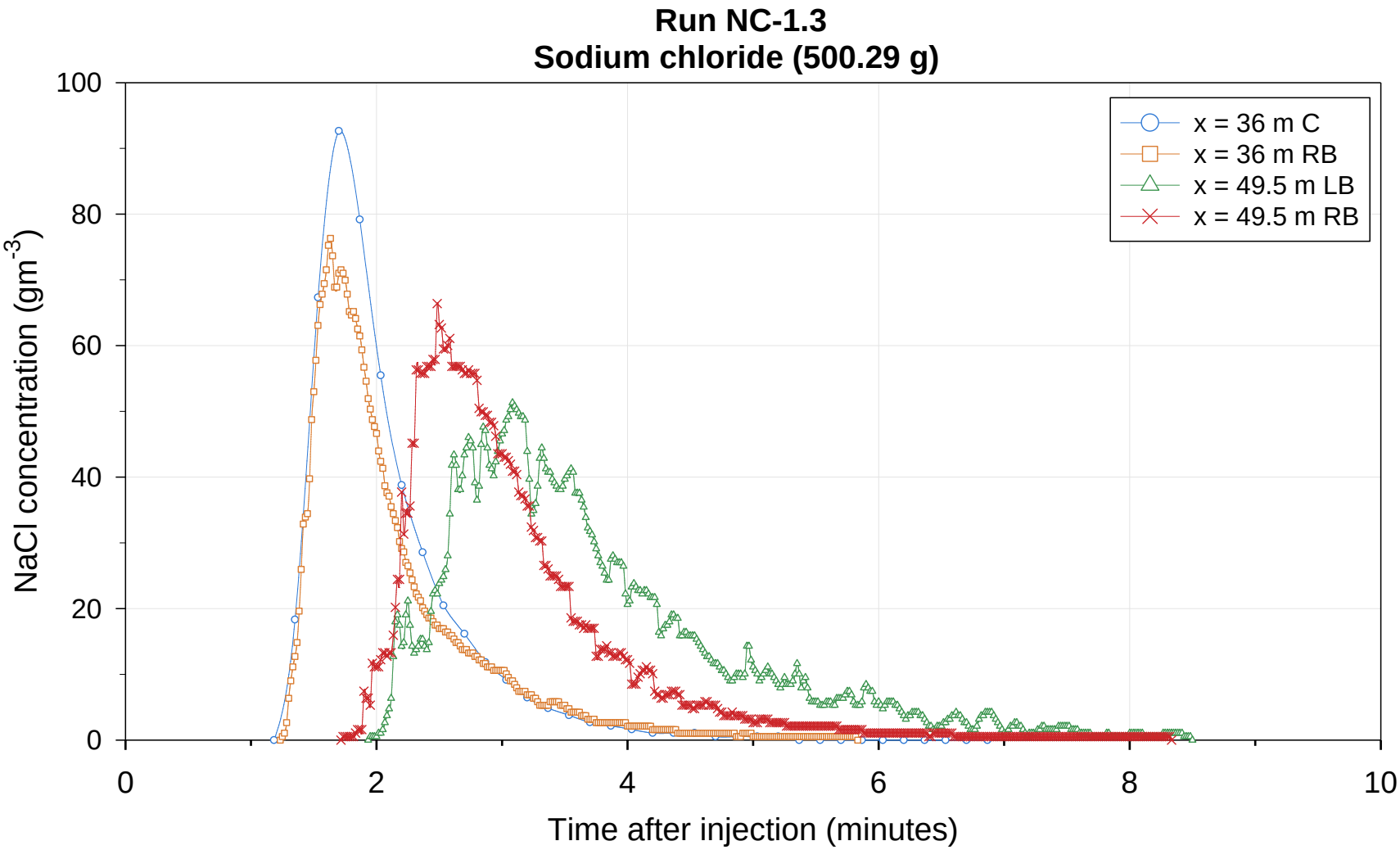

Figure F 5. Sodium chloride concentration during run NC-1.3.

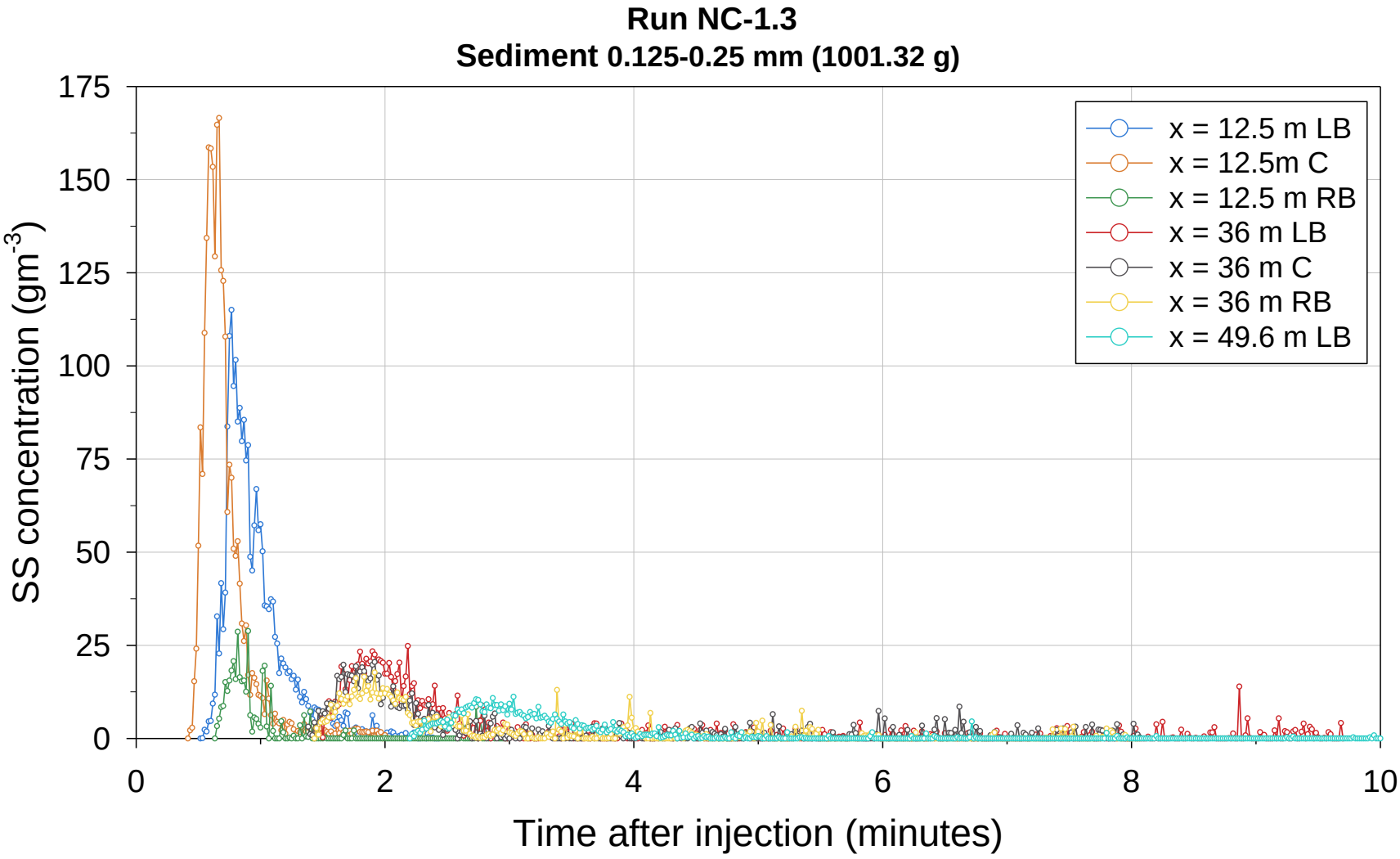

Figure F 6. Suspended sediment concentration during run NC-1.3.

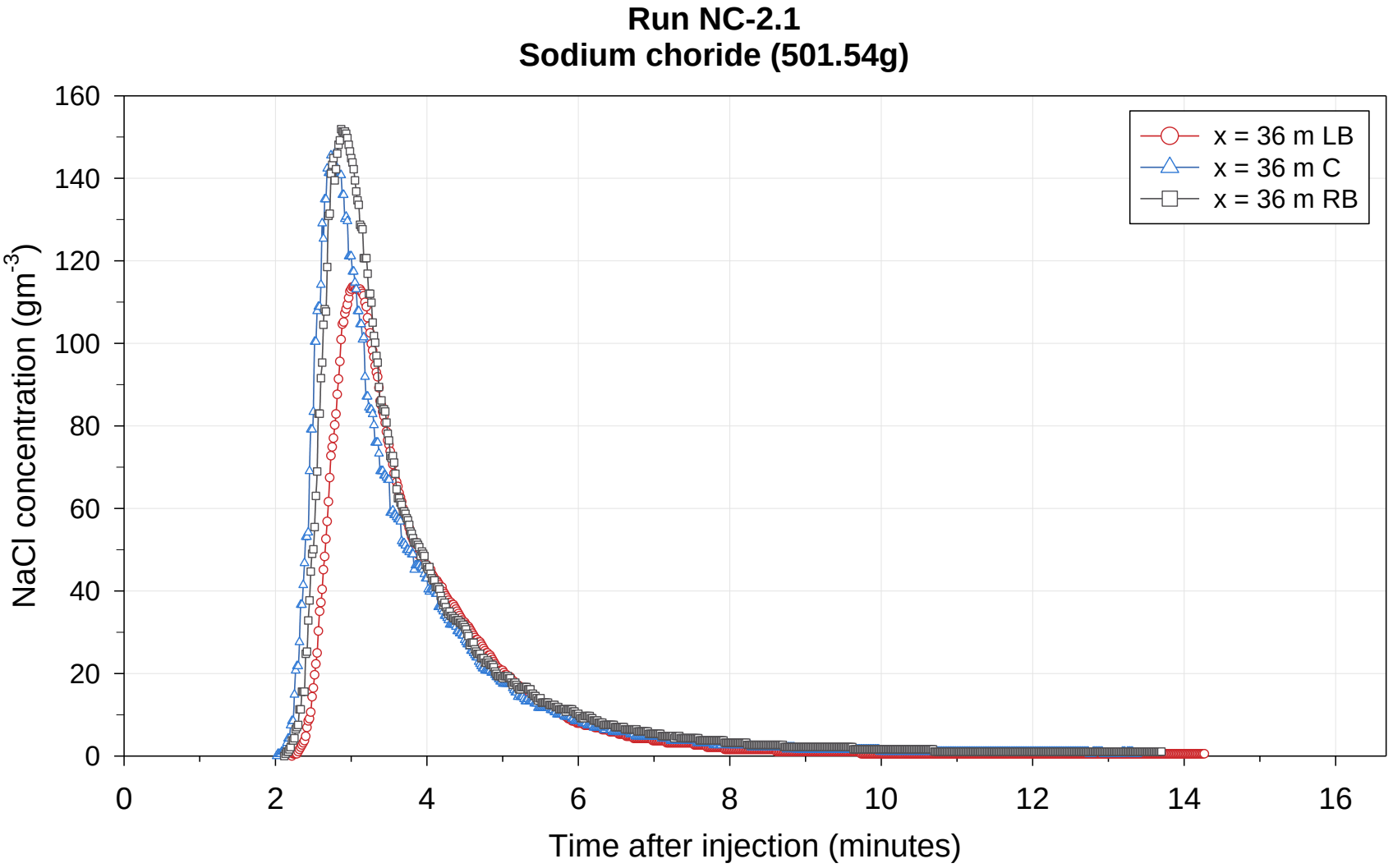

Figure F 7. Sodium chloride concentration during run NC-2.1.

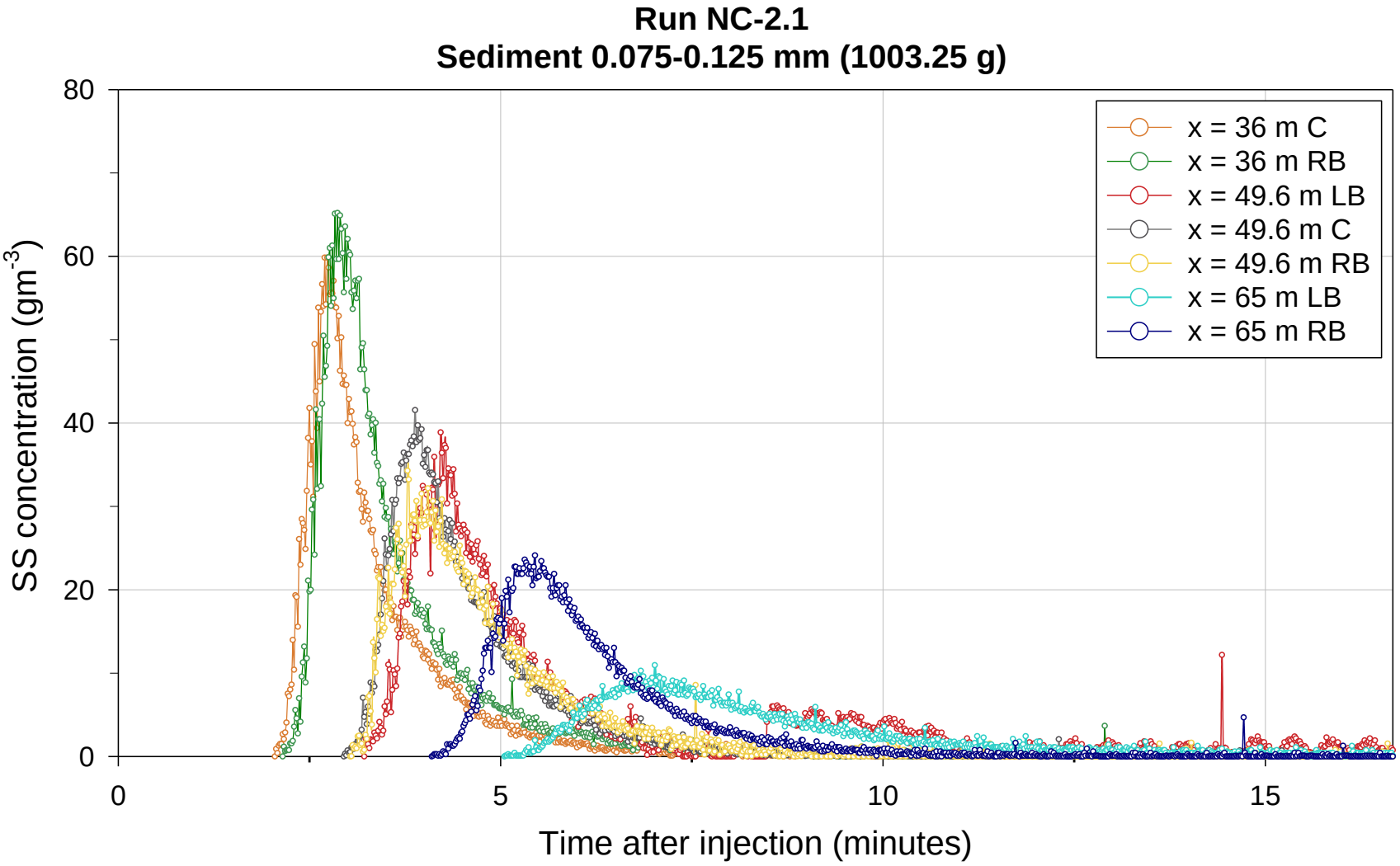

Figure F 8. Suspended sediment concentration during run NC-2.1.

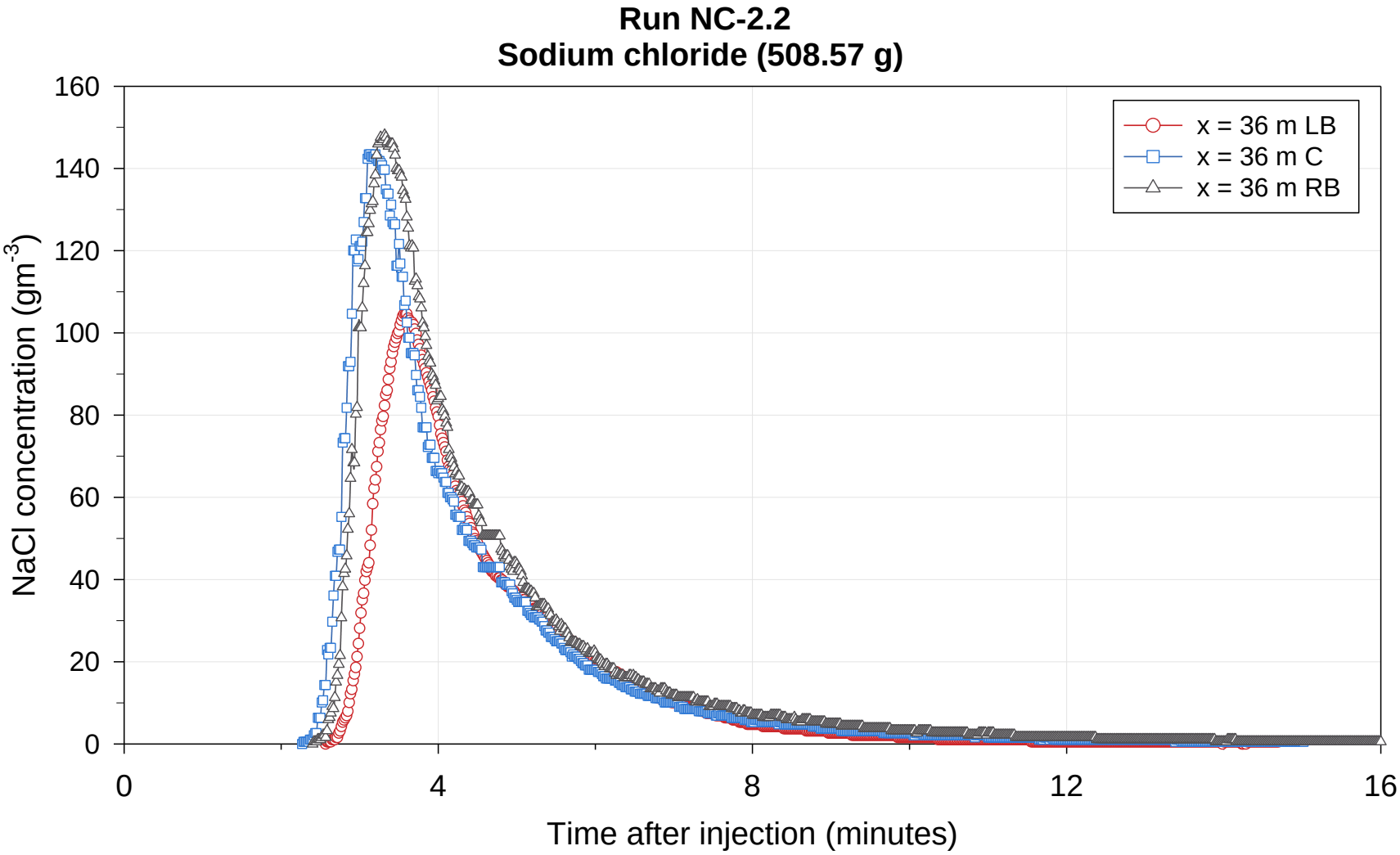

Figure F 9. Sodium chloride concentration during run NC-2.2.

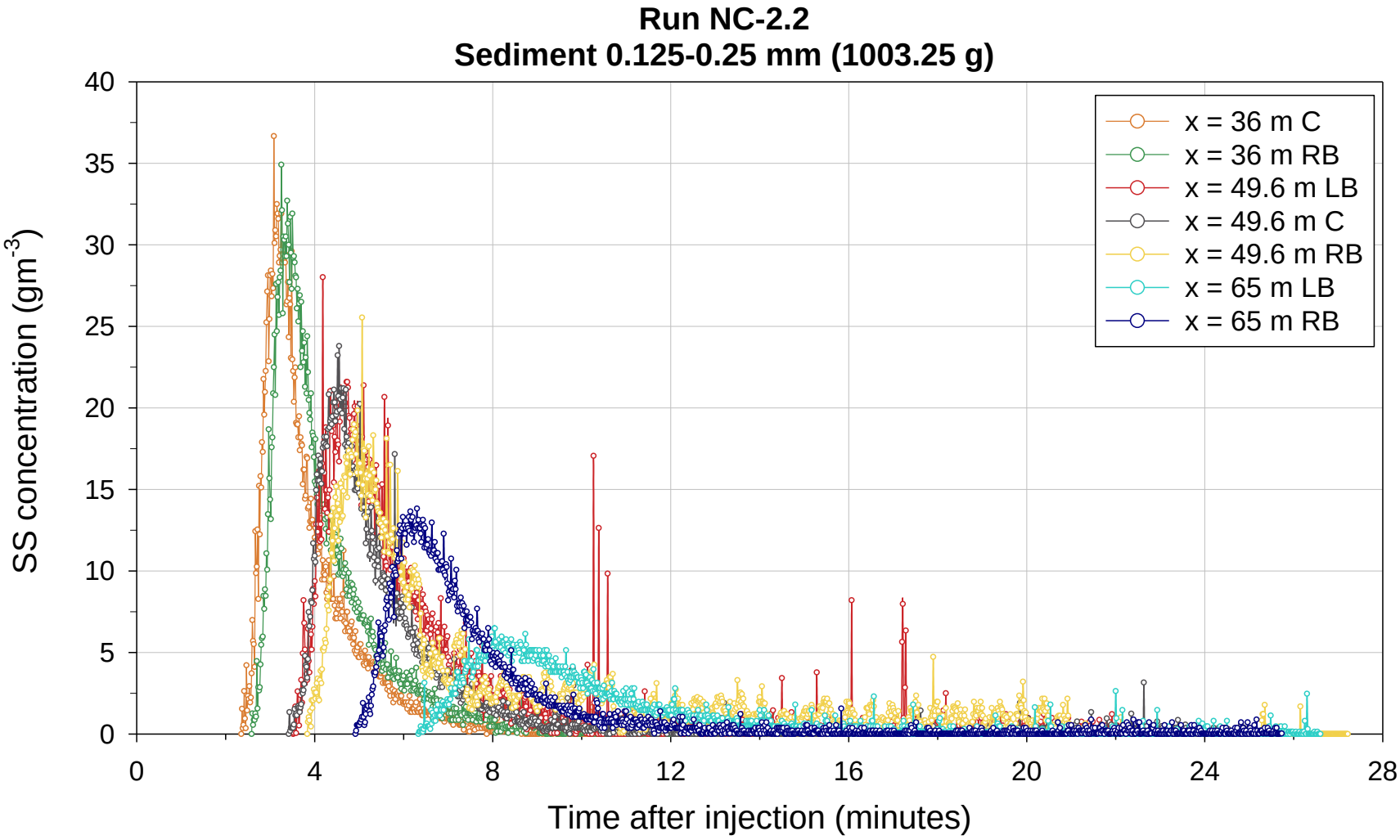

Figure F 10. Suspended sediment concentration during run NC-2.2.

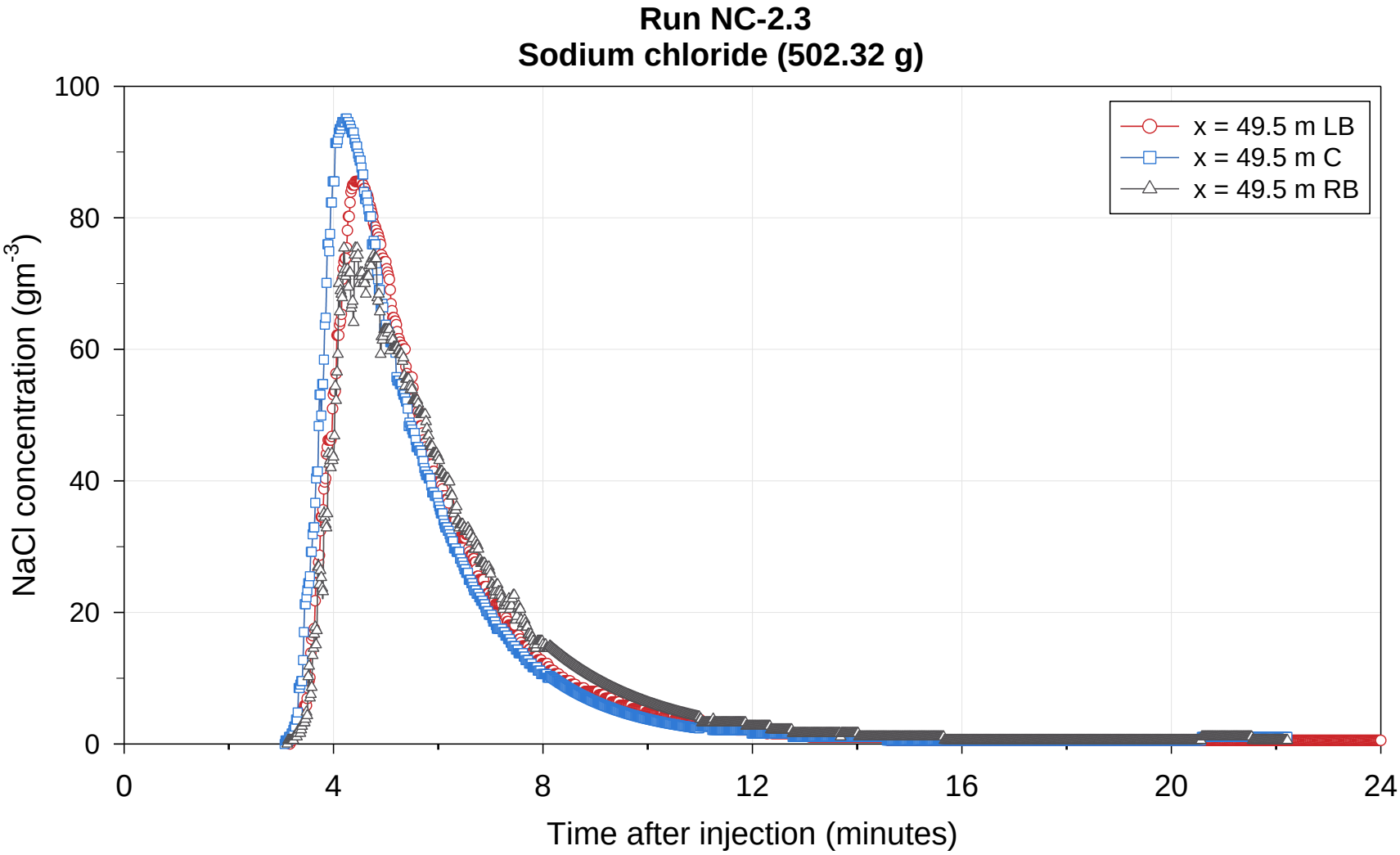

Figure F 11. Sodium chloride concentration during run NC-2.3.

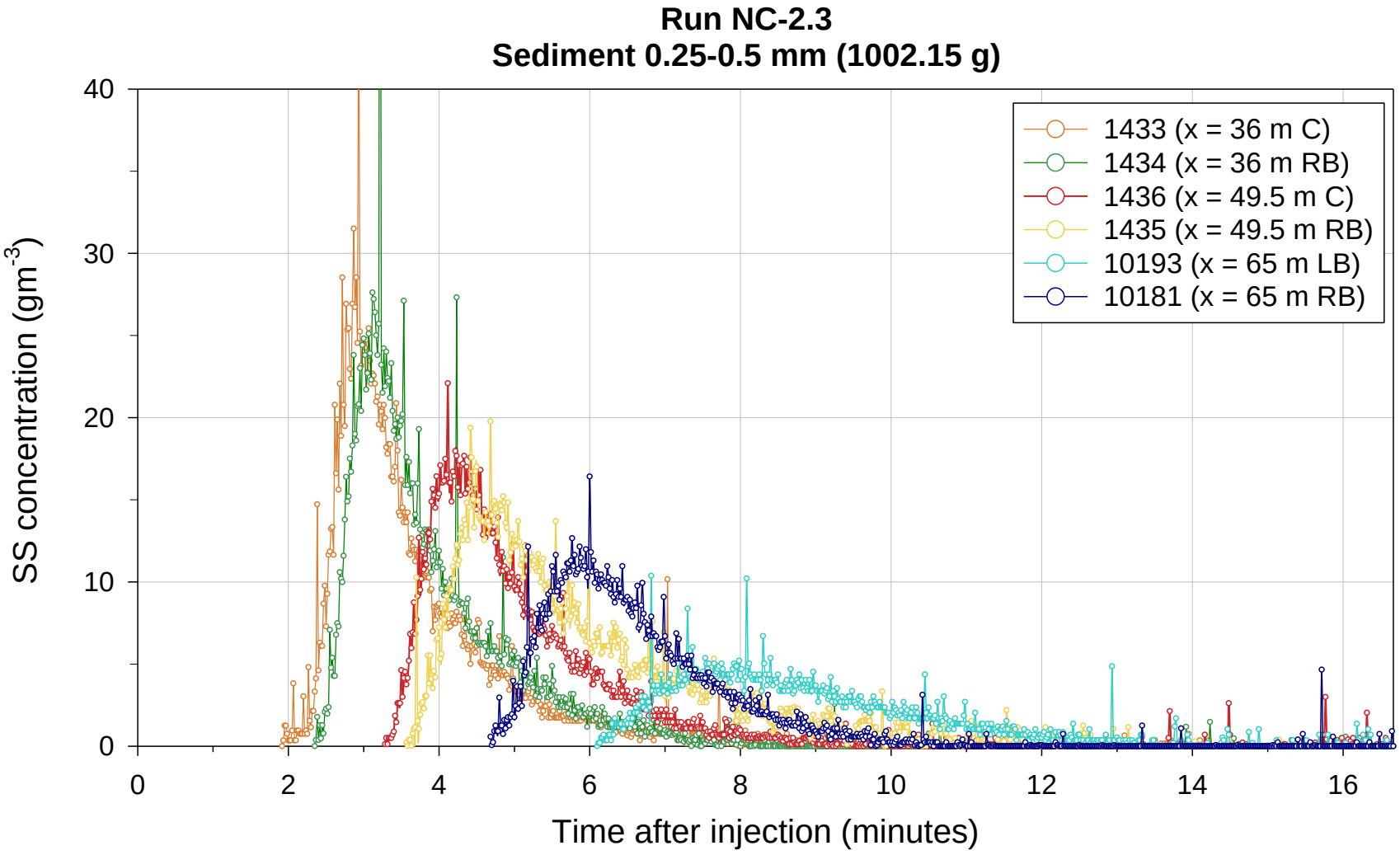

Figure F 12. Suspended sediment concentration during run NC-2.3.

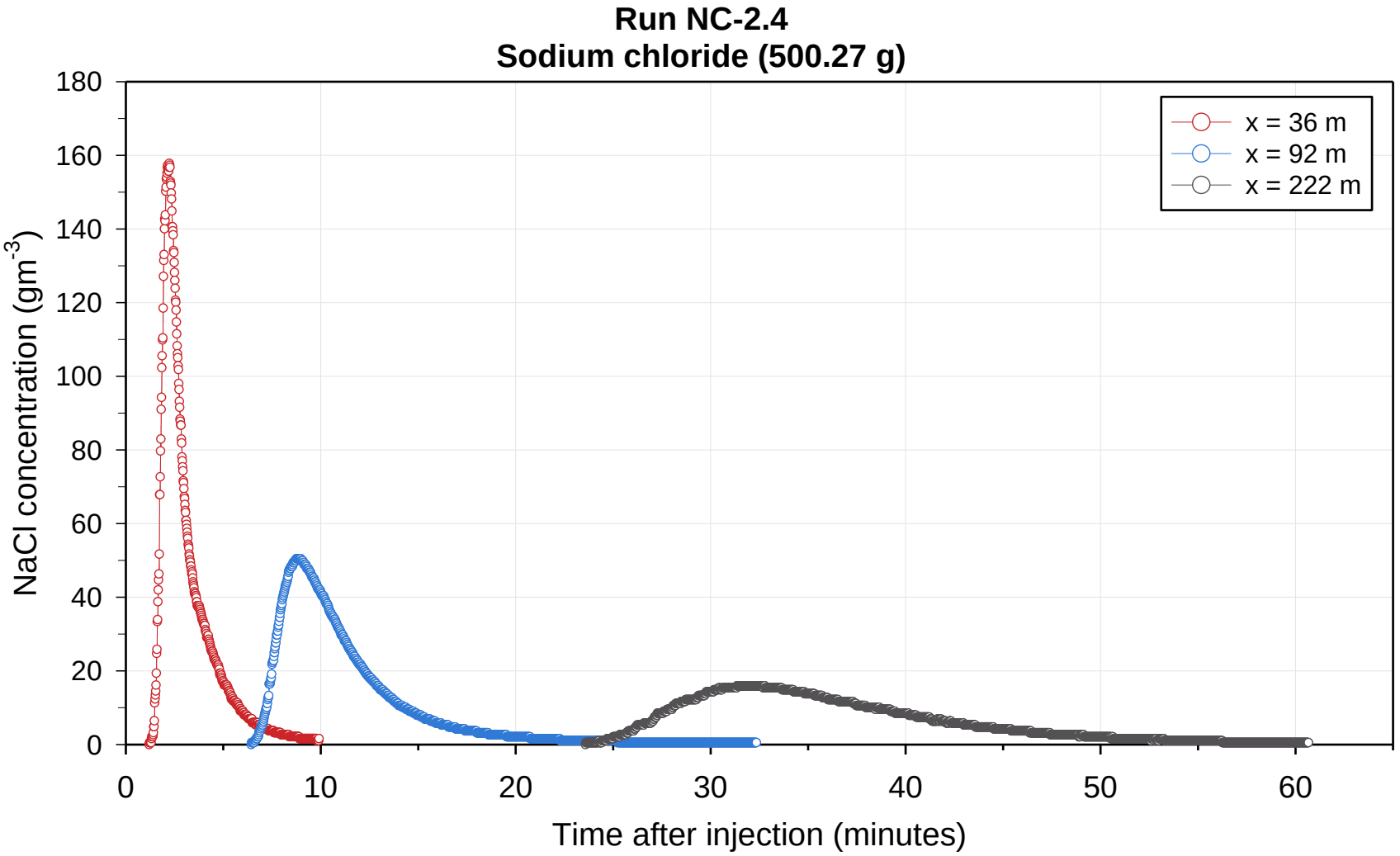

Figure F 13. Sodium chloride concentration during run NC-2.4.

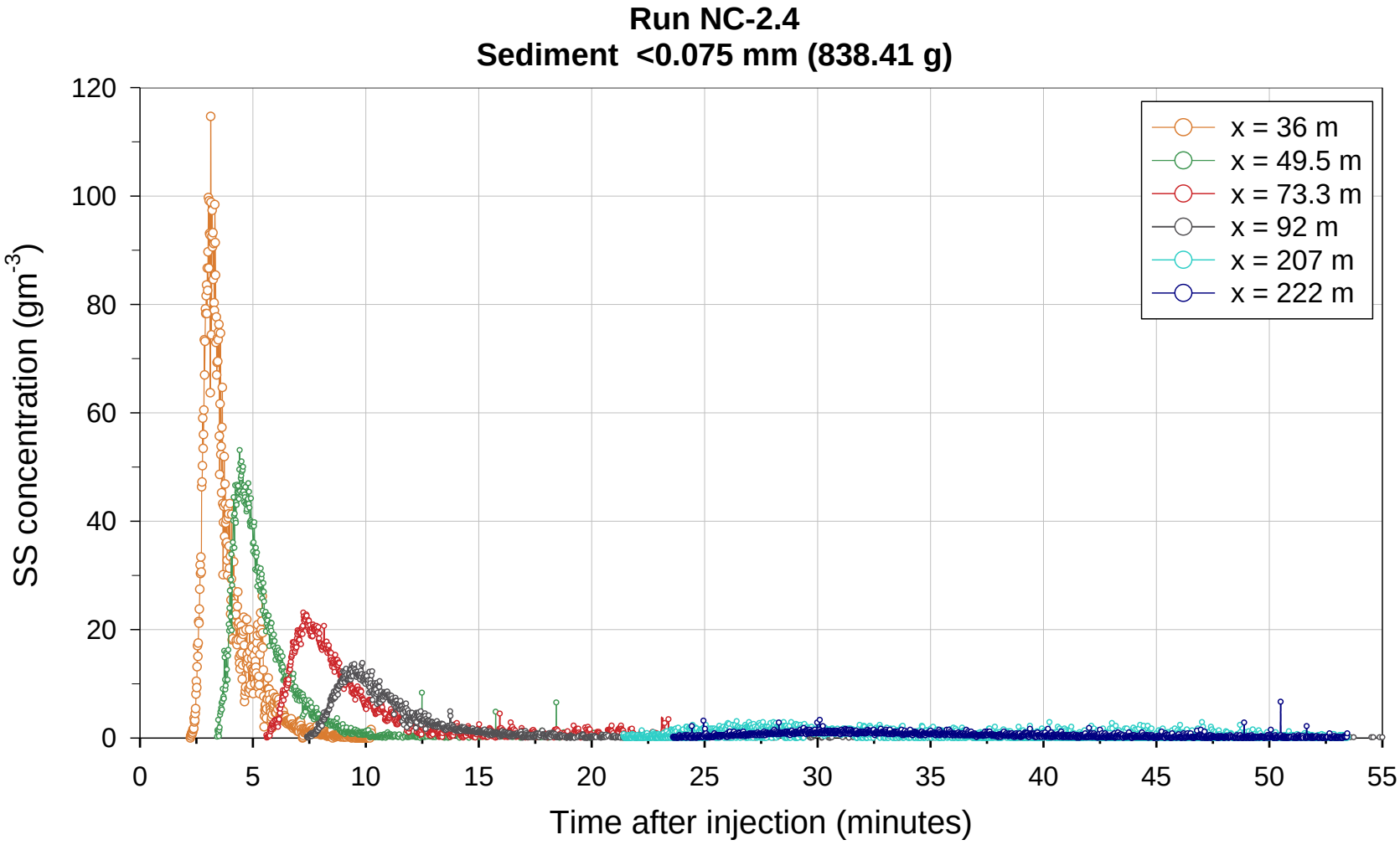

Figure F 14. Suspended sediment concentration during run NC-2.4.

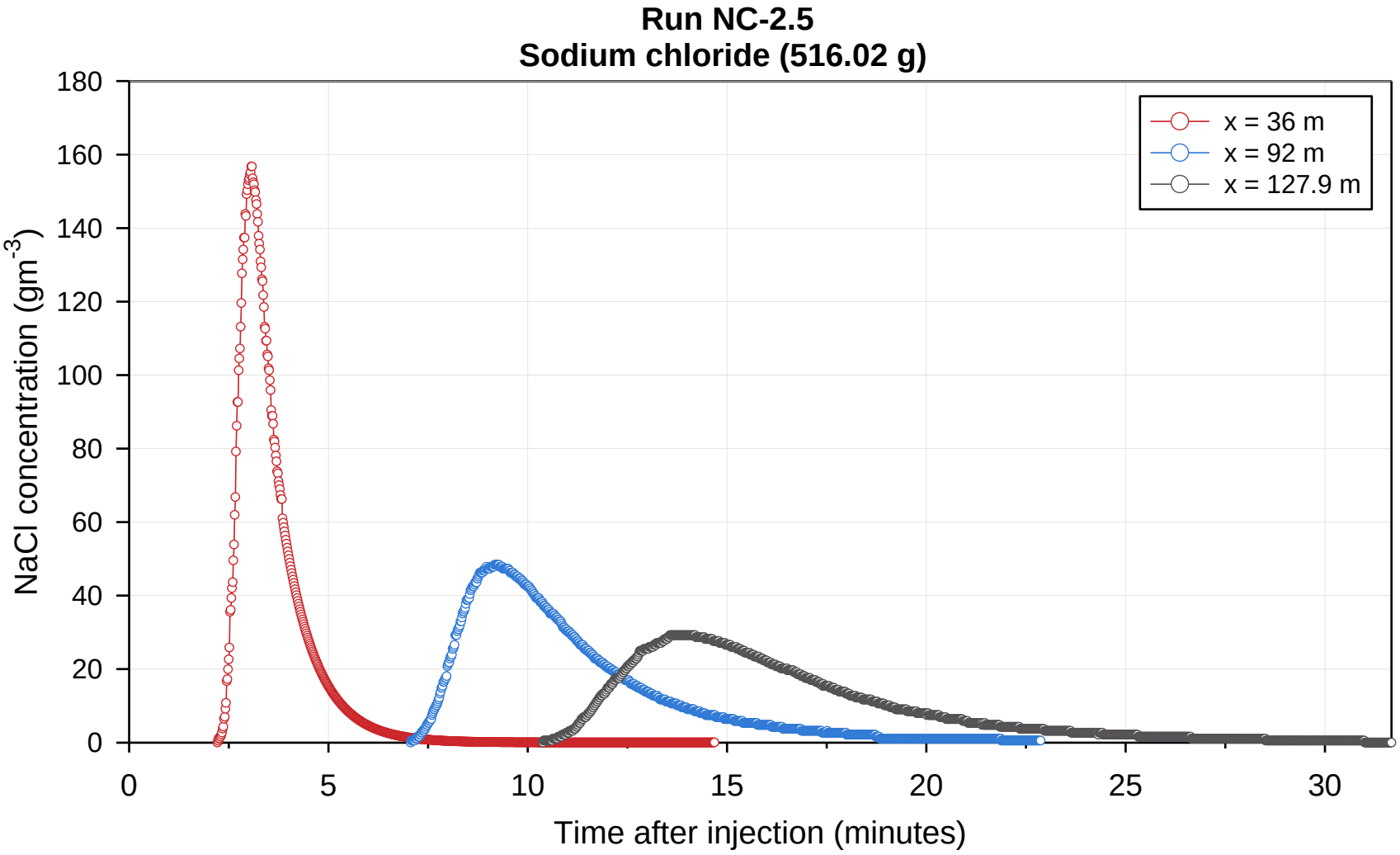

Figure F 15. Sodium chloride concentration during run NC-2.5.

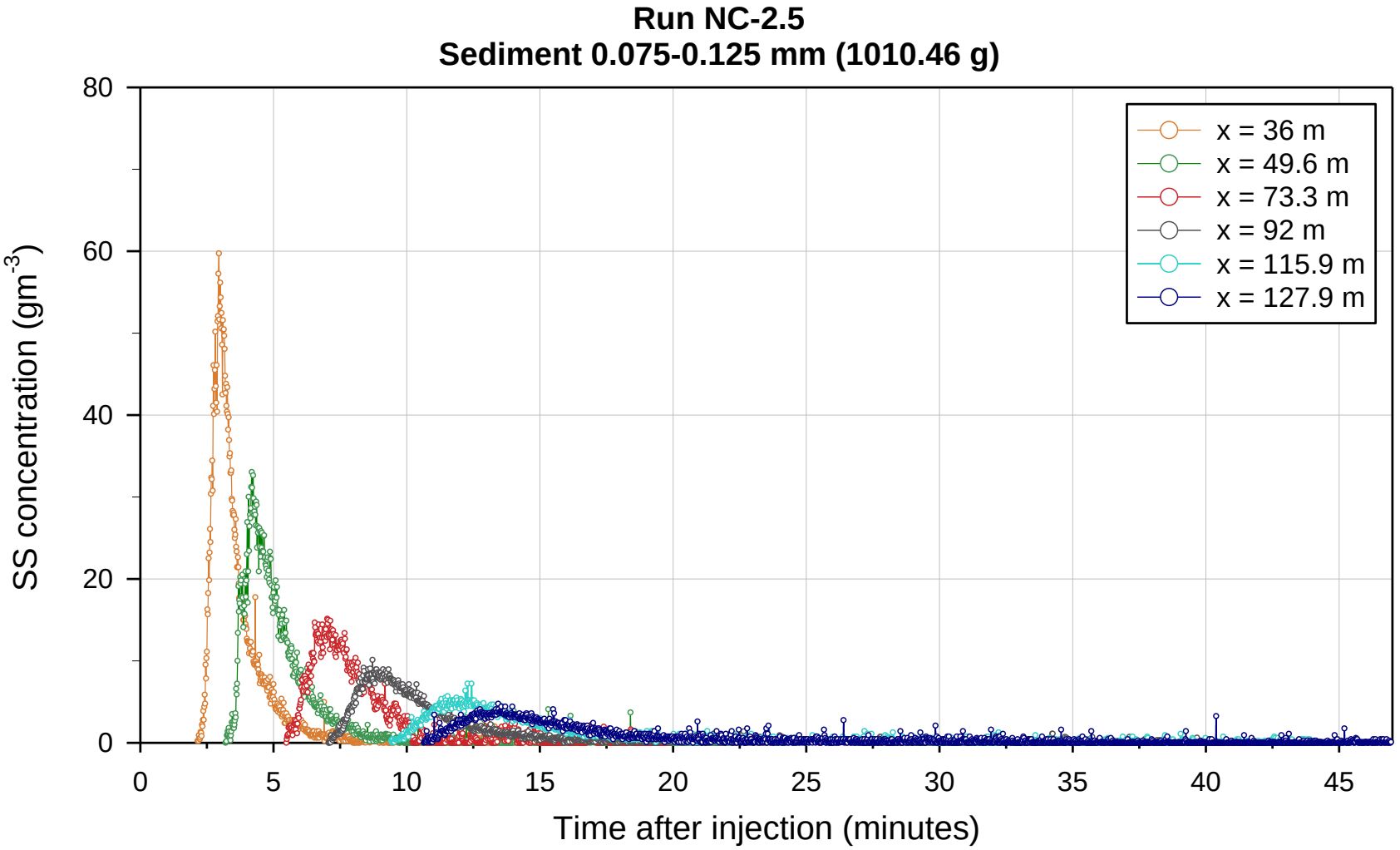

Figure F 16. Suspended sediment concentration during run NC-2.5.

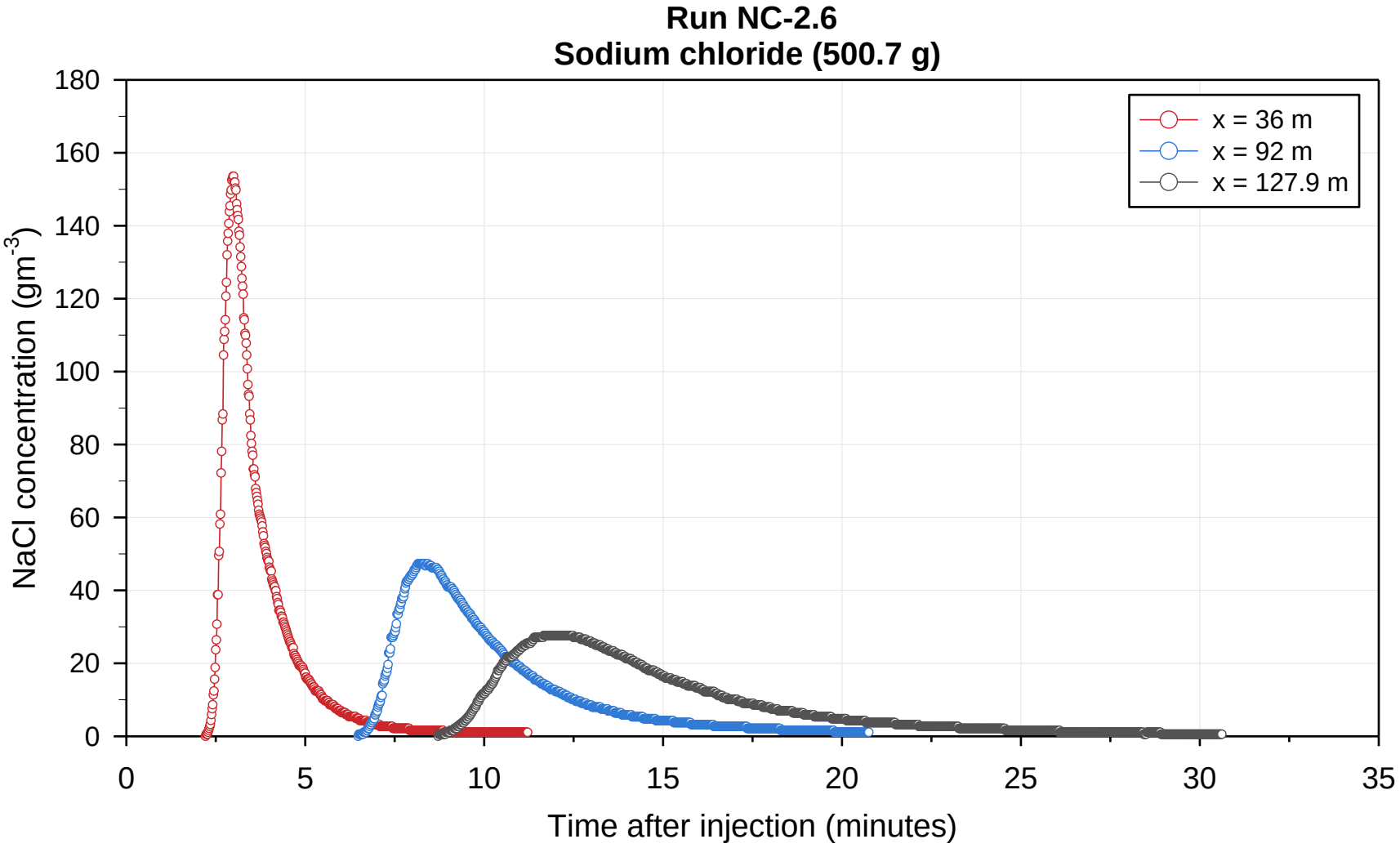

Figure F 17. Sodium chloride concentration during run NC-2.6.

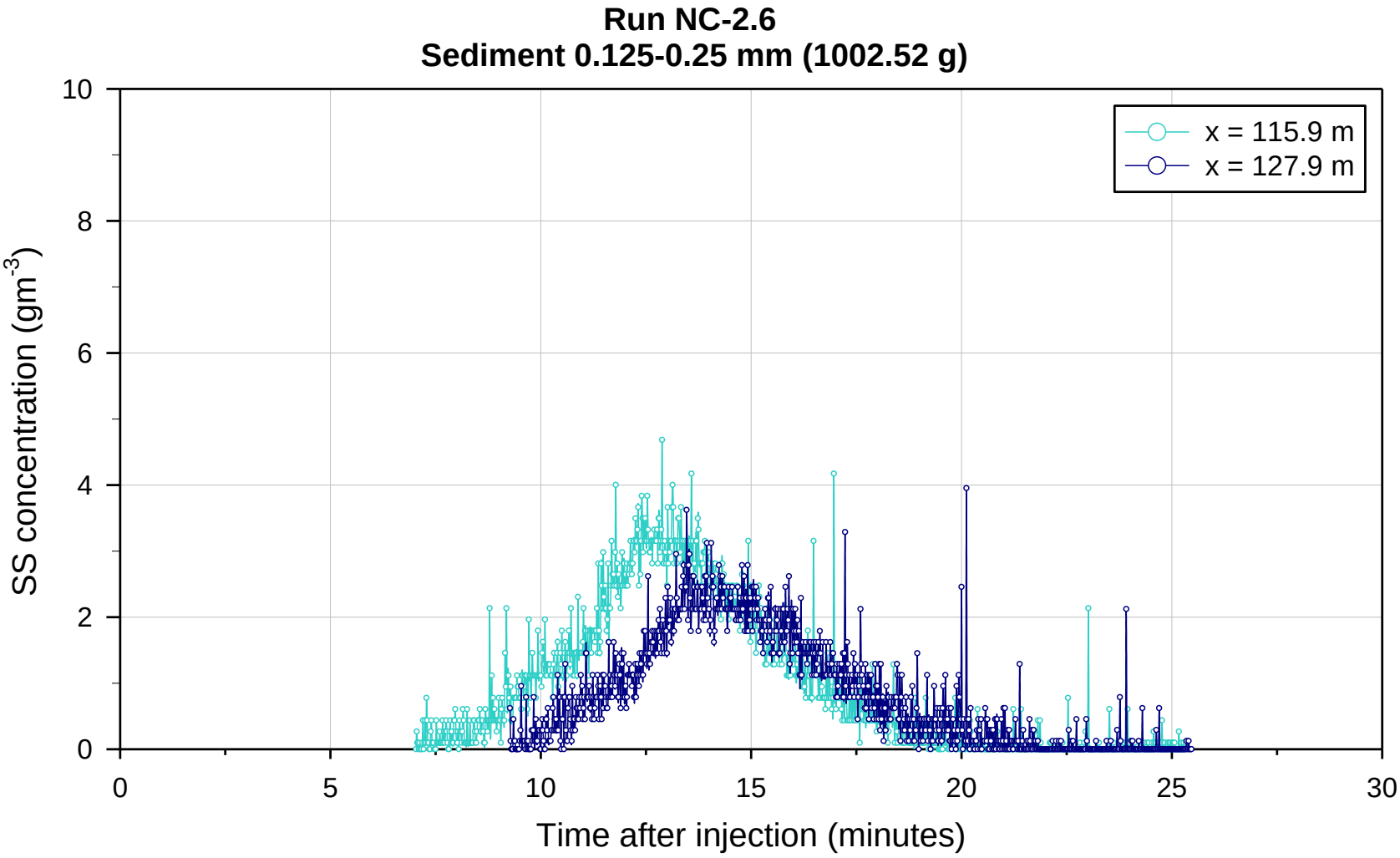

Figure F 18. Suspended sediment concentration during run NC-2.6.

Appendix G

Relative errors for peak concentration, time to peak, start, and duration of the curves modeled using the longitudinal dispersion coefficients from the predictive formulas in the concrete channel at x = 370.15 m.

Table G 1. Peak concentration relative errors to observed data (concrete channel).

Reference	K_x	C_{peak} relative error (%) $\frac{\text{Modeled value} - \text{observed value}}{\text{Observed value}}$									
		Run								Average	CV
		CC-2	CC-3	CC-4	CC-5	CC-6	CC-7	CC-8	CC-9		
Elder (1959)	0.03	453	479	484	531	483	609	500	511	506	9
Taylor (1954)	0.06	324	344	348	384	348	444	360	369	365	10
Devens (2006)	0.08	264	281	285	316	284	367	295	302	299	10
Parker (1961)	0.11	199	213	216	242	216	284	225	231	228	11
McQuivey and Keefer (1974)	0.15	158	170	173	195	172	231	180	185	183	12
Ribeiro et al. (2010)	0.15	156	167	170	192	170	228	177	182	180	12
Sattar & Gharabaghi (2015) (F1)	1.13	-5	-1	0	8	0	22	3	5	4	202
Sattar & Gharabaghi (2015) (F2)	1.23	-9	-5	-4	4	-4	17	-1	1	0	-3565
Iwasa & Aya (1991)	3.36	-44	-42	-41	-37	-41	-29	-40	-39	-39	-12
Disley et al. (2015)	3.56	-46	-43	-43	-38	-43	-31	-41	-40	-41	-11
Sahay (2013)	5.06	-54	-52	-52	-48	-52	-41	-50	-50	-50	-8
Wang et al (2017)	5.23	-55	-53	-53	-49	-53	-42	-51	-50	-51	-8
Etemad-Shahidi and Taghipour (2012)	6.50	-59	-58	-57	-54	-57	-48	-56	-55	-56	-6
Deng et al. (2001)	6.62	-60	-58	-58	-54	-58	-48	-56	-56	-56	-6
Wang and Huai (2016)	6.77	-60	-58	-58	-55	-58	-49	-57	-56	-56	-6
Koussis & Mirassol (1998)	6.80	-60	-58	-58	-55	-58	-49	-57	-56	-56	-6
Zeng & Huai (2014)	6.99	-61	-59	-59	-55	-59	-50	-57	-57	-57	-6
Liu (1977)	7.01	-61	-59	-59	-55	-59	-50	-58	-57	-57	-6
Kashefipur & Falconer (2002) (F1)	8.15	-63	-62	-61	-58	-61	-53	-60	-60	-60	-5
Li et al. (2013)	8.67	-65	-63	-63	-59	-63	-54	-61	-61	-61	-5
Seo & Cheong (1998)	9.05	-65	-64	-63	-60	-63	-55	-62	-62	-62	-5
Sahay & Dutta (2009)	9.39	-66	-64	-64	-61	-64	-56	-63	-62	-62	-5

Reference	K_x	C_{peak} relative error (%) $\frac{\text{Modeled value} - \text{observed value}}{\text{Observed value}}$									
		Run								Average	CV
		CC-2	CC-3	CC-4	CC-5	CC-6	CC-7	CC-8	CC-9		
Alizadeh et al. (2017)	9.55	-66	-64	-64	-61	-64	-56	-63	-62	-63	-5
Kashefipur & Falconer (2002) (F2)	11.85	-69	-68	-67	-65	-67	-60	-67	-66	-66	-4
Fischer (1975)	17.42	-74	-73	-72	-70	-72	-67	-72	-71	-71	-3
Oliveira et al. (2017)	79.26	-84	-83	-83	-81	-83	-79	-82	-82	-82	-2

Table G 2. Peak time relative errors to observed data (concrete channel).

Reference	K_x	t_{peak} relative error (%) $\frac{\text{Modeled value} - \text{observed value}}{\text{Observed value}}$									
		Run								Average	CV
		CC-2	CC-3	CC-4	CC-5	CC-6	CC-7	CC-8	CC-9		
Elder (1959)	0.03	4	4	5	4	3	3	4	4	4	17
Taylor (1954)	0.06	4	4	5	4	3	3	4	4	4	17
Devens (2006)	0.08	4	4	5	4	3	3	4	4	4	17
Parker (1961)	0.11	4	4	5	4	3	3	4	4	4	17
McQuivey and Keefer (1974)	0.15	3	4	5	3	3	3	4	3	4	18
Ribeiro et al. (2010)	0.15	3	4	5	3	3	3	4	3	4	18
Sattar & Gharabaghi (2015) (F1)	1.13	3	3	4	3	3	3	4	3	3	20
Sattar & Gharabaghi (2015) (F2)	1.23	3	3	4	3	3	3	4	3	3	20
Iwasa & Aya (1991)	3.36	1	2	3	1	1	1	2	1	2	37
Disley et al. (2015)	3.56	1	1	3	1	1	1	2	1	1	47
Sahay (2013)	5.06	0	1	2	0	0	0	1	0	1	104
Wang et al (2017)	5.23	0	1	2	0	0	0	1	0	1	104
Etemad-Shahidi and Taghipour (2012)	6.50	-1	0	1	-1	-1	-1	0	-1	0	-123
Deng et al. (2001)	6.62	-1	0	1	-1	-1	-1	0	-1	0	-123
Wang and Huai (2016)	6.77	-1	0	1	-1	-1	-1	0	-1	0	-123
Koussis & Mirassol (1998)	6.80	-1	0	1	-1	-1	-1	0	-1	0	-123
Zeng & Huai (2014)	6.99	-1	0	1	-1	-1	-1	0	-1	0	-123
Liu (1977)	7.01	-1	0	1	-1	-1	-1	0	-1	0	-123
Kashefipur & Falconer (2002) (F1)	8.15	-1	-1	0	-1	-2	-2	-1	-1	-1	-50

Reference	K_x	t_{peak} relative error (%) $\frac{\text{Modeled value} - \text{observed value}}{\text{Observed value}}$									
		Run								Average	CV
		CC-2	CC-3	CC-4	CC-5	CC-6	CC-7	CC-8	CC-9		
Li et al. (2013)	8.67	-2	-1	0	-2	-2	-2	-1	-2	-2	-38
Seo & Cheong (1998)	9.05	-2	-2	-1	-2	-3	-3	-1	-2	-2	-31
Sahay & Dutta (2009)	9.39	-2	-2	-1	-2	-3	-3	-1	-2	-2	-31
Alizadeh et al. (2017)	9.55	-3	-2	-1	-3	-3	-3	-2	-3	-2	-26
Kashefipur & Falconer (2002) (F2)	11.85	-4	-4	-3	-4	-4	-4	-3	-4	-4	-16
Fischer (1975)	17.42	-7	-7	-6	-7	-8	-8	-7	-7	-7	-8
Oliveira et al. (2017)	79.26	-36	-35	-35	-36	-36	-36	-35	-36	-35	-1

Table G 3. Start time relative errors to observed data (concrete channel).

Reference	K_x	t_{start} relative error (%) $\frac{\text{Modeled value} - \text{observed value}}{\text{Observed value}}$									
		Run								Average	CV
		CC-2	CC-3	CC-4	CC-5	CC-6	CC-7	CC-8	CC-9		
Elder (1959)	0.03	13	14	17	17	14	14	14	14	15	10
Taylor (1954)	0.06	12	13	16	15	13	12	12	13	13	10
Devens (2006)	0.08	11	12	15	14	12	11	11	12	12	11
Parker (1961)	0.11	10	10	13	12	10	10	10	10	11	13
McQuivey and Keefer (1974)	0.15	8	9	12	11	9	8	8	9	9	14
Ribeiro et al. (2010)	0.15	8	8	11	11	8	8	8	8	9	14
Sattar & Gharabaghi (2015) (F1)	1.13	-7	-7	-5	-5	-7	-8	-8	-7	-7	-16
Sattar & Gharabaghi (2015) (F2)	1.23	-8	-8	-6	-6	-8	-8	-8	-8	-7	-14
Iwasa & Aya (1991)	3.36	-21	-22	-20	-20	-22	-22	-22	-22	-21	-4
Disley et al. (2015)	3.56	-22	-23	-21	-21	-23	-23	-23	-23	-22	-4
Sahay (2013)	5.06	-27	-29	-27	-27	-29	-29	-29	-29	-28	-3
Wang et al (2017)	5.23	-28	-29	-28	-28	-29	-30	-30	-29	-29	-3
Etemad-Shahidi and Taghipour (2012)	6.50	-32	-33	-31	-32	-33	-33	-33	-33	-33	-3
Deng et al. (2001)	6.62	-32	-34	-32	-32	-34	-34	-34	-34	-33	-3
Wang and Huai (2016)	6.77	-33	-34	-32	-33	-34	-34	-34	-34	-34	-3
Koussis & Mirassol (1998)	6.80	-33	-34	-32	-33	-34	-34	-34	-34	-34	-3
Zeng & Huai (2014)	6.99	-33	-35	-33	-33	-35	-35	-35	-35	-34	-3

Reference	K_x	t_{start} relative error (%) $\frac{\text{Modeled value} - \text{observed value}}{\text{Observed value}}$									
		Run								Average	CV
		CC-2	CC-3	CC-4	CC-5	CC-6	CC-7	CC-8	CC-9		
Liu (1977)	7.01	-33	-35	-33	-33	-35	-35	-35	-35	-34	-3
Kashefipur & Falconer (2002) (F1)	8.15	-36	-38	-36	-36	-38	-38	-38	-38	-37	-2
Li et al. (2013)	8.67	-37	-39	-38	-38	-39	-39	-39	-39	-39	-2
Seo & Cheong (1998)	9.05	-38	-40	-38	-39	-40	-40	-40	-40	-39	-2
Sahay & Dutta (2009)	9.39	-39	-40	-39	-39	-40	-41	-41	-40	-40	-2
Alizadeh et al. (2017)	9.55	-39	-41	-39	-39	-41	-41	-41	-41	-40	-2
Kashefipur & Falconer (2002) (F2)	11.85	-43	-45	-44	-44	-45	-46	-46	-45	-45	-2
Fischer (1975)	17.42	-51	-53	-52	-52	-53	-54	-54	-53	-53	-2
Oliveira et al. (2017)	79.26	-80	-82	-81	-82	-82	-82	-82	-82	-82	-1

Table G 4. Duration relative errors to observed data (concrete channel).

Reference	K_x	Duration relative error (%) $\frac{\text{Modeled value} - \text{observed value}}{\text{Observed value}}$									
		Run								Average	CV
		CC-2	CC-3	CC-4	CC-5	CC-6	CC-7	CC-8	CC-9		
Elder (1959)	0.03	-83	-82	-82	-82	-82	-82	-82	-82	-83	0
Taylor (1954)	0.06	-78	-77	-77	-77	-77	-77	-77	-77	-77	-1
Devens (2006)	0.08	-75	-74	-74	-74	-74	-74	-74	-74	-74	-1
Parker (1961)	0.11	-70	-68	-68	-68	-68	-68	-68	-68	-68	-1
McQuivey and Keefer (1974)	0.15	-65	-64	-64	-64	-64	-64	-64	-64	-64	-1
Ribeiro et al. (2010)	0.15	-65	-63	-63	-63	-63	-63	-63	-63	-63	-1
Sattar & Gharabaghi (2015) (F1)	1.13	-10	-5	-5	-5	-5	-5	-5	-5	-5	-35
Sattar & Gharabaghi (2015) (F2)	1.23	-7	-1	-1	-1	-1	-1	-1	-1	-2	-94
Iwasa & Aya (1991)	3.36	48	57	57	57	57	57	57	57	56	6
Disley et al. (2015)	3.56	52	61	61	61	61	61	61	61	60	6
Sahay (2013)	5.06	78	90	90	90	90	90	90	90	88	5
Wang et al (2017)	5.23	80	93	93	93	93	93	93	93	92	5
Etemad-Shahidi and Taghipour (2012)	6.50	99	113	113	113	113	113	113	113	111	5
Deng et al. (2001)	6.62	101	115	115	115	115	115	115	115	113	4
Wang and Huai (2016)	6.77	103	117	117	117	117	117	117	117	115	4
Koussis & Mirassol (1998)	6.80	103	118	118	118	118	118	118	118	116	5

Reference	K_x	Duration relative error (%) $\frac{\text{Modeled value} - \text{observed value}}{\text{Observed value}}$									
		Run								Average	CV
		CC-2	CC-3	CC-4	CC-5	CC-6	CC-7	CC-8	CC-9		
Zeng & Huai (2014)	6.99	105	120	120	120	120	120	120	120	118	4
Liu (1977)	7.01	105	121	121	121	121	121	121	121	119	5
Kashefipur & Falconer (2002) (F1)	8.15	120	136	136	136	136	136	136	136	134	4
Li et al. (2013)	8.67	126	143	143	143	143	143	143	143	141	4
Seo & Cheong (1998)	9.05	130	148	148	148	148	148	148	148	146	4
Sahay & Dutta (2009)	9.39	134	151	151	151	151	151	151	151	149	4
Alizadeh et al. (2017)	9.55	135	153	153	153	153	153	153	153	151	4
Kashefipur & Falconer (2002) (F2)	11.85	159	180	180	180	180	180	180	180	177	4
Fischer (1975)	17.42	206	232	232	232	232	232	232	232	229	4
Oliveira et al. (2017)	79.26	453	529	529	529	529	529	529	529	520	5

Appendix H

Relative errors for peak concentration, time to peak, start, and duration of the curves modeled using the longitudinal dispersion coefficients from the predictive formulas in the natural channel at x = 127.9 m.

Table H 1. Peak concentration relative errors to observed data (natural channel).

Reference	**K_x**	**C_{peak} relative error (%)** $\frac{\text{Modeled value} - \text{observed value}}{\text{Observed value}}$		
		Run		Average
		NC-5	NC-6	
Ribeiro et al. (2010)	0.01	332	345	338
Seo & Cheong (1998)	0.02	262	273	267
Elder (1959)	0.04	152	159	155
Deng et al. (2001)	0.04	150	157	154
McQuivey and Keefer (1974)	0.06	113	119	116
Taylor (1954)	0.07	94	99	96
Disley et al. (2015)	0.07	91	96	94
Sattar & Gharabaghi (2015) (F1)	0.10	63	68	66
Parker (1961)	0.19	22	25	24
Kashefipur & Falconer (2002) (F1)	0.23	10	13	12
Devens (2006)	0.25	6	10	8
Fischer (1975)	0.38	-12	-10	-11
Alizadeh et al. (2017)	0.39	-13	-11	-12
Kashefipur & Falconer (2002) (F2)	0.44	-17	-15	-16
Li et al. (2013)	0.62	-29	-27	-28
Sahay (2013)	0.84	-37	-36	-37
Wang and Huai (2016)	0.92	-40	-38	-39
Wang et al (2017)	0.96	-41	-39	-40
Zeng & Huai (2014)	0.96	-41	-39	-40
Sahay & Dutta (2009)	0.99	-41	-40	-40
Etemad-Shahidi and Taghipour (2012)	1.55	-50	-48	-49
Sattar & Gharabaghi (2015) (F2)	1.90	-52	-51	-52
Liu (1977)	2.71	-56	-55	-55
Oliveira et al. (2017)	3.51	-58	-56	-57
Iwasa & Aya (1991)	3.61	-58	-56	-57
Koussis & Mirassol (1998)	6.84	-56	-55	-56

Table H 2. Peak time relative errors to observed data (natural channel).

Reference	K_x	t_{peak} relative error (%) $\frac{\text{Modeled value} - \text{observed value}}{\text{Observed value}}$		
		Run		Average
		NC-5	NC-6	
Ribeiro et al. (2010)	0.01	12	25	18
Seo & Cheong (1998)	0.02	12	24	18
Elder (1959)	0.04	11	24	18
Deng et al. (2001)	0.04	11	24	18
McQuivey and Keefer (1974)	0.06	11	24	17
Taylor (1954)	0.07	11	24	17
Disley et al. (2015)	0.07	11	23	17
Sattar & Gharabaghi (2015) (F1)	0.10	10	23	17
Parker (1961)	0.19	9	21	15
Kashefipur & Falconer (2002) (F1)	0.23	8	20	14
Devens (2006)	0.25	8	20	14
Fischer (1975)	0.38	5	17	11
Alizadeh et al. (2017)	0.39	5	17	11
Kashefipur & Falconer (2002) (F2)	0.44	4	16	10
Li et al. (2013)	0.62	1	13	7
Sahay (2013)	0.84	-3	8	3
Wang and Huai (2016)	0.92	-4	7	2
Wang et al (2017)	0.96	-4	6	1
Zeng & Huai (2014)	0.96	-4	6	1
Sahay & Dutta (2009)	0.99	-5	6	0
Etemad-Shahidi and Taghipour (2012)	1.55	-13	-3	-8
Sattar & Gharabaghi (2015) (F2)	1.90	-18	-9	-13
Liu (1977)	2.71	-28	-20	-24
Oliveira et al. (2017)	3.51	-36	-29	-32
Iwasa & Aya (1991)	3.61	-37	-30	-33
Koussis & Mirassol (1998)	6.84	-58	-53	-55

Table H 3. Start time relative errors to observed data (natural channel).

Reference	**K_x**	**t_{start} relative error (%)** $\frac{\text{Modeled value} - \text{observed value}}{\text{Observed value}}$		
		Run		Average
		NC-5	NC-6	
Ribeiro et al. (2010)	0.01	25	41	33
Seo & Cheong (1998)	0.02	22	37	30
Elder (1959)	0.04	13	27	20
Deng et al. (2001)	0.04	13	27	20
McQuivey and Keefer (1974)	0.06	8	22	15
Taylor (1954)	0.07	5	18	12
Disley et al. (2015)	0.07	4	18	11
Sattar & Gharabaghi (2015) (F1)	0.10	-1	11	5
Parker (1961)	0.19	-13	-3	-8
Kashefipur & Falconer (2002) (F1)	0.23	-18	-8	-13
Devens (2006)	0.25	-20	-10	-15
Fischer (1975)	0.38	-30	-21	-26
Alizadeh et al. (2017)	0.39	-30	-22	-26
Kashefipur & Falconer (2002) (F2)	0.44	-33	-25	-29
Li et al. (2013)	0.62	-42	-35	-38
Sahay (2013)	0.84	-50	-44	-47
Wang and Huai (2016)	0.92	-52	-46	-49
Wang et al (2017)	0.96	-53	-48	-50
Zeng & Huai (2014)	0.96	-54	-48	-51
Sahay & Dutta (2009)	0.99	-54	-48	-51
Etemad-Shahidi and Taghipour (2012)	1.55	-65	-60	-63
Sattar & Gharabaghi (2015) (F2)	1.90	-70	-66	-68
Liu (1977)	2.71	-77	-74	-75
Oliveira et al. (2017)	3.51	-81	-79	-80
Iwasa & Aya (1991)	3.61	-82	-79	-80
Koussis & Mirassol (1998)	6.84	-90	-88	-89

Table H 4. Duration relative errors to observed data (natural channel).

Reference	**K_x**	**Duration relative error (%)** $\frac{\text{Modeled value} - \text{observed value}}{\text{Observed value}}$		
		Run		Average
		NC-2.5	NC-2.6	
Ribeiro et al. (2010)	0.01	-78	-79	-78
Seo & Cheong (1998)	0.02	-74	-75	-75
Elder (1959)	0.04	-63	-65	-64
Deng et al. (2001)	0.04	-63	-65	-64
McQuivey and Keefer (1974)	0.06	-56	-60	-58
Taylor (1954)	0.07	-52	-56	-54
Disley et al. (2015)	0.07	-52	-55	-53
Sattar & Gharabaghi (2015) (F1)	0.10	-44	-48	-46
Parker (1961)	0.19	-26	-32	-29
Kashefipur & Falconer (2002) (F1)	0.23	-18	-24	-21
Devens (2006)	0.25	-16	-22	-19
Fischer (1975)	0.38	2	-5	-2
Alizadeh et al. (2017)	0.39	3	-5	-1
Kashefipur & Falconer (2002) (F2)	0.44	8	0	4
Li et al. (2013)	0.62	26	17	22
Sahay (2013)	0.84	45	34	40
Wang and Huai (2016)	0.92	51	40	45
Wang et al (2017)	0.96	54	42	48
Zeng & Huai (2014)	0.96	54	42	48
Sahay & Dutta (2009)	0.99	56	44	50
Etemad-Shahidi and Taghipour (2012)	1.55	89	74	81
Sattar & Gharabaghi (2015) (F2)	1.90	106	90	98
Liu (1977)	2.71	138	120	129
Oliveira et al. (2017)	3.51	163	143	153
Iwasa & Aya (1991)	3.61	166	145	156
Koussis & Mirassol (1998)	6.84	234	208	221